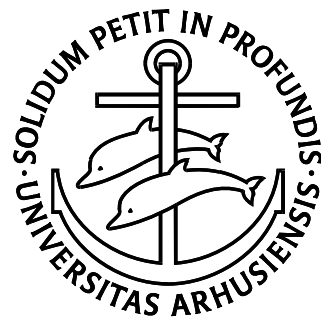


Development of a novel biomaterial:

A nanotechnological approach

PhD thesis

Thomas Hartvig Lindkær Jensen



Faculty of Health Sciences

University of Aarhus

2009

Development of a novel biomaterial:

A nanotechnological approach

PhD thesis

Thomas Hartvig Lindkær Jensen



Faculty of Health Sciences
University of Aarhus

Supervisors

Main Supervisor:

Prof. Kjeld Søballe, MD, DMSc
Department of Orthopaedic Surgery,
Aarhus University Hospital, Denmark

Project Supervisors:

Prof. Flemming Besenbacher, DSc
Interdisciplinary Nanoscience Center
Aarhus University, Denmark

Prof. Cody Bünger, MD, DMSc
Department of Orthopaedic Surgery,
Aarhus University Hospital, Denmark

Evaluation committee

Associate Prof. Jesper Skovhus Thomsen, PhD, DSc
Institute of Anatomy,
University of Aarhus, Denmark

Prof. John Jansen, DDS, PhD
Department of Periodontology and Biomaterials
Radboud University, Nijmegen, Netherlands

Prof. Michael Horton
London Centre for Nanotechnology and Dept. of Medicine
London University College, United Kingdom

Preface

This thesis is based on work carried out during my three years as PhD student at the Faculty of Health Sciences, Aarhus University, 2005-2009. The experiments were conducted at the Orthopaedic Research Laboratory, Aarhus University Hospital, Interdisciplinary Nanoscience Center (iNANO), Aarhus University, and Orthopaedic Biomechanics Laboratory, Hennepin Medical County Center, Minneapolis, USA.

I wish to express gratitude to my supervisors, Kjeld Søballe, Flemming Besenbacher & Cody Bünger for kind and supportive supervision and for offering the opportunity of doing interdisciplinary research. Thanks to my co-supervisors, Morten Foss & Jens Vinge Nygaard for mentoring in the scientific community and sharing expert knowledge. Thanks to Alireza Dolathshahi-Pirouz at iNANO for fruitful collaboration on several projects and for sharing both my cheers and frustrations with experimental work. Thanks to Jørgen Baas and Thomas Jakobsen at ortholab for crucial guidance and aid in animal studies.

Special thanks to everyone at ortholab and iNANO for invaluable help and a jolly work environment. Anette Baatrup, Anna Bay Nielsen, Jane Pauli, Lisa Feng & Anette Milton from Ortholab helped with cell studies and animal studies. Marianne Toft Vestergård, Henrik Saxø, Mikkel Saxø & Kazra Zainali from Ortholab and David Kraft from School of Odontology helped with animal studies. Jaques Chevallier, Gurvinder Singh, Anne Gry Hemmersam & Mads Bruun Hovgaard from iNANO helped with surface analysis techniques. Rune Hoff Lauridsen, Jette Lovmand & Mogens Duch from iNANO helped with cell microscopy. Jenny Malmström from iNANO helped with QCM-D. Joan Bechtold, Tony Meglich and Barbara Stickney from Minneapolis helped with animal studies. To my beloved Nina and our children, Anna and Jakob, thank you for enduring me as a PhD student and thank you for being my blessing and foremost inspiration.

Acknowledgements - disclosures

The studies were financially supported by the following non-commercial institutions: A.P. Møller Foundation, Augustinus Foundation, Danish Agency for Science, technology and Innovation, Danish Orthopaedic Research Society and Korning Foundation.

The following companies contributed with materials: Arla Foods AMBA (Bovine Milk Osteopontin), Biomet Inc. (Implants), Depuy (Implants).

Contents

1. LIST OF APPENDED PAPERS, 6
2. ABSTRACT, 7
3. BACKGROUND, 9
 - 3.1 Biomaterials and biocompatibility, 9
 - 3.2 Nanoscience in biocompatibility, 10
 - 3.3 Proteins on a surface, 11
 - 3.3.1 General, 11
 - 3.3.2 Fibronectin, 13
 - 3.3.3 Osteopontin, 14
 - 3.4 Cells on a surface, 15
 - 3.4.1 General, 15
 - 3.4.2 Bone cells on osteopontin, 17
 - 3.5 Bone tissue interaction with a biomaterial, 18
 - 3.5.1 General, 18
 - 3.5.2 Orthopaedic implant research, 19
 - 3.5.3 Bone biology, 20
 - 3.5.3.1 Osteopontin in Bone Biology, 21
 - 3.5.4 Osteopontin in biomaterials tested *in vivo*, 22
 - 3.5.5 HA/PDLLA composites, 22
 - 3.6 Conclusions on background and synthesis of scientific problem, 24
4. OUTLINE OF STUDIES INCLUDING HYPOTHESES, 25
 - 4.1 Paper I, 25
 - 4.2 Paper II, 25
 - 4.3 Paper III, 26
 - 4.4 Paper IV, 27
5. EXPERIMENTAL METHODS, 28
 - 5.1 Material characterization techniques, 28
 - 5.1.1 Atomic force microscopy, 28
 - 5.1.1.1 Contact mode AFM, 30
 - 5.1.1.2 Tapping mode AFM, 31
 - 5.1.2 Electron microscopy, 32
 - 5.1.2.1 Transmission electron microscopy, 33
 - 5.1.2.2 Scanning electron microscopy, 33
 - 5.1.3 X-ray photoelectron spectroscopy, 34
 - 5.1.4 Water contact angle, 35
 - 5.1.5 X-ray diffraction, 36
 - 5.1.6 Material characterization in thesis, 38
 - 5.1.6.1 Paper I & II, 39
 - 5.1.6.2 Paper III & IV, 41
 - 5.2 Protein adsorption analysis techniques, 42
 - 5.2.1 Quartz crystal microbalance with dissipation, 43
 - 5.2.2 Atomic Force Microscopy – scratching technique, 45
 - 5.2.3 Ellipsometry, 46
 - 5.2.4 Combining QCM-D, AFM scratching and Ellipsometry, 47
 - 5.2.5 Protein adsorption in thesis, 49
 - 5.2.5.1 Paper I, 49
 - 5.2.5.2 Paper II, 49
 - 5.3 Cell observation techniques, 49
 - 5.3.1 Differential interference contrast microscopy, 50

5.3.2	Fluorescence microscopy,	51
5.3.3	Cell observation in thesis,	52
5.3.3.1	Paper II,	52
5.4	<i>In vivo</i> testing techniques,	54
5.4.1	Study design,	55
5.4.1.1	Histomorphometry,	57
5.4.1.2	Push-out test,	58
5.4.2	Implant coating preparation,	59
5.4.3	<i>In vivo</i> studies in thesis,	59
5.4.3.1	Histomorphometry and push-out test in thesis,	59
5.4.3.2	Implant coating preparation in thesis,	60
5.4.3.3	Paper III,	61
5.4.3.4	Paper IV,	62
6.	SUMMARY OF RESULTS,	64
6.1	Paper I,	64
6.2	Paper II,	66
6.3	Paper III,	68
6.4	Paper IV,	69
7.	DISCUSSION,	72
7.1	Protein Adsorption,	72
7.1.1	Single protein characteristics?,	72
7.1.2	Surface roughness and topography also influence protein adsorption,	73
7.1.3	Fibronectin adsorption on hydroxyapatite and gold,	75
7.1.4	Osteopontin adsorption on hydroxyapatite and gold,	76
7.2	Osteoconductivity,	78
7.2.1	What exactly is in the coatings?,	79
7.2.2	Animals and study design,	83
7.2.3	Osteoconductivity of a PDLLA/HA composite,	84
7.2.4	Osteoconductivity of OPN functionalized PDLLA/HA composite,	85
8.	OUTLOOK,	87
9.	REFERENCES,	88
10	ENGLISH & DANISH RESUMÉ,	97
11	APPENDIX	
	Papers I – IV	
	List of not appended papers	
	Theses from the orthopaedic research group	

1. List of appended articles

This thesis is based on the following papers:

- I. **Enhanced surface activation of fibronectin upon adsorption on hydroxyapatite**
Dolatshahi-Pirouz A*, Jensen T*, Foss M, Chevallier J, Besenbacher F.
Langmuir, 2009 Feb; 25(5):2971-2978
* These authors contributed equally to this work
- II. **Interaction of human mesenchymal stem cells with osteopontin coated hydroxyapatite surfaces**
Jensen T, Dolatshahi-Pirouz A, Foss M, Baas J, Kassem M, Bünger C, Søballe K, Besenbacher F.
Colloids and Surfaces B: Biointerfaces (Accepted)
- III. **Hydroxyapatite nanoparticles in PDLA coatings on porous titanium implants conducts bone formation**
Jensen T, Jacobsen T, Baas J, Nygaard J, Dolatshahi-Pirouz A, Hovgaard M, Foss M, Bünger C, Besenbacher F, Søballe K.
Journal of Biomedical Materials Research A (Submitted)
- IV. **Osteopontin functionalization of HA particles in a PDLA/HA composite promotes bone formation**
Jensen T, Baas J, Dolathshahi-Pirouz A, Singh G, Nygaard J, Foss M, Bünger C, Besenbacher F, Søballe K.
(In preparation)

The manuscripts are found in the Appendix as part of the thesis.

2. Abstract

A main focus in current biomaterial research is to develop materials capable of evoking a desired tissue response. Biodegradable biomaterials that stimulate generation of specific tissues are highly anticipated in surgery, as they could provide a breakthrough in reconstruction of lost organs or tissue. A strategy in developing appropriate bioactive properties is to integrate specific signals in the material, e.g. by adding cell signaling proteins which induce a physiological effect. Consequently much research effort is put into identifying potential signaling proteins and adapting their functionality to a biomedical device. Throughout the experimental work in this thesis a systematic step-by-step approach has been carried out with the final aim to develop a material suitable for guided bone formation. The starting point was the simplified model system of adsorption of relevant proteins on biomaterial surfaces. The progress required switching between synthesis and characterization of the increasingly complex material and testing on relevant biological systems.

The initial experiments included observation of protein adsorption on hydroxyapatite (HA) with a gold surface used as a reference surface for comparison. The adsorption of two relevant proteins, bovine serum fibronectin and bovine milk osteopontin, was studied with nanotechnological methods (Quartz crystal microbalance with dissipation, Ellipsometry and atomic force microscopy). The techniques in combination allow for estimation of single protein physical characteristics such as foot print area, height, rigidity, associated water and exposure to the liquid phase. Both fibronectin and osteopontin appeared more spread out and exposed to the liquid phase on HA as compared to gold. These characteristics are considered compatible with a more cell active configuration on HA.

Osteopontin from bovine milk is a relatively new protein in biomaterials research, and therefore found suitable for further studies. Two cell studies with human mesenchymal stem cells were setup to evaluate the activity of bovine milk OPN cell binding domains when preadsorbed on HA. Cell motility, cell spreading and focal adhesion spot formation was observed. Again gold was used as a reference surface and both HA and gold surfaces preadsorbed with serum proteins were included as controls. OPN was found to induce cell motility, cell spreading and formation of focal adhesion spots, but exclusively when adsorbed on HA. These results strongly indicate that OPN adsorption on HA favors presentation of cell binding domains. This conclusion is in line with results obtained from the protein adsorption studies.

Having established the adsorption characteristics and *in vitro* activity we setup two *in vivo* studies aimed at utilizing the HA/OPN effect in a biomaterial. The *in vivo* studies were setup in two stages: Initially the osteoconductivity of a 50/50 vol% composite of *poly-D,L-Lactic-Acid* (PDLLA) and 20-70 nm HA nanoparticles was compared to that of pure PDLLA. The materials were applied as thin coatings on experimental cylindrical titanium implants and tested in sheep with a 2 mm gap for 12 weeks. On 40% of the composite coated implants the coating was replaced with a layer of new bone, whereas no bone formation had followed resorption of pure PDLLA. In the second *in vivo* study, OPN was adsorbed at the HA nanoparticles before mixing with PDLLA. Two composites, one with OPN and one without OPN, were compared in a similar canine study with 4 weeks observation time. The osteoconductivity of the OPN/HA composite was close to 100% higher than the pure HA composite. Thus it was shown that OPN bulk functionalization of a composite can aid in providing osteoconductivity to materials intended for guided bone formation.

The work in this thesis emphasizes the strength of a combined nanoscience/*in vitro/in vivo* approach. It allows for deductive step-by-step development of a biomaterial tailor-made for the application.

3. Background

3.1 Biomaterials and Biocompatibility.

Throughout history the idea of inserting foreign objects into the human body has emerged numerously. The earliest known examples of medical purpose include suturing of wounds and replacement of teeth with materials of biological origin. Following implementation of statistical methodology in medicine the benefits of carefully selected and crafted materials to recover or replace physiologic disabilities have been well established. For the last 50 years innovative devices such as joint replacements, pacemakers, lenses, cochlear implants and artificial heart valves and blood vessels have significantly extended the life time and life quality in society [1]. These devices are termed “implantable medical devices”, and the materials suitable for producing them are termed “biomaterials”. Although highly successful in several clinical applications the design of such implantable devices is yet far from its optimum. Development in material designs made possible by nanoscience holds promise of hitherto unprecedented material properties [2]. Consequently, the anticipation and inspiration for further research in biomaterials and implantable medical devices intensifies. The interdisciplinary research area is more active and innovative than ever and ranges from physics and chemistry through molecular and cell biology to medicine.

The unifying property of biomaterials is biocompatibility. The commonly referred-to definition of biocompatibility was conceded by the European Society for Biomaterials in 1986 as “*The ability of a material to perform with an appropriate host response in a specific application*” [3]. No particular parameters or tests are specified in the broad definition. An example of biocompatibility, which emphasizes the sensitivity of the definition, is that of orthopaedic joint replacements. The traditional titanium joint replacement is considered biocompatible in that it is non-toxic, evokes a low adverse tissue response and replaces the joint functionality. The biocompatibility, however, of a similar implant including a surface modification that improves the implant fixation is higher, because better mechanical endurance in the bone/prosthesis interface is more appropriate for the specific application.

The ultimate goal of biocompatible materials in regenerative medicine is that of reconstructing any tissue or organ *in situ* from scratch. For instance, the optimal joint replacement would temporarily replace the joint functionality, and in time degrade while being replaced by new healthy bone tissue formed by the host. Such extreme interpretations of biocompatibility may seem

futuristic, but are, in fact, much closer than one would expect. With the aid of cells cultured *ex vivo* with an appropriate biomaterial and inserted in rabbits Oberpenning et al succeeded in *de novo* engineering of a fully functional bladder [4]. In such intriguing new treatments consisting of genuine tissue engineering, the cell preculturing step is vital and the biomaterial presence is merely for the sake of maintaining structure.

To solve similar and more advanced tasks without cell preculturing high demands of biomaterial properties are necessary. A material intended for templating formation of new tissue exclusively with the aid of resident cells should, as in the case of the theorized optimal joint replacement, provide adequate functional integrity and gradually degrade as cells reconstitute the tissue. Presumably, this could be obtained if the biomaterial is designed to be susceptible to the physiological remodelling process, i.e. the material is resorbed by tissue specific macrophages followed by reconstitution of the intended tissue by the tissue specific blasts. In this thesis development of a multipurpose orthopaedic biomaterial was attempted by functionalizing a material with a protein known to play a key role in the bone remodelling process. The experimental work included material component characterization at the nanoscale and testing with *in vitro* cell response studies and *in vivo* tissue response studies. The following sections provide background of the concepts and basics of the scientific approach.

3.2 Nanoscience in biocompatibility

Nanoscience is defined as the exploration and manipulation of phenomena in the size range below 100 nm. The dedication to study the smallest observable events occurring isolated or as part of a larger system holds relevance to virtually all other scientific areas. Richard Feynmann hypothesized the emergence of nanoscience in a lecture in 1959, wherein it was suggested, that chemical reactions could be manipulated mechanically. Actualization of nanoscience adheres to the invention of the scanning tunnelling microscope (1981) and later on the atomic force microscope (1986), both by Binning & Rohrer, which allowed for direct observation of single atoms.

The relevance of nanoscience in biocompatibility is the opportunity to synthesize and characterize biomaterials and their interaction with physiological entities such as amino acids, proteins, DNA and lipids at single molecule scale. This holds tremendous potential for design of biomaterials tailor-made for the application. The characterization methods, however, are extremely sensitive and only highly simplified model systems with a high degree of control can be reasonably analyzed. In contrast the biomaterial/tissue interaction represents a complex biological system. In

this alleged revolutionary, but highly paradoxical combination of an infinitesimally small investigation scope and the intricacy of living tissue a reductionistic approach is necessary. The challenge is to carefully select and characterize in isolation, a molecular effect which is fundamental to the entire system. Making use of such simplified test systems require follow-up investigations with broader model systems such as *in vitro* cell response studies and *in vivo* tissue response studies evolved around the fundamental effect. Consequently, nanoscience in biocompatibility provides the fundamental base of an interdisciplinary research effort.

In this thesis, methods with resolution at the nanoscale are used to characterize the surfaces and materials used and their interaction with relevant proteins. As will be described in the following section protein/surface interactions is considered a feasible fundamental molecular effect in biocompatibility.

3.3 Protein adsorption on a surface

An essential issue in biocompatibility is the events occurring at the interface between tissue and biomaterial. When a device is introduced in the body it is rapidly covered with a layer of biomolecules, including proteins from serum. The biolayer formation precedes cell interaction and is considered decisive regarding the tissue response [5]. Studying proteins on surfaces is a feasible starting point for a rational biomaterial design and much research effort is put into understanding protein adsorption on biomaterials [6-10].

3.3.1 General

Adsorption of proteins is energetically favourable if the Gibbs free energy is negative, meaning that the process of going from a solvated state to a surface adsorbed state must be exothermic. A decrease in the Gibbs free energy can result from a decrease in enthalpy and/or an increase in entropy. Enthalpy describes the thermodynamic potential of a system and entropy describes the degrees of freedom for a system. In case of adsorbing proteins the change in enthalpy is dominated by contributions from hydrophilic/hydrophobic and electrostatic forces in the protein interaction with surface and solvent [11,12], whereas the change in entropy is dominated by changing of protein structure upon adsorption [12].

The detailed relation of Gibbs free energy to atomic scale forces is beyond the scope of this thesis. To provide a simplified model two arbitrary forces in the adsorption process are considered: i) The protein/substrate forces and ii) the internal protein forces upholding the 3D

structure in solution. The protein/substrate forces, if attractive, tend to drive an adsorption and spread the 3D protein structure out on the surface corresponding to an enthalpy decrease. In case of rigidly structured proteins this can be counteracted by the strong internal forces working to maintain the 3D structure (Fig. 1a). In case of more flexible proteins with weaker internal forces the adsorption may result in breaking down of the internal protein structure, which corresponds to an enthalpy gain and thus reinforcement of the adsorption (Fig. 1b). With repulsive protein/substrate forces the enthalpy gain from breaking down of protein structure may be the only drive for adsorption (Fig. 1c&d). An illustration of the simplified model is presented in figure 1:

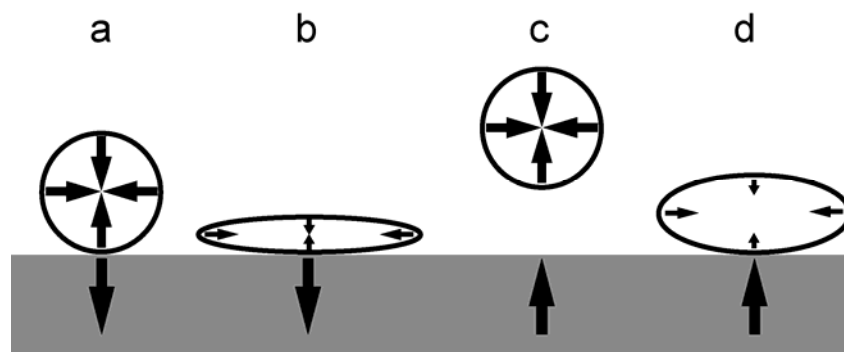


Figure 1. Simplified model of protein adsorption. Large arrows in proteins correspond to high internal protein force and small arrows to low internal protein force. Arrows in the substrate designate attractive (pointing downward) and repulsive (pointing upward) protein/surface forces. The illustration arbitrarily depicts the forces involved in protein adsorption. Attractive forces between substrate and protein tend to adsorb the protein on the surface, this effect may be counteracted by strong internal forces (a) or reinforced by breaking down of weak internal forces (b). Repulsive forces between substrate and protein tends to repel proteins from the surface; in combination with strong internal forces this leads to no adsorption (c), but with weak internal forces the breaking down of internal structure may lead to enthalpy driven adsorption (d).

Both the protein/substrate and internal forces are influenced by physicochemical conditions. For instance, changing temperature, ionic strength or pH-value of solution may have a high impact on both forces and consequently, the protein adsorption.

Adsorption potentially changes protein conformation and consequently, the protein domains presented to the protein exterior are modified. Such changes might serve as an adsorption driven mechanism to alter protein functionality by covering or uncovering functional protein domains. The orientation of adsorbed proteins is of similar importance, e.g. cell-interacting protein sequences must be oriented away from the biomaterial for cell availability. As will be described in the following section (3.4) a particular protein sequence (Arginine – Aspartic Acid – Glycine (RGD)) is of high importance to cell/surface interactions [1].

In the work on this thesis, the adsorption of two proteins, fibronectin and osteopontin, were analyzed. This section includes two short descriptions of the proteins and why they are considered relevant in the context of biocompatibility.

3.3.2 Fibronectin

Fibronectin (Fn) is a 450 kDa extracellular protein found as a soluble form in serum and as an integrated form in all connective tissues. Fn is fundamental in the interplay between cells and the extracellular matrix (ECM) [13] and Fn knock-out is not compatible with life [14]. The protein consists of two identical monomers both containing a cell binding domain with an integrin binding RGD sequence. The protein, furthermore, contains specific binding sites for several ECM components. The availability of the RGD-sequences depends on the conformation of the protein. In solved form at physiological conditions the protein is compact with an oblate ellipsoidal shape (Fig. 2a) [15,16], where the RGD-sequences are hidden.

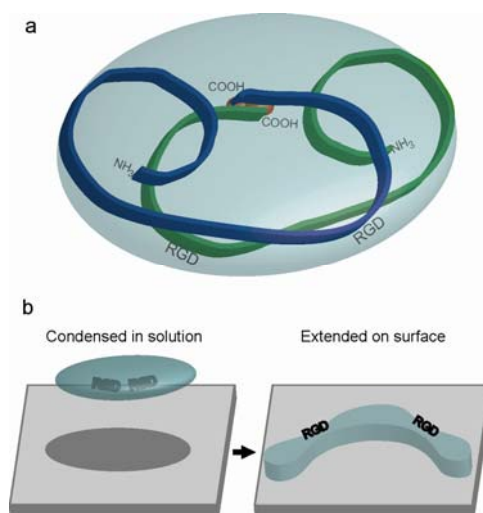


Figure 2. Model illustration of Fn modified from reference [17]. In (a) the detailed structure of the heterodimeric protein in solution is shown. In (b) the conformation change into extended state as a result of surface adsorption is depicted.

If ionic strength is increased the solved protein changes conformation into an extended state [18] where the RGD-sequences are exposed. Transformation into the extended state has also been observed as a result of surface adsorption (Fig. 2b) [17,19] and, furthermore, it is reported that hydrophilic substrates are more active in inducing the extended conformation state [17]. Besides detailed reports on surface conformation, there are several studies on *in vitro* and *in vivo* activity of Fn integrated in biomaterials. These will not be dealt with in detail as Fn was not studied further than characterising the adsorption.

Fn conformational change as a result of adsorption represents a potential molecular effect of importance to material biocompatibility. Apparently, the cell activity of serum fibronectin adsorbing on an implanted device depends on the surface properties. The first paper in this thesis studies RGD-sequence availability of fibronectin adsorbed on hydroxyapatite (HA). Model simulations of Fn adsorption on HA argue that adsorption with the RGD-sequences exposed is energetically favourable [20]. Furthermore, HA containing polymer preadsorbed with Fn lead to higher cell activity as measured by cell survival in comparison to pure polymer preadsorbed with Fn [21]. Studying Fn adsorption on HA holds relevance both to biomaterials and bone biology in that HA is a widely used biomaterial in orthopaedics and the most abundant mineral solid in vertebrates.

3.3.3 Osteopontin

Osteopontin (OPN) was recognized in bovine bone in 1985 and later in human bone in 1988 [22,23]. The protein is part of a group of genetically linked bone proteins with similar structure and function called small integrin binding ligand N-glycosylated proteins (SIBLINGs). SIBLINGs are considered important in the generation and remodelling of skeletal tissue [24]. OPN is a 44 kDa extracellular protein found abundantly in mineralized tissues such as bone and teeth [25]. Besides smaller representations in the kidney and epithelial lining cells, OPN is present in body secretions such as urine, saliva, milk and bile, and it is upregulated in many physiological and pathological phenomena including nidation in the uterus and remodelling, inflammation, neoplastic invasion and metastasizing in any tissue [26,27].

This work focuses on the influence of OPN on the generation of bone tissue, where it is produced by cells of the osteocytic and osteoclastic cell lines [28-30]. Knock-out of OPN has been shown *in vivo* to drastically impair the remodelling process and fracture healing in bone [31-33]. For this reason OPN attracts much interest in the orthopaedic biomaterials community. The protein in solution is described as a random coil without secondary structure and this is not changed by adsorption on HA [34,35]. It contains an N-terminal polyaspartic HA-binding domain, a cell binding domain including an RGD- and a SVVYGL-sequence, a thrombin cleavage site, a CD44 binding domain and several phosphorylation and glycosylation sites (Fig. 3) [24,36-38].

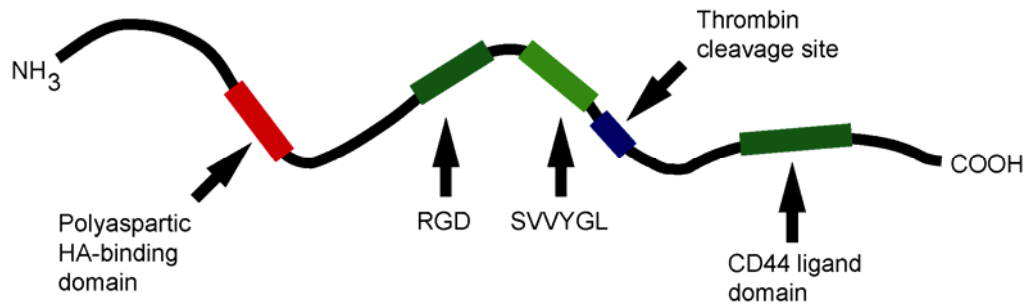


Figure 3. Model illustration of full length osteopontin adopted from reference [36].

Removal of the C-terminal fragment by thrombin cleavage is reported important for the cell activity [39,40]. Besides evidence that OPN maintains a random coil structure following adsorption on HA [35] there is, to the authors knowledge, only limited descriptions of adsorbed OPN in the literature. As will be described later (3.4.2) there is, however, evidence that the availability of the cell binding domain can be controlled with adsorption substrate chemistry.

A problem in using OPN in a biomaterial context is high pricing and low availability. In contrast to Fn, OPN is not abundant in serum, which would make it more available. This problem could be overcome by using an alternative source of OPN. One potential source is OPN from the waste products of cheese production with bovine milk. Both cleaved and full-length OPN occur in bovine milk, but at least 75% is cleaved (internal communication).

Using proteins from other species poses a risk of adverse tissue reaction. Bovine OPN, however, is very similar to human OPN as the protein is highly conserved among species [38]. Through the studies, which are aimed at developing a biomaterial for clinical use, careful considerations should be paid to both local and systemic adverse reactions. Both acute and chronic immunological reactions as well as transfer of diseases must be anticipated. Not only is the peptide sequence of bovine milk OPN different, but also the posttranslational modifications might differ significantly from that of human OPN in general and from that of bone derived human OPN in particular. Nonetheless, a pure OPN resource capable of delivering by the pound requires attention as the price of 50 µg recombinant OPN is currently priced in the range of 300 euros.

Three of the studies in this thesis focus on taking advantage of the practically limitless amount of OPN available from bovine milk. This was done in three steps: i) characterize the adsorption on a well established and well characterized biomaterial, ii) confirm interaction with relevant human cells *in vitro* & iii) apply the biomaterial with adsorbed OPN in a relevant *in vivo* study. In the following chapters on *in vitro* cell studies and *in vivo* animal studies short reviews on contextual OPN function are supplied.

3.4 Cells on a surface

3.4.1 General

Cells are the basic vital units of living tissue. Any response arising from a (non-releasing) biomaterial is essentially the actions of cells transiently or permanently residing on the surface. These in turn are influenced by the proteins on the surface. *In vitro* cell studies are ideal extensions of protein studies as they allow direct observation of cell interaction with a protein layer on a surface. It is recognized that cell interaction with a 2D surface is a simplification of physiological conditions that usually involves full immersion of the cell in a 3D organic environment including the presence of other cell types, endocrine/paracrine effects and potentially an inflammatory response. Although *in vitro* cells on a surface for these reasons cannot be expected to fully reflect *in vivo* responsiveness it is, nonetheless, a widely used approach for studying biomaterial surface effects on cell functionality [1].

The versatility of *in vitro* cell studies is affirmed by the vast amount of well established readily applicable analysis techniques. There among microscopy techniques and biochemical quantification methods covering all aspects of cell morphology and biomolecules. In this thesis only motility and cytoskeleton morphology is investigated. Figure 4 illustrates a cell on a surface and two components of preeminent importance to cell motility and cytoskeleton morphology: The actin cytoskeleton and focal adhesion spots.

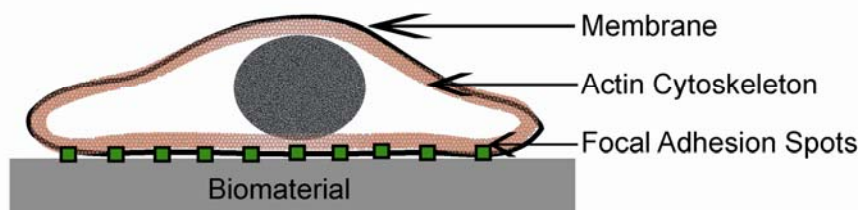


Figure 4. Cross-section of a cell attached to a surface. The membrane, actin cytoskeleton and focal adhesion spots are depicted.

The actin cytoskeleton is an ordered assembly of actin proteins into a network of seven nm fibrils. Actin fibrils are most abundant in the cell periphery, and are the dominant part of the cytoskeleton which includes several other fibrillar and binding structures [41]. The fibrillar actin network is anchored to the inner cell membrane via membrane associated protein complexes, e.g. focal adhesion spots (Fig. 5). These protein complexes constitute the mechanical contacts with surrounding cells and extracellular matrix (ECM). Any force posed thereupon is conveyed to the

cytoskeleton. In turn, any force exerted by the cytoskeleton is conveyed to the surroundings via the same protein complexes. This arrangement explains how actin fibrils play a key role in either maintaining the structural integrity or initiating movement of the cell [41].

Focal adhesion spots (FAS) (Fig. 5) adhere cells to the ECM. A biomaterial designed to interact with cells in a fashion that mimics cell interaction in its natural environment relies on establishment of FAS. They comprise a functional connection between cells and surroundings that not only is implicated in mechanical functions, but also influences differentiation and proliferation of cells [42]. Aforementioned asparagine – aspartic acid – glycine (RGD) amino acid sequence is pivotal for FAS formation. The RGD-sequence is ligand to the external part of the membrane spanning integrins (Fig. 5) which are part of FAS. Bone cells, including osteoblasts, osteoclasts and osteocytes contain integrins that interact specifically with the RGD-sequence [43]. The initiating event of FAS formation is clustering of integrins in the cell membrane [44]. Consequently, a biomaterial engineered with small spacing between RGD-sequences on the surface gives a higher chance of FAS formation by bringing integrins in vicinity of each other [44]. Being that FAS provide mechanical linkage to a surface, they are important for adhesion of cells and morphological responses such as cell spreading, cell elongation and cell motility. Consequently, these cell responses can be controlled through FAS by altering the RGD density on a surface [44-48].

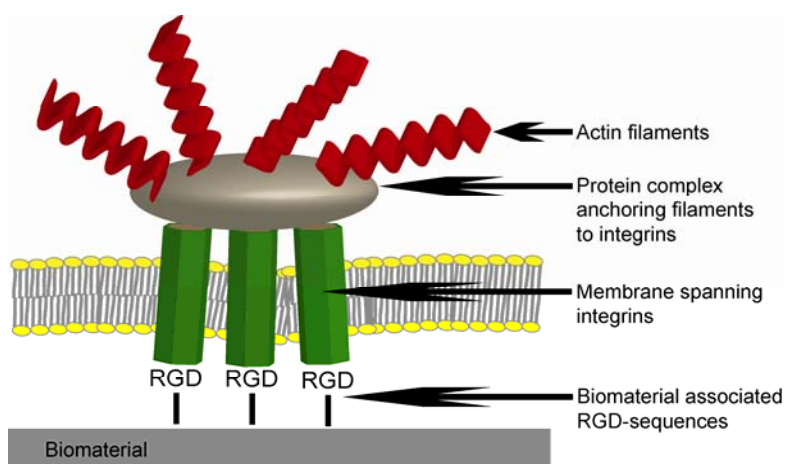


Fig. 5. Simplified close-up illustration of a focal adhesion spot. The relationship between RGD-sequences on the surface and the membrane spanning integrin complex is of crucial importance to focal adhesion spot formation.

3.4.2 Bone cells on osteopontin

The cell studies performed in this thesis observe the impact on bone derived mesenchymal stem cell motility and cytoskeleton morphology of bovine milk OPN adsorbed on HA. Cell motility is an issue of great importance in tissue healing and remodelling processes, where

vigorous cell recruitment and chemotaxis of cells takes place. Both cells of the osteocytic and osteoclastic cell lines contain the specific membrane integrins capable of binding to the cell binding domain of OPN. *In vitro* cell biological studies have reported OPN induced motility of mesenchymal stem cells [29], osteoblasts [49] and osteoclasts [30]. The effect depends of interaction between the cell binding domain of OPN and the cell integrins [29,30,49], but the CD44 ligand [29,30,50] and the SVVYGL sequence [49] has also been shown to induce cell motility [29,30,50]. It can be speculated if OPN's primary mode of action is simply that of inducing cell motility. Indeed, it can be concluded that if OPN from bovine milk can be applied to a biomaterial and induce cell motility, the biomaterial is functionalized with a cell signal which is common for OPN.

From *in vitro* studies aimed at applying OPN to biomaterials it is reported that cell adhesion depends to a high degree of the substrate chemistry. Amine end-groups enhance the OPN mediated adhesion and spreading area of bovine endothelial cells as compared to carboxylic, hydroxylic and methylic functionalized surfaces [7]. It is furthermore reported that OPN attached to a 2-D interfacial collagen layer enhances the cell adhesion of the mouse pre-osteoblastic MC3T3-E1 cell line [51], whereas on HA no such influence was seen [52]. From these studies, it is evident that the nature of the surface to which OPN is adsorbed influences cell interaction. The effect on mesenchymal stem cell motility and cytoskeleton morphology of bovine milk OPN adsorbed on HA has to the author's knowledge not been reported in the literature.

3.5 Bone tissue interaction with a biomaterial

3.5.1 General

In vivo testing is decisive regarding the clinical applicability of a biomaterial. An implanted foreign object will initially be covered with blood that coagulates within the first few hours. Within the first week, the blood clot is replaced with granulation tissue, which is loose connective tissue with potential to remodel either into dense fibrous tissue (scar tissue) or reconstituted original tissue [1]. Formation of dense fibrous tissue is termed "Fibrous encapsulation" and the tissue response is termed "foreign body reaction". It is considered an effect of particular macrophages (foreign body giant cells) formed in response to the foreign object. They struggle to engulf the macrosized foreign object, and in the useless process, they release cytokines

that attract and activate fibroblasts to encapsulate the object instead of phagocytosis [1]. This is by far the most common outcome - even with biomaterials considered biocompatible – and it potentially leads to failure of implants. Development of bioactive biomaterials is with the intention of affecting the process towards reconstitution of tissue instead of fibrous encapsulation.

Granulation tissue formed in non-critical bone defects is usually completely remodelled into new bone by the combined actions of osteoclasts and osteoblasts [53,54]. If, however, an object is inserted into the bone defect it will be encapsulated in fibrous tissue and the newly forming bone will reach only to the perimeter of the fibrous capsule. Two biomaterials commonly used in orthopaedics, HA and titanium, are exceptions to this rule. When they are inserted fibrous encapsulation is minimal and the newly forming bone reaches to the implant surface. This ability of HA and titanium holds tremendous importance in orthopaedic implants for weight bearing applications, but the underlying mechanisms are not completely enlightened. In case of HA the bone forming activity is considered an effect of mineral dissolution and precipitation on the surface, which combined with protein/surface interactions leads to recruitment and activation of bone forming cells [55]. It has furthermore been reported that the bone formation on implant surfaces, both HA and titanium, is preceded by formation of an afibrillar interfacial zone rich in osteopontin and other SIBLINGs, which may act in recruiting and activation of bone active cells [56].

As mentioned (in section 3.1) an orthopaedic joint replacement can benefit from a surface modification that heightens the mechanical fixation in bone. Formation of mineralized bone tissue on the surfaces of titanium and HA-covered implants improves fixation because mineralized tissue provides stronger anchorage than fibrous tissue. This ability of titanium and HA to mediate structural and functional bone integration of weight bearing implants is termed “osseointegration”. In 1965 dental implants of titanium were introduced by Swedish orthopaedic surgeon Per-Ingvar Brånemark [57] and titanium is nowadays by far the most widely used metal in orthopaedic and dental implants. In 1987 hip prostheses with a suitable thin HA coating were introduced by Geesink et al [58]. In experimental settings a HA coating results in better osseointegration than a titanium surface [59], but it is yet to be seen if HA coatings used in clinical settings improve long term joint replacement survival compared to titanium [60,61]. In contrast to titanium, HA and other calcium phosphates in various shapes and formulations has also found wide clinical application as osteoconductive fillers in bone defects [62].

3.5.2 Orthopaedic implant research

The aim of this thesis is to develop and test a multipurpose orthopaedic material for guided bone formation. If such a material is applied to a joint replacement it will guide formation of bone on the implant surface and improve osseointegration. For the *in vivo* experimental work in this thesis, osseointegration of orthopaedic implants was chosen for being a suitable and highly relevant model system.

There is a strong scientific rationale for studying and attempting to improve osseointegration. The duration of orthopaedic joint replacements is limited and revision surgery of loosened implants constitutes a substantial fraction of total surgeries [63]. Improvement of longevity would have a large socioeconomical impact. The currently dominating strategy for further improving osseointegration is endorsement of bone tissue formation on the implant surface. This research is encouraged by the fact that early stable fixation is a prerequisite for a favourable long term prognosis [48, 49]. In our group, a sensitive method for evaluating implant osseointegration is well established [59]. It consists of mechanical testing to evaluate fixation strength and estimation of volumetric tissue fractions around the implant to evaluate the tissue response. Mechanical testing provides results of direct clinical relevance, whereas estimation of volumetric tissue fractions provides insight into the underlying mechanism.

The animal studies performed in this thesis observe the impact on osseointegration of three different implant coatings. i) A pure polymer coating of poly-D,L-lactic-acid (PDLLA), ii) a 50/50 vol% composite coating of PDLLA and HA nanoparticles and iii) a 50/50 vol% composite coating wherein the particles are functionalized with OPN. The following sections provide a short overview of basic bone biology with emphasis on the *in vivo* function of OPN. In conclusion of the background section a short overview of *in vivo* studies on PDLLA/HA composites and a short overview of OPN's *in vivo* effect in the context of biomaterials is presented.

3.5.3 Bone Biology

The skeleton provides a stable basis for the movement apparatus and protection to vital organs in the skull, chest and pelvis. It, furthermore, contains the hematopoietic tissue and the largest mineral reservoir in the body. The skeleton functions are constantly adapting to the environmental stresses. Load endurance is increased as a response to mechanical stress, erythrocyte production is enhanced as a response to blood loss and resorption of mineralized tissue is enhanced as a response to falling serum levels of calcium and phosphate.

The mechanical basis of bones is brought about by a highly organized structure of HA nanocrystallites and collagen fibrils [64]. The combination of the hardness of HA and the tensile strength of collagen, henceforward referred to as mineralized bone tissue, provides a lightweight material with adequate mechanical properties. The bone macrostructures are divided in cortical and trabecular bone. Cortical bone is found in the perimeter of bones, and it comprises a near continuous phase of mineralized bone tissue. Trabecular bone comprises a spongelike structure of mineralized bone tissue with the hematopoietic tissue intertwined.

The mineralized bone tissue is constantly renewing itself through the combined actions of osteoclasts and osteoblasts. The process consisting of resorption by osteoclasts followed by deposition of new mineralized bone tissue by osteoblasts is called bone remodelling (Fig. 6).

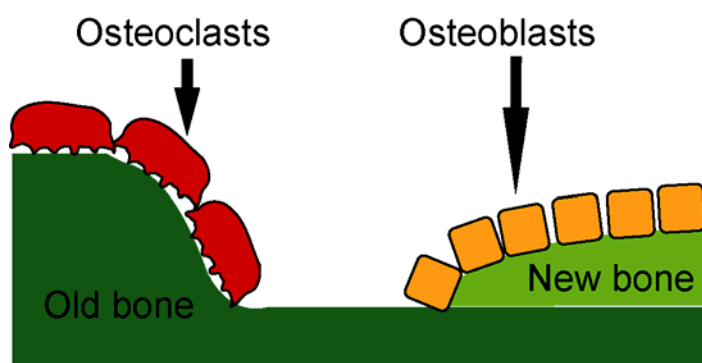


Figure 6. The sequential events taking place during remodelling of mineralized bone tissue. The process moves like a train (moving leftward) lead by resorbing osteoclasts followed by depositing osteoblasts. The local signal that triggers activation and “locomotion” of the remodelling event are largely unknown but OPN is expected to play a key role.

Remodelling is particularly active during healing of, for instance, a fracture or the surgically inflicted bone defect wherein an orthopaedic implant is inserted [53,54]. During remodelling the osteoclasts have a positive influence through paracrine factors on the new bone deposition of the osteoblasts [65].

3.5.3.1 Osteopontin in bone biology.

The signal that initiates remodelling locally is not fully understood. It attracts large interest in the orthopaedic biomaterials community and in general, because many diseases arise from dyscoordinated bone remodelling [65,66]. There is strong evidence, however, that osteopontin holds a key role in the remodelling process.

The influence of OPN on osteoclast activity is relatively well established. It is reported that osteoclast dependent downregulation of bone mechanical endurance in response to

limb immobilization is reduced in osteopontin knock-out mice [32]. Ovariectomy induced osteoporosis is also reduced in osteopontin knock-out mice [33]. It is furthermore reported that osteoclast presence and activity are dramatically upregulated as a response to enhanced OPN production by osteocytes and osteoblasts in bone exerted to mechanical stress [67]. As suggested by these *in vivo* studies the osteoclast activity is highly dependent on OPN. This is also strongly suggested by *in vitro* studies reporting a direct positive influence on osteoclast activity by OPN [68-71].

The influence of OPN on osteoblasts is less clarified. In one aspect based on *in vitro* studies OPN appears to induce the bone deposition by promoting pre-osteoblast attachment [51,72] and migration of mesenchymal stem cells [29] and osteoblasts [49]. Differentiation towards bone deposition by osteoblasts has furthermore, been reported to be stimulated by OPN [72-74]. In another aspect, also based on *in vitro* studies, OPN is a potent inhibitor of HA *de novo* formation and growth in a dose dependent manner [75,76]. This is contradictory to the osteoblast activation, which tends to result in HA production. It may be that OPN interferes with the extracellular phase separation of calcium and phosphate to control the size of forming HA-crystallites and limit deposition on formed crystallites.

3.5.4 OPN in biomaterials tested *in vivo*

Although not completely clarified the current evidence of OPN function in bone biology motivates studies of OPN in biomaterials. *In vivo* studies on potential usage of OPN in biomaterials suggest that the protein can be used both in an effort to increase bone formation and to avoid adverse tissue reactions. Coralline porous HA granulae coated with full length OPN were used in a rabbit cranial bone substitute model, where a positive effect of OPN on bony ingrowth from the periphery of the surgically produced defect was observed, whereas no effect in bony growth on the granulae was found [77]. OPN on the surface of positively charged poly(2-hydroxy-methacrylate) (p(HEMA)) has furthermore, been shown to decrease thickness of fibrous encapsulation as compared to OPN on negatively charged p(HEMA) [78]. This result is in agreement with the fact that the foreign body reaction to subcutaneous poly-vinyl-alcohol sponges is more active in OPN knock-out mice than in wild-type mice [79]. The inhibiting effect on the foreign body reaction is likely an effect of OPN tending to induce tissue specific macrophages, e.g. osteoclasts, as opposed to formation of foreign body giant cells.

3.5.5 PDLLA/HA composites

In the process of choosing a biomaterial suitable for OPN integration both the observations on adsorption and cell interaction along with the function of the protein had to be considered. It was decided that HA with surface adsorbed OPN should be central in the biomaterial design. In this context, composites of HA-particles and biodegradable polymers seemed an ideal design frame for testing the effect of OPN *in vivo*. The basic motivation for combining HA with biodegradable polymers is to design biomaterials with both the well established osteoconductive properties of HA and the versatility of polymers for engineering desired shapes and mechanical properties. Both HA and biodegradable polymers are present transiently following implantation and thus suitable for applications requiring time-limited presence.

PDLLA is a biodegradable polyester used in many biomaterials applications and for this reason considered the most important biodegradable polymer [1]. It was originally introduced to the medical field as a suture material. The use of poly-D,L-lactic-acid (PDLLA) as biodegradable polymer in HA containing composites is well established for *in vivo* purposes [80-84]. The polymer in pure form has furthermore, been used as a drug delivery coating on orthopaedic implants [85-91]. The chemical structure of the polymer is depicted in figure 7.

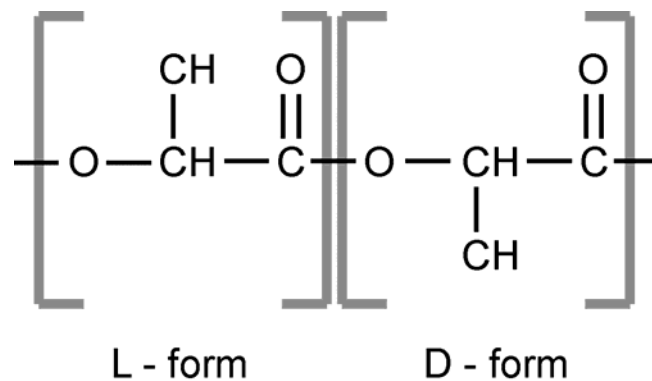


Figure 7. The enantiomeric lactic acid monomers of poly-D,L-lactic-acid (PDLLA).

Lactic acid molecules of D and L form are present in equal amounts. Bulk PDLLA is a non-crystalline material with mechanical properties depending of the polymer backbone length [92]. In watery environment the polymer is predominantly degraded by spontaneous hydrolysis and lowering of the pH-value has a strong enhancing effect on this process [93]. The ultimate degradation product is lactic acid, which is readily metabolized in the citric acid cycle, why PDLLA is considered non-toxic.

Addition of HA to biocompatible polymers has consistently been reported to improve the osteoconductive material properties [81,82,84,94-96]. In addition it has been reported that use of

HA nanoparticles as opposed to microparticles in a composite leads to higher cell attachment and proliferation *in vitro* [97]. This is considered an effect of higher surface presentation of HA, which has been shown to be positively correlated with osteoconductivity *in vivo* [83]. It has furthermore, been shown *in vitro* that the effect of cell binding proteins on cell survival in PDLLA scaffolds are potentiated by HA-particle presence [21].

In the work on this thesis PDLLA was combined with HA-particles sized 20 – 70 nm in a 50/50 vol% composite and applied to experimental titanium implants to test osseointegration in comparison to pure PDLLA. The particle size and volumes were selected to ensure high surface presentation of HA. In a follow-up study OPN was preadsorbed on the HA-particles to bulk functionalize the composite and test the impact in a similar setting. To the authors knowledge bulk functionalization of biodegradable nanocomposites with osteopontin has not been described in the literature.

3.6 Conclusions on background and synthesis of scientific problem

The background presented in section 3.1 to 3.5 provides an overview of the basics of biomaterials science and part of the existing literature of relevance to the work in this thesis. The included references are not intended as being an exhaustive literature review, but to present the necessary background for a meaningful synthesis of scientific problems to solve. Evidently surface adsorbed proteins hold great importance in biocompatibility and studying spontaneous adsorption on known biocompatible materials is a feasible approach for understanding the mechanisms of biocompatibility. This line of thought encouraged studying the adsorption of fibronectin and osteopontin on HA. In extension of such gained knowledge it is appealing to use proteins as integral parts of biomaterials as they offer opportunities for providing specific functionality to the material. As described osteopontin is a candidate protein for providing a local signal to endorse the remodelling process. This motivated further studies on cells and animals aimed at using OPN from bovine milk as an integral part of a biomaterial. In this context, a composite of PDLLA and HA particles seems ideal as a biomaterial in which OPN could be integrated.

Throughout the background section, it has been mentioned - to the authors knowledge – what has not been reported in the existing literature. These statements coincide with the scientific problems dealt with in this thesis. The following section contains short outlines including hypotheses on the four studies on which the thesis is based. The hypotheses are based on the presented background.

4. Outline of studies including hypotheses.

This short outline of the studies included in the papers I – IV, is included to clearly state the hypotheses and provide a thread through the next section on experimental methods (Section 5). Each technical description in section 5 is followed by a short outline of usage and results with reference to this synopsis. In section 6 a full overview of the results is provided and section 7 contains an overall discussion with perspectives. Sections 4, 6 & 7 are not intended to replace the appended articles, but to provide a meaningful frame for the presentation of the experimental techniques and how they are combined.

4.1 Paper I

Hypothesis: Adsorption of Fn on a HA surface leads to a higher exposure of the cell binding domain as compared to adsorption on a gold surface. The hypothesis is tested by analysing the adsorption of Fn from different bulk concentrations on HA and on gold as a reference substrate. Monoclonal antibodies directed against the cell binding domain (CBD) was used to probe the availability of CBD.

Material characterization techniques: Atomic Force Microscopy (AFM), X-ray diffraction (XRD) (Fig. I).

Protein adsorption analysis techniques: Quartz Crystal Microbalance with dissipation (QCM-D), AFM and Ellipsometry (ELM) (Fig. I).

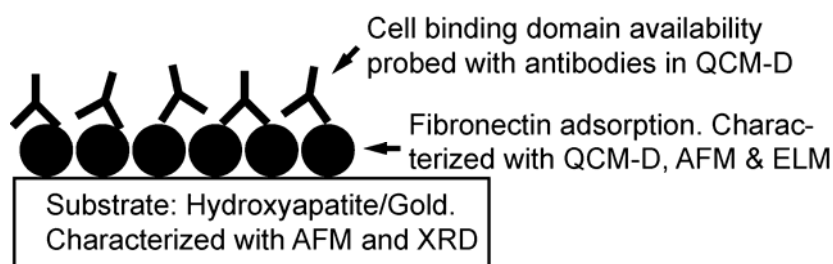


Figure I. Paper I at a glance.

4.2 Paper II

Hypothesis: Adsorption of OPN from bovine milk on a HA surface leads to higher exposure of the cell binding domain as compared to adsorption on a gold surface and this effect is reflected in the initial cell/surface interaction. The hypothesis is tested by analysing the adsorption of OPN on HA

and gold along with initial cell motility, cell spreading and cell cytoskeleton on the resulting protein layer.

Material characterization techniques: AFM, XRD (Fig. II)

Protein adsorption analysis techniques: QCM-D, ELM (Fig. II)

Cell observation techniques: Differential interference contrast microscopy, Fluorescence microscopy (Fig. II).

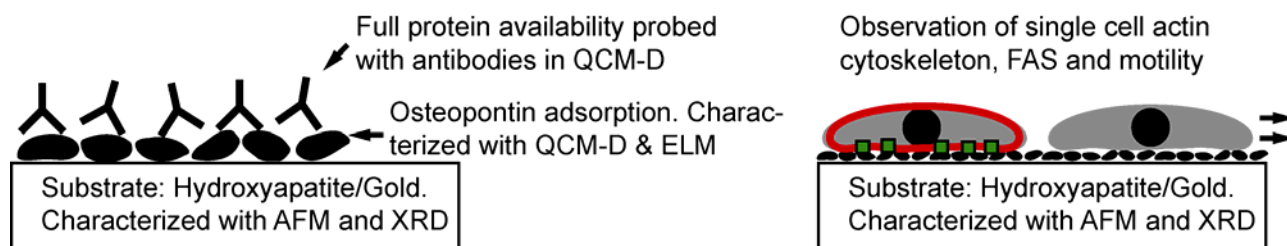


Figure II. Paper II at a glance.

4.3 Paper III

Hypothesis: HA nanoparticle addition to a PDLLA implant coating improves the osseointegration of coated implants. The hypothesis is tested *in vivo* by applying pure PDLLA and the PDLLA/HA composite as thin coatings on experimental cylindrical titanium implants and tested in sheep with a 2 mm gap for 12 weeks.

Material characterization techniques: Transmission electron microscopy, Scanning electron microscopy, Atomic Force Microscopy (Fig. III)

***In vivo* testing:** Sheep gap implant model - Push-out test, Histomorphometry (Fig. III)

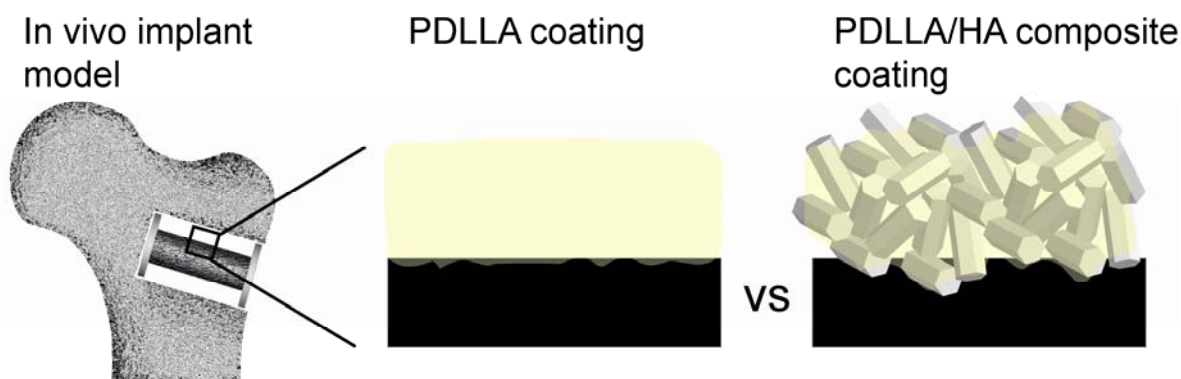


Figure III. Paper III at a glance.

4.4 Paper IV

Hypothesis: OPN-functionalization of the HA-nanoparticles enhances osteoconductivity as compared to a pure PDLLA/HA composite. The hypothesis is tested *in vivo* by applying OPN functionalized composite and pure composite as thin coatings on experimental cylindrical titanium implants and tested in a canine model with a 0.75 mm gap for 4 weeks.

Material characterization techniques: X-ray photoelectron spectroscopy (Fig. IV)

In vivo testing: Canine gap implant model - Push-out test, Histomorphometry (FIG IV).

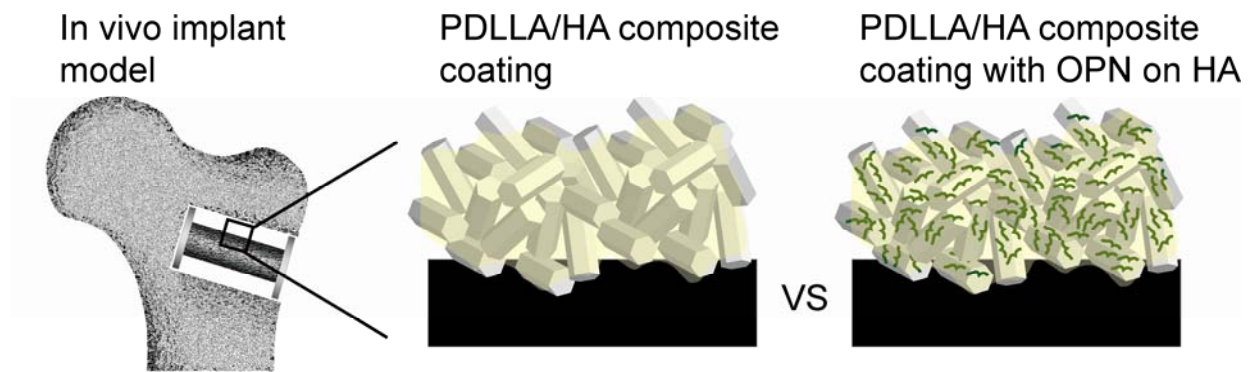


Figure IV. Paper IV at a glance.

5. Experimental methods

This section is divided in 4 subdivisions – Material characterization methods, Protein adsorption analysis techniques, cell observation techniques and *in vivo* testing techniques. At the end of each subdivision a short outline of the usage and results is added with reference to the papers outlines in section 4. The methods descriptions should provide a medical candidate the knowledge necessary for reading the papers.

5.1 Material characterization methods

5.1.1 Atomic force microscopy

Atomic force microscopy (AFM) is a scanning probe microscopy technique with nanoscale resolution allowing for direct observation of extremely small structures such as proteins, DNA or nanoparticles. The technique was invented in 1986 [98] and widely applied for its intriguing versatility allowing for imaging of virtually any surface in both ambient and liquid environment [99]. The probe consists of an extremely sharp tip mounted at the end of a small cantilever (Fig. 8). Deflections of the cantilever in the z-direction (up/down) are quantified by detection of a laser beam reflected from the upper surface of the cantilever. When a sample surface is raster scanned underneath the tip a height image of the surface can be created from continuous detection of cantilever deflections. Nanoscale resolution of sample positioning is accomplished by placing the sample on a very accurate piezoscanner driven by piezoelement deformation.

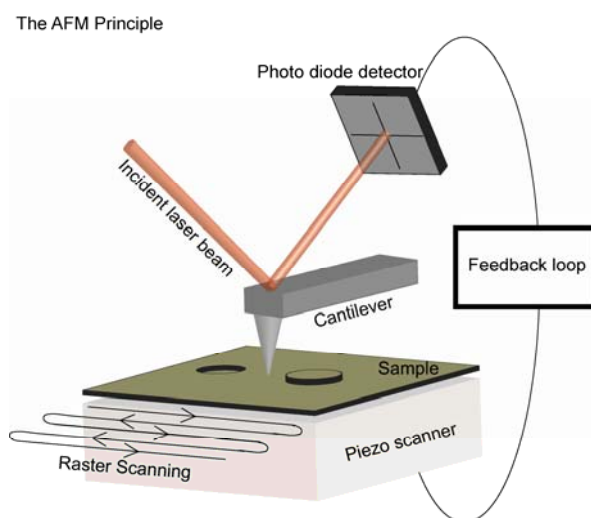


Figure 8. Model illustration of a typical atomic force microscopy setup. Central to the technique is tip which detects the surface features of a sample scanned underneath the tip. The deflections of the cantilever as a result of the surface features are detected and integrated in a feedback loop with the scanner position.

The resolution in the z-dimension depends on the system setup. For the microscope and cantilevers used in this thesis it is estimated to be one nm. The lateral imaging resolution (x and y) depends of the tip sharpness. In theory the highest resolution is the width of the tip apex. Concavities smaller than the apex are not detected because the tip passes over without changing of height. The width of an infinitely thin convexity is detected as the apex width and broader convexities are always overestimated by the apex width. This phenomenon is called tip convolution.

During a scan, the tip is in immediate vicinity of the sample where electrostatic forces, Van der Waal forces, meniscus forces and chemical forces of the tip/sample interaction are detected. The net force is in the range of 10^{-9} N and depends of the tip/sample distance - attractive forces dominate in the distance (>0.2 nm) with a maximum at 0.3 nm and repulsing forces dominate in the vicinity (<0.2 nm) [99] (Fig. 9).

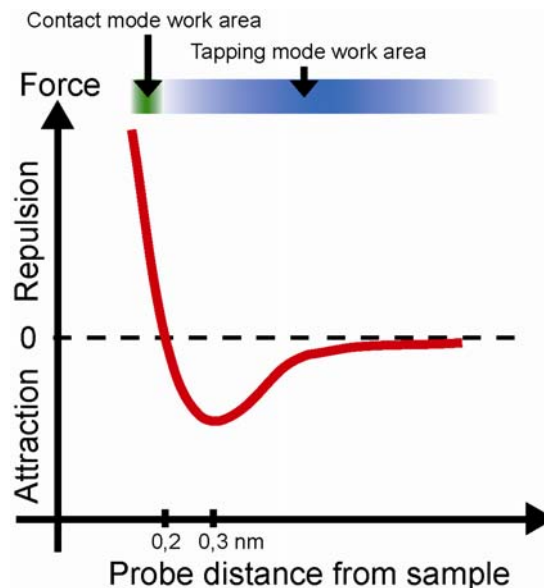


Figure 9. Typical force-distance curve of an AFM-tip and a surface. In the distance attractive forces dominate and repulsive forces dominate in at lower distance (contact between tip and surface).

Imaging can be done either from detection of the distant attractive forces or the near repulsive forces. With the attractive forces, the sample is detected as cantilever deflections towards the surface produced by the distant attraction forces. With the repulsive forces, the sample is detected as cantilever deflections resulting from the near repulsive forces and thus imaging is obtained from a closer tip/sample interaction. Detection of the distant attractive forces is not suitable for imaging in ambient conditions, because attractive meniscus forces arising from a layer of contaminating water on the sample surface produces erratic sticking, known as “snap-in”, of the

tip to the sample [100]. This results in artefacted images. In the following sections only imaging from the near repulsive forces is described as all imaging in this thesis was done in ambient conditions AFM.

AFM imaging using the near repulsive forces can be done in static and dynamic mode. Static refers to imaging with a constant deflection of the cantilever and dynamic refers to imaging with an oscillating cantilever. Static mode is known as `contact mode` and dynamic mode as `tapping mode`. These terms will be used throughout the thesis. As described in the following sections the methods are suitable for different applications.

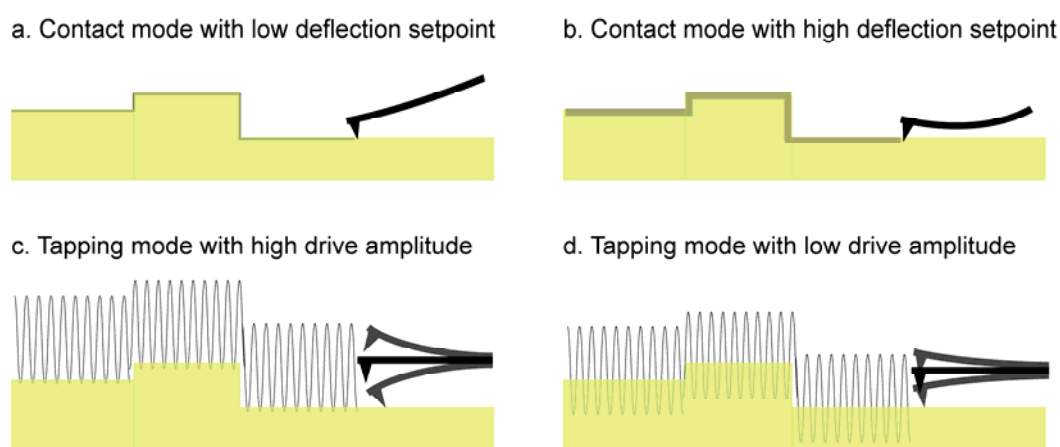


Figure 10. Different settings in contact mode and tapping mode alter the force between tip and sample. As described in the text the optimal settings depends on the sample to image or manipulate.

5.1.1.1 Contact mode AFM

In contact mode, the cantilever is kept at a constant z-position by a feedback loop between the laser beam detector and the piezoscanner. Before a scan is initiated the piezoscanner pushes the sample against the tip until the deflection setpoint is reached. The selection of deflection depends on the sampling – a high deflection setpoint corresponds to a high tip/sample force (Fig. 10b) and a low deflection setpoint corresponds to low tip/sample force (Fig. 10a). Cantilevers with low spring constants are more sensitive in that a higher deflection can be obtained with a lower tip/sample force. During a scan imaging is obtained from the changes in z-dimension necessary to maintain a constant deflection.

Contact mode is disadvantageous for delicate samples. To avoid scratching of soft surfaces a cantilever with very low spring constant is required along with careful selection of deflection set-point. Despite diligent efforts unrecognized surface scratching may still bias the imaging. In addition small mobile structures like proteins are likely pushed around on the surface

instead of being detected by the tip. Contact mode is considered suitable only for robust samples that are not susceptible to disruptive effects of the tip. As described in section 5.3.2 contact mode can be used alternatively to remove proteins in a small area on a surface allowing for height measurement of the protein layer.

5.1.1.2 Tapping mode AFM

In dynamic mode, the cantilever is oscillating at its resonance frequency. The frequency and amplitude depends on the cantilever and is usually in the range of 50 – 500 kHz and 1 - 10 nm respectively. A drive amplitude lower than the amplitude of free oscillations is selected for the scanning. Before a scan is initiated the piezoscanner pushes the sample against the oscillating tip until the drive amplitude is reached. This is obtained when the tip intermittently “taps” the surface in the repulsion regime (Fig. 9). During a scan, the amplitude is kept constant by a feedback loop between the laser beam detector and the piezoscanner. The selection of amplitude depends on the sampling. With high amplitude (close to free oscillations) the tip movement is interrupted close to the extremity of the oscillation and only a small part of the kinetic energy of the oscillating cantilever is propagated to the sample (Fig. 10c). With low amplitude the tip is interrupted earlier in the oscillation and more kinetic energy is propagated to the sample (Fig. 10d). During a scan imaging is obtained from the changes in z-dimension necessary to maintain the constant amplitude.

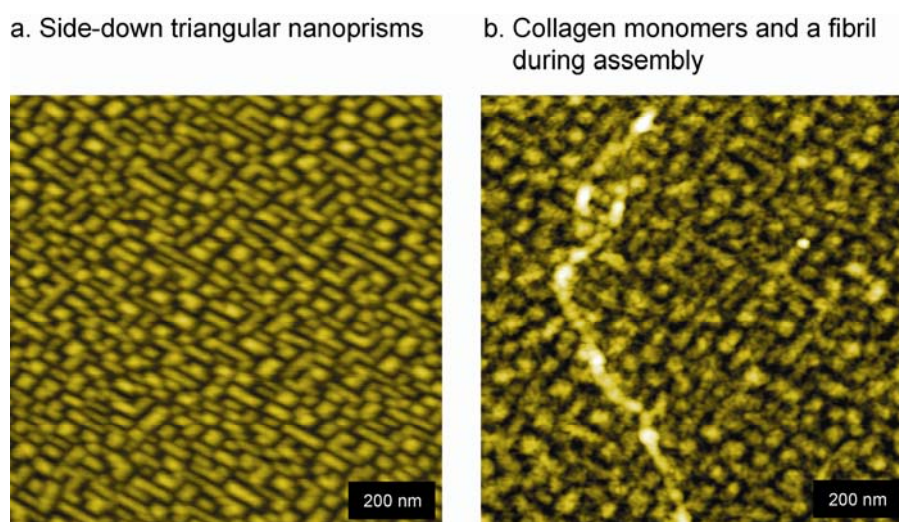


Figure 11. Tapping mode AFM picture examples from a pilot study on the influence of surface nanostructures on collagen surface fibrillation. Picture (a) shows the clean surface with triangular nanoprisms oriented in two directions and picture b shows the same surface covered with tropocollagen and a larger fibrillar collagen structure in the process of assembly/elongation.

Tapping mode AFM is suitable for imaging of delicate biological structures such as proteins (Fig. 11). Although the tip moves through the water contamination layer the problem of meniscus force drag can be minimized by choosing a cantilever with high spring constant [101]. Tapping mode is furthermore, less likely to distort soft samples and relocate moveable structures. This is due to the intermittent surface contact, which can be minimized in force by choosing as high an amplitude as possible and still maintain a stable scan (“soft-tapping”) (Fig. 10c).

5.2.2 Electron Microscopy

Electron microscopy (EM) is a microscopy technique similar to conventional light microscopy. In EM, however, electrons are used for imaging and the resolution is several times higher. Electrons are accelerated with an electron gun to near light speed velocity, where propagation takes place in wave motion with a wavelength below 1 nm. Light rays in a conventional light microscope propagate at a wavelength of 400 – 700 nm. This difference along with principal differences in the sample interaction allows for the higher resolution of EM. In contrast to light microscopy, imaging of living organisms is not possible because vacuum is necessary for EM. In figure 12 the basic outline of an electron microscope along with the possible electron interactions with a sample is illustrated.

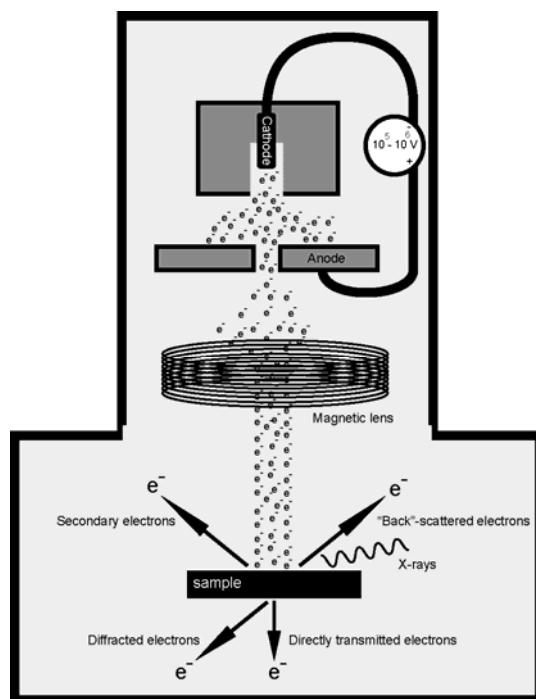


Figure 12. Electrons are accelerated with an electron cannon at the top and directed with electromagnetic lenses to impinge on the sample. The incident electrons can either transmit directly, diffract, punch secondary electrons from the sample, scatter or cause emission of x-rays.

A beam of electrons is bombarded into the sample and an image is created from detection of the electrons. Electron microscopy is divided in two principally different imaging techniques. i) Transmission electron microscopy - imaging by detection of directly transmitted electrons going through the sample (Fig. 12) and ii) Scanning electron microscopy - imaging by detection of secondary or “back”-scattered electrons from the sample surface (Fig. 12).

5.1.2.1 Transmission Electron Microscopy (TEM)

In TEM the electrons are manipulated to arrive in a parallel beam normal to the sample surface in areas of few nanometers up to several micrometers in diameter. Diffracted electrons can be used to characterize crystal structure, whereas the directly transmitted electrons can be used for imaging. In the following only imaging is considered. Equivalent to conventional bright field microscopy, image contrast is produced by obstruction of electrons in dense areas of the sample and less obstruction through less dense areas. The transmitted beam carrying information is magnified below the sample and detected by a CCD camera.

Apart from scanning tunneling microscopy, TEM has the highest magnification of all microscopy techniques ($\times 100.000+$) which allows for direct observation of crystal planes as described in section 3.2.4. There are, however, drawbacks to the technique. Samples cannot be more than a few hundred nanometers thick and must be able to tolerate high vacuum. Biological samples require complete dehydration and casting into a suitable polymer.

5.1.2.2 Scanning Electron Microscopy (SEM)

In SEM the electron beam is focused with a collecting lens to produce secondary electrons, “back”-scattered electrons and x-rays on a confined area of the sample surface (Fig. 12). The image resolution depends on the size of this focus “spot” which is typically 1 – 5 nm. The secondary electrons are suitable for imaging of topography as the contrast originates from height gradients on the sample surface. Imaging using “Back”-scattered electrons rely on contrast emanating from variation in chemical composition in the sample, *i.e.* high- z atoms (z = proton number) produce more scattered electrons. The X-rays can be used to identify elemental composition with a spectroscopy technique similar to XPS (Section 5.2.3). In the following only imaging from secondary electrons is considered.

Imaging is obtained by ongoing detection of secondary electrons during a raster scan on the sample surface. The process maps the intensity of secondary electrons. When the incident

electron beam is normal to the sample surface the secondary electron intensity is low due to the minimal area covered by the beam. When the beam is incident on a slope the intensity is higher due to the higher area illuminated. The contrast is produced by these intensity differences which results in 3D like images of the surface topography.

A major drawback to the technique is that samples must be electrically conductive. Non-conductive materials are prone to electron charging, which results in artefacted imaging and sample heating. It is furthermore, difficult to obtain high resolution of samples with low-z atoms because the electron beam more easily penetrates instead of producing secondary electrons from the surface. These restrictions to SEM are particularly relevant to imaging of polymers and biological samples, which are neither electrically conductive nor possess high-z atoms. The problem can be overcome by sputtering a thin layer of conductive high-z atoms on the sample, e.g. gold, palladium or platinum [100]. Alternatively, the vacuum can be lowered slightly to introduce gaseous molecules to the sample surface. These molecules can act as charge decouplers and the limitation to conductive materials can be overcome [100].

5.1.3. X-ray photoelectron spectroscopy (XPS)

XPS is a surface chemistry analysis technique based on the photoelectric effect. The method allows for both relative quantification of surface elements and chemical bond types of the single elements. When an atom is intercepted with x-ray radiation the electrons are set in oscillating motion. This effect is used in XRD by detecting diffraction patterns of the resulting radiation emitted. Apart from oscillation, it also occurs that electrons are knocked completely out of the atom by the incoming X-ray. This electron emission is suitable for chemical analysis in that the kinetic energy of a “knocked out” electron is a reflection of the binding energy originally maintaining the electron within the atom. The electron binding energy is element specific and detection thereof allows for elemental identification.

XPS is basically radiating a sample with X-rays and detect the number and energy of “knocked out” electrons (Fig. 13). The procedure is done in vacuum to avoid contamination of the sample and biasing detection of photoelectrons from gases.

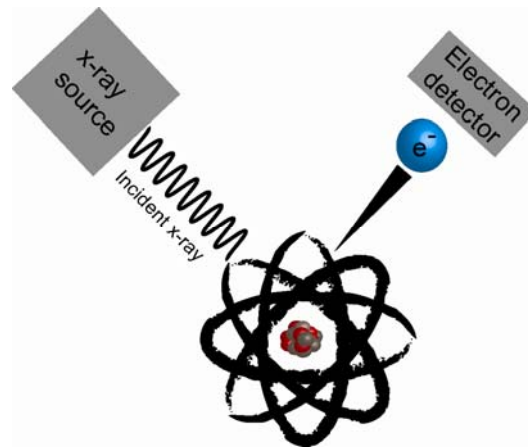


Figure 13. X-ray photoelectron spectroscopy is based on the photochemical effect. Incident electromagnetic waves in the x-ray regime knock out electrons from the sample atoms. By detection of the kinetic energy of these electrons the elements emitting them can be identified.

By using a fixed energy of incoming x-rays the binding energies corresponding to emitted electrons can be calculated with the following equation:

$$E_{\text{binding}} = E_{\text{incoming xrays}} - E_{\text{kinetic}}$$

Where E_{binding} is the binding energy of the emitted electron, $E_{\text{incoming xrays}}$ the energy of incoming x-rays and E_{kinetic} the kinetic energy of the emitted electron. By using a constant energy x-ray source the electron emitting elements can be identified from E_{binding} and the electron intensities are correlated to the amount of the identified element [102]. This basic operation where all possible binding energies are detected is called a survey spectroscopy. With repetitive scanning of the photoelectrons from a single element (high resolution spectroscopy) it is furthermore possible to deconvolute the chemical binding types of the element because different binding types introduce small shifts in the electron binding energy.

5.1.4. Water contact angle

Water contact angle measurement is a method to estimate the hydrophobicity of a substrate surface. When a droplet of water is placed on a substrate the spreading of the water on the surface is determined by three interfacial forces: i) the tension between substrate and gas (γ_{SG}), ii) the tension between water and gas (γ_{WG}) and iii) the tension between water and substrate (γ_{WS}) (Fig. 14).

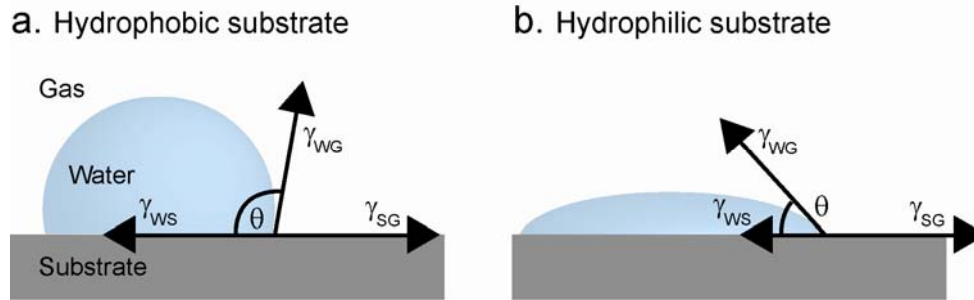


Figure 14. A droplet on a hydrophobic surface and a droplet on a hydrophilic surface. The water contact angle is lower on the hydrophilic surface. Arrows designate surface tensions - (γ_{SG}) is the surface tension in the substrate/gas interface, (γ_{WG}) is the surface tension in the water/gas interface and (γ_{WS}) is the surface tension in the water/substrate interface.

When the three tension forces reach equilibrium, the water droplet will rest on the surface. At this state, the tension forces are related as described by the Young equation [103]:

$$0 = \gamma_{WS} + (\gamma_{WG} \times \cos \theta) - \gamma_{SG}$$

Where θ is the water contact angle and γ_{WS} , γ_{WG} and γ_{SG} as described above. In case of high γ_{WS} , the contact angle is high and in case of low γ_{WS} the contact angle is low. Thus substrate surface chemistries consisting of hydrophilic (polar) groups resulting in low γ_{WS} gives a low contact angle and substrate surface chemistries consisting of hydrophobic (apolar) groups resulting in high γ_{WS} gives a high contact angle [103]. The interpretation of contact angles, however, is not straightforward as the surface topography and chemical heterogeneity have also been reported to have a significant influence [1,104]. In biomaterials science the water contact angle along with detailed description of surface topography with, for instance, AFM is a valuable technique for characterizing basic surface properties [1].

5.1.5. X-ray diffraction

X-ray diffraction (XRD) is a diffraction based method for characterizing the atomic structure of crystals. Diffraction is loosely defined as bending of waves around small obstacles. In XRD the waves are electromagnetic radiation in the x-ray regime and the obstacles are atoms in a crystal structure. A bending event is the result of an incoming electromagnetic wave setting an electron in oscillating motion, which results in a new electromagnetic wave being emitted in a random direction. When an X-ray beam enters a crystal the bending events can act in concert to produce a new detectable X-ray beam (constructive interference). Certain conditions regarding

incoming x-rays and crystal structure must be present for constructive interference to occur. These conditions are summed up in Bragg's law (or the Bragg condition) [105]:

$$n\lambda = 2 \times d \times \sin(\theta),$$

where n is a whole number integer, λ is the wavelength of incident light, d is the plane spacing (See following and Fig. 15c), θ is the angle between incident beam and crystal plane. Diffraction events not fulfilling the Bragg condition will not produce constructive interference.

Analysis of crystal structure by X-ray diffraction is possible due to the high order of structure found in crystals. This ordered structure is defined by the unit cell, which is the irreducible arrangement of atoms describing the smallest repeated structure in the crystal. The rhombohedral unit cell of hydroxyapatite and its arrangement in a hexagonal crystal structure is schematically shown in figure 15a&b.

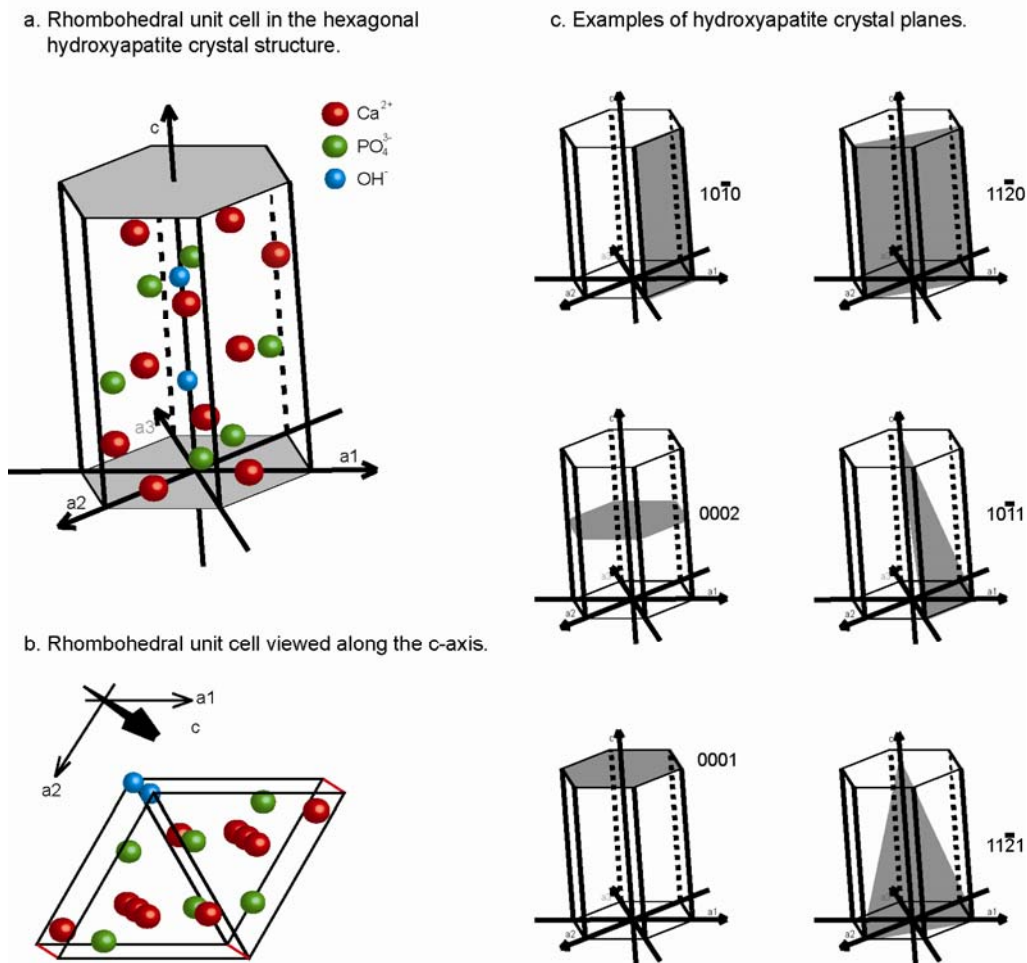


Figure 15. (a) & (b) illustrates the atoms and positions in the rhombohedral unit cell of hydroxyapatite. Some of the diffraction planes, which can be identified with x-ray diffraction are shown in (c).

A bulk crystal is simply a stacking of unit cells. For crystallographic purposes the unit cell can be used to define alignments of atoms in 2D planes with a uniform spacing throughout the bulk crystal. In figure 15c some of the numerous planes in the hexagonal hydroxyapatite structure are shown. These periodic planes are ideal for diffraction with x-rays as the spacing between planes and the x-ray wavelength are in the same range.

If an x-ray is beamed through an unknown powder sample of randomly oriented crystal particles the Bragg condition is occasionally fulfilled by planes lying with the correct angle and spacing. As rotation of the planes around an axis parallel to the incident beam produces a corresponding rotating diffracted beam and the randomly oriented crystals in a powder represents all degrees of rotation, the diffraction from a powder produces a cone shaped array of waves for each plane (Fig. 16).

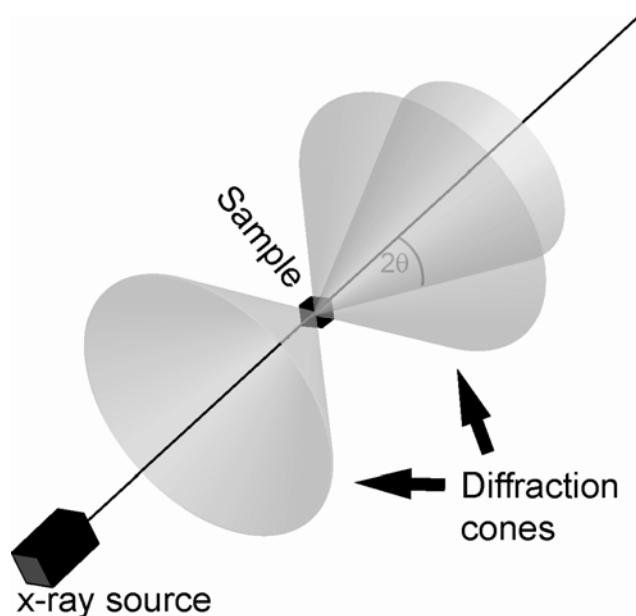


Figure 16. Diffraction cones from a crystal sample. The diffraction angle for one of the cones is marked.

By measuring the angles of all the “diffraction cones” to the incident beams (2θ) a set of plane spacings can be derived from the Bragg equation. As the plane spacings are unique to the crystal structure the unknown crystal can be identified.

5.1.6 Material characterization in thesis

The described techniques for material characterization are used throughout the papers. In the following the usage and results in individual papers is outlined and data examples not included in the papers are shown.

5.1.6.1 Paper I & II

Tapping mode AFM was used to characterize surface topography. Figure 14 depicts the gold and hydroxyapatite coated quartz crystals (Q-sense, Göteborg, Sweden) used in the quartz crystal microbalance experiments (described in section 5.3.1) and cell experiments (described in section 5.4). A Nanoscope IV AFM (Veeco Instruments Inc., NY, USA) was used with NSG01 silicon cantilevers (NT-MDT, Moscow, USA) with tip curvature radius below 10 nm, a spring constant of 5.5 N/m and a typical resonance frequency of 150 kHz.

Water contact angle measurements were carried out with the sessile drop method using a DSA100 (Krüss, Hamburg, Germany). Both gold and HA surfaces were found to be very hydrophilic with a contact angle below 10° (Data not shown).

X-ray diffraction was performed by Jaques Chevallier with a Bruker D8 Discover Diffractometer (Bruker AXS inc., Madison, WI USA) to confirm the presence of crystalline hydroxyapatite on the HA coated quartz crystals. Grazing incidence diffraction was necessary to achieve detectable diffraction cones, due to extremely low diffraction from the very thin layer of HA (app. 10 nm). By using a very low angle between the quartz crystal and the incident beam (grazing incidence) the effective amount of HA analyzed is maximized and scattering from the underlying layer is minimized [106]. The results are depicted in the intensity vs 2θ plot in fig. 18a.

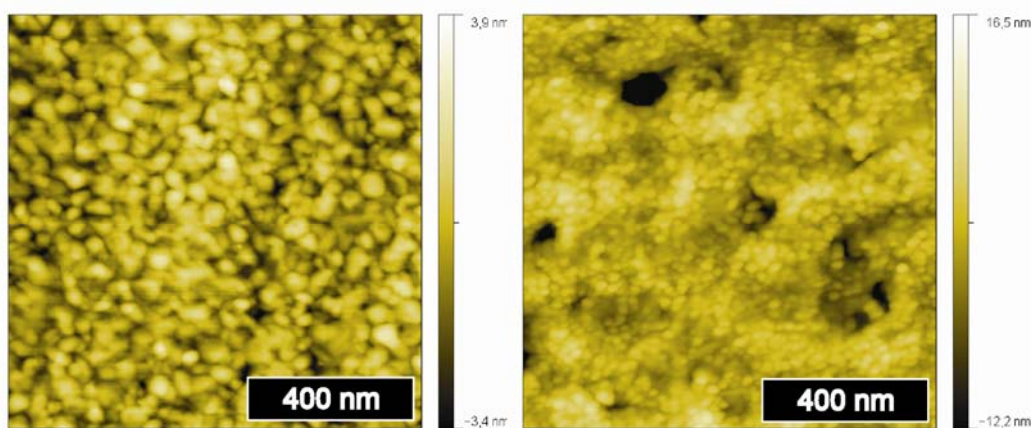
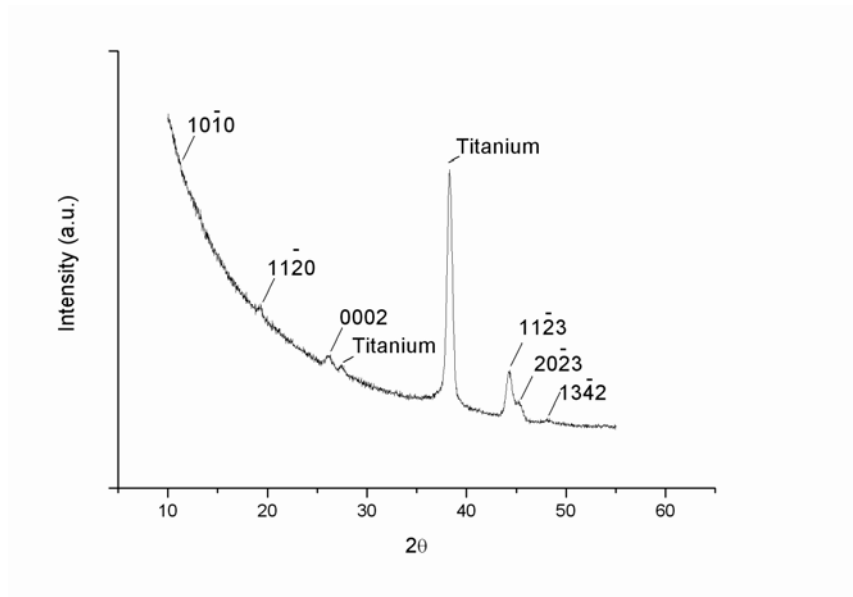


Fig. 17. AFM images of the gold (left) and hydroxyapatite (right) surfaces used in paper I & II. The pictures confirm presence of a similar grainy topography on both surfaces. The grains on the HA-surface are smaller than those on gold. The pictures were used to derive the root mean square roughness which is included in both paper I & II as 2.2 nm and 0.9 nm in average. This is considerably lower than the dimensions of the proteins studied.

a



b

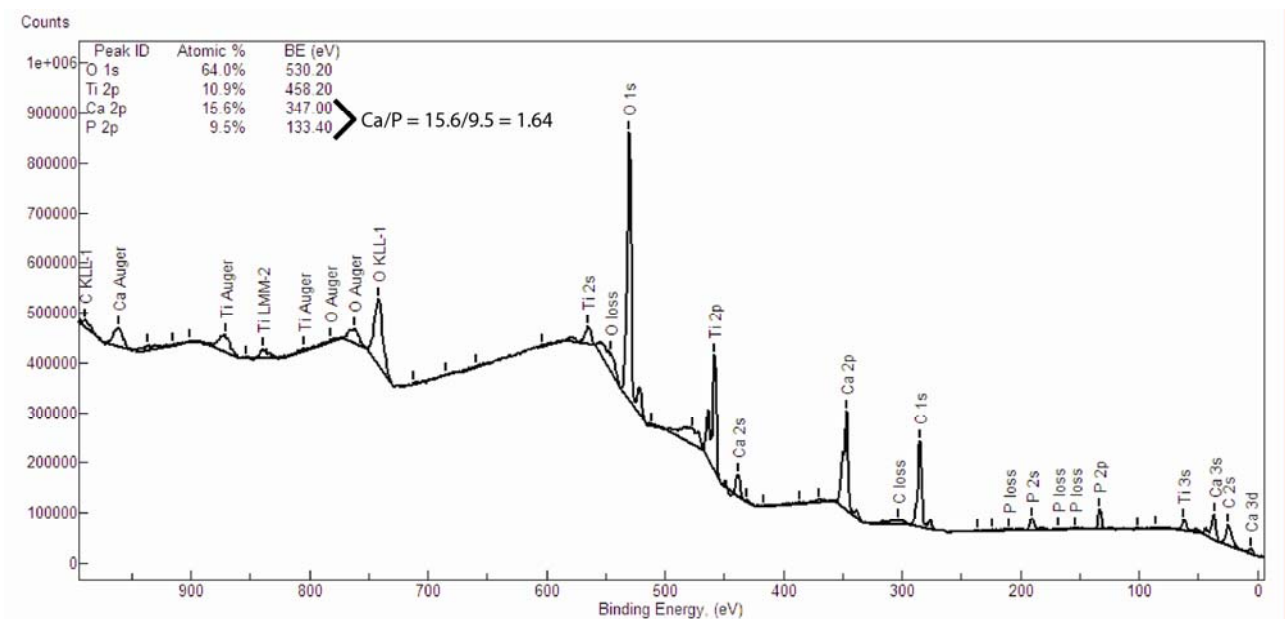


Figure 18. a) Diffraction angles from the hydroxyapatite surface coating used in paper I & II. The regular noise level decreasing from left to right is reflection of x-rays owing to the low angle of incidence. The intensity peaks distinguished with the software applied with the apparatus are marked with the matching diffraction plane from HA. Peaks from the underlying titanium are present. Usually three specific peaks/planes are considered sufficient to identify a crystal. In this measurement 6 peaks specific to HA are identified using unit cell parameters $a = 9.43 \text{ \AA}$ and $c = 6.88 \text{ \AA}$ [107] and it is thus concluded that the surface coating contains crystalline hydroxyapatite. b) XPS survey scan provided by Q-sense of the HA-coated QCM-D crystals used in thesis. The Ca/P ratio resembles that of stoichiometric HA (1.67).

AFM and XRD were done to characterize the commercially available quartz crystals (Q-sense, Göteborg, Sweden). The HA-coated crystals are fabricated in a collaboration between two

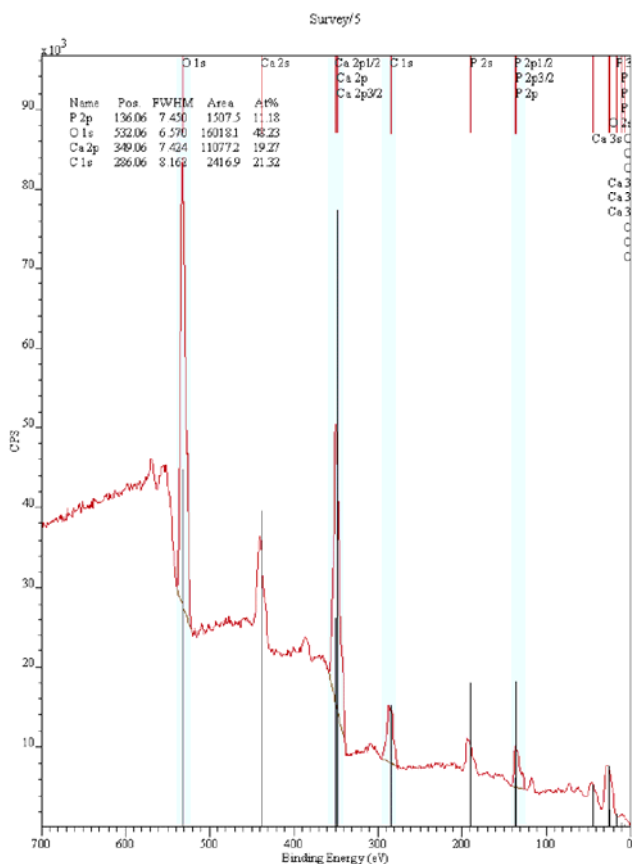
companies, Q-sense and Promimic (Göteborg, Sweden), using a technique patented by Promimic [108]. The technique is based on precipitating HA nanoparticles in solutions containing organic compounds with different functional groups. One of the functional groups attach the organic compound to the nanoparticles surfaces and by choice of remaining functional groups the technique can be used to functionalize the nanoparticles. For instance, organic compounds attaching to the nanoparticles and presenting positively charged groups to the exterior can be used to direct the nanoparticles to a negatively charged oxide surface, e.g. titanium on a Q-sense quartz crystal. The organic compounds can be removed afterwards by heating to leave a thin monolayer of HA-particles. An XPS survey scan provided by Q-sense of a HA-coated Q-sense crystal (identical to those used in the thesis) is shown in figure 18b.

5.1.6.2 Paper III & IV:

The 20 – 70 nm HA particles included in the HA containing composites were pictured with TEM on a CM20 TEM (Philips, Amsterdam, Netherlands) to confirm particle size and crystal structure. SEM was performed on a NOVA-scan 600 (FEI, Hillsboro Oregon, USA) to measure the thickness of a pure polymer coating and a polymer/HA composite coating on titanium. Both TEM pictures of particles and SEM pictures of the coatings are included in paper III. AFM was also used to estimate particle size and furthermore, the surface features of the PDLLA and the PDLLA/HA composite coatings. The results are included in paper III.

XPS was used to quantify the elemental composition of pure HA-particles and HA-particles preadsorbed with OPN. Survey scans were performed by Gurvinder Singh with an Axis Ultra XPS (Kratos Analytical, Manchester, England). A monochromated Al-K α x-ray beam of 1.5 kV was used for electron exciting and the pass energy to the electron detector was 1600 e-volt. Three sweeps of 120 seconds detection per scan. Figure 16 shows two representative survey scans.

a. Survey XPS on HA nanoparticles



b. Survey XPS on HA nanoparticles with OPN

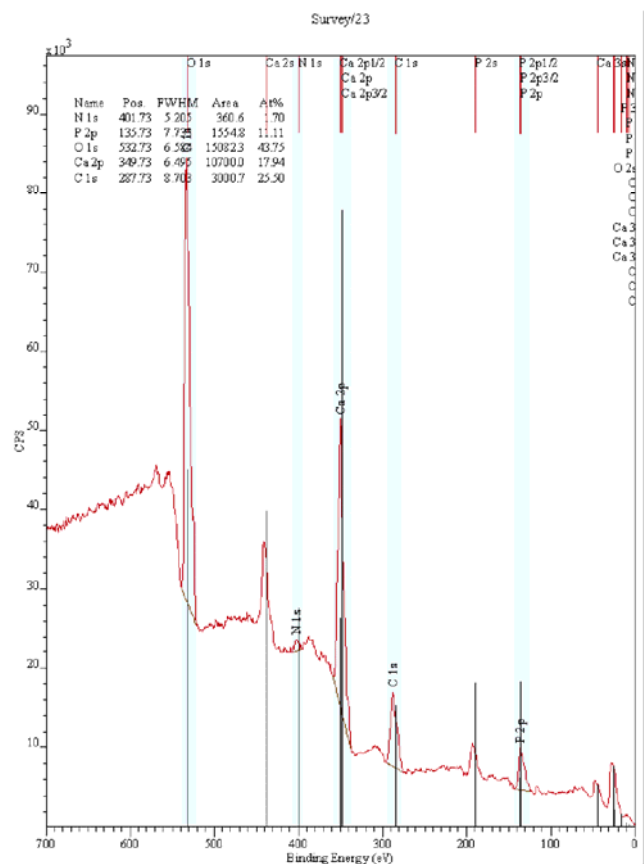


Figure 19. XPS survey scans of HA particles (a) and HA particles with OPN (b). The binding energy increases from right to left. This presentation is normally used as it reflects the increase in kinetic energy of detected photoelectrons from left to right. Six scans were performed on both pure HA-particles and HA-particles with OPN preadsorbed. The full dataset is included in paper IV. The HA particles chemical composition corresponds to that of stoichiometric HA (a). Appearance of 1.70% nitrogen when protein adsorbs onto the HA particles (b) corresponds with literature.

5.2 Protein adsorption analysis

Protein adsorption is of major interest in biomaterial design. In the following section three methods for studying protein adsorption are presented. Quartz crystal microbalance with dissipation monitors the surface mass density (weight/area) and mechanical properties of adsorbing protein layers including coupled water. AFM scratching and ellipsometry measures the thickness of protein layers without coupled water. This quantity can be used to derive the surface mass density of dried protein layers. The data obtained with the methods provide information about the surface mass densities of adsorbed protein layers in the range of nanogram/cm². This sensitivity is sufficient to estimate the area taken up by a single protein if the molecular weight is known.

5.2.1 Quartz crystal microbalance with dissipation (QCM-D)

QCM-D is a direct quantification technique for monitoring changes in mass and mechanical properties of substances on surfaces. The technique was originally developed for detection of gas adsorption but has recently proven suitable for detection of biological molecules such as proteins adsorbing from liquid [6,8,10,109]. The technique differs principally from alternative methods in that not only the dry mass is detected, but also the coupled water. It is versatile in that adsorption on any surface can be tested with a resolution of less than 10 ng/cm^2 . This resolution corresponds approximately to one isolated amino acid for each 2 nm^2 . As proteins consist of several hundred amino acids bound together the QCM-D is evidently suitable for analysis of protein adsorption.

The basic principle of QCM-D measurements relies on the oscillations of a thin quartz crystal sensor (Fig. 20a). The oscillations are brought about by applying an alternating current across the sensor. This produces oscillating deformations according to the piezoelectric properties of the crystal. Specific crystal cutting ensures that the deformations are in shear mode – *i.e.* parallel to the crystal side surface (Fig. 20b).

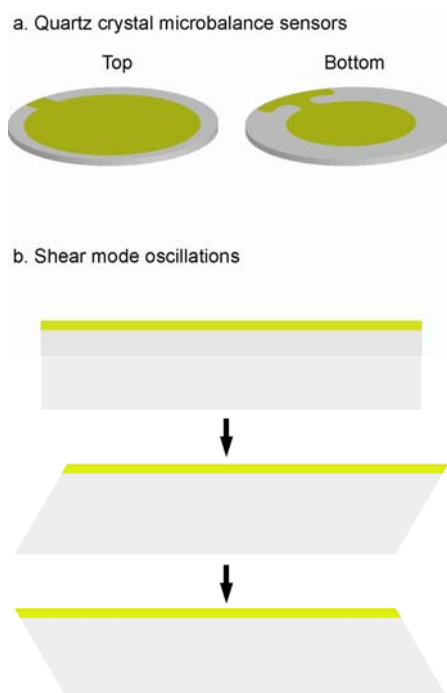


Figure 20. Illustration of the QCM-D crystal sensors (a) used for protein adsorption experiments in paper I & II. Shear mode oscillations as a result of applying an alternating current across the crystal are shown in (b).

During a measurement, the sensor is sequentially oscillated at the fundamental resonance frequency and the odd overtones (1st, 3rd, 5th, 7th etc). The fundamental resonance

frequency for the sensors is approximately 4.95 MHz. When a mass is added or subtracted from the surface – e.g. adsorbing proteins, the resonance frequencies of the sensor changes proportionally. The relationship is expressed in the Sauerbrey equation:

$$(2) \quad \Delta m = -\frac{C}{n} \Delta f_n$$

Where Δm is the change in surface mass density (ng/cm^2), C is the mass sensitivity constant ($17.7 \text{ ng}/\text{cm}^2 \text{ Hz}^{-1}$ for a 4.95 MHz crystal), n (1, 3, 5...) is the overtone number, and Δf_n is the frequency shift of the n 'th overtone. With the Sauerbrey equation, the change in mass on the surface can be directly calculated from the detected change in resonance frequencies.

Besides detecting the shifts in resonance frequencies, a QCM-D apparatus also detects the change in energy dissipation. The dissipation is the amount of energy lost relative to the energy stored during an oscillation cycle. High dissipation corresponds to a high damping effect on the oscillation and vice versa. It is defined as:

$$(3) \quad D = \frac{E_{\text{lost}}}{2\pi \cdot E_{\text{stored}}}$$

In general the dissipation increases with addition of mass but the proportion is related to the viscoelastic properties of the material adsorbed. It is intuitively meaningful that a very rigid addition will introduce a low damping effect on the oscillating sensor, whereas a loose “fluffy” addition has a higher damping effect on the crystal. Although other factors affect the dissipation it is considered a quantitative representation of the viscoelastic properties of the added material. From the frequency and dissipation shifts the shear viscosity, shear elasticity and thickness of the added material can be estimated with the Voigt model [110].

The Sauerbrey equation (eq. 2) states that the calculated surface mass density should be the same regardless of overtone. This holds true only for rigid additions in that non-rigid additions have a frequency dependent impact on the shift in resonance frequency. This means that the Sauerbrey equation is not suitable for surface mass density calculations of non-rigid additions because it will give different surface mass densities with different overtones. If the dissipation is

high this problem can be solved by using the thickness derived from the Voigt model to estimate surface mass density, where the viscoelastic properties are accounted for.

QCM-D results must be evaluated with caution because not only the dry mass of the adsorbed material is quantified. In case of proteins adsorbing from water, there are large frequency and dissipation contributions from coupled water. Comparison of QCM-D data can be biased by relatively different contributions of coupled water. In general, the more water coupled to a protein layer – the higher massed and less rigid a layer observed with QCM-D [9,10,111]. This potential bias can be accounted for by measuring the dry mass with an alternative surface analysis technique. Quantification of coupled water by combining dry mass methods with QCM-D also provides further insight to the status of adsorbed proteins. The two following sections on AFM scratching technique and ellipsometry present two methods for measuring the dry mass of proteins on a surface.

5.2.2 Atomic Force Microscopy – scratching technique

With a combination of contact mode AFM (section 3.2.1.1) and tapping mode AFM (section 3.2.1.2) the thickness of protein layers can be determined [112,113]. The protein layer is scratched from the surface in a $1 \times 1 \mu\text{m}$ area with contact mode AFM and subsequently the scratched area along with surrounding intact protein layer is scanned with tapping mode AFM.

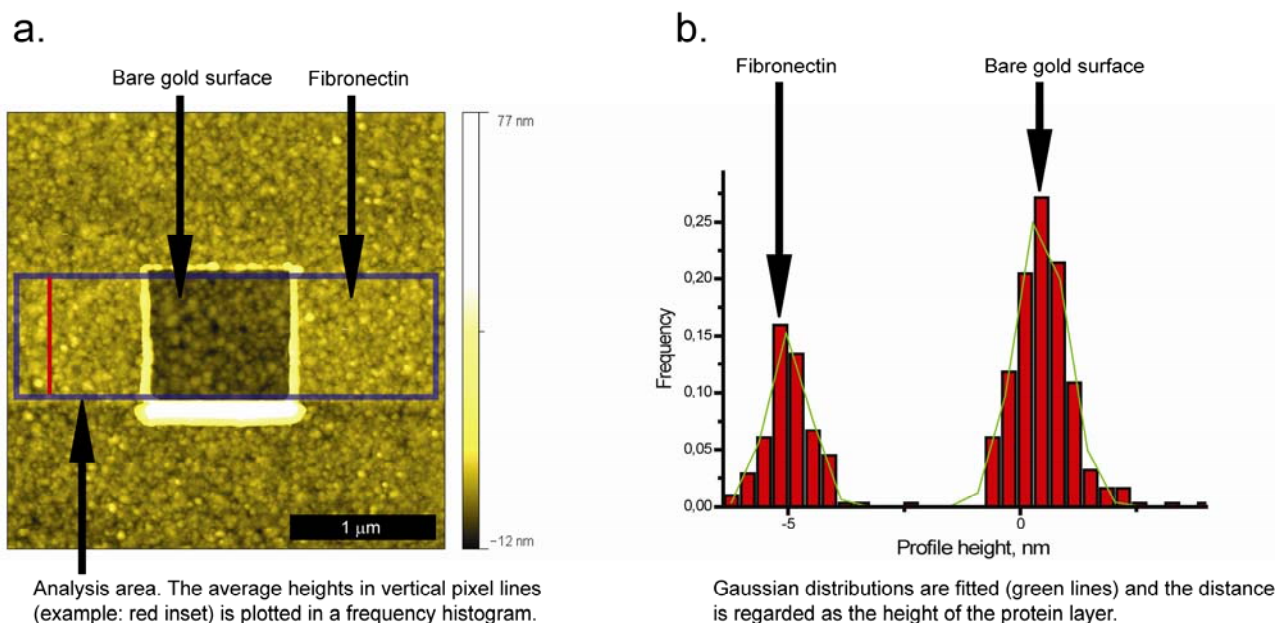


Figure 21. A $3 \times 3 \mu\text{m}$ tapping mode AFM image of protein coated surface after scratching in the center $1 \times 1 \mu\text{m}$ area (a). In (b) the resulting frequency/height histogram is shown. The distance between peaks of fitted Gaussian distributions is regarded as the height of the protein layer.

Prior to performing the scratching the maximum deflection setpoint during contact mode scratching must be identified. This is done by scanning the bare surface with increasing deflection setpoint until the surface is distorted. Protein dislocation is performed at half the deflection necessary to distort the surface. The height difference between scratched and non-scratched areas is the thickness of the dry protein layer (Fig. 21). The surface mass density (weight/area) can be derived with the volumetric density of proteins (Height \times volumetric density).

5.2.3 Ellipsometry

Ellipsometry is an optical technique suitable for quantification of thin film thickness with a spatial resolution down to 0,1 nm. It is a well established technique for detection of protein adsorption at solid/liquid interfaces [114]. In contrast to QCM-D it measures only the dry mass of adsorbed material. The method relies on detection of the changes in two polarization characteristics of elliptically polarized light when reflected from a surface (Fig. 22).

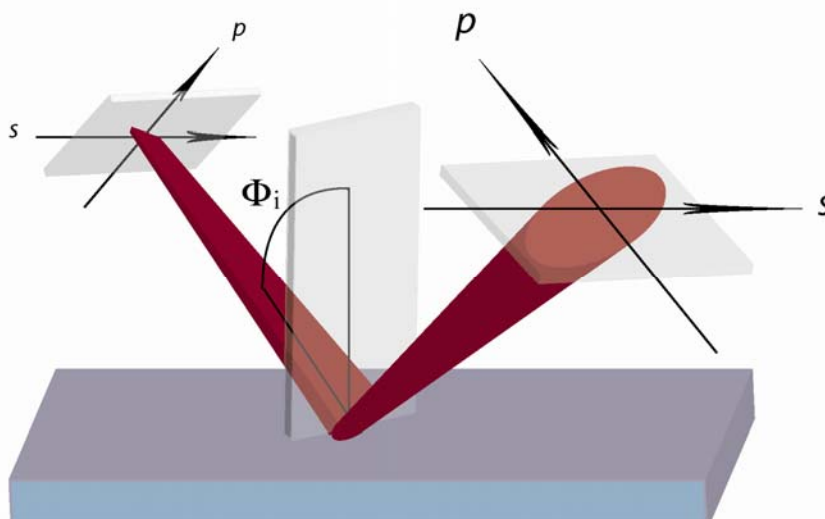


Figure 22. Illustrations of Ellipsometry principle. Elliptically polarized light is beamed on a surface and the change of polarization in the reflected light when a mass is added to the surface is detected. The principle allows for dynamic detection of protein adsorption.

Reflection changes the elliptical polarization to an extent dependent of the refractive index of the surface. The ellipsometer measures i) the change in ratio of electric field amplitudes of the p- to the s- component (Ψ), and ii) the change in phase separation between the p- and the s- component (Δ) (Fig. 14). The data relates to the complex reflectance ratio given by the fundamental ellipsometry equation:

$$\rho = \frac{R_p}{R_s} = \tan(\Psi)e^{i\Delta}$$

where ρ is the complex reflectance ratio, R_p and R_s the reflection coefficients for the p- and s-components as given by the Fresnel equations, $\tan(\psi)$ the electrical field amplitude ratio of the p- to s-components and $e^{i\Delta}$ the phase change. Using layer-by-layer combination of Fresnel equations optical models can be setup to derive the thickness of films [115]. The surface mass density of nonhydrated protein films were calculated from the derived thickness with de Feijter's formula [116]:

$$\Gamma_{\text{Ellipsometry}} = d \frac{n_{\text{protein}} - n_{\text{buffer}}}{dn/dc}$$

where d is the thickness of the protein film, dn/dc the refractive index increment for a protein concentration change, n_{protein} and n_{buffer} the refractive indices of protein and buffer.

5.2.4 Combining QCM-D, AFM scratching and Ellipsometry

Throughout the protein studies done QCM-D was considered the central measuring technique. In contrast to ellipsometry and AFM scratching it is a direct technique providing both surface mass density and viscoelastic properties on adsorbed proteins in its natural environment. As described QCM-D holds an inherent disadvantage in that the detected response contains both a contribution from adsorbing proteins and the associated water. The relative contributions of protein and water cannot be distinguished from the QCM-D results alone and thus conclusions on protein characteristics based on QCM-D alone are biased. In this section, it is described how the AFM scratching and ellipsometry techniques can be used to support the QCM-D results to omit this bias and furthermore provide additional data of interest regarding adsorbed proteins. The relation between QCM-D, ellipsometry and AFM scratching is best approached by an illustration depicting what the techniques detect (Fig. 23).



Figure 23. The different techniques estimate different aspects of the protein characteristics. QCM-D detects both the adsorbed proteins and the associated water directly (a). Ellipsometry detection is modelled to a theoretical dense uniform layer of dry protein mass (b). AFM scratching measures a dry mass height, which is dominantly a contribution from the protein dry mass (c). Ellipsometry estimates can be directly combined with QCM-D estimated. As the AFM scratching is unlikely to be completely packed as a result of water evaporation the combination of QCM-D and AFM scratching must be done as a plot with several points (As done in paper I).

QCM-D detects the surface mass density of both the proteins and the associated water embedded in the protein structure and in immediate vicinity. Ellipsometry data is through an optical model used to derive an imaginary homogenous thickness of mass exclusively made of dry protein. From this quantity, the dry surface mass density is calculated. AFM scratching measures the height of the protein after dehydration in vacuum. The resulting protein layer height after dehydration is solely comprised of the protein dry mass - albeit with some small voids likely present between proteins and within protein structure. By multiplying with the volumetric density of proteins the surface mass density of dry protein mass can be estimated. As these alleged voids will overestimate the surface mass density of the protein layer as measured with AFM, the combination of QCM-D and AFM scratching should be done in a plot. Assuming that the voids comprise a constant overestimation of the AFM measured surface mass densities, the slope of a QCM-D vs AFM scratching plot with several coupled surface mass densities can be used to estimate the water factor of the QCM-D.

In literature the ratio between QCM-D obtained hydrated surface mass density and dry surface mass density is commonly termed the “water factor”. A water factor of 3 corresponds to a 75% contribution from water to the QCM-D response. The water factor itself is a parameter of interest as it varies with different proteins and a change of configuration may be corresponded by a change in the water factor [9,10]. When the water factor is known QCM-D results can be used to estimate foot print of single proteins and viscoelastic properties can be estimated with respect to the protein dry mass.

In the following outline of protein adsorption as performed in paper I & II the protein characteristics are presented from the perspective of single proteins. Thus, what is presented in the

following are single protein interpretations of the surface mass densities of protein layers as observed with the respective techniques.

5.2.5 Protein adsorption in thesis

Protein adsorption analysis with the described techniques was done in paper I and II.

5.2.5.1 Paper I

With a combination of QCM-D and AFM scratching fibronectin was found to adsorb onto HA with a larger foot print area and a higher exposure of cell binding domains. Ellipsometry was used to support the AFM scratching technique. Exposure of cell binding domains was quantified with monoclonal antibody binding and unspecific binding was estimated with unspecific antibodies. A Q-Sense AB E4 system (Q-sense, Göthenborg, Sweden) was used for the QCM-D measurements. A Nanoscope IV (Veeco Instruments Inc., NY, USA) was used with NSG01 silicon cantilevers (NT-MDT, Moscow, USA) with tip curvature radius below 10 nm, a spring constant of 5.5 N/m and a typical resonance frequency of 150 kHz was used for AFM. An ELX-02C (DRE GmbH, Ratzeburg, Germany) rotating analyzer ellipsometer with a single wavelength $\lambda=632.8$ nm He-Ne laser was used for ellipsometry measurements.

5.2.5.2 Paper II

With a combination of QCM-D and ellipsometry osteopontin was found to adsorb onto HA with a larger foot print area and a higher exposure of the entire protein. Exposure of the entire protein was quantified with polyclonal antibody binding. Unspecific binding was estimated with unspecific antibodies. A Q-Sense AB E4 system (Q-sense, Göthenborg, Sweden) was used for the QCM-D measurements and an ELX-02C (DRE GmbH, Ratzeburg, Germany) rotating analyzer ellipsometer with a single wavelength $\lambda=632.8$ nm He-Ne laser was used for ellipsometry measurements.

5.3 Cell observation techniques

In extension of the protein adsorption studies two different microscopy techniques for investigating the initial cell interactions with the adsorbed proteins were used. Differential interference contrast microscopy is applicable for living cells on surfaces without staining. Imaging

of the cell surface is obtained. Fluorescence microscopy is applicable for fixated cells and requires staining with fluorescence labelled dyes. Intracellular moieties such as cytoskeleton can be imaged.

5.3.1. Differential interference contrast reflection microscopy (DIC)

DIC is a light microscopy technique performed with minor modifications of a conventional light microscope and the resolution is equal to that of conventional light microscopy (0.2 μm). The technique is applicable for translucent materials, which allows for direct observation of living cells.

The contrast generating principle is based on interference. The illuminating system produces two slightly separated beams of linearly polarized light (Fig. 24a). The beams are polarized with 90° to each other (Fig. 24b) and the phase difference can be manipulated.

a. The two beams are slightly separated

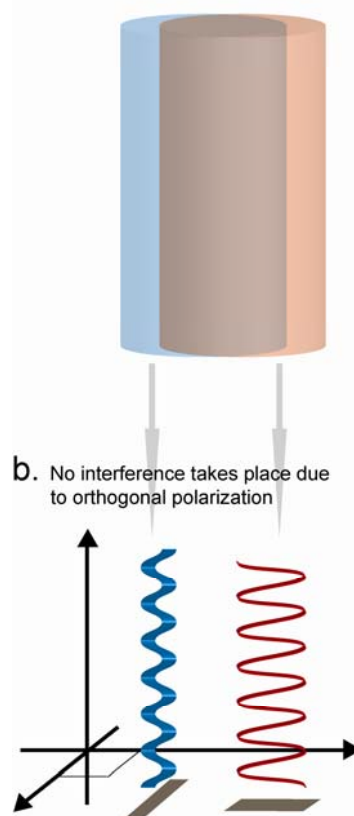


Figure 24. The principle illumination in differential interference microscopy. The incident beam consists of two slightly separated beams (a) with orthogonal polarization (b), which ensures that no interference takes place.

When the double beam is reflected from the sample surface the phases are slightly shifted due to differences in path length arising from height gradients in the sample. In areas where the two beams hit equal material heights the phases are not shifted. The reflected and still separated

beams carrying topography information from the sample are merged to one beam with a single polarization. This allows for interference to take place. Adjacent wavefronts reflected from areas with no height gradient will interfere according to the phase difference selected for the incident beam. Usually 90° phase separation is selected which results in 50% light intensity from flat areas (Fig. 25a). Adjacent wavefronts from areas with a height gradient contains phase shifts different from the incident beam. This can either result in constructive interference creating a higher light intensity (Fig 25c) or in destructive interference creating lower intensity (Fig 25b).

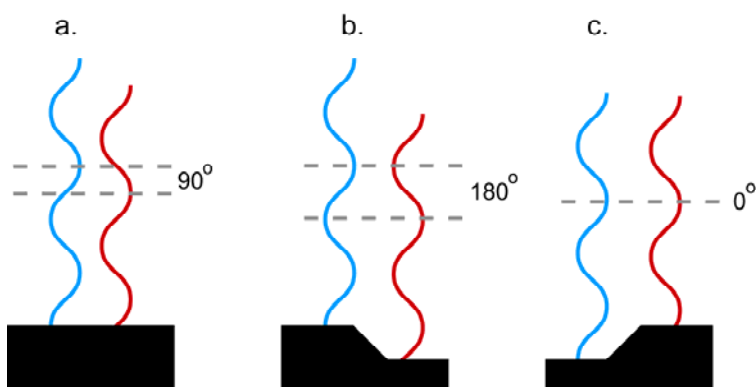


Figure 25. The double beam of DIC is reflected from the sample surface with no change of phase (a), with change of phase resulting in destructive interference (b) or in constructive interference (c). This comprises the contrast generating principle of DIC.

The DIC technique is suitable for observation of cell movements. At present, development in image acquisition allows for dynamic recording of detailed cellular events such as membrane extension and intracellular organelle movements [117,118].

5.3.2 Fluorescence Microscopy (FM)

FM is a technique that allows for selective imaging of intracellular substances such as protein aggregates and organelles. FM is performed on a fluorescence microscope which apart from a different illuminating system is similar to a conventional light microscope and has the same resolution. Samples with cells must be fixated and stained to achieve imaging.

FM is based on fluorescence from fluorophore containing dyes. A fluorophore is a molecule that is excited with a specific wavelength and consequently, emits light of a different specific wavelength. During staining the intracellular component of interest is specifically labeled with a fluorophore containing dye. The requirement for specific binding is in some cases obtained with naturally occurring dyes – e.g. diamidino-phenylindole (DAPI) for imaging of DNA (Fig. 26a). In other cases a combination of monoclonal antibodies binding to the component of interest

and fluorophore labeled antibodies binding to the tail of the monoclonal antibody can be used – e.g. for staining of vinculin, which is part of the membrane spanning protein complexes introduced in section 3.4.1 (FAS – Fig. 5 & Fig 26b).

During imaging a fluorophore is excited with light of the wavelength specific to the fluorophore. The following emission of fluorescent light is detected as in conventional light microscopy and an image of the component location is formed. The emitted light is very weak, and it is necessary to filter away reflections of incident light. If a sample is stained with different dyes an image must be created for each dye and subsequently merged to map the relative locations.

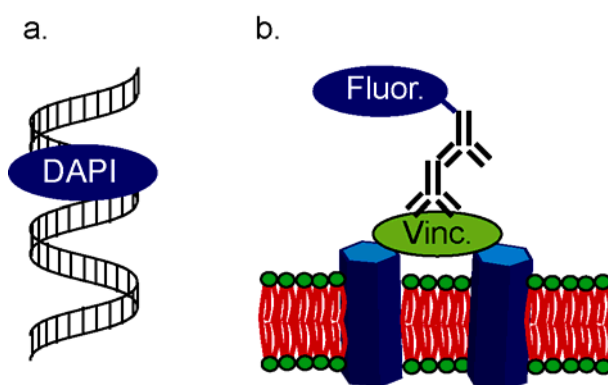


Figure 26. (a): DAPI directly binding to DNA. (b): Primary antibody binding to vinculin in a focal adhesion spot and secondary antibody with fluorophore binding to the primary antibody tail.

FM is a very important technique for qualitatively locating intracellular components of interest. The technique can also be used for quantitative purposes, where the signal intensity is correlated to presentation of e.g. membrane proteins [119,120]. Developing methods for incorporating fluorophores in living cells facilitates hitherto unprecedented qualitative and quantitative insight into cell biology [121].

5.3.3 Cell observation in thesis

5.3.3.1 Paper II

For the cell experiments, adult human mesenchymal stem cells (hMSC) transduced with the telomerase reverse transcriptase gene (hTERT) (often named hMSC-TERT) was employed [122]. These cells exhibited 4.3 population doublings per week and the cells were used at a population doubling level (PDL) 266 at which level recent studies using the same cells have reported osteogenic potential [123,124].

DIC was used to observe the initial cell motility in the period 1 – 7h following incubation. In the first hour (0 – 1h) many cells were still floating in solution. The substrates used were HA with OPN, gold with OPN and as controls HA and gold not preadsorbed with OPN. All surfaces were immersed in serum containing media 15 minutes before cell incubation. A Leica DM 6000B microscope (Leica Microsystems GMBH, Wetzlar, Germany) with a mounted incubator was used for imaging. Cell position was defined as center of mass as detected with the grain analysis tool of the basic ImageJ software [125] and distance between centers of mass was calculated for each 28 minutes (Fig. 27). OPN was found to induce cell motility in the observation period, but exclusively when adsorbed on HA.

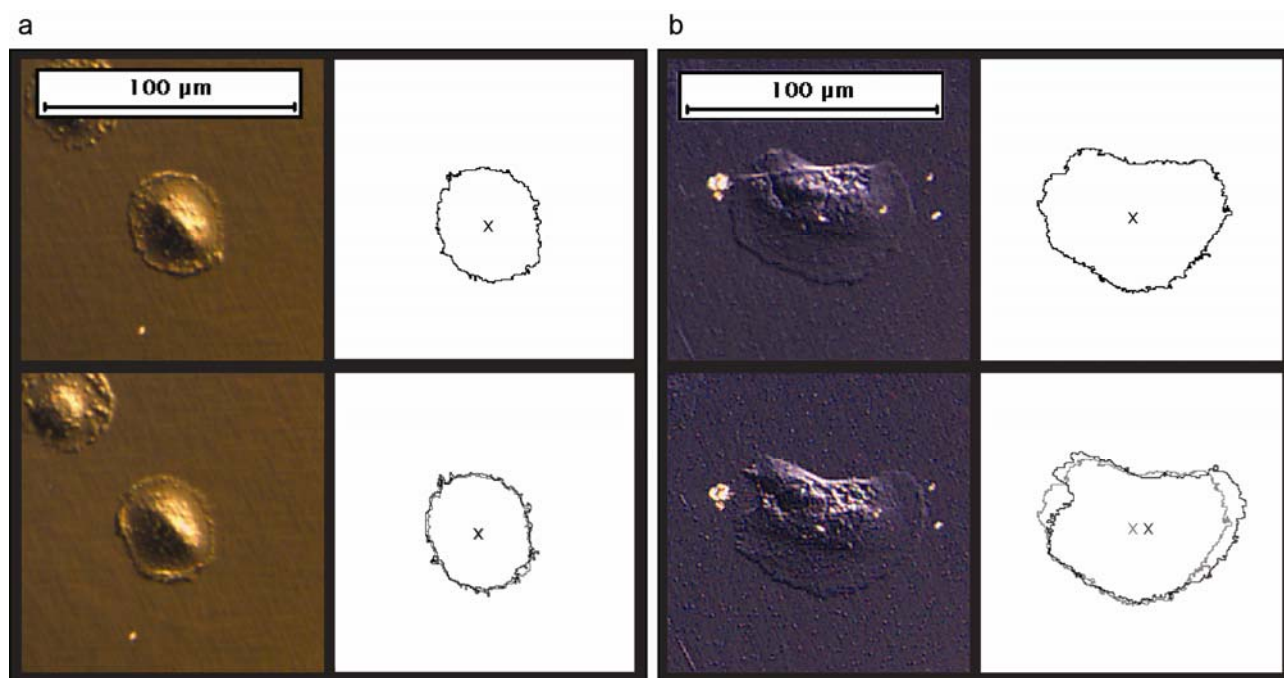


Figure 27. Two examples of cells pictured with 28 minute intervals. The time difference between upper row and lower row of images is 28 minutes. A non-migrating cell on gold preadsorbed with OPN (a) and a mobile cell on HA preadsorbed with OPN (b) are depicted. The outlines display the cell borders and center of mass detected with ImageJ. In lower row outlines before and after 28 minutes are merged to display the detected migration. The cell in b migrates app. 5 μm.

FM was used to image morphology of cells fixated at 1h, 3h, 6h and 24h. Substrates and setup were identical with that used in the DIC study. Cell area and cell roundness was estimated with fluorescence imaging of actin cytoskeleton and distribution of FAS was estimated with fluorescence imaging of vinculin. A Leica DM 6000B microscope (Leica Microsystems GMBH, Wetzlar, Germany) was used for imaging and the basic ImageJ software grain analysis tool [125] was used to estimate area and roundness, whereas vinculin distribution was estimated by eye. It was

found that OPN induced a larger cell area and decreased the cell roundness (cell elongation) at all time points but exclusively when attached to HA. The distribution of vinculin in cells on HA preadsorbed with OPN was found to be in agreement with that expected from cells during active migration, whereas the vinculin on remaining surfaces was uncharacteristic. This difference was most outspoken at 3h. In Figure 28 an alleged migrating cell and an alleged non-migrating cell 3h following incubation are shown.

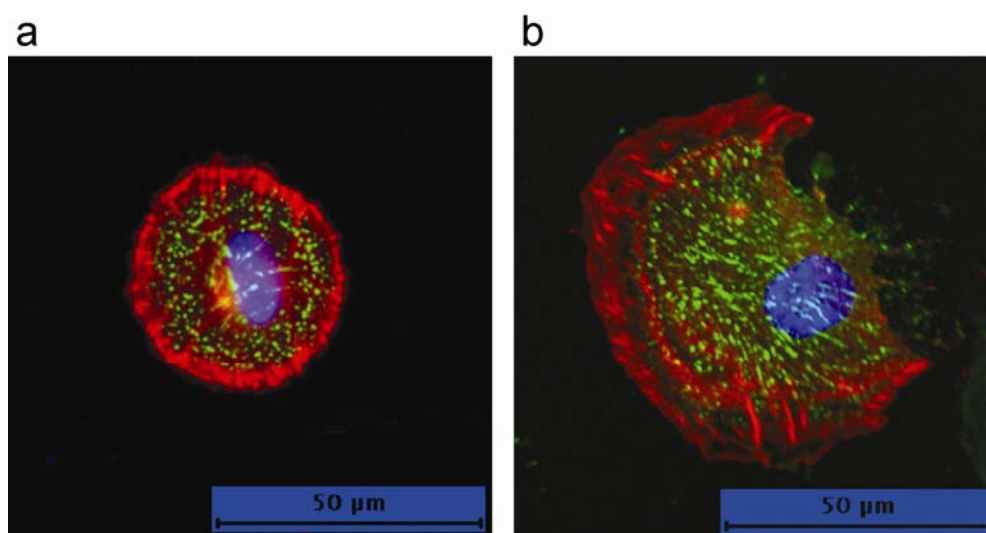


Figure 28. Examples of cells during the initial interaction with surfaces at 3h after incubation. The cell shapes (cf. figure 27) and vinculin distributions suggest that the cell in (a) (substrate: gold preadsorbed with OPN) is non-migrating and the cell in (b) (substrate: HA preadsorbed with OPN) is migrating.

The cell studies provide strong evidence that the observed differences in protein adsorption are a reflection of a specific interaction between HA and OPN, which favours presentation of the cell binding domain.

5.4 In vivo testing techniques

The following sections introduce an *in vivo* model suitable for evaluating osseointegration of bone implants. Based on the results from the protein and cell studies two *in vivo* studies were setup for evaluating the impact of a composite implant coating consisting of HA nanoparticles, proteins and a biodegradable polymer (Poly-D,L-Lactic Acid (PDLLA)). The following sections describe the *in vivo* study design and the technique used for producing the coatings tested.

5.4.1 Study design.

The implant model imitates the close bone/implant interaction of implants in cementless arthroplastic surgery. The model addresses tissue level response by evaluating early periimplant tissue formation and mechanical implant fixation. This approach holds clinical relevance in that the long term survival of implants is correlated to the initial fixation of implants [48, 49]. The fixation in turn is a reflection of the tissue composition in the bone/implant interface.

The basic premises of the bone implant model are i) Insertion of a small cylindrical experimental implant in a suitable bone site (Fig. 29a), ii) After observation time the bone site including implant is harvested and prepared for histomorphometry (Fig. 29b) and mechanical push-out testing (Fig. 29c). Implants are inserted bilaterally to create paired data, making each animal its own control. This reduces the interanimal variation. The dimensions of the implant are usually one cm in length and 6 – 8 mm in diameter. Implants can be inserted to fit the drilled bone defect or larger diameter end-caps can be applied to maintain them with a uniform gap to the bone defect. After harvesting and before preparation the specimens are kept in freezer, which tends to erupt the cells. The inner 7 mm of implant is used for histomorphometry and the outer 3 mm for push-out testing (Fig. 29b&c). Histomorphometry quantifies the tissue around the implant thereby providing a detailed evaluation of the host response to the implant surface. Push-out testing quantifies the mechanics of controlled failure by pushing the implant out of the bone site.

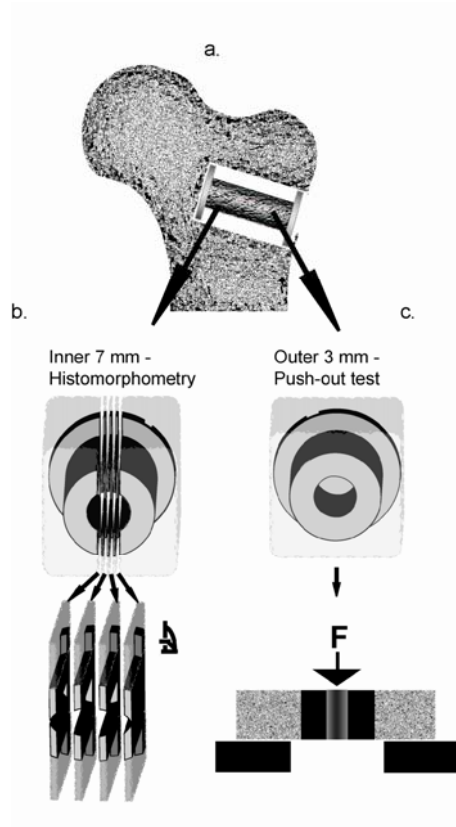


Figure 29. Implant insertion (a), vertical sectioning of the inner seven mm for histomorphometry (b) & the outer 3 mm for push-out test (c).

The choice of species and implant site is aimed at imitating clinical conditions. Of the commonly used species used for bone studies canine is preferred due to high resemblance with humans regarding bone structure [126] (The choice of animals used in the thesis will be discussed in section 7.2.2). In line with clinical conditions implantation is preferably done within the trabecular bone of the proximal or distal parts of long bones. The rationale number of animals included was calculated as follows:

$$n = 2(Z_{2\alpha} + Z_{\beta})^2 \times sd^2 / MIREDF^2 = 2(1.96 + 0.84)^2 \times 50^2 / 70^2 \approx \underline{\underline{8}}$$

Where n is sample size, $Z_{2\alpha}$ and Z_{β} the z-values for risk of error of first and second kind respectively, sd the standard deviation and MIREDF the minimal relevant difference. The risk of error of the first kind (false positive) was set to 5% and the risk of error of the second kind (false negative) was set to 20%. From previous experience with the experiment, the standard deviation was set to 50% and the minimal relevant difference to 70%. As shown in the calculation this results in a sample size of 8. Using 10 animals seems feasible in that some loss of data must be expected.

In our group, the animal model has been used for evaluating the osseointegrative impact of several different modifications of implant surfaces. The push-out test is of direct clinical relevance, whereas histomorphometry is a descriptive technique to theoretically support the push-out test. In the following two sections, the basics of histomorphometry and push-out test are presented.

5.4.1.1 Histomorphometry

Histomorphometry is defined as a method for estimating e.g. volumetric and surface area fractions of specific tissue presentations samples presented in 2D sections. Four vertical sections parallel to the implant axis are cut from the inner 7 mm of the implant (Fig. 29b). The 2D representations of mineralized bone tissue, fibrous tissue or marrow-like tissue in the estimated are estimated by counting the coincidence of the tissue types with superimposed probing grids. Areal representation on an implant surface is estimated by counting tissue coincidences with a line grid where it intercepts the implant surface [127], and volumetric representation in a gap is estimated by counting the tissue coincidences with points in point grids [128]. The estimated 2D tissue representations are representative of the actual sections if the sampling intensity is adequate. This is obtained by increasing the number of lines/points in the probing grid until reproducibility between independent counts.

In the two animal studies of this thesis, the periimplant tissue fractions were estimated separately in two zones of interest (Fig. 30).

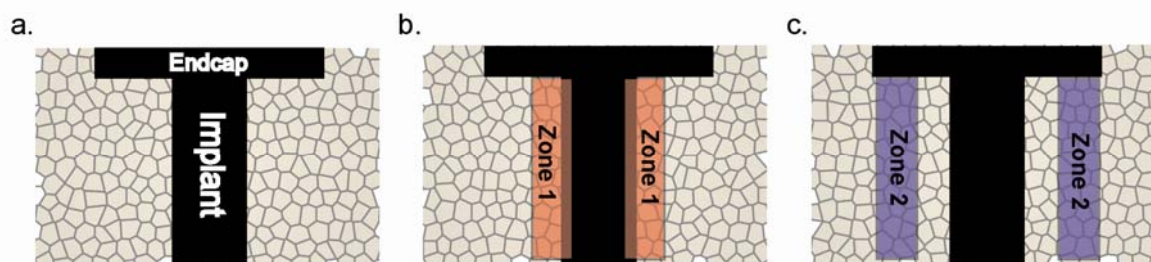


Figure 30. Illustrations of sections as produced from specimen preparation (cf. Fig. 29b). Two zones are defined and the histomorphometric analysis is performed separately in these zones.

Using the counted 2D tissue estimates as representative estimates of areal fractions on the entire implant surface and volumetric fractions in the entire gap requires observation of three

premises in the sectioning [127]: 1) a vertical axis of the specimen is identified, 2) sections are cut parallel to the vertical axis and 3) sections are randomly orientated around the axis. It is furthermore, a requirement that the line grids for estimation of areal surface representation are weighted proportionally to the sine of the angle between axis and line grid [127]. The bias of estimating area and volumetric tissue distributions as done in this thesis is negligible [129]. In our group, the method has been established and refined. Exhaustive evaluation of the technique and its bias can be found in reference [129].

5.4.1.2 Push-out test

Push-out test quantifies the mechanical fixation of the experimental implants. The as-prepared outer 3 mm of implant and periimplant tissue are placed on a supporting metal jig with a suitable opening as recommended [130]. The cortical side of the 3 mm implant stub is pointed upward and the implant was pushed in the trabecular direction. Axial force is applied to the implant with a constant displacement rate of 5 mm/min. The force needed to uphold the displacement rate during pushing of the implant out of the periimplant tissue is monitored and registered by a computer. Figure 31 illustrates a typical force/displacement curve obtained with the procedure.

From the obtained curve, the shear stiffness is estimated from calculation of the maximum slope between two measure points, the shear strength as the maximum stress observed and the total energy absorption as the area under the curve until failure.

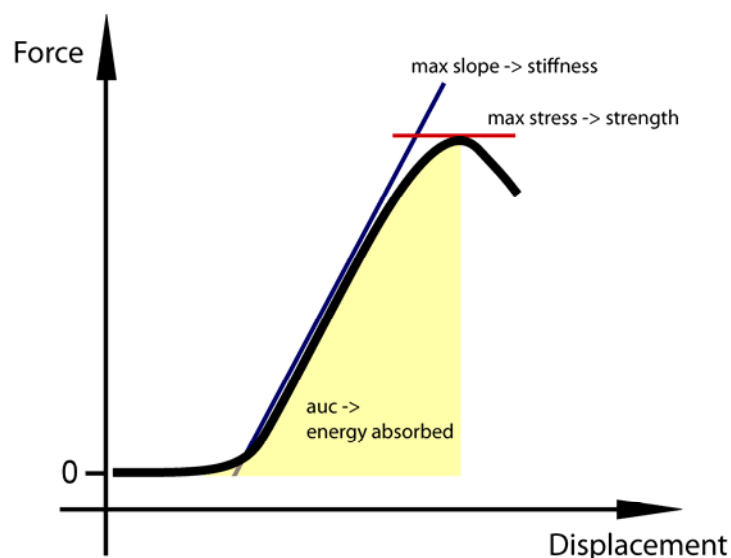


Figure 31. Typical force/displacement curve for implant push-out tests. The dotted blue lines depicts the maximum slope, which is used to estimate stiffness. The red dotted line depicts the maximum stress which is used to estimate the maximum strength of fixation. The area under the curve is used to estimate the total energy absorbed in the fixation until failure.

5.4.2 Implant coating preparation

The coatings tested in the two animal studies of this thesis were inspired by the “cold coating technique” or “dip-coating technique” for metallic implants introduced in 2001 [131]. The technique is simple, but versatile in that it can be applied to any structure. PDLLA is added to a suitable organic solvent, e.g. chloroform or ethylacetate, and allowed to dissolve homogeneously during light stirring. The coating is performed by dipping the implant in the solution, which leaves a small amount on the implant surface. After evaporation of the organic solvent a pure thin PDLLA film is left on the implant. The technique is not only versatile with respect to the object to be coated but also in that proteins [87,90,91], bisphosphonates [85,86] and antibiotics [88,89] can be added to the coating with maintained functionality.

5.4.3 In vivo studies in thesis

5.4.3.1 Histomorphometry and push-out test in thesis.

Histomorphometry was performed blinded on an Olympus BX-50 microscope using a stereological toolbox including software and automated stage (CAST-grid Olympus Denmark A/S, Ballerup, Denmark). Zones of interest (Fig. 30b&c) were defined at $\times 12.5$ magnifications and counting with superimposed probing grids was done at $\times 100$ magnification. In both studies reproducibility was obtained by using 5×5 points in the point grid and 10 lines in the line grid for each frame. Mechanical push-out test was done with an Instron universal test machine (Model 4302, Instron, UK).

The reproducibility was evaluated by calculating the coefficient of variance (CV) for four implants from paper IV randomly picked for double counting. CV was calculated with following equation:

$$CV = s / \bar{x} \quad , \quad s = \sqrt{(1/(2 \times k)) \times \sum d^2} \quad ,$$

where x is the mean value of the first and the second measurements, k is the number of double estimates and d is the difference between the first and the second measurements of the individual parameters. The CV for the different tissues is listed in table 1:

	New bone	Fibrous tissue	Marrow tissue
<i>Area fractions zone 1</i>	15%	7%	8%
<i>Area fractions zone 2</i>	16%	16%	8%
<i>Volume fract. zone 2</i>	9%	42%	7%

Table 1. Coefficient of variation (in percent) for double counts of four randomly picked implants from paper IV.

The reproducibility is high and comparable to previous studies using the same model [129]. The coefficient of variance reflects not only the intraobserver reproducibility, but also the sampling intensity – *i.e.* at equal sampling intensity, very low tissue representations are less accurately reproduced in comparison to high tissue representations. This tendency is observed with the relatively high CV for volume estimation of fibrous tissue in zone 2 (42%).

5.4.3.2 Implant coating preparation in thesis

The “cold coating technique” [131] was performed with addition of HA-nanoparticles to the PDLLA-solution with and without OPN preadsorption. Granulate PDLLA was purchased as Resomer203 (Boehringer-Ingelheim GmbH, Ingelheim, Germany). HA particles in the size 20 – 70 nm and an effective area of 110 m²/g were purchased as an ethanol suspension (Berkeley Advanced Biomaterials, Ca, USA). Ethanol was evaporated in an exicator under vacuum conditions and 1g of dried particles were resuspended in 20 ml milliQ water with probe sonication for 1 minute. The pH-value reached 10.5 and was adjusted to 7.4 with 1M phosphoric acid, shortly probe sonicated again and immediately immersed in liquid nitrogen to avoid aggregation. OPN in an amount corresponding to coverage of half the effective area of the particles was added after pH adjustment. The frozen particles with or without OPN were freeze-dried until all water was evaporated and particles ready for mixing with PDLLA. The final dip coating was done in three different solutions to produce three different coatings: i) A pure PDLLA coating – implants were dipped in ethylacetate solution of 100 mg PDLLA in 1.5 ml ethylacetate, ii) A PDLLA/HA composite coating of 50% PDLLA and 50% particles by volume - 50 mg PDLLA and 125 mg HA particles in 1.5 ml ethylacetate; the suspension was probe sonicated before dipping the implants & iii) A PDLLA/HA composite coating with OPN preadsorbed on the particles - 50 mg PDLLA and 125 mg HA particles including OPN in 1.5 ml ethylacetate; the suspension was probe sonicated before dipping the implants.

5.4.3.3 Paper III

The osseointegration of small experimental implants coated with pure PDLLA or PDLLA/HA composite without OPN preadsorption was tested. Porous-coated titanium alloy (Ti-6Al-4V) implants manufactured by Biomet Inc. (Warsaw, IN, USA) were used for the experiment. The implants were cylindrical with a height of 10 mm and 6 mm in diameter. The porous titanium surface was plasma-sprayed, giving a mean pore diameter of 480 μm and a porosity of 44% (as specified by the manufacturer). Endcaps of 10 mm in diameter were used to center the implant and provide a uniform 2 mm gap in a 10 mm drill hole (Fig. 32). Histomorphometry was divided in two zones – zone 1 included the implant surface and inner most 500 μm of periimplant tissue. The inner boundary of the implant surface was selected as the average of highest and lowest levels in the porous structure, but valleys beneath were also included in the histomorphometry. Zone 2 included 1000 μm from the outer boundary of zone 1.

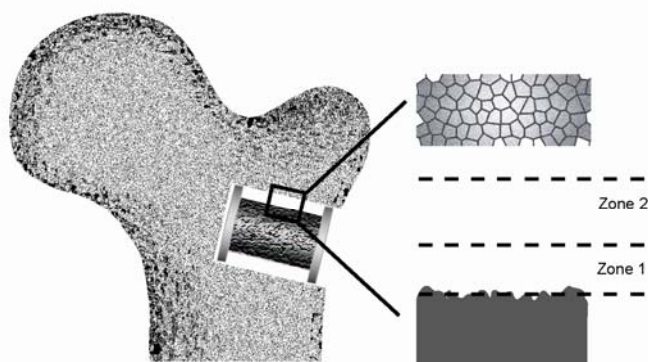


Figure 32. Implantation in humerus and histomorphometric zones used in paper III. The gap was 2 mm, the inner zone was 0.5 mm and zone 2 was 1 mm.

The implants were inserted in the proximal humerii of sheep and the observation time was 12 weeks. The mechanical fixation was improved at least ten-fold in the PDLLA/HA composite group. The histomorphometry revealed that the HA/PDLLA composite coating had conducted formation of new bone on 39.3% of the implant surface and fibrous tissue for the remaining (58.3%), whereas the pure PDLLA coated implants were almost completely encapsulated in fibrous tissue and marrow tissue (96.2% and 3.6% respectively) and almost no newly formed bone was observed. No differences were observed in the gap. As expected from the literature

addition of HA particles to PDLHA improved osteoconductivity. The PDLHA/HA composite appears suitable for guided bone formation.

5.4.3.4 Paper IV

The osseointegration of small experimental implants coated with a PDLHA/HA composite without OPN or PDLHA/HA composite with OPN preadsorption was tested. The implants had a titanium porous coating (Porocoat) manufactured by Depuy Inc. (Warsaw, IN, USA). Dimensions including porous coating are length 10 mm and diameter 6 mm. The porosity is provided by multiple layers of titanium beads sintered on to the core implant giving an average porosity of 40% by volume and average pore size of 250 μm with lowest porosity and pore size (20%, 100 μm) at the core implant and highest at the outer boundary (90%, 500 μm) [132]. Endcaps of 7.5 mm in diameter were attached to implant ends to center the implant and provide a uniform 0.75 mm gap in a 7.5 mm drill hole (Fig. 33). As illustrated the implant surface porosity is very different from that used in paper III (Fig. 32). Zone 1 was defined as the innermost 400 μm starting from the surface of the core implant and zone 2 was defined as starting from the outer boundary of zone 1 and reaching to the outermost 10% of the gap. In zone 1 (Fig. 33) histomorphometry of surface area fractions alone was done as the small spaces between titanium beads was not suitable for estimation of volumetric fractions. In Zone 2 surface area fractions were estimated on the outer rim of the porocoat and volume fractions in the gap.

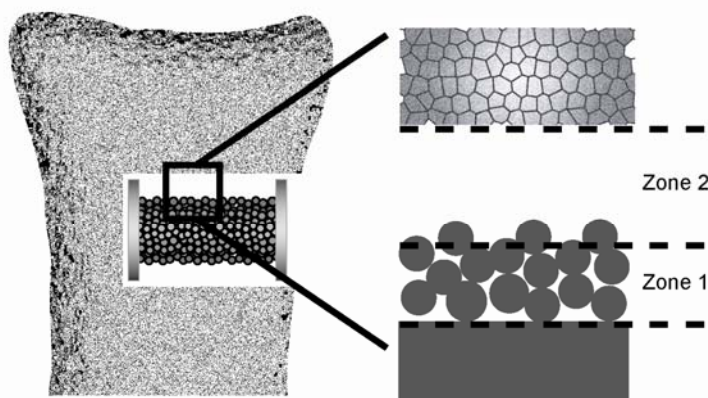


Figure 33. Implantation in tibia and histomorphometric zones used in paper IV. The gap from outer rim of the porocoat was 0.75 mm. The inner zone was 0.4 mm from the inner core implant and zone 2 was from outer boundary of zone 1 to the outer most 10% of the gap.

The implants were inserted in the proximal tibia of canine and the observation time was 4 weeks. The mechanical fixation was slightly improved by OPN preadsorption on the HA particles, but not significantly. In zone 1 OPN addition resulted in significantly more bone formation on the inner surfaces of the porocoat, but no differences were observed in neither area nor volume fractions of zone 2. A non-significant tendency towards more bone formation on the porocoat surface in zone 2 was observed. The study confirms that addition of OPN can improve the osteoconductivity of the PDLLA/HA composite. As the method does not address molecular or cellular effects it can not be concluded how the OPN presence exactly influences the tissue response.

6. Summary of results

This summary contains the most important results of the papers with emphasis on the underlying mechanisms. The most important graphs from studies are copy-pasted from the papers.

6.1 Paper I

Fibronectin adsorption on HA was studied with QCM-D, AFM scratching and ellipsometry. Gold was used as a reference substrate. The adsorption characteristics including foot print area, water content and rigidity of Fn adsorbing from different bulk concentrations was characterized from surface mass densities. In addition cell binding domain availability was estimated with antibody probing on both substrates at different Fn bulk concentrations.

On both surfaces Fn adsorbed in full monolayers from all bulk concentrations without islands or holes in the coverage. The thickness of dried protein layers as measured with AFM scratching was found to vary between approximately 2 nm for the lowest surface mass density obtained with the lowest bulk concentration and 5 nm for the highest surface mass density obtained with the highest bulk concentration. The water content of the protein layers (or more precisely: the contribution of associated water to the QCM-D response) was found to be approximately 75% and unchanged regardless of surface chemistry or surface mass density.

The rigidity of adsorbed proteins was found on both surfaces to correlate negatively with surface mass density, *i.e.* highly spread proteins (low surface mass density) were more rigid than less spread proteins (high surface mass density). It was furthermore found that the Fn concentration in the adsorption media influenced the adsorption characteristics regardless of surface chemistry - high concentration tended towards less spreading of protein (high surface mass density) and low concentration tended towards high spreading (low surface mass density). This tendency is clear from figure 34 wherein the surface mass densities are plotted against the bulk Fn concentrations used.

As for comparing the effect of surface chemistry it was found that Fn adsorption on HA resulted in lower surface mass densities corresponding to single Fn molecules spreading out more and obtaining a larger foot print area as compared to gold. This is seen in figure 33 wherein each bulk concentration resulted in a lower surface mass density on HA. Equal protein spreading, however, could be obtained by using a high bulk concentration on HA and a low bulk concentration on gold – e.g. 20 µg/ml on gold and 100 µg/ml on HA (Fig. 34).

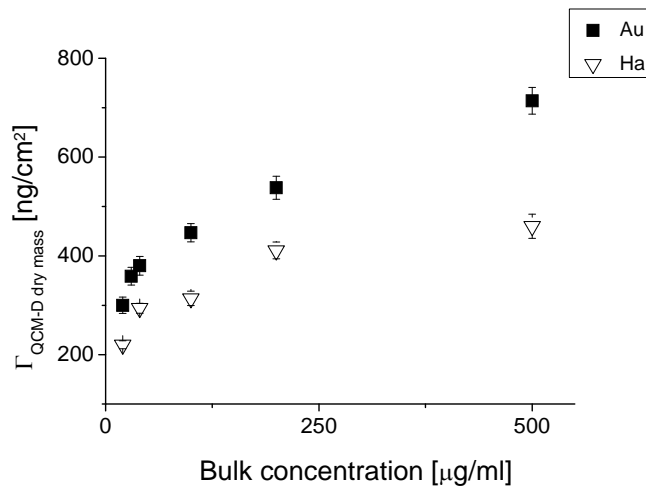


Figure 34. The dry surface mass densities obtained with QCM-D combined with AFM scratching at different bulk concentrations of fibronectin on hydroxyapatite (HA) and gold (Au). It is observed that higher surface mass densities in general were formed gold. Also, a lower bulk concentration results in lower surface mass densities. With the AFM it was confirmed that all bulk concentrations resulted in full surface coverage, which necessarily leads to the conclusion that the single Fn molecules obtain different conformations, in this case observed as different surface spreading areas, depending of surface chemistry and bulk concentration.

In general the amount of antibody binding was found to be higher the more the protein was spread out. As adsorption on HA from a fixed bulk concentration resulted in relatively higher spreading on the surface compared to gold, Fn on HA did bind more antibodies. However, when comparing the antibody binding with respect to the protein spreading areas, there was no difference - *i.e.* similar spreading areas on HA and gold had the same availability of cell binding domains regardless of surface chemistry. This is exemplified in figure 35, where the two QCM-D dry masses at 300 ng/cm² (on gold obtained with bulk Fn concentration 20 μg/ml and on HA with 100 μg/ml) bind almost the same amount (app. 0.75) of monoclonal antibodies.

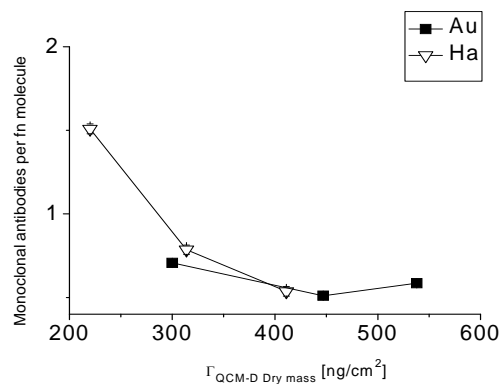


Figure 35. Estimated amount of binding on each fibronectin molecule of monoclonal antibodies directed against the cell binding domain of fibronectin. It is observed that the binding is approximately the same with similar surface mass densities regardless of surface chemistry.

6.2 Paper II

Adsorption of bovine milk osteopontin on HA and gold was observed with QCM-D and ellipsometry. Full protein availability of adsorbed OPN was estimated with probing on both surfaces by polyclonal antibodies directed against the entire protein. A single bulk concentration was used. The cell interaction of the adsorbed proteins was evaluated by observing the initial cell motility, actin cytoskeleton and FAS in bone marrow derived mesenchymal stem cells on the resulting protein layers.

The results from QCM-D and ellipsometry are very similar to that found with Fn. The water content did not change significantly with adsorption substrate and OPN resulted in a larger surface mass density on HA corresponding to a higher spreading as compared to gold (Tbl. 2). This resulted in higher antibody binding indicating an overall higher availability of the protein on HA (Tbl. 2). The rigidity of OPN was also found to be higher in the more spread proteins on HA. This is presented as the average dissipation change (ΔD) per frequency change (Δf) (Tbl. 2). No molecular tests were available to evaluate potential biological effects of the observed adsorption characteristics. Given that the entire protein is observed to be more available to antibodies it is expected that the cell binding domain is also more available.

The two cell studies profoundly reflected the observed differences in protein adsorption. OPN adsorbed on HA was compared to OPN adsorbed on gold and HA/gold preadsorbed with serum as controls. Cell motility was observed with DIC from 1h following incubation and through the following 6h. Observation of actin cytoskeleton and FAS with fluorescence microscopy was done at time points 1h, 3h, 6h and 24h following incubation. It was observed that the cell motility was significantly increased by OPN preadsorbed on HA in comparison to remaining groups (Fig. 36).

Substrate\Protein properties	$\Gamma_{\text{QCM-D}}$ (ng/cm ²)	$\Gamma_{\text{Ellipsometry}}$ (ng/cm ²)	Water factor $\Gamma_{\text{qcm-D}}/\Gamma_{\text{Ellipsometry}}$	Endpoint $\Delta D_7/\Delta f_7$ (10 ⁻⁸ Hz ⁻¹)	Antibody per OPN
Hydroxyapatite	288 +/- 11 (n=7)	95 +/- 17 (n=4)	3.0 +/- 0.5	-0.078 +/- 0.003 (n=7)	0.57 +/- 0.02 (n=3)
Gold	637 +/- 7 (n=9)	240 +/- 9 (n=3)	2.65 +/- 0.10	-0.0975 +/- 0.0010 (n=9)	0.141 +/- 0.004 (n=3)

Table 2. Characteristics of OPN adsorption on hydroxyapatite and gold as observed with QCM-D and ellipsometry using one bulk concentration (100µg/ml). The surface mass density is lower on HA, but the water factors are not significantly different. The average dissipation per OPN mass adsorbed on HA is app. 20% lower compared to gold. The availability of the entire protein is higher as estimated by amount of polyclonal antibodies binding to each OPN molecule.

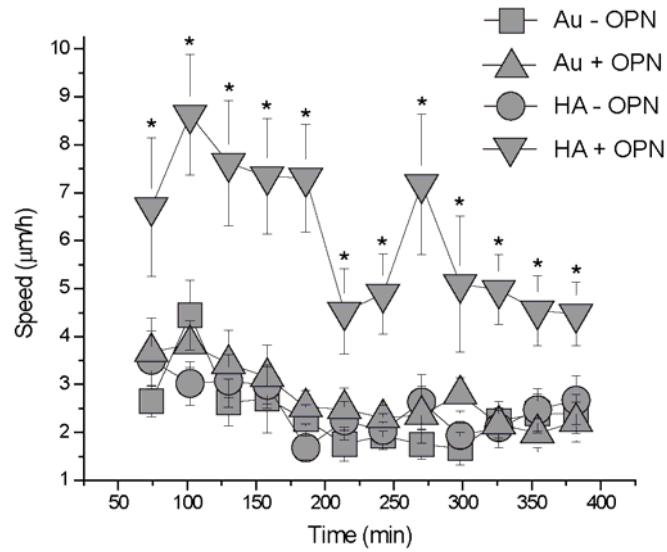


Figure 36. Cell migration velocity in 28 minute intervals, from period 1 – 7h following incubation. (*): p-value less than 0.05 compared to remaining surfaces. It is observed that cell velocity on HA preadsorbed with OPN (HA + OPN) is significantly higher during the entire observation period compared to remaining surfaces (Au with OPN and HA/Au immersed in the serum containing media without preadsorption).

The actin pictures were used to estimate cell area and roundness (cell spreading) and the vinculin pictures to estimate formation and distribution of FAS. It was found that OPN induced the cell spreading significantly at all time points, but exclusively when attached to HA (Fig. 37). OPN adsorbed on HA furthermore, induced formation of FAS with a distribution resembling that expected from cells during active movement.

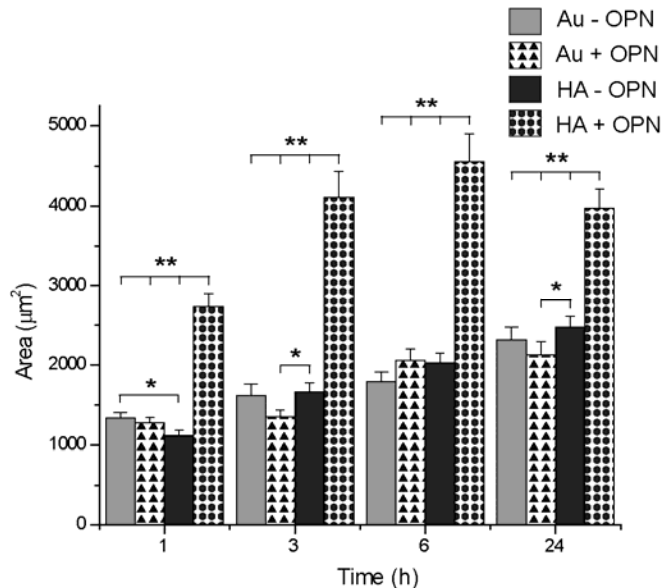


Figure 37. Cell area at 1h, 3h, 6h and 24h. (*): p-value less than 0.05, (**): p-value less than 0.01. It is observed that the area is dramatically larger on HA preadsorbed with OPN in all time-points.

6.3 Paper III

Osseointegration of experimental implants with a PDLLA coating or a PDLLA/HA composite coating was tested in a sheep bone gap implant model. 20 – 70 nm HA nanoparticles were mixed with PDLLA in a 50/50 vol% composition. HA-particles were present in the composite surface but apparently not homogeneously dispersed as observed with AFM.

The *in vivo* results confirmed that HA enhanced the osteoconductive properties of the coating, thereby improving the osseointegration significantly. The mechanical implant fixation was dramatically improved and this corresponded to a significantly higher amount of mineralized bone tissue formed on the composite coated implants (Tbl. 3 & Fig 38).

<i>Implant coating\Parameter</i>	<i>Ultimate shear strength (MPa)</i>	<i>Apparent shear stiffness (MPa/mm)</i>	<i>Total energy absorption (J/m²)</i>
PDLLA	0.06 (0 – 0.10)	0.07 (0 – 0.20)	11 (0 – 20)
PDLLA/HA	1.20 (0.12 – 2.33)*	7.20 (0.40 – 16.20)*	110 (23 – 369)*

(P-value below 0.05 with Wilcoxon signed ranks hypothesis test is denoted with a *)

Table 3. Results from mechanical push-out test - [median (interquartile range)]

(): p-value less than 0.01. The PDLLA/HA composite coating resulted in a significantly improved fixation in all parameters.*

The osteoconductive effect is localized to the surface or the immediate vicinity of the composite (Fig. 31). At several places mineralized bone tissue was seen in direct contact with remaining composite, whereas practically no mineralized bone tissue was observed on PDLLA (Fig. 31). The 2 mm gaps of both implant groups were filled with marrow like tissue dominated by adipocytes and very limited ingrowth of mineralized bone tissue from the drill hole periphery was observed. The method used deals with tissue level responses and no attempt was done at analysing or quantifying cells.

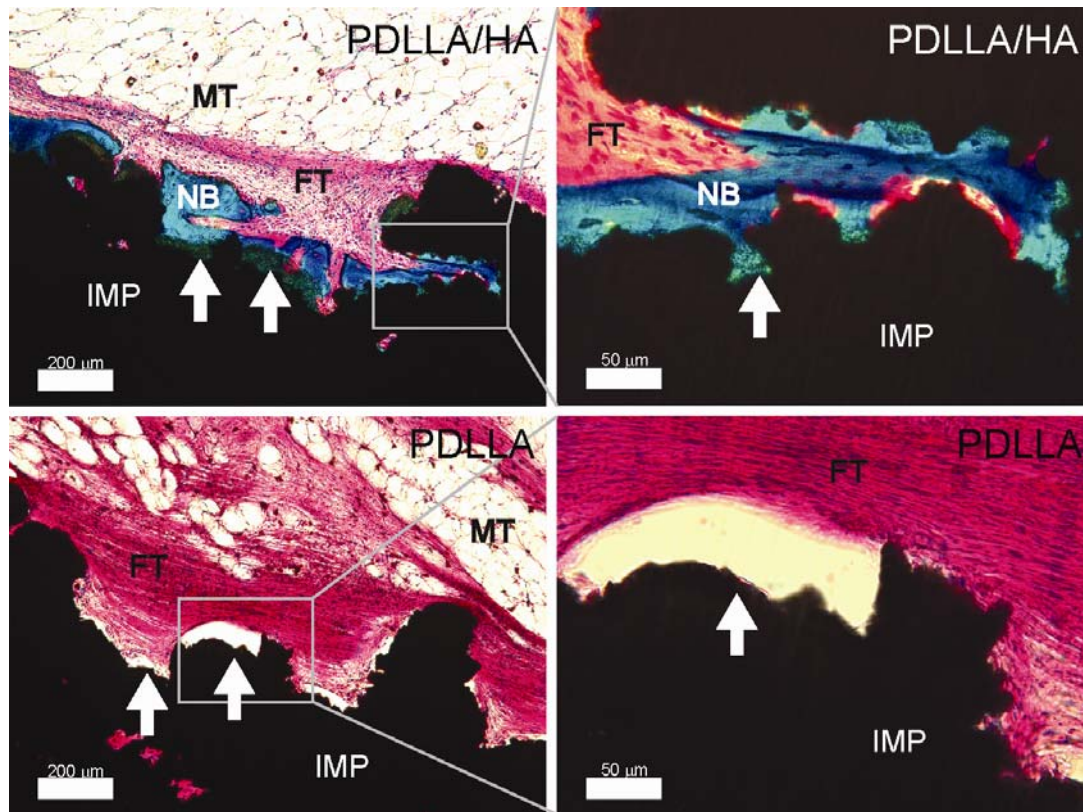


Figure 38. Representative pictures of the implant (IMP) surfaces from paper III. New bone (NB) is observed in direct contact with both remaining composite and bare titanium. The PDLLA coated implant is exclusively covered with fibrous tissue (FT). In the gap marrow-like tissue dominated by adipocytes is observed (MT). White arrows point out coating remains on both coatings. The remaining PDLLA/HA composite absorbs some green dye, but is easily distinguished from the mineralized bone tissue. Remaining PDLLA coating appears as voids with no material as the polymer is solved in acetone during preparation.

6.4 Paper IV

Osseointegration of experimental implants with a PDLLA/HA composite coating or a PDLLA/HA composite coating with OPN preadsorption on the HA particles was tested in a canine 0.75 mm bone gap implant model. 20 – 70 nm HA nanoparticles were mixed with PDLLA in a 50/50 vol% composition and OPN preadsorption was done with a protein amount corresponding to half coverage of the entire effective area of the particles. XPS confirmed proteins on the HA particles prior to mixing with PDLLA (Fig. 19).

The presence of coating remains on the implants after the observation time was too low to estimate. From observation, it is estimated that coating was present on less than 1% of the surfaces. The fixation of implants coated with OPN containing composite as compared to the pure composite was slightly improved but not significantly (Tbl. 4). The composite coating including OPN was furthermore, found to significantly enhance formation of bone on the inner surfaces of the porous coating (zone 1) as compared to the pure composite, whereas no differences were observed

in the tissues formed in the gaps (zone 2). In figure 39 representative sections of the implant surfaces are presented.

Implant coating\Parameter	Total energy absorption (J/m ²)	Ultimate shear strength (MPa)	Apparent shear stiffness (MPa/mm)
PDLLA/HA - OPN	462 ± 306	2.5 ± 1.5	16.1 ± 8.7
PDLLA/HA + OPN	635 ± 450	2.8 ± 2.4	16.5 ± 13.5

Table 4. Results from mechanical push-out test [mean ± sd] The OPN functionalized PDLLA/HA composite coating performs better in all parameters, the total energy absorption in particular, but no significant differences are observed.

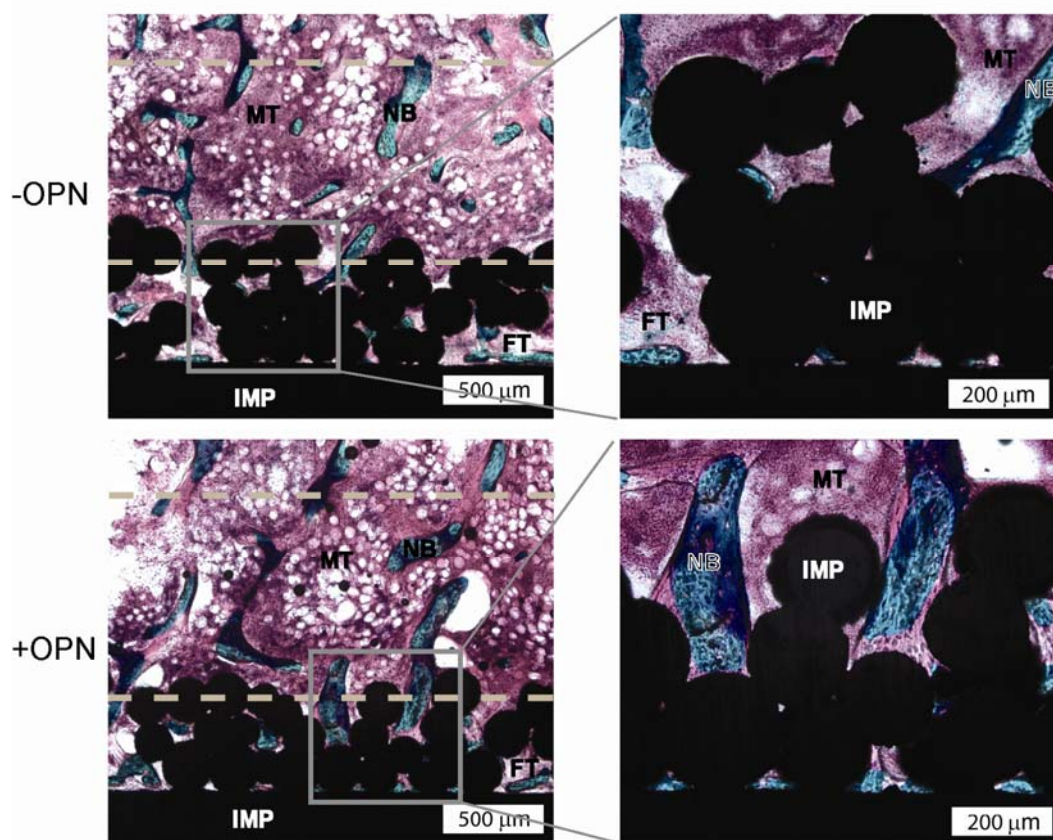


Figure 39. Representative pictures of the implant (IMP) surfaces. The dotted grey lines on the left hand images mark the zone boundaries. New bone (NB) is observed in the gap and in direct contact with the implant. In the gap marrow-like tissue with adipocytes and hematopoietic cells is observed (MT). Fibrous tissue (FT) is sparse in this particular animal, but small amounts are seen in the inner porosities where it was usually found. As suggested by the images it was found with histomorphometry that significantly more bone was in contact with the implant surface in the inner zone 1.

The osteoconductive effect of OPN addition is localized to the surface or the immediate vicinity of the composite. The gaps were primarily filled with hematopoietic marrow tissue with interspersed lipocytes (Fig. 39). Mineralized bone tissue in trabecular presentations were

seen throughout the gap, and they appeared to be in contact both with the bone in the drill hole periphery and the bone on the implant surface (Fig. 39).

7. Discussion

The discussion is divided in two subdivisions each aimed at discussing two central mechanism dealt with in this thesis: i) Protein adsorption and ii) osteoconductivity.

7.1 Protein adsorption

7.1.1 Single protein characteristics?

It has been mentioned several times that the methods can be used to estimate single protein characteristics. The output data from QCM-D, AFM scratching and ellipsometry, however, are from detection of protein layers and the question arises: Is it feasible to estimate single protein characteristics from the detected protein layers? Some of the assumptions relating to this problem will be discussed in the following two paragraphs.

A protein layer described by its surface mass density (SMD – (weight/area)) can be used to calculate directly the area of single proteins with Avogadro's number and the molecular weight (MW) of the protein. This, however, assumes that the surface is completely covered with protein, which is very unlikely given that adsorbed proteins do not have a geometry allowing for complete packing (Fig 40a). It is more likely that proteins are rounded, which unavoidably leads to voids between proteins, even at closest packing (Fig. 40b). Optimal packing is also a rather unlikely situation as it would require site specific adsorption or postadsorptive protein-protein mediated organisation. Thus random adsorption at available sites is a more realistic scenario (Fig. 40c). Figure 40c realistically depicts the projected surface area by spheres adsorbing randomly on a surface. In case of fibronectin and osteopontin a circular projection area cannot be expected as the proteins are anisotropic in solution [16,34] and not likely to adsorb with uniform circular projections. The proteins can adsorb in different orientations, which, depending on protein shape, will lead to varying initial projection areas. Following initial adsorption structural rearrangements of the protein - depending on the surface/protein and internal forces as described in section 3.3.1 - tend to spread it on the surface. This phenomena is also known as relaxation.

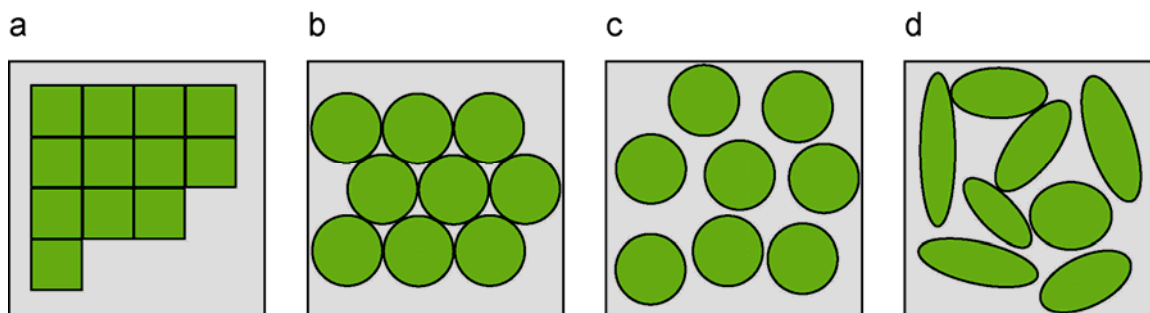


Figure 40. Theoretical modes of protein adsorption. (a) illustrates an example of complete protein packing which requires unrealistic protein foot prints. (b) illustrates a more likely scenario with circular projection areas which doesn't allow for complete coverage despite of optimal packing. (c) illustrates random adsorption of single proteins with a uniform circular foot print area (d) illustrates random adsorption followed by relaxation to individual foot print areas depending on the available surface space.

If proteins initially lie close as a result of high adsorption rate on the surface the spreading may be inhibited by adjacently located proteins. Thus the spreading of the proteins on a surface is a combined effect between spreading speed and adsorption rate [133]. Spreading speed is an effect of the specific surface/protein interaction and the adsorption rate is predominantly influenced by the flux of proteins to the surface, which is proportional to the concentration of proteins in the adsorption media. In effect, the projection areas of proteins at finalized adsorption should be considered a spectrum arising from an ensemble of different protein orientations and levels of spreading (Fig. 33d). As the surface mass density of proteins excluding the associated water can be estimated rather precisely, it can be calculated with high certainty how many proteins adsorb on the surface. Single proteins, however, display different foot print areas, viscoelastic properties, water factors and exposure to the liquid phase. Consequently, any statement on single protein characteristics are averages describing general tendencies of proteins in the adsorbed protein layers.

7.1.2 Surface roughness and topography also influence protein adsorption.

In paper I & II, the adsorption of Fn and OPN on gold and HA is studied. Two potential confounders to the obtained results should be mentioned – surface roughness and topography.

As measured by AFM the roughness of HA (RMS roughness = 2.2 ± 0.2 nm) was slightly larger than that of gold (RMS roughness = 0.9 ± 0.2 nm). Increased roughness brought about by surface structures larger than the adsorbing proteins will logically lead to a higher amount of adsorption as more adsorption sites are available. With very small roughness in range or smaller than the size of the adsorbing proteins this logical reasoning is no longer viable. There is, however,

some evidence that increase of surface roughness, even in ranges much smaller than the adsorbing protein, leads to a higher amount of protein adsorption [8,134-136]. The mechanism involved in this higher adsorption is not clear as it doesn't follow the increase in surface area. From the observed roughnesses of the HA and gold surfaces used in paper I and II, it can be expected that the adsorption on the HA surfaces should be modestly higher.

The RMS roughness used in this thesis is a parameterization of the general valley-to-top distance on a surface. In this presentation of surfaces, topographical characteristics of importance may be neglected. In case of the HA and gold surfaces used in paper I and II, there is evidently from figure 14 a difference in the grain size, with the HA grains (App. 15 - 20 nm in diameter) being smaller than the gold grains (App. 30 - 40 nm in diameter). On HA compared to gold this corresponds to a higher surface curvature (smaller diameter) of the topographical features on the surface. This may influence the characteristics of adsorbing proteins. In a recent study, it was shown that protein spreading on nanospheres of radii ranging from 7.5 – 82.5 nm was highly influenced by the curvature [137]. The effect was speculated to depend on the shape of adsorbing proteins in that albumin, which is a globular structure, only spread out on the large spheres with low curvature, whereas fibrinogen, which is a rod-like structure, only spread out on the small spheres with high curvature [137]. Based on these results it must be concluded that an unaccountable bias from the different topographies used in this thesis is present. It should, however, be emphasized that a study on protein adsorption on spheres does not accurately reflect the situation of curvatures on a surface. In a study of fibronectin, albumin and fibrinogen adsorption on flat silica and surface immobilized silica spheres of 7, 14 and 21 nm it was found that the amount of adsorbed Fn and albumin was the same regardless of substrate [138]. Furthermore, the adsorption of fibrinogen was found to be slightly lower on the large immobilized particles with low curvature as compared to the small particles, which is contradictory to the results from reference [137]. The effect of surface curvatures on protein adsorption is not completely enlightened and the direction of the alleged bias can hardly be reasonably distinguished.

In conclusion, the observations on protein adsorption performed on HA and gold are not alone influenced by the surface chemistry. Nonetheless, considering the small differences in substrate roughness and topography these parameters are not considered large enough to alter or omit conclusions on the influence of HA and gold on Fn and OPN adsorption.

7.1.3 Fibronectin adsorption on HA and gold

In paper I, a simple explanation to the observations on Fn adsorption is suggested: On both substrates the adsorption of Fn is followed by spreading on the surface; this spreading is more pronounced on HA. If, however, the adsorption rate is high the spreading is limited by protein-protein contact, *i.e.* the surface is too crowded with proteins to allow for full spreading. This limiting effect of high bulk concentration on protein surface spreading has been reported previously for Fn adsorption on a variety of substrates [8,139,140].

Besides observation of this well known phenomenon it is also observed that on HA as compared to gold, there is a tendency towards higher availability of the cell binding domain. This is probably a result of the relatively higher protein spreading. Several studies have shown that antibodies can be applied in combination with QCM-D studies as a binding probe to estimate epitope availability [6,8,134]. In particular the availability of Fn cell binding domains has been reported to be reduced by the protein crowding effect that limits spreading [8]. The overlap in CBD availability as seen in figure 28 argues that there are no orientational effects in the adsorption that otherwise would have resulted in different CBD availabilities at equal Fn surface mass densities. The overall interpretation of Fn adsorption on HA and gold is summed up in figure 27:

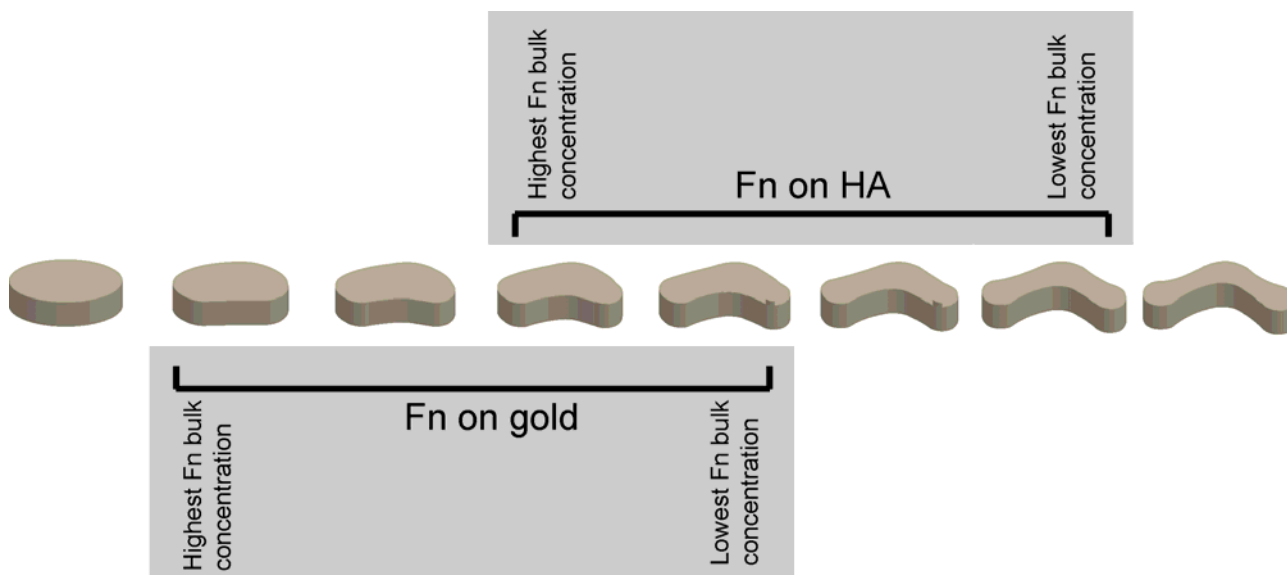


Figure 41. Suggested characteristics of Fn adsorbed on HA and gold. Adsorbed proteins are not drawn to scale. The combined effect of Fn concentration in adsorption media and surface spreading lead to different suggestible conformations of adsorbed Fn. The data suggest that the surface spreading event is more pronounced on HA resulting in the spectrum of HA-adsorbed Fn to be more to the right in the figure. The cell binding domain is not included in the protein illustration, but the data suggest that they are more available on the proteins to the right side.

Paper I thus argues that Fn characteristics on HA and gold is to be understood as two segments of the same continuous spectrum of protein spreading and cell binding domain availability. In each resulting protein layer, there are likely all degrees of protein spreading present, but low bulk concentration adsorbing on HA is the optimal condition for forming a protein layer that favours large protein spreading and high cell binding domain availability.

The study provides evidence that the cell interaction of surface adsorbed Fn can be controlled with substrate and adsorption media concentration. The study, however, does not include an actual cell interaction experiment and the relevance of the observed effect remains unclear.

It is furthermore, debatable how suitable an unspecific antibody works as control for the antibody binding experiment aimed at evaluating the CBD availability (or full protein availability as done in paper II). The ideal control would be antibodies which, apart from the antigen binding site, are identical to the antibodies binding to the CBD. And even better if the antigen binding domain of the control antibody specifically targeted other parts of the fibronectin molecule. Evidently, the control antibodies (polyclonal rabbit bovine serum albumin antibodies) resemble the CBD binding antibodies in terms of geometry, but differ in other aspects (e.g. peptide sequence and posttranslational modifications) besides the antigen binding site. These differences provide an alternative explanation for the observed differences in antibody binding – it may be that fibronectin attracts many proteins more avidly when attached to HA, and the difference between CBD binding antibody and the control antibodies arises from other differences than the antigen binding domains. This potential bias to the conclusions could have been further analyzed by testing the adsorption of “irrelevant” proteins such as albumin or bovine milk osteopontin on fibronectin in the alleged different surface adsorption conformations.

7.1.4 Osteopontin adsorption on HA and gold

The results from OPN adsorption are comparable to those obtained with Fn adsorption. OPN spread out more with higher exposure and formed a more rigid protein layer on HA. The water response of the QCM-D results amounted to approximately 75% on both HA and gold and thus found to be in range with what was observed for Fn in paper I. The thickness of dried OPN layers was not measured with the AFM scratching technique. From comparison with paper I it is expected that the thickness would be in range with the lowest thicknesses obtained with Fn (1 – 2 nm).

The full protein availability of the adsorbed protein was tested with polyclonal antibodies against full length OPN from bovine milk. As unspecific controls we used polyclonal rabbit bovine serum albumin antibodies. It should, however, be noted that the unspecific control antibodies cannot be considered perfect controls as they might differ from the OPN antibodies in other aspects than the antigen binding domain, which may also affect the binding to the OPN protein layers. Previous discussion on antibody controls found in the final paragraph of section 7.1.3 (Fibronectin adsorption on HA and gold) is also valid for the probing of full length OPN.

In contrast to paper I, wherein the CBD availability of Fn was estimated with monoclonal antibodies, the CBD activity was tested with cells. Cell motility, cell spreading and FAS are extremely sensitive parameters for the presentation of RGD-sequences [44-48], why they were feasible for evaluating the cell interaction with adsorbed OPN. From cell biological studies it is furthermore, evident that cell motility is a basic mode of OPN action [29,30,49,50], why this should be regarded as a basic biomaterial effect of OPN functionalization.

It is recognized that gold is generally not considered a favourable material in the context of biomaterials. Using titanium instead of gold as a reference material might have added more clinical relevance to the cell studies. It is also recognized that cell studies evaluating osteogenic differentiation and proliferation may be more relevant in the context of osteoconductive biomaterials. Such parameters may to a higher degree reflect a potential clinical application of OPN. The initial cell interactions as analyzed in this study are, nonetheless, considered more directly sensitive to an effect of surface adsorbed protein orientation/conformation. Time-lapsed differentiation/proliferation studies over weeks may be influenced by cell mediated and spontaneous exchanging of proteins in the protein layers as well as cell-cell interactions. As will be discussed in the following, the direct imaging analyses chosen in this study are focused on cell effects, which less ambiguously can be related to the presentation of the RGD-sequence of OPN. Cell motility, in addition, is particularly relevant in functionalization of biomaterials as it may provide a chemotactic signal in porous structures, e.g. tissue engineering scaffolds, to improve invasion with relevant cells.

All results obtained from the cell studies indicate a higher presentation of RGD-sequences of OPN adsorbed on HA. The interpretation of results is summed up in figure 42, wherein suggested characteristics of OPN adsorbed on HA and gold are illustrated.

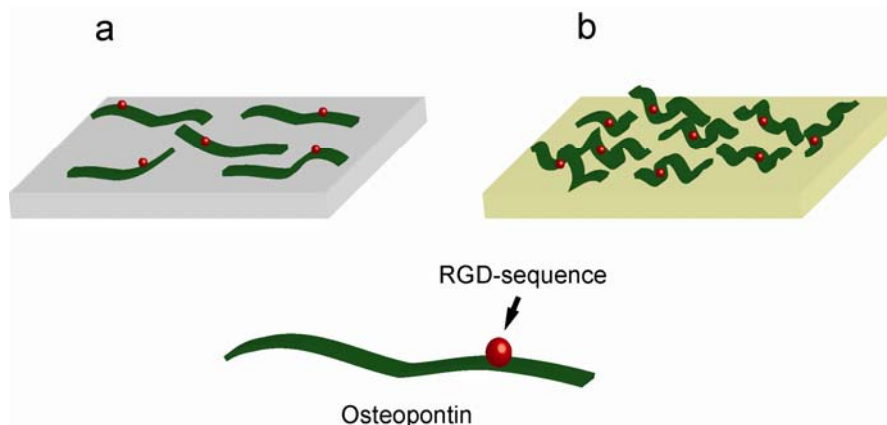


Figure 42. Suggestive illustrations of OPN adsorbed on HA (a) and OPN adsorbed on gold (b). The spacing between proteins is exaggerated. On HA the molecules are more spread with more surface contact. All RGD-sequences are available. On gold the molecules are more folded and spreading is lower. The RGD-sequences are less available due to embedding within the folded structure. In the figure the proteins on HA are furthermore drawn as being oriented with the cell binding domain away from the HA surface, whereas on gold the orientation is random.

Paper II thus argues that HA compared to gold provides a surface chemistry on which OPN from bovine milk adsorbs in a conformation/orientation that favours interaction with cells to induce cell motility and spreading. There is, however, a lag of evidence that the observed effect of OPN on cells is, in fact, the result of the CBD interacting with the integrins of the cells. This could have been done with control studies including antibodies directed against the integrins or soluble RGD-sequences to omit integrin activity [51]. A similar approach with monoclonal antibodies directed against specific peptide sequences on OPN might also have been useful in distinguishing the effect of the three sequences, RGD, SVVYGL and CD44-ligand, in the cell interaction. A similar cell study with osteoclasts could also have added to the feasibility of using OPN in an orthopaedic biomaterial.

7.2 Osteoconductivity

As stated earlier the osteoconductivity is defined as the ability of a material to support growth of bone tissue. A few synthetic materials display osteoconductive properties that have shown clinically significant usage in orthopaedic surgery. These include HA, calcium phosphate and silica containing bioactive glass [42,55,62]. The mechanism of the osteoconductive properties is not completely understood. It is considered a combination of dissolution/precipitation on the material surface combined with protein/surface interactions. In this thesis, the protein/surface interactions of HA is directly addressed. As stated in the introduction the scientific approach used could provide insight into the functions at molecular scale of biomaterials - in this case shedding

light upon the question: How does protein adsorption affect HA osteoconductivity? The data obtained in paper I & II, suggest that relevant proteins adsorb in a conformation/orientation that favours presentation of peptide sequences that interact with bone cells. The *in vivo* studies presented as paper III & IV are extensions of these *in vitro* studies.

The osteoconductivity evaluated *in vivo* is that of a biodegradable material for guided bone formation. The motivation for mixing PDLA with HA was to develop a material that both holds the osteoconductivity of HA and the versatility in shaping and mechanical properties of polymers. As will be discussed in the following sections the data obtained in *the in vivo* studies on PDLA/HA composites (paper III & IV) add further consistency to the notion that protein adsorption plays a role in the osteoconductivity of HA. Following section (7.2.1) provides a discussion of the coating procedure to clarify exactly what the tissue meets in the conducted animal studies. This is followed up by a short section (7.2.2) on the animal study designs and finally two sections (7.2.3 & 7.2.4) discussing the osteoconductivity of the composites used in paper III & IV.

7.2.1 What exactly is in the coatings used in the animal studies?

The as-received HA particles (Berkeley Advanced Biomaterials, Ca, USA) are evidently composed of HA as confirmed by the TEM analysis (presented in paper III) and the XPS analysis (Fig. 17). During the first step in the preparation, the particles are vacuum dried to omit the ethanol carrier and resuspended in milliQ water. In this step, some particles are solved in the water phase, but how many? HA is usually considered very stable in water - physiological concentrations of calcium and phosphate (~1 mM) are sufficient to prevent HA dissolution. To reassure that this is also evident with the HA nanoparticles used in this thesis, an estimate based on observation of pH-value is presented in the following: If the hydroxyl groups released from the HA particle solvation is regarded as the only contribution to the increase in pH-value, the pH-value can be used to estimate the amount of HA solved. If an entire gram of pure HA (2 OH- groups per molecule and molecular weight is 1000 g/mol) is solved in 20 ml milliQ the released hydroxyl-ions would result in a pH-value of 13 corresponding to 0.002 mol OH- in 20 ml or 10^{-1} mol/l OH-. The observed pH-value of 10.5 corresponds to an increase in OH- from 10^{-7} mol/l to $10^{-3.5}$ mol/l. Based on these assumptions it can be estimated that less than 1 percent ($10^{-3.5}/10^{-1} = 0.0032$) of the added HA nanoparticles are solved in the milliQ phase. Considering that phosphate also increase the pH-value, it can be safely reassured that by far most of the HA particles are preserved.

Addition of OPN to the HA particles presumably results in the protein adsorbing on the particles. From the dry surface mass density found in paper II it can be estimated that each OPN molecule corresponds to a surface area of 49 nm². As discussed in section 7.1.1 this is not the true area of the protein, but nonetheless, the average area occupied by each protein including the average surrounding non-occupied area. Assuming that OPN adsorbs with the same average area on the HA particles and that each particle is assumed rod-shaped with a diameter of 20 nm and a length of 70 nm the theoretical maximum amount of OPN adsorbing on each HA particle can be estimated to be 89 OPN/particle. Although OPN is a flexible protein which, like fibrinogen, can be expected to “curl” around high surface curvatures [137] it is probably an exaggeration to include the entire area of a particle to be available for adsorption. From paper I, it is noticed that concentration in adsorption media must also be considered, as this can alter the protein area. This effect, however, was found in a later study to be very limited in case of OPN adsorption on HA (Not appended article nr. 2). It is furthermore, undesired with free non-adsorbed OPN when the entire mixture was frozen in liquid nitrogen. In the coating preparation for paper IV the amount of OPN added was therefore, selected to cover half of the effective area of the HA particles corresponding to 45 OPN/particle on average. The lowest Fn film thickness measured in paper I with AFM scratching was app. 2 nm which was obtained QCM-D measured surface mass density half that obtained with OPN. In this context, the thickness of an OPN layer on HA can be expected to be in the range of 1 nm.

The composition of the HA particles alone and the HA particle/OPN mixture after freeze-drying was confirmed with XPS (Fig. 16). Although the results resemble that obtained in a similar study of protein adsorption on HA particles [141] it is not certain that the OPN molecules are actually adsorbed on the particles. AFM was also done on the freeze-dried OPN preadsorbed HA particles (Fig. 43). Particles with expected sizes were recaptured, but compared to AFM images of pure HA-particles presented in paper III, they appear somewhat more “fuzzy”, which can probably be ascribed to adsorbed proteins. As evident from Paper III, Fig. 4 the image scanning was very irregular, which is likely caused by tip pollution from debris picked up from the sample. All in all, there is considerable evidence that OPN is actually adsorbed onto the HA-particles.

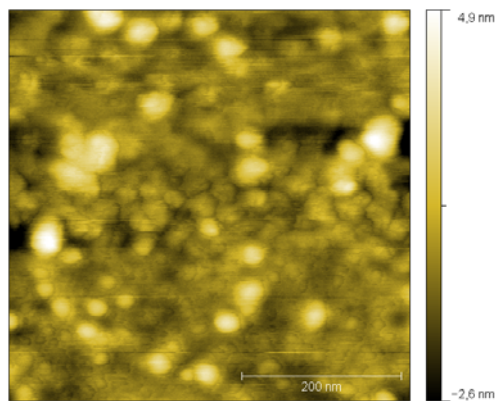


Figure 43. AFM scanning of HA-particles preadsorbed with OPN. The image was not included in paper IV due to low quality. The HA-particles are seen with a “fuzzy” appearance which is likely a result of OPN adsorption.

The last step of the coating procedure was the actual mixing of particles with PDLLA in ethylacetate. The first issue of this procedure concerns the homogeneity of the resulting material and the second issue concerns the extremely harsh treatment of the included surface adsorbed proteins. The approach regarding optimization of homogeneity was to keep the particle/polymer dispersion as dispersed as possible with probe sonication during dip-coating. This was done to ensure that 50% PDLLA and 50% HA by volume in the ethylacetate stays on the implant surface. In this approach, the resulting composite homogeneity relies on coincidental aggregation of the particles during evaporation of the ethylacetate: If the particles by coincidence pack completely (Fig. 44a) the resulting composite will be inhomogeneous because the particles will form a small volume aggregate as compared to the polymer. Realistically the particles will form a random aggregate which heightens the tendency towards formation of a homogeneous composite (Fig. 44b). In theory a perfect composite could be made if the volume ratio of polymer to particles is chosen so the polymer exactly fills the void between randomly aggregated particles.

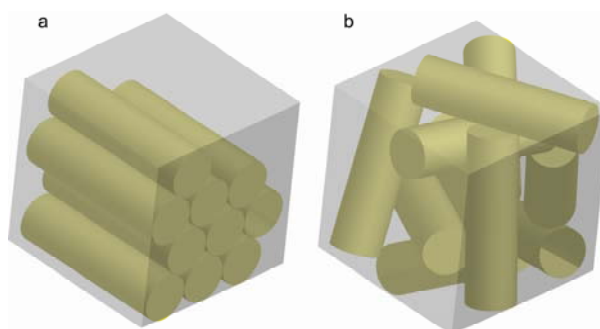


Figure 44. Polymer and particles in a PDLLA/HA composite drawn to scale: Ten HA particles (20 nm width and 70 nm length) and an equal volume of polymer. Optimal packing of HA particles (a) leads to an inhomogeneous composite, whereas random aggregation leads to higher homogeneity due to larger volume between particles (b).

A perfect composite without voids can be obtained only if the HA particles aggregate into one large aggregate from single freely flowing particles or very small aggregates (Fig. 31a). It is, however, more likely, that during the aggregation, intermediary sized aggregates form, and aggregation of these leads to voids filled alone with polymer (Fig. 31b). This explains the inhomogeneous presentation of PDLLA and HA particles observed with AFM as presented in paper III.

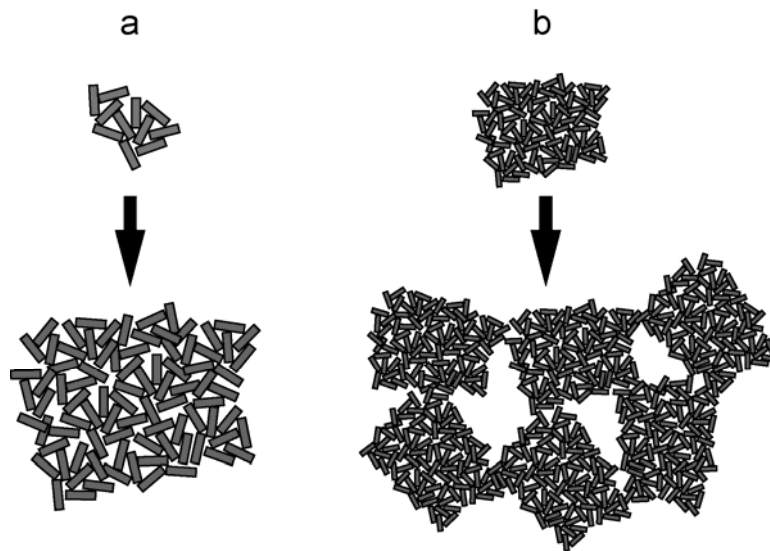


Figure 45. HA particle aggregation during evaporation of ethylacetate affects the homogeneity of the resulting coating. If HA particles aggregate into a total aggregate from single free particles or very small aggregates (a) a perfect composite can be expected. If, however, larger aggregates form and aggregate with similar large aggregates voids (of pure polymer) are formed in the composite.

With all considerations and analysis taken together a final illustration of the composite drawn to scale can be presented (Fig. 46)

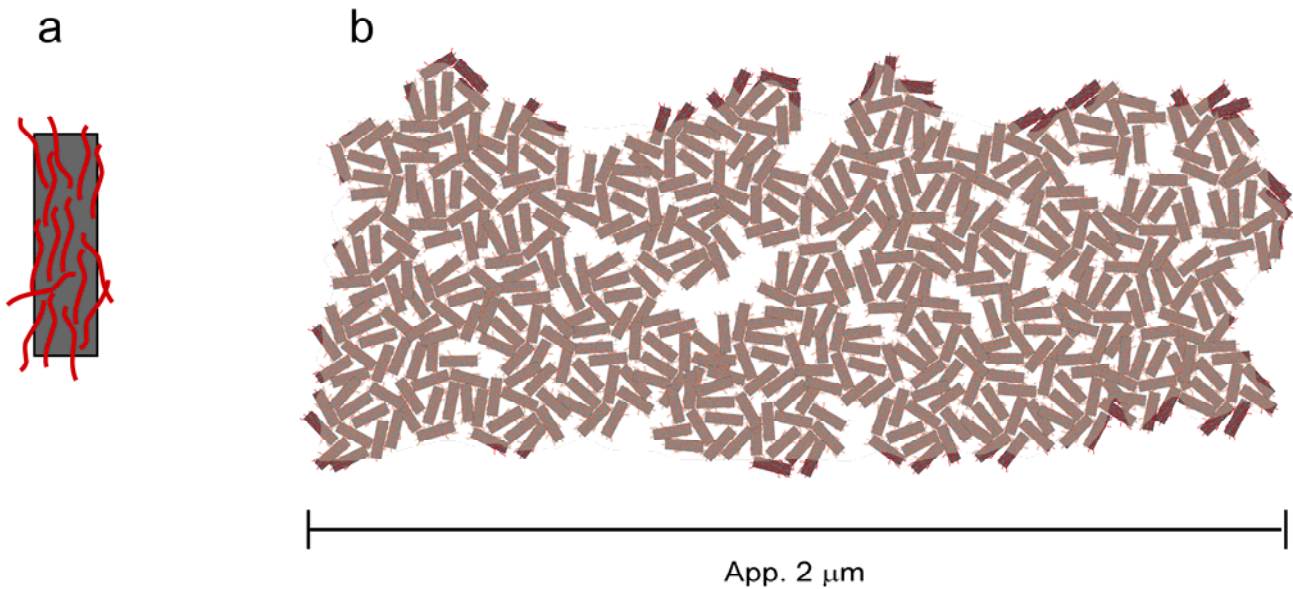


Figure 46. (a) suggested drawn-to-scale illustration of a single HA-particle with OPN adsorbed. (b) suggested drawn-to-scale illustration of the composite in $2 \times 1 \mu\text{m}$ cross section.

The status of the particle adsorbed OPN after mixing with PDLLA in ethylacetate is not known and was not tested. It is well known that solvent properties are important for protein integrity [12]. There is, nevertheless, some comfort in the fact that OPN has no secondary or tertiary structure that could be rearranged by exertion to an organic solvent [34]. sorption on a particle surface can furthermore, be speculated to provide protection against the organic solvent phase. With these speculations and the large amount of OPN used it can be reasonably expected that the activity of OPN is at least partially maintained. Further comfort is found in the literature reporting that proteinaceous growth factors added directly to a PDLLA/ethylacetate solution and applied with dip-coating to an experimental titanium implant maintain activity after release *in vivo* [87]. This is also reported from a similar coating technique using chloroform as solvent instead of ethylacetate [142] and this particular coating has also been shown to maintain protein activity during 14 months of storage [143].

7.2.2 Animals and study design

The choice of different animals for study III and IV is obviously disputable. The setup for doing large animal studies is very demanding and time consuming. Such issues as availability of animals, surgical expertise and surgical equipment admittedly outweighed the respect for scientific correctness. The problem is that the osteoconductive effect of HA addition to PDLLA as observed in paper III with sheep, cannot be directly extrapolated to paper IV using canine as animal. It might

be that the effect of adding HA to PDLLA would have no effect in canine. It is, nonetheless, evident that pure HA as a coating displays osteoconductive properties in both sheep [144-146] and canine [59,147,148]. It is also recognized that both sheep and canine are widely used animals for orthopaedic research [126]. All in all, it is considered feasible to consider study III and IV qualitatively comparable.

Two other striking differences between paper III and IV are the observation times (paper III: 12 weeks, paper IV: 4 weeks) and the implants (paper III: Plasma sprayed porous coating from Biomet in 2 mm gap, paper IV: Porocoat from Depuy in 0.75 mm gap). The study in paper III is considered preliminary to study IV, and the differences were introduced as improvements to study IV based on the preliminary results from study III. 12 weeks observation was chosen for study III. This should allow estimation of the full tissue response as influenced by the temporarily present coating. A large gap (2 mm) was chosen to heighten sensitivity towards the coating osteoconductivity in isolation from the bone regenerative activity in drill hole periphery and also to allow for, as expected before the study, a distant osteoconductive effect of HA particles released from the coating. The PDLLA/HA composite without OPN turned out to be highly osteoconductive, but only on the surface. This combined with the large (2 mm) gap resulted in the observed lag of bony bridging between drill hole periphery and bone formed on the implant surface – even at the relatively long (12 weeks) observation period. As a consequence it was decided in paper IV to use a porous coating with a higher surface area (i.e. Depuy Porocoat) with a smaller (0.75 mm) gap. The larger implant surface area coated was expected to overall heighten the impact of the local osteoconductive effect and the smaller gap should heighten the chance of bony bridging between implant and drill hole periphery. Although bony bridging is desired as it generates a firm osseointegration it can also blur modest effects of surface modifications as high ingrowth from the bone periphery might cancel out small differences originating from the implant/issue interface. For this reason, the observation time was set to four weeks.

7.2.3 Osteoconductivity of a PDLLA/HA composite

As expected addition of HA nanoparticles had a positive impact on the osteoconductive response of the host. The observed improvement of osteoconductivity is in agreement with previous *in vivo* studies on HA particle addition to PDLLA [81,82,84]. Evidently from the results the coatings were partly resorbed during the 12 weeks observation time. It is, however, a big draw-back to the study that the coating amount prior to implantation was not

estimated by weight or image analysis of the implants with coating. Without this information, the relative degradation rates of the coatings cannot be estimated. It is, however, a reasonable statement that both coatings went through some resorption and the composite was partly replaced by new bone and fibrous tissue, whereas the polymer was replaced alone by fibrous tissue.

The mechanism underlying the improved osteoconductivity is and was not expected to be clear from the results. The animal study design only addresses tissue level response and molecular mechanisms cannot be indulged from the results. In extension of the results from paper I and II it is, nonetheless, considered a feasible theory that selective conformation and perhaps orientation of proteins adsorbing from serum on the surface presented HA particles may play an important part. In a recent *in vitro* study it was shown that cell adhesion and survival on PDLA/HA composite scaffolds was significantly improved by preadsorption with serum proteins and this effect was not seen in pure PDLA scaffolds [21]. This, at least, confirms that protein adsorption on HA as compared to adsorption on pure PDLA leads to an improved cell activity.

In paper III the discussion is limited to an argumentation that the osteoconductive properties known to be an inherent ability of HA can be applied to PDLA by mixing 20 – 70 nm HA particles and PDLA in a 50/50 vol% composite. No speculations on the effect of protein adsorption are included.

7.2.4 Osteoconductivity of an OPN bulk functionalized PDLA/HA composite.

The PDLA/HA composite was slightly improved by OPN preadsorption on the particles in that significantly more bone formation was observed on implants coated with the OPN containing composite. Very small amounts of coating remains were present on the implants and these were not quantified. Similarly to paper III, the osteoconductivity was limited to the surface or vicinity of the composite, but bony bridging was observed in the gap which accounts for the generally higher fixation observed in paper IV as compared to paper III. The significantly higher amount of formed bone on implants coated with OPN containing composite was in the inner porosities of the porocoat and to a lesser extent on the outermost lining of the porocoat. This explains how the improved osteoconductivity by OPN addition had only a small impact on the fixation.

The animal study addresses only tissue level response and the mechanisms involved in the improved osteoconductivity can only be speculated. In the hypothesis (OPN addition can improve the composite osteoconductivity) it was implied that this should be an effect of surface

adsorbed OPN interacting with cells. Indeed it was furthermore, implied that both osteoclasts and osteoblasts should be attracted and activated resulting in guided remodelling of the synthetic material into new bone (Fig. 47).

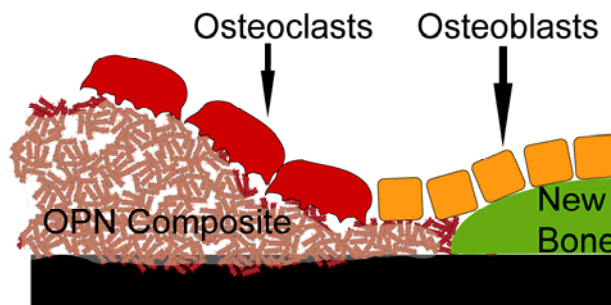


Figure 47. Guided remodelling of the OPN containing composite, c.f. Fig. 6. The illustration depicts the most optimistic interaction scenario between cells and material. Osteoclasts resorb the composite and osteoblasts rebuild it in new bone. Other scenarios are also possible – see text.

There are, however, other scenarios, which might lead to the observed improvement of osteoconductivity. The OPN presence in the coating may alter the spontaneous resorption of the coating, thereby making more HA available for cell interaction and/or dissolution. It may also be that OPN adsorbed on the particles has a positive effect on cells, but from an unknown mechanism. The bottom-line is: An effect was observed, but there is a giant leap from protein and cell studies to animal studies. The mechanism is suggested to be that of particle adsorbed OPN interacting with bone active cells during degradation of the material (Fig. 47). To bridge the theoretical gap between *in vitro* and *in vivo* studies further studies should be included. *In vitro* cell studies similar to those presented in paper II on the composites used *in vivo* could probably strengthen the suggested mechanism. In addition a study on osteoclast resorption activity *in vitro* seems purposeful. *In vivo* studies where osteoblasts and osteoclasts on the composites are identified and quantified could also enlighten the involved mechanisms. Overall the results are encouraging in that it was proven that OPN from bovine milk might serve as an additive in biodegradable osteoconductive materials.

8. Outlook

In the research field of “smart” materials that are capable of degrading while guiding formation of new tissue, there are yet several scientific problems to solve. It is an issue to evoke a response that results in new tissue formation while simultaneously ensuring a suitable degradation. In theory osteopontin might serve as a solution. It may provide a controlled degradation through the action of osteoclasts and in turn through direct/indirect interaction with osteoblasts promote deposition of new bone. The intended formulation of the OPN containing composite was in the shape of a scaffold that could template bone formation into a 3D structure instead of on the surface of an implant. All though attempts were done at preparing an OPN containing PDLA/HA composite scaffold it never came to a usable formulation. A scaffold is, nonetheless, still considered the preferred application and suggestion for further research. And also a necessity in the future generations of implants that are completely remodelled into new bone.

As for the theorized optimal implant, which is totally resorbed and replaced with new bone tissue, it is recognized that this thesis provides a protein functionality approach and the results are of modest significance – if any at all? There is no certainty that a bulk presentation of the material as a scaffold or a solid is useful. And indeed it is recognized that in the future of biomaterials there is probably no use for full length proteins. Active peptide sequences covalently linked to polymeric molecules is an emerging and very promising strategy for applying specific protein properties to biomaterials [149]. An important aspect of this research is strategically related to the work in this thesis: The approach has proven particularly useful in obtaining cell controlled polymer degradation - for instance, by inserting peptide sequences in the polymer that are sensitive to cleavage by tissue degrading enzymes [150,151]. Perhaps the combination of a polymer that is sensitive to tissue degrading enzymes combined with protein sequences that attract and activate macrophages, e.g. osteoclasts, could be a useful way of controlling biomaterial degradation. It is the hope of the author that the work presented in this thesis will inspire further research in making biomaterials susceptible to remodelling.

9. References

1. Ratner B. Biomaterials Science, An introduction to Materials in Medicine. Elsevier Academic Press 2004.
2. Whitesides GM. Nanoscience, nanotechnology, and chemistry. *Small* 2005;1(2):172-9.
3. Williams DF. Definitions in biomaterials. Proceedings of a consensus conference of the european society for biomaterials, Vol. 4. Chester, England, March 3-5 1986. Elsevier 1987.
4. Oberpenning F, Meng J, Yoo JJ, Atala A. De novo reconstitution of a functional mammalian urinary bladder by tissue engineering. *Nat Biotechnol* 1999;17(2):149-55.
5. Kasemo B. Biological surface science. *Surface Science* 2002;500(656-677):656.
6. Hemmersam AG, Foss M, Chevallier J, Besenbacher F. Adsorption of fibrinogen on tantalum oxide, titanium oxide and gold studied by the QCM-D technique. *Colloids Surf B Biointerfaces* 2005;43(3-4):208-15.
7. Liu L, Chen S, Giachelli CM, Ratner BD, Jiang S. Controlling osteopontin orientation on surfaces to modulate endothelial cell adhesion. *J Biomed Mater Res A* 2005;74(1):23-31.
8. Hovgaard MB, Rechendorff K, Chevallier J, Foss M, Besenbacher F. Fibronectin adsorption on tantalum: the influence of nanoroughness. *J Phys Chem B* 2008;112(28):8241-9.
9. Höök F, Kasemo B, Nylander T, Fant C, Sott K, Elwing H. Variations in coupled water, viscoelastic properties, and film thickness of a Mefp-1 protein film during adsorption and cross-linking: a quartz crystal microbalance with dissipation monitoring, ellipsometry, and surface plasmon resonance study. *Anal Chem* 2001;73(24):5796-804.
10. Höök F, Vörös J, Rodahl M, Kurrat R, Böni P, Ramsden J, Textor M, Spencer N, Tengvall P, Gold J and others. A comparative study of protein adsorption on titanium oxide surfaces using in situ ellipsometry, optical waveguide lightmode spectroscopy and quartz crystal microbalance/dissipation. *Colloids and surfaces B: Biointerfaces* 2002;24(2):155 - 170.
11. Arai T, Norde W. The behavior of some model proteins at solid-liquid interfaces 1. Adsorption from single protein solutions. *Colloids and surfaces* 1990;51:1 - 15.
12. Malmsten M. *Biopolymers at Interfaces*, 2nd edition. Marcel Dekker, New York 2003.
13. Johansson S, Svineng G, Wennerberg K, Armulik A, Lohikangas L. Fibronectin-integrin interactions. *Front Biosci* 1997;2:d126-46.
14. Watt FM, Hodivala KJ. Cell adhesion. Fibronectin and integrin knockouts come unstuck. *Curr Biol* 1994;4(3):270-2.
15. Sjöberg B, Eriksson M, Österlund E, Pap S, Österlund K. Solution structure of human plasma fibronectin as a function of NaCl concentration determined by small-angle X-ray scattering. *Eur Biophys J* 1989;17(1):5-11.
16. Sjöberg B, Pap S, Österlund E, Österlund K, Vuento M, Kjems J. Solution structure of human plasma fibronectin using small-angle X-ray and neutron scattering at physiological pH and ionic strength. *Arch Biochem Biophys* 1987;255(2):347-53.
17. Bergkvist M, Carlsson J, Oscarsson S. Surface-dependent conformations of human plasma fibronectin adsorbed to silica, mica, and hydrophobic surfaces, studied with use of Atomic Force Microscopy. *J Biomed Mater Res A* 2003;64(2):349-56.
18. Ugarova TP, Zamarron C, Veklich Y, Bowditch RD, Ginsberg MH, Weisel JW, Plow EF. Conformational transitions in the cell binding domain of fibronectin. *Biochemistry* 1995;34(13):4457-66.
19. Wolff C, Lai CS. Fluorescence energy transfer detects changes in fibronectin structure upon surface binding. *Arch Biochem Biophys* 1989;268(2):536-45.

20. Shen JW, Wu T, Wang Q, Pan HH. Molecular simulation of protein adsorption and desorption on hydroxyapatite surfaces. *Biomaterials* 2008;29(5):513-32.
21. Woo KM, Seo J, Zhang R, Ma PX. Suppression of apoptosis by enhanced protein adsorption on polymer/hydroxyapatite composite scaffolds. *Biomaterials* 2007;28(16):2622-30.
22. Fisher LW, Hawkins GR, Tuross N, Termine JD. Purification and partial characterization of small proteoglycans I and II, bone sialoproteins I and II, and osteonectin from the mineral compartment of developing human bone. *J Biol Chem* 1987;262(20):9702-8.
23. Franzén A, Heinegård D. Isolation and characterization of two sialoproteins present only in bone calcified matrix. *Biochem J* 1985;232(3):715-24.
24. Qin C, Baba O, Butler WT. Post-translational modifications of sibling proteins and their roles in osteogenesis and dentinogenesis. *Crit Rev Oral Biol Med* 2004;15(3):126-36.
25. McKee MD, Nanci A. Osteopontin at mineralized tissue interfaces in bone, teeth, and osseointegrated implants: ultrastructural distribution and implications for mineralized tissue formation, turnover, and repair. *Microsc Res Tech* 1996;33(2):141-64.
26. Denhardt DT, Noda M. Osteopontin expression and function: role in bone remodeling. *J Cell Biochem Suppl* 1998;30-31:92-102.
27. Giachelli GM, Schwartz SM, Liaw L. Molecular and cellular biology of osteopontin : Potential role in cardiovascular disease. *Trends Cardiovasc Med* 1995;5(3):88-95.
28. Malaval L, Modrowski D, Gupta AK, Aubin JE. Cellular expression of bone-related proteins during in vitro osteogenesis in rat bone marrow stromal cell cultures. *J Cell Physiol* 1994;158(3):555-72.
29. Raheja LF, Genetos DC, Yellowley CE. Hypoxic osteocytes recruit human MSCs through an OPN/CD44-mediated pathway. *Biochem Biophys Res Commun* 2008;366(4):1061-6.
30. Chellaiah MA, Hruska KA. The integrin alpha(v)beta(3) and CD44 regulate the actions of osteopontin on osteoclast motility. *Calcif Tissue Int* 2003;72(3):197-205.
31. Duvall CL, Taylor WR, Weiss D, Wojtowicz AM, Guldborg RE. Impaired angiogenesis, early callus formation, and late stage remodeling in fracture healing of osteopontin-deficient mice. *J Bone Miner Res* 2007;22(2):286-97.
32. Ishijima M, Rittling SR, Yamashita T, Tsuji K, Kurosawa H, Nifuji A, Denhardt DT, Noda M. Enhancement of osteoclastic bone resorption and suppression of osteoblastic bone formation in response to reduced mechanical stress do not occur in the absence of osteopontin. *J Exp Med* 2001;193(3):399-404.
33. Yoshitake H, Rittling SR, Denhardt DT, Noda M. Osteopontin-deficient mice are resistant to ovariectomy-induced bone resorption. *Proc Natl Acad Sci U S A* 1999;96(14):8156-60.
34. Fisher LW, Torchia DA, Fohr B, Young MF, Fedarko NS. Flexible structures of SIBLING proteins, bone sialoprotein, and osteopontin. *Biochem Biophys Res Commun* 2001;280(2):460-5.
35. Gericke A, Qin C, Spevak L, Fujimoto Y, Butler WT, Sorensen ES, Boskey AL. Importance of phosphorylation for osteopontin regulation of biomineralization. *Calcif Tissue Int* 2005;77(1):45-54.
36. Wang KX, Denhardt DT. Osteopontin: role in immune regulation and stress responses. *Cytokine Growth Factor Rev* 2008;19(5-6):333-45.
37. Giachelli CM, Steitz S. Osteopontin: a versatile regulator of inflammation and biomineralization. *Matrix Biol* 2000;19(7):615-22.
38. Sørensen ES, Højrup P, Petersen TE. Posttranslational modifications of bovine osteopontin: identification of twenty-eight phosphorylation and three O-glycosylation sites. *Protein Sci* 1995;4(10):2040-9.

39. Smith LL, Cheung HK, Ling LE, Chen J, Sheppard D, Pytela R, Giachelli CM. Osteopontin N-terminal domain contains a cryptic adhesive sequence recognized by alpha9beta1 integrin. *J Biol Chem* 1996;271(45):28485-91.
40. Senger DR, Perruzzi CA, Papadopoulos-Sergiou A, Van de Water L. Adhesive properties of osteopontin: regulation by a naturally occurring thrombin-cleavage in close proximity to the GRGDS cell-binding domain. *Mol Biol Cell* 1994;5(5):565-74.
41. Geneser F. *Histologi - på molekylærbiologisk grundlag*. Munksgård 1999.
42. Marquis ME, Lord E, Bergeron E, Drevelle O, Park H, Cabana F, Senta H, Faucheux N. Bone cells-biomaterials interactions. *Front Biosci* 2009;14:1023-67.
43. Schaffner P, Dard MM. Structure and function of RGD peptides involved in bone biology. *Cell Mol Life Sci* 2003;60(1):119-32.
44. Cavalcanti-Adam EA, Volberg T, Micoulet A, Kessler H, Geiger B, Spatz JP. Cell spreading and focal adhesion dynamics are regulated by spacing of integrin ligands. *Biophys J* 2007;92(8):2964-74.
45. Arnold M, Cavalcanti-Adam EA, Glass R, Blummel J, Eck W, Kantlehner M, Kessler H, Spatz JP. Activation of integrin function by nanopatterned adhesive interfaces. *Chemphyschem* 2004;5(3):383-8.
46. Houseman BT, Mrksich M. The microenvironment of immobilized Arg-Gly-Asp peptides is an important determinant of cell adhesion. *Biomaterials* 2001;22(9):943-55.
47. Maheshwari G, Brown G, Lauffenburger DA, Wells A, Griffith LG. Cell adhesion and motility depend on nanoscale RGD clustering. *J Cell Sci* 2000;113 (Pt 10):1677-86.
48. Schuler M, Owen GR, Hamilton DW, de Wild M, Textor M, Brunette DM, Tosatti SG. Biomimetic modification of titanium dental implant model surfaces using the RGDSP-peptide sequence: a cell morphology study. *Biomaterials* 2006;27(21):4003-15.
49. Shin H, Zygourakis K, Farach-Carson MC, Yaszemski MJ, Mikos AG. Attachment, proliferation, and migration of marrow stromal osteoblasts cultured on biomimetic hydrogels modified with an osteopontin-derived peptide. *Biomaterials* 2004;25(5):895-906.
50. Weber GF, Ashkar S, Glimcher MJ, Cantor H. Receptor-ligand interaction between CD44 and osteopontin (Eta-1). *Science* 1996;271(5248):509-12.
51. Liu L, Qin C, Butler WT, Ratner BD, Jiang S. Controlling the orientation of bone osteopontin via its specific binding with collagen I to modulate osteoblast adhesion. *J Biomed Mater Res A* 2007;80(1):102-10.
52. Bernardis MT, Qin C, Jiang S. MC3T3-E1 cell adhesion to hydroxyapatite with adsorbed bone sialoprotein, bone osteopontin, and bovine serum albumin. *Colloids Surf B Biointerfaces* 2008;64(2):236-247.
53. Einhorn TA. The cell and molecular biology of fracture healing. *Clin Orthop Relat Res* 1998(355 Suppl):S7-21.
54. Frost HM. The biology of fracture healing. An overview for clinicians. Part I. *Clin Orthop Relat Res* 1989(248):283-93.
55. Ducheyne P, Qiu Q. Bioactive ceramics: the effect of surface reactivity on bone formation and bone cell function. *Biomaterials* 1999;20(23-24):2287-303.
56. Puleo DA, Nanci A. Understanding and controlling the bone-implant interface. *Biomaterials* 1999;20(23-24):2311-21.
57. Brånemark PI. Osseointegration and its experimental background. *J Prosthet Dent* 1983;50(3):399-410.
58. Geesink RG, de Groot K, Klein CP. Chemical implant fixation using hydroxyl-apatite coatings. The development of a human total hip prosthesis for chemical fixation to bone

- using hydroxyl-apatite coatings on titanium substrates. *Clin Orthop Relat Res* 1987(225):147-70.
59. Søballe K. Hydroxyapatite ceramic coating for bone implant fixation. Mechanical and histological studies in dogs. *Acta Orthop Scand Suppl* 1993;255:1-58.
 60. Gandhi R, Davey JR, Mahomed NN. Hydroxyapatite coated femoral stems in primary total hip arthroplasty: a meta-analysis. *J Arthroplasty* 2009;24(1):38-42.
 61. Goosen JH, Kums AJ, Kollen BJ, Verheyen CC. Porous-coated femoral components with or without hydroxyapatite in primary uncemented total hip arthroplasty: a systematic review of randomized controlled trials. *Arch Orthop Trauma Surg* 2008.
 62. Lind MC, Jensen TB, Laursen M, Overgaard S, Søballe K, Bünger CE. [Clinical use of bone graft substitutes in orthopedic surgery. Status and future possibilities]. *Ugeskr Laeger* 2003;165(39):3712-7.
 63. Annual report 2007. Danish Hip Arthroplasty Registry. 2007.
 64. Hauge Bünger M, Foss M, Erlacher K, Bruun Hovgaard M, Chevallier J, Langdahl B, Bünger C, Birkedal H, Besenbacher F, Skov Pedersen J. Nanostructure of the neurocentral growth plate: Insight from scanning small angle X-ray scattering, atomic force microscopy and scanning electron microscopy. *Bone* 2006;39(3):530-41.
 65. Matsuo K, Irie N. Osteoclast-osteoblast communication. *Arch Biochem Biophys* 2008;473(2):201-9.
 66. Hollinger J. *Bone Regeneration and Repair, Biology and Clinical Applications*. Humana Press 2005.
 67. Terai K, Takano-Yamamoto T, Ohba Y, Hiura K, Sugimoto M, Sato M, Kawahata H, Inaguma N, Kitamura Y, Nomura S. Role of osteopontin in bone remodeling caused by mechanical stress. *J Bone Miner Res* 1999;14(6):839-49.
 68. Chellaiah M, Hruska K. Osteopontin stimulates gelsolin-associated phosphoinositide levels and phosphatidylinositol triphosphate-hydroxyl kinase. *Mol Biol Cell* 1996;7(5):743-53.
 69. Chellaiah M, Kizer N, Silva M, Alvarez U, Kwiatkowski D, Hruska KA. Gelsolin deficiency blocks podosome assembly and produces increased bone mass and strength. *J Cell Biol* 2000;148(4):665-78.
 70. Ross FP, Chappel J, Alvarez JI, Sander D, Butler WT, Farach-Carson MC, Mintz KA, Robey PG, Teitelbaum SL, Cheresch DA. Interactions between the bone matrix proteins osteopontin and bone sialoprotein and the osteoclast integrin alpha v beta 3 potentiate bone resorption. *J Biol Chem* 1993;268(13):9901-7.
 71. Suzuki K, Zhu B, Rittling SR, Denhardt DT, Goldberg HA, McCulloch CA, Sodek J. Colocalization of intracellular osteopontin with CD44 is associated with migration, cell fusion, and resorption in osteoclasts. *J Bone Miner Res* 2002;17(8):1486-97.
 72. Yabe T, Nemoto A, Uemura T. Recognition of osteopontin by rat bone marrow derived osteoblastic primary cells. *Biosci Biotechnol Biochem* 1997;61(4):754-6.
 73. Liu YK, Uemura T, Nemoto A, Yabe T, Fujii N, Ushida T, Tateishi T. Osteopontin involvement in integrin-mediated cell signaling and regulation of expression of alkaline phosphatase during early differentiation of UMR cells. *FEBS Lett* 1997;420(1):112-6.
 74. Kojima H, Uede T, Uemura T. In vitro and in vivo effects of the overexpression of osteopontin on osteoblast differentiation using a recombinant adenoviral vector. *J Biochem* 2004;136(3):377-86.
 75. Boskey AL, Maresca M, Ullrich W, Doty SB, Butler WT, Prince CW. Osteopontin-hydroxyapatite interactions in vitro: inhibition of hydroxyapatite formation and growth in a gelatin-gel. *Bone Miner* 1993;22(2):147-59.

76. Hunter GK, Kyle CL, Goldberg HA. Modulation of crystal formation by bone phosphoproteins: structural specificity of the osteopontin-mediated inhibition of hydroxyapatite formation. *Biochem J* 1994;300 (Pt 3):723-8.
77. Gordjestani M, Dermaut L, De Ridder L, De Waele P, De Leersnijder W, Bosman F. Osteopontin and bone metabolism in healing cranial defects in rabbits. *Int J Oral Maxillofac Surg* 2006;35(12):1127-32.
78. Liu L, Chen G, Chao T, Ratner BD, Sage EH, Jiang S. Reduced foreign body reaction to implanted biomaterials by surface treatment with oriented osteopontin. *J Biomater Sci Polym Ed* 2008;19(6):821-35.
79. Tsai AT, Rice J, Scatena M, Liaw L, Ratner BD, Giachelli CM. The role of osteopontin in foreign body giant cell formation. *Biomaterials* 2005;26(29):5835-43.
80. Hasegawa S, Ishii S, Tamura J, Furukawa T, Neo M, Matsusue Y, Shikinami Y, Okuno M, Nakamura T. A 5-7 year in vivo study of high-strength hydroxyapatite/poly(L-lactide) composite rods for the internal fixation of bone fractures. *Biomaterials* 2006;27(8):1327-32.
81. Hasegawa S, Neo M, Tamura J, Fujibayashi S, Takemoto M, Shikinami Y, Okazaki K, Nakamura T. In vivo evaluation of a porous hydroxyapatite/poly-DL-lactide composite for bone tissue engineering. *J Biomed Mater Res A* 2007;81(4):930-8.
82. Hasegawa S, Tamura J, Neo M, Goto K, Shikinami Y, Saito M, Kita M, Nakamura T. In vivo evaluation of a porous hydroxyapatite/poly-DL-lactide composite for use as a bone substitute. *J Biomed Mater Res A* 2005;75(3):567-79.
83. Kim SS, Ahn KM, Park MS, Lee JH, Choi CY, Kim BS. A poly(lactide-co-glycolide)/hydroxyapatite composite scaffold with enhanced osteoconductivity. *J Biomed Mater Res A* 2007;80(1):206-15.
84. Kim SS, Sun Park M, Jeon O, Yong Choi C, Kim BS. Poly(lactide-co-glycolide)/hydroxyapatite composite scaffolds for bone tissue engineering. *Biomaterials* 2006;27(8):1399-409.
85. Greiner S, Kadow-Romacker A, Lubberstedt M, Schmidmaier G, Wildemann B. The effect of zoledronic acid incorporated in a poly(D,L-lactide) implant coating on osteoblasts in vitro. *J Biomed Mater Res A* 2007;80(4):769-75.
86. Greiner S, Kadow-Romacker A, Wildemann B, Schwabe P, Schmidmaier G. Bisphosphonates incorporated in a poly(D,L-lactide) implant coating inhibit osteoclast like cells in vitro. *J Biomed Mater Res A* 2007;83(4):1184-91.
87. Lamberg A, Schmidmaier G, Søballe K, Elmengaard B. Locally delivered TGF-beta1 and IGF-1 enhance the fixation of titanium implants: a study in dogs. *Acta Orthop* 2006;77(5):799-805.
88. Lucke M, Schmidmaier G, Sadoni S, Wildemann B, Schiller R, Haas NP, Raschke M. Gentamicin coating of metallic implants reduces implant-related osteomyelitis in rats. *Bone* 2003;32(5):521-31.
89. Price JS, Tencer AF, Arm DM, Bohach GA. Controlled release of antibiotics from coated orthopedic implants. *J Biomed Mater Res* 1996;30(3):281-6.
90. Schmidmaier G, Wildemann B, Ostapowicz D, Kandziora F, Stange R, Haas NP, Raschke M. Long-term effects of local growth factor (IGF-I and TGF-beta 1) treatment on fracture healing. A safety study for using growth factors. *J Orthop Res* 2004;22(3):514-9.
91. Wildemann B, Sander A, Schwabe P, Lucke M, Stockle U, Raschke M, Haas NP, Schmidmaier G. Short term in vivo biocompatibility testing of biodegradable poly(D,L-lactide)--growth factor coating for orthopaedic implants. *Biomaterials* 2005;26(18):4035-40.
92. Perego G, Domenico C, Bastioli C. Effect of Molecular Weight and Crystallinity on Poly(lactic acid) Mechanical Properties. *Journal of Applied Polymer Science* 1996;59:37 - 43.

93. Belbella A, Vauthier C, Fessi H, Devissaguet J, Puisieux F. In vitro degradation of nanospheres from poly(D,L-lactides) of different molecular weights and polydispersities. *International Journal of Pharmaceutics* 1996;129:95 - 102.
94. Kim HW, Kim HE, Salih V. Stimulation of osteoblast responses to biomimetic nanocomposites of gelatin-hydroxyapatite for tissue engineering scaffolds. *Biomaterials* 2005;26(25):5221-30.
95. Teng SH, Lee EJ, Yoon BH, Shin DS, Kim HE, Oh JS. Chitosan/nanohydroxyapatite composite membranes via dynamic filtration for guided bone regeneration. *J Biomed Mater Res A* 2008.
96. Venugopal J, Low S, Choon AT, Kumar AB, Ramakrishna S. Electrospun-modified nanofibrous scaffolds for the mineralization of osteoblast cells. *J Biomed Mater Res A* 2008;85(2):408-17.
97. Heo SJ, Kim SE, Wei J, Hyun YT, Yun HS, Kim DH, Shin JW. Fabrication and characterization of novel nano- and micro-HA/PCL composite scaffolds using a modified rapid prototyping process. *J Biomed Mater Res A* 2008.
98. Binnig G, Quate CF, Gerber C. Atomic force microscope. *Phys Rev Lett* 1986;56(9):930-933.
99. Giessibl F. Advances in atomic force microscopy. *Reviews of modern physics* 2003;75:949-983.
100. Kumar C. *Nanosystem Characterization Tools in the Life Sciences*. Wiley-VCH 2006.
101. Constant A, J. Putman KOVdW, Bart G, De Grooth, Niek F, Van Hulst, and Jan Greve. Tapping mode atomic force microscopy in liquid. *Appl Phys Lett* 1994;64(18):2454-6.
102. Briggs D, Grant JT. *Surface Analysis by Auger and X-Ray Photoelectron Spectroscopy*. IM Publications 2003.
103. Barnes GT, Genth IR. *Interfacial science, An Introduction*. Oxford University Press 2005.
104. Sun T, Feng L, Gao X, Jiang L. Bioinspired surfaces with special wettability. *Acc Chem Res* 2005;38(8):644-52.
105. Cullity BD, Stock SR. *Elements of X-ray Diffraction*, 3rd edition. Prentice Hall 2001.
106. Als-Nielsen J, McMorrow D. *Elements of Modern X-Ray Physics*. New York : John Wiley, 2000.
107. Posner A, Perloff A, Diori A. Refinement of the hydroxyapatite structure. *Acta Crystallographica* 1958;11:308-309.
108. Kjellin P. Patent: "Production of nanosized calcium phosphate particles as powder or coating via bifunctional precursors". Pub. No.: WO/2009/070106 04/06/2009.
109. Rodahl M, Höök F, Krozer A, Brzezinski P, Kasemo B. Quartz crystal microbalance setup for frequency and q-factor measurements in gaseous and liquid environments. *Review of Scientific Instruments* 1995;66(7):3924-3930.
110. Voinova MV, Rodahl M, Jonson M, Kasemo B. Viscoelastic Acoustic Response of Layered Polymer Films at Fluid-Solid Interfaces: Continuum Mechanics Approach. *Physica Scripta* 1999;59(5):391 - 396.
111. Vörös J. The density and refractive index of adsorbing protein layers. *Biophys J* 2004;87(1):553-61.
112. Lubarsky GV, Browne MM, Mitchell SA, Davidson MR, Bradley RH. The influence of electrostatic forces on protein adsorption. *Colloids Surf B Biointerfaces* 2005;44(1):56-63.
113. Lubarsky GV, Davidson MR, Bradley RH. Hydration-dehydration of adsorbed protein films studied by AFM and QCM-D. *Biosens Bioelectron* 2007;22(7):1275-81.
114. Arwin H. Ellipsometry on thin organic layers of biological interest: characterization and applications. *Thin Solid Films* 2000;377-378(377):48-56.

115. Arwin H. Ellipsometry, *Physical Chemistry of Biological Interfaces*. CRC press 2000:577-607.
116. De Feijter JA, Benjamins J, Veer FA. Ellipsometry as a tool to study the adsorption behavior of synthetic and biopolymers at the air-water interface. *Biopolymers* 1978;17(7):1759 - 1772.
117. Hill DB, Macosko JC, Holzwarth GM. Motion-enhanced, differential interference contrast (MEDIC) microscopy of moving vesicles in live cells: VE-DIC updated. *J Microsc* 2008;231(3):433-9.
118. Goldberg DJ, Burmeister DW. Stages in axon formation: observations of growth of *Aplysia* axons in culture using video-enhanced contrast-differential interference contrast microscopy. *J Cell Biol* 1986;103(5):1921-31.
119. Beningo KA, Dembo M, Kaverina I, Small JV, Wang YL. Nascent focal adhesions are responsible for the generation of strong propulsive forces in migrating fibroblasts. *J Cell Biol* 2001;153(4):881-8.
120. Zaidel-Bar R, Ballestrem C, Kam Z, Geiger B. Early molecular events in the assembly of matrix adhesions at the leading edge of migrating cells. *J Cell Sci* 2003;116(Pt 22):4605-13.
121. Lippincott-Schwartz J, Patterson GH. Development and use of fluorescent protein markers in living cells. *Science* 2003;300(5616):87-91.
122. Simonsen JL, Rosada C, Serakinci N, Justesen J, Stenderup K, Rattan SI, Jensen TG, Kassem M. Telomerase expression extends the proliferative life-span and maintains the osteogenic potential of human bone marrow stromal cells. *Nat Biotechnol* 2002;20(6):592-6.
123. Bjerre L, Bünger CE, Kassem M, Mygind T. Flow perfusion culture of human mesenchymal stem cells on silicate-substituted tricalcium phosphate scaffolds. *Biomaterials* 2008;29(17):2616-27.
124. Mygind T, Stiehler M, Baatrup A, Li H, Zou X, Flyvbjerg A, Kassem M, Bünger C. Mesenchymal stem cell ingrowth and differentiation on coralline hydroxyapatite scaffolds. *Biomaterials* 2007;28(6):1036-47.
125. Abramoff MD, Maengelhaes PJ, Ram SJ. Image Processing with ImageJ. *Biophotonics International* 2004;11(7):36-42.
126. Aerssens J, Boonen S, Lowet G, Dequeker J. Interspecies differences in bone composition, density, and quality: potential implications for in vivo bone research. *Endocrinology* 1998;139(2):663-70.
127. Baddeley AJ, Gundersen HJ, Cruz-Orive LM. Estimation of surface area from vertical sections. *J Microsc* 1986;142(Pt 3):259-76.
128. Sumner DR, Bryan JM, Urban RM, Kuszak JR. Measuring the volume fraction of bone ingrowth: a comparison of three techniques. *J Orthop Res* 1990;8(3):448-52.
129. Baas J. Adjuvant therapies of bone graft around non-cemented experimental orthopedic implants stereological methods and experiments in dogs. *Acta Orthop Suppl* 2008;79(330):1-43.
130. Dhert WJ, Verheyen CC, Braak LH, de Wijn JR, Klein CP, de Groot K, Rozing PM. A finite element analysis of the push-out test: influence of test conditions. *J Biomed Mater Res* 1992;26(1):119-30.
131. Schmidmaier G, Wildemann B, Stemberger A, Haas NP, Raschke M. Biodegradable poly(D,L-lactide) coating of implants for continuous release of growth factors. *J Biomed Mater Res* 2001;58(4):449-55.
132. Smith TS. Characterization of Porous Coatings. In: *Advances in Biomaterials*, edited by Lee SM, CRC Press, 1987.

133. van Eijk MCP, Stuart MAC. Polymer Adsorption Kinetics: Effects of Supply Rate. *Langmuir* 1997;13(20):5447-5450.
134. Dolatshahi-Pirouz A, Rechendorff K, Hovgaard MB, Foss M, Chevallier J, Besenbacher F. Bovine serum albumin adsorption on nano-rough platinum surfaces studied by QCM-D. *Colloids Surf B Biointerfaces* 2008;66(1):53-9.
135. Müller B, Riedel M, Roger M, De Paul SM, Hofer R, Heger D, Grützmacher D. Impact of nanometer-scale roughness on contact-angle hysteresis and globulin adsorption. *Journal of Vacuum Science & Technology B: Microelectronics and Nanometer Structures* 2001;19(5):1715-1720.
136. Rechendorff K, Hovgaard MB, Foss M, Zhdanov VP, Besenbacher F. Enhancement of protein adsorption induced by surface roughness. *Langmuir* 2006;22(26):10885-8.
137. Roach P, Farrar D, Perry CC. Surface tailoring for controlled protein adsorption: effect of topography at the nanometer scale and chemistry. *J Am Chem Soc* 2006;128(12):3939-45.
138. Lord MS, Cousins BG, Doherty PJ, Whitelock JM, Simmons A, Williams RL, Milthorpe BK. The effect of silica nanoparticulate coatings on serum protein adsorption and cellular response. *Biomaterials* 2006;27(28):4856-62.
139. Guemouri L, Ogier J, Zekhnini Z, Ramsden JJ. The architecture of fibronectin at surfaces. *Journal of Chemical Physics* 2000;113(18):8183 - 8186.
140. Sousa SR, Moradas-Ferreira P, Barbosa MA. TiO₂ type influences fibronectin adsorption. *J Mater Sci Mater Med* 2005;16(12):1173-8.
141. Capriotti LA, Beebe TP, Jr., Schneider JP. Hydroxyapatite surface-induced peptide folding. *J Am Chem Soc* 2007;129(16):5281-7.
142. Schmidmaier G, Wildemann B, Bail H, Lucke M, Fuchs T, Stemberger A, Flyvbjerg A, Haas NP, Raschke M. Local application of growth factors (insulin-like growth factor-1 and transforming growth factor-beta1) from a biodegradable poly(D,L-lactide) coating of osteosynthetic implants accelerates fracture healing in rats. *Bone* 2001;28(4):341-50.
143. Wildemann B, Lubberstedt M, Haas NP, Raschke M, Schmidmaier G. IGF-I and TGF-beta 1 incorporated in a poly(D,L-lactide) implant coating maintain their activity over long-term storage-cell culture studies on primary human osteoblast-like cells. *Biomaterials* 2004;25(17):3639-44.
144. Moroni A, Cadossi M, Romagnoli M, Faldini C, Giannini S. A biomechanical and histological analysis of standard versus hydroxyapatite-coated pins for external fixation. *J Biomed Mater Res B Appl Biomater* 2008;86B(2):417-21.
145. Moroni A, Pegreff F, Hoang-Kim A, Tesei F, Giannini S, Wippermann B. Fixation of HA-coated unicortical locking screws in a sheep gap model: a comparative biomechanical study. *J Orthop Trauma* 2008;22(1):37-42.
146. Sachse A, Wagner A, Keller M, Wagner O, Wetzel WD, Layher F, Venbrocks RA, Hortschansky P, Pietraszczyk M, Wiederanders B and others. Osteointegration of hydroxyapatite-titanium implants coated with nonglycosylated recombinant human bone morphogenetic protein-2 (BMP-2) in aged sheep. *Bone* 2005;37(5):699-710.
147. Baas J, Elmengaard B, Jensen TB, Jakobsen T, Andersen NT, Søballe K. The effect of pretreating morselized allograft bone with rhBMP-2 and/or pamidronate on the fixation of porous Ti and HA-coated implants. *Biomaterials* 2008;29(19):2915-22.
148. Søballe K, Mouzin OR, Kidder LA, Overgaard S, Bechtold JE. The effects of hydroxyapatite coating and bone allograft on fixation of loaded experimental primary and revision implants. *Acta Orthop Scand* 2003;74(3):239-47.

149. Lutolf MP, Hubbell JA. Synthetic biomaterials as instructive extracellular microenvironments for morphogenesis in tissue engineering. *Nat Biotechnol* 2005;23(1):47-55.
150. Kim J, Park Y, Tae G, Lee KB, Hwang SJ, Kim IS, Noh I, Sun K. Synthesis and characterization of matrix metalloprotease sensitive-low molecular weight hyaluronic acid based hydrogels. *J Mater Sci Mater Med* 2008;19(11):3311-8.
151. Raeber GP, Lutolf MP, Hubbell JA. Molecularly engineered PEG hydrogels: a novel model system for proteolytically mediated cell migration. *Biophys J* 2005;89(2):1374-88.

10. English and Danish Resumé

English Resumé

A primary focus area in development of new biomaterials is degradable materials capable of evoking a desired tissue response following implantation. Such materials could provide a large medical breakthrough as they can be used to reconstruct lost organs or tissue segments by evoking a tissue response that results in regeneration of tissue. A common strategy in the development of suitable material properties consists of integrating specific physiological effects in the material, e.g. by adding signaling proteins capable of influencing the tissue response in a desired direction. The work in this strategy comprises identification of potential signaling proteins and integrating them in a biomaterial while maintaining the protein functionality.

In this thesis, it is attempted to develop and test a novel biomaterial suitable for templated regeneration of mineralized bone tissue. The biomaterial is designed with the aim of integrating a surface protein not previously used in a biomaterials context. It is known to play a key role in remodeling of mineralized bone tissue. The idea is that the protein will trick the cells in the body to include the biomaterial in the routine bone remodeling process – *i.e.* resorption of the material by osteoclasts and bone regeneration by the osteoclasts.

The development takes place in three steps: i) The adsorption on hydroxyapatite (HA) of the remodeling protein (OPN) and a previously well described protein is characterized, ii) The interaction of HA adsorbed OPN mesenchymal stem cells is analyzed & iii) The protein is incorporated in a composite consisting of a biodegradable polymer and HA particles in nanosize. Before mixing of polymer and particles the OPN is adsorbed on to the HA particles. The OPN containing polymer/HA composite was shown to be better at stimulating formation of mineralized tissue than pure polymer and a corresponding composite excluding OPN. Thus it is shown that OPN with advantage can be integrated in a biomaterial intended for guided formation of mineralized bone formation. It was furthermore, found successful to approach development of a novel biomaterial from a molecular mechanism consisting of the spontaneous adsorption of OPN on HA.

Danish Resumé

Et primært fokusområde i udviklingen af nye biomaterialer er nedbrydelige materialer som kan udløse et specifikt respons efter indsættelse i kroppen. Den slags materialer kan betyde et stort medicinsk gennembrud, da de kan bruges til at rekonstruere tabte organer eller vævssegmenter ved at udløse et vævsrespons der resulterer i regeneration af væv. En anvendt strategi i udviklingen af passende materialeegenskaber består af at integrere specifikke fysiologiske effekter i materialet, fx ved at tilsætte signalproteiner som kan påvirke vævsresponsen i den ønskede retning. Arbejdet i denne strategi består af at identificere potentielle signalproteiner og efterfølgende integrere dem i et biomateriale med bibeholdelse af proteinets funktionalitet.

I denne afhandling gøres et forsøg på at udvikle og teste et nyt biomateriale, der kan bruges som skabelon til gendannelse af mineraliseret knoglevæv. Biomaterialet designes mhp integrering af et overfladeprotein, som ikke tidligere er anvendt i biomaterialesammenhæng. Det vides at spille en vigtig rolle i remodellering af mineraliseret knoglevæv. Tanken er, at proteinet kan snyde kroppens celler til at inkludere biomaterialet i remodelleringsprocessen som den normalt foregår i kroppen - dvs ved materialenedbrydning af osteoklaster og knoglegenopbygning af osteoblaster.

Udviklingen af biomaterialet foregår i tre skridt: i) Adsorptionen på hydroxyapatit (HA) af remodelleringsproteinet (OPN) samt et tidligere velbeskrevet protein karakteriseres, ii) det HA adsorberede OPNs interaktion med mesenchymale stamceller analyseres & iii) OPN inkorporeres i et komposit bestående af et biodegradabelt polymer og HA-partikler i nanostørrelse. Før blanding af polymeret og partiklerne, adsorberes OPN på HA partiklerne. Komposittet med OPN vises at være bedre til at stimulere nydannelse af mineraliseret knoglevæv end rent polymer og et tilsvarende komposit uden OPN. Det vises hermed at OPN med fordel kan integreres i et biomateriale mhp at guide nydannelse af mineraliseret knoglevæv. Desuden lykkedes det i tilgangen at fremstille et nyt biomateriale ud fra en identificeret molekylær mekanisme bestående af OPNs spontane adsorption på HA.

11. Appendix

Contents:

Paper I: Enhanced surface activation of fibronectin upon adsorption on hydroxyapatite

Paper II: Interaction of human mesenchymal stem cells with osteopontin coated hydroxyapatite surfaces

Paper III: Hydroxyapatite nanoparticles in PDLA coatings on porous titanium implants conduct bone formation

Paper IV: Osteopontin functionalization of HA particles in a PDLA/HA composite promotes bone formation.

List of not appended papers

Theses from the orthopaedic research group

Enhanced Surface Activation of Fibronectin upon Adsorption on Hydroxyapatite

A. Dolatshahi-Pirouz,[†] T. Jensen,[†] M. Foss,* J. Chevallier, and F. Besenbacher

Interdisciplinary Nanoscience Center (iNANO) and Department of Physics and Astronomy, Aarhus University, DK-8000 Aarhus C, Denmark

Received June 30, 2008. Revised Manuscript Received December 2, 2008

In this study the adsorption characteristics and the structure of fibronectin adsorbed on hydroxyapatite (Ha) and a reference gold substrate (Au) is examined by quartz crystal microbalance with dissipation (QCM-D) and atomic force microscopy (AFM) at the following concentrations: 20 $\mu\text{g/mL}$, 30 $\mu\text{g/mL}$, 40 $\mu\text{g/mL}$, 100 $\mu\text{g/mL}$, 200 $\mu\text{g/mL}$, and 500 $\mu\text{g/mL}$. The conformational changes of the fibronectin molecules upon surface binding were examined as well with monoclonal antibody directed against the cell binding-domain (CB domain) of fibronectin. The QCM-D and AFM results show that the fibronectin uptake is larger on Au as compared with Ha regardless of the protein bulk concentration used in the experiment, suggesting that the individual fibronectin molecules in general attach to the surfaces in a more unfolded configuration on Ha. Moreover the dissipation values obtained with QCM-D indicate that the individual fibronectin molecules bind in a more compact and rigid configuration on Au compared to the Ha surface. In particular the monoclonal antibody data show that the CB domain on fibronectin is more available on Ha, where such cell-recognizing abilities are more pronounced at low fibronectin surface coverage. The results demonstrate that the detailed molecular structure of fibronectin and its functional activity depend significantly on both the underlying surface chemistry as well as the fibronectin surface coverage.

Introduction

When designing new surfaces for orthopedic implants, it is important to ensure a fast bone in-growth, a high degree of mechanical stability of the implant and to minimize the inflammatory responses and the release of any toxic substances during the clinical use of the implant. Different types of biomaterials such as stainless steel and tantalum has been introduced, but metals such as titanium and titanium alloys still range among the most important biomaterials because of their high degree of biocompatibility.¹ However, in most cases bone cement is needed to ensure long-term success of the implant by making it mechanically stable. Numerous attempts have been made to modify implant surfaces to achieve a successful biointegration without the use of bone cement, e.g. by coating the implant with sophisticated bioceramics and different types of apatites.¹

A widely used apatite coating is hydroxyapatite (Ha) [$\text{Ca}_{10}(\text{PO}_4)_6(\text{OH})_2$], which is the most abundant apatite in human bone and often considered as “the golden standard” in orthopedics. Ha displays a desirable bone–tissue response as compared to bare metal implants including absence of intervening fibrous tissue between bone and implant, lack of inflammation, and strong binding to bone.^{1–6} However, the detailed mechanisms of this biocompatible behavior are still not fully understood. The biocompatibility of an implant is related to how the adhering cells interact with the implant surface, when the implant is inserted

in the body.^{1,8} These cellular responses are in turn influenced by proteins adsorbing on the implant from the body fluids. Accordingly, the arriving cells sense the protein layer covering the surface when they arrive on the surface, thereby “seeing” the implant surface properties through the protein layer.^{7,8} The cellular response therefore depends on the detailed properties of the resulting interfacial protein layer.

One of the most important proteins that interact with cells is fibronectin (Fn), which is a large dimeric glycoprotein present in the extracellular matrix (ECM) consisting of two almost identical modules with a molecular weight around 250 kDa. Each subunit is composed of three different regions: two regions which bind to heparin and collagen, and a cell-binding domain (CB domain) containing an Arg-Gly-Asp (RGD) amino acid sequence. The native structure of Fn is stabilized by short-ranged electrostatic interactions and resembles a compact oblate ellipsoid with a hidden CB domain at pH and ionic strengths similar to physiological conditions.^{9,10} However, at high ionic strengths the Fn molecule undergoes conformational changes that results in an open and highly unfolded Fn configuration known as the extended/activated state,¹¹ where the hidden CB domain on Fn becomes available for cell recognition. From atomic force microscopy (AFM) and electron microscopy studies it is suggested that a similar conformational change and subsequent surface activation occur after Fn is adsorbed on either hydrophilic or charged substrates.^{12–14} In its surface-activated state Fn is responsible for directing several different types of cellular

* Corresponding author. E-mail: foss@inano.dk.

[†] These authors contributed equally to this work.

(1) Ratner, B. D.; Hoffman, A. S.; Schoen, F. J.; Lemons, J. E. *Biomaterials Science*, 2nd ed.; Elsevier: San Diego, 2004.

(2) Jarcho, M. *Clin. Orthop.* **1981**, *157*, 259–278.

(3) Geesink, R. G. T.; Groot, K. D.; Klein, C. P. A. T. *J. Bone Joint Surg.* **1988**, *70B*, 17–22.

(4) Winter, M.; Griss, P. P.; Groot, K. D. *Biomaterials* **1981**, *2*, 159–60.

(5) Bauer, T. W.; Geesink, R. G. T.; Zimmerman, R.; McMahon, J. T. *J. Bone Joint Surg.* **1991**, *73A*, 1439–1452.

(6) Block, M. S.; Finger, I. M.; Fontenot, M. G.; Kent, J. N. *Int. J. Oral Maxillofac. Implants* **1989**, *4*, 219–224.

(8) Kasemo, B. *Surface Sci.* **2002**, *500*, 656–677.

(7) Malmsten, M.; *Biopolymers at interfaces*, 2nd ed.; Marcel Dekker, Inc.: New York, 2003.

(9) Sjöberg, B.; Eriksson, M.; Österlund, E.; Pap, S.; Österlund, K. *Eur. Biophys. J.* **1989**, *17*, 5–11.

(10) Sjöberg, B.; Pap, S.; Österlund, E.; Österlund, K.; Vuento, M.; Kjems, J. *Arch. Biochem. Biophys.* **1987**, *255*, 347–354.

(11) Ugarova, T. P.; Zamarron, C.; Veklich, Y.; Bowditch, R. D.; Ginsberg, M. H.; Weisel, J. W.; Plow, E. F. *Biochemistry* **1995**, *34*, 4457–4466.

(12) Wolff, C.; Lai, C.-S. *Arch. Biochem. Biophys.* **1989**, *268*, 536–545.

(13) Erickson, H. P.; Carrel, N. A. *J. Biol. Chem.* **1983**, *258*, 14539–14544.

(14) Bergkvist, M.; Carlsson, J.; Oscarsson, S. *J. Biomed. Res.* **2003**, *64A*, 349–356.

responses on biomaterial substrates including cell migration, proliferation, differentiation, organization of the cytoskeleton, and the initial cell attachment.^{15–21}

The effect of the detailed surface chemistry on the interfacial protein adsorption has been extensively studied on different types of ceramic coatings, metallic and chemically functionalized surfaces.^{22–32}

For these interfacial protein adsorption studies with different surface chemistries, some general trends have already been established in the past, most of them related to how the surface chemistry influences the protein conformation and the protein surface mass uptake. For instance, in ref 31 the interaction of Fn on Au, titanium oxide, and tantalum surfaces was studied with the QCM-D technique, and it was concluded that the Fn surface mass uptake and the structural properties of the individual Fn molecules are influenced by the substrate chemistry.

The same conclusion was reported in ref 32 where the adsorption of fibrinogen was studied on Au, titanium oxide, and Ha by the QCM-D technique in combination with the grazing angle infrared analysis technique.

The objective of the present study is to examine the adsorption of Fn on Ha both with respect to the amount of Fn bound to the surface and the activity of the individual Fn molecules on the respective surfaces with Au as a reference surface. The Fn adsorption behavior was characterized at several concentrations in order to explore whether the cell-recognizing ability of Fn depended on the surface mass uptake and to examine the adsorption isotherm curves belonging to Fn.

Materials and Methods

Proteins and Antibodies. Fn extracted from bovine plasma with a molecular weight of 450 kDa was purchased from Sigma-Aldrich (Denmark), and bovine IgG monoclonal anti-Fn (150 kDa³³) directed against an epitope located on the cell-binding domain (CB domain) of Fn was purchased from The Antibody Shop (Australia). To test for unspecific binding, rabbit IgG polyclonal BSA antibodies were purchased from Sigma-Aldrich (Denmark). The proteins and antibodies were stored at $-50\text{ }^{\circ}\text{C}$ before use. The Fn and the antibodies

were dissolved in a 10 mM Tris buffer with 1 mM CaCl and 100 mM NaCl adjusted with HCl and NaOH to a pH value around 7.79 at 22 °C. It has previously been shown that Fn when dissolved in a buffer similar to the one used here adapts to a compact disclike configuration with the dimensions 13.8 nm \times 1.44 nm.^{9,10} The following Fn concentrations were chosen: 20 $\mu\text{g/mL}$, 30 $\mu\text{g/mL}$, 40 $\mu\text{g/mL}$, 100 $\mu\text{g/mL}$, 200 $\mu\text{g/mL}$, and 500 $\mu\text{g/mL}$, which were below and over the physiological Fn level (150–300 $\mu\text{g/mL}$).¹ Antibody–antigen interactions with the adsorbed Fn layer was investigated for the Fn concentrations 20 $\mu\text{g/mL}$, 100 $\mu\text{g/mL}$, and 200 $\mu\text{g/mL}$. The protein and antibody solutions were stored at 4 °C until use, and no solutions were used for more than seven days.

Quartz Crystal Microbalance (QCM-D). Quartz crystal microbalance with dissipation (QCM-D) is a well-established technique for real time characterization and quantification of protein adsorption on surfaces.³⁴ The technique relies on monitoring the resonance frequency of a quartz crystal oscillating in the shear mode, where the change in resonance frequency is related to changes in the adsorbed mass on the crystal.^{34,35} In the case of a thin nondissipative layer with no slip with respect to surface adsorption, the frequency shift and the adsorbed surface mass density, $\Gamma_{\text{QCM-D}}$, are proportional as it is seen from the simple Sauerbrey equation:³⁵

$$\Gamma_{\text{QCM-D}} = -\frac{C}{n} \Delta f_n \quad (1)$$

where C is the mass sensitivity constant (17.7 ng/cm² Hz⁻¹ for a 5 MHz crystal), n (1, 3, 5...) is the overtone number, and Δf_n is the frequency shift of the n th overtone. In addition to the frequency shifts, the corresponding shift in dissipation factor ΔD is also monitored, with the dissipation being defined as

$$D = \frac{E_{\text{lost}}}{2\pi E_{\text{stored}}} \quad (2)$$

where E_{lost} is the energy dissipated during each oscillation cycle, and E_{stored} is the total energy of the system. A low dissipation is required in order to ensure that the Sauerbrey equation is a good and valid approximation, in which case the $1/n$ scaling as indicated in formula 1 is also fulfilled. In the following, the seventh overtone ($n = 7$) was chosen whenever the Sauerbrey equation was employed in the further data analysis.

In the case of a very dissipative system the simple Sauerbrey eq 1 is no longer valid, and it is necessary to use a more complex model, e.g. the Voight model.³⁶ Furthermore, it is important to realize that the QCM-D measured frequency shift is not only associated with the resulting mass uptake of the proteins on the surface but that it also might be due to the hydration of the proteins and trapped water in the pores of the protein film.^{37,38} All experiments were carried out at a flow rate of 500 $\mu\text{L/min}$ and a dispense volume at 500 μL at 22 °C using a Q-Sense AB E4 system. Crystals applied in the QCM-D measurements were ozone-cleaned with UV (BioForce, Ames, IA) for 25–30 min before each experiment.

Characterization of Surfaces. Quartz crystal microbalance (QCM) crystals coated with 100 nm Au (AT-cut QSX 301) or a 10 nm thin layer of Ha on top of the Au layer (AT-cut QSX 327) were purchased from Q-Sense AB, Sweden. The root-mean-square roughness (rms value) and the percentagewise increase in surface area as compared to a completely flat surface were determined with atomic force microscopy (AFM). The AFM images were acquired

(15) Kowalczyńska, H. M.; Nowak-Wyrzykowska, M.; Dobkowski, J.; Kolos, R.; Kaminski, J.; Makowska-Cynka, A.; Marciniak, E. *J. Biomed. Mater. Res.* **2001**, *61A*, 260–269.

(16) Kowalczyńska, H. M.; Nowak-Wyrzykowska, M.; Kolos, R.; Dobkowski, J.; Kaminski, J. *J. Biomed. Mater. Res.* **2004**, *72A*, 228–236.

(17) Keselowsky, B. G.; Collard, D. M.; Garcia, A. J. *J. Biomed. Mater. Res.* **2003**, *66A*, 247–259.

(18) Burridge, K.; Fath, K.; Kelly, T.; Nuckolls, G.; Turner, C. *Annu. Rev. Cell. Biol.* **1988**, *4*, 487–525.

(19) Burridge, K.; Chrzanowska-Wodnicka, M. *Annu. Rev. Cell. Dev. Biol.* **1996**, *12*, 463–519.

(20) Wittmer, C. R.; Phelps, J. A.; Saltsman, W. M.; Tassel, P. R. *Van. Biomaterials* **2007**, *28*, 851–860.

(21) Grinnell, F.; Feld, M. K. *J. Biol. Chem.* **1982**, *257*, 4888–4893.

(22) Höök, F.; Rodahl, M.; Kasemo, B.; Brzezinski, P. *Proc. Natl. Acad. Sci. U.S.A.* **1998**, *95*, 12271–12276.

(23) Wertz, C. F.; Santore, M. M. *Langmuir* **2001**, *17*, 3006–3016.

(24) Yongli, C.; Xiufang, Z.; Yandao, G.; Nanming, Z.; Tingying, Z.; Xinqi, S. *J. Colloid Interface Sci.* **1999**, *214*, 38–45.

(25) Rodahl, M.; Höök, F.; Fredriksson, C.; Keller, C. A.; Krozer, A.; Brzezinski, P.; Voinova, M.; Kasemo, B. *Faraday Discuss.* **1997**, *107*, 229–246.

(26) Roach, P.; Farrar, D.; Pery, C. C. *J. Am. Chem. Soc.* **2005**, *127*, 8168–8173.

(27) Wassel, D. T. H.; Hall, R. C.; Embery, G. *Biomaterials* **1995**, *16*, 697–702.

(28) Tsumagari, A.; Nakamura, S.; Hashimoto, K.; Toda, Y.; Yamashita, K. *Bioceramics* **1999**, *12*, 361–364.

(29) Botelho, C. M.; Brooks, R. A.; Kawai, T.; Ogata, S.; Ohtsuki, C.; Best, S. M.; Lopes, M. A.; Santos, J. D.; Rushton, N.; Bonfield, W. *Key Eng. Mater.* **2005**, *284–286*, 461–464.

(30) Deligianni, D.; Korovessis, P.; Porte-Derrieu, M. C.; Amedee, J. J. *Spinal Disord. Tech.* **2005**, *18*, 257–262.

(31) Hemmersam, A. G.; Rechendorff, K.; Foss, M.; Sutherland, D. S.; Besenbacher, F. *J. Colloid Interface Sci.* **2008**, *320*, 110–116.

(32) Monkawa, A.; Ikoma, T.; Yunoki, S.; Yoshioka, T.; Tanaka, J.; Chakarov, D.; Kasemo, B. *Biomaterials* **2006**, *27*, 5748–5754.

(33) Berg, J. M.; Tymoczko, J. L.; Stryer, L. *Biochemistry*, 5th ed.; W. H. Freeman and Company: New York, 2002.

(34) Rodahl, M.; Höök, F.; Krozer, A.; Brzezinski, P.; Kasemo, B. *Rev. Sci. Instrum.* **1995**, *66*, 3924–3930.

(35) Sauerbrey, G. *Z. Phys.* **1959**, *155*, 206–222.

(36) Voinova, M. V.; Rodahl, M.; Jonson, M.; Kasemo, B. *Phys. Scr.* **1999**, *59*, 391–396.

(37) Höök, F.; Kasemo, B.; Nylander, T.; Fant, C.; Sott, K.; Elwing, H. *Anal. Chem.* **2001**, *73*, 5796–5804.

(38) Höök, F.; Vörös, J.; Rohdahl, M.; Kurrat, R.; Böni, P.; Ramsden, J. J.; Textor, M.; Spencer, N. D.; Tengvall, P.; Gold, J.; Kasemo, B. *Colloid Surf. B* **2002**, *24*, 155–170.

in tapping mode using a commercial Nanoscope IIIA Multimode SPM (Veeco Instruments, Santa Barbara, CA) at scan frequencies 1–2 Hz under ambient conditions, applying a silicon cantilever (NSG01, NT-MDT, Russia) with a typical resonance frequency around 150 kHz, a spring constant of 5.5 N/m, and a tip radius below 10 nm. The AFM images (512 × 512 pixels) were all quadratic with linear dimensions of 1, 3, and 5.5. By using SPIP for analyzing the AFM images, the following rms values 0.91 ± 0.14 nm on Au and 2.2 ± 0.2 nm on the Ha surface were attained and the surface area increase compared to a flat surface was determined to be $0.45 \pm 0.08\%$ for Au and $1.3 \pm 0.3\%$ for Ha (for a detailed description, see ref 39).

The Ha coatings were examined with grazing incidence X-ray diffraction (XRD), and several peaks which belong to the crystalline phase of Ha were observed alongside the prominent Au peaks from the supporting Au layer below the Ha coating, proving that the Ha coating was crystalline (data not shown). Moreover, a dissolution test was conducted on the Ha crystals to further test the crystalline phase of Ha by QCM-D by injecting Tris buffer in the QCM-D chambers and examining the QCM-D response over a time span of 30 h. No sign of thin film degradation was observed by the associated QCM-D frequency shift, which indicates that at least during this time span the Ha substrates are stable/crystalline and suitable for QCM-D experiments. The wetting behavior of the surfaces was determined by measuring the contact angle by the sessile drop method, after the substrates were standard treated with UV light/ozone for 25–30 min (Bioforce) using the contact angle instrument model DSA100 (Krüss, Borssteler Chaussee, Germany). Both the Ha and Au coatings were found to be highly hydrophilic after UV treatment with a contact angle below 10° .

Ellipsometry. Ellipsometry is a well-established technique which has been applied for decades to study interfacial protein adsorption.^{7,37,38} It allows in situ kinetic studies at the solid–liquid interface with a time resolution down to milliseconds and a thickness resolution around 0.1 nm.

Real-time protein measurements were conducted with an ellipsometer from DRE GmbH, Germany, model ELX-02c, equipped with a single wavelength $\lambda = 632.8$ nm He–Ne laser in liquid environment at room temperature with a fixed angle of incidence at 70° .

The principle behind using ellipsometry to study protein adsorption is quite simple and relies on the changes in the polarization of elliptically polarized light reflected from a surface onto which proteins are adsorbed. These changes are monitored by measuring the changes in the ellipsometric angles (Δ, ψ) during the protein adsorption, and the recorded signals are subsequently converted to a thickness value for the protein film. From the measured thickness value, d , the surface mass density, $\Gamma_{\text{ellipsometry}}$, of the adsorbed protein film is easily determined by means of the de Feijters formula:⁴⁰

$$\Gamma_{\text{ellipsometry}} = d \frac{n_{\text{protein}} - n_{\text{buffer}}}{dn/dc} \quad (3)$$

where dn/dc is the refractive index increment for a given concentration change, n_{protein} the refractive index of the protein, and n_{buffer} the refractive index of the buffer. The dn/dc value of proteins are typically around $0.18 \text{ cm}^3/\text{g}$,³⁸ and the refractive indexes used for the protein layer and the buffer in this study were $n_{\text{protein}} = 1.465$ and $n_{\text{buffer}} = 1.335$, respectively.³⁸ The value $n_{\text{protein}} = 1.465$ is an appropriate choice for a homogeneous and uniform surface coverage, which is expected at the high protein concentrations employed in this work. All experiments were carried out in real time by injection of 1 mL protein solution into the ellipsometer chamber, and immediately before each measurement the samples were ozone-cleaned with UV (Bioforce, USA) for 25–30 min.

Atomic Force Microscopy (AFM) Tip Scratch Method. The thickness of the dehydrated protein film formed on the Ha and Au surfaces was determined by the AFM tip scratch method^{41–43} using a commercial Nanoscope IIIA Multimode SPM (Veeco Instruments, Santa Barbara, CA). The applied silicon cantilevers (NSG01, NT-MDT, Russia) had a resonance frequency around 150 kHz, a spring constant of 5.5 N/m, and a tip curvature radius below 10 nm. After the QCM-D experiments, the quartz crystals with the adsorbed Fn layer were rinsed gently once in deionized water in order to remove buffer salt from the surface and subsequently blow dried with nitrogen (Purity, 99.7%) and kept under vacuum at room temperature before AFM imaging. The protein film was carefully removed from the quartz crystals by operating the AFM tip in the contact mode with a procedure similar to the one employed previously,^{41,42} until an area was scratched free of Fn with the AFM tip. The force needed to displace the proteins was adjusted with the deflection set point until an appropriate force was delivered to the sample, leaving the underlying substrate unaffected by the force load but still capable of removing all proteins from the selected area. Initial testing on bare substrates revealed that a deflection set point above 0.5 V on Au and above 1.2 V on HA distorted the substrate topographies. In the protein layer height measurements the deflection set points were set at 0.5 V on the Fn-coated Au and 1.2 V on Fn-coated Ha to ensure maximum Fn displacement efficiency without damaging the underlying substrate. By applying a higher load force, the AFM tip was able to scratch on the underlying substrate, confirming that the Fn layer was efficiently removed from the surface. Subsequently, the height differences between the protein film and the bare substrate areas were determined by operating the AFM in the tapping mode at scan frequencies between 1–1.5 Hz under ambient conditions.

Statistical Analysis. Whenever two different mean values were compared, a t test was carried out to determine if there were any significant differences between the two means. A two-sided p value less than 0.05 was considered significant. Unless stated otherwise data is presented as mean \pm standard error of mean. Statistical analysis was performed with GraphpadInstat 3.0 (GraphPad Software, Inc., La Jolla, CA).

Result and Discussion

Fn Adsorption Monitored by QCM-D. Typical QCM-D shifts in frequency, Δf_7 , and dissipation, ΔD_7 , are shown in Figure 1A,B, for the adsorption of Fn and antibodies at the bulk concentration $20 \mu\text{g/mL}$ on Ha and Au surfaces, respectively. The baseline at the beginning of the adsorption process corresponds to the baseline signal from pure Tris buffer prior to protein injection. Both after the initial Fn injection and after a subsequent antibody injection an immediate decrease in frequency, Δf_7 , and increase in dissipation, ΔD_7 , is observed as depicted from Figure 1A,B. A test for unspecific antibody binding to the surfaces showed an unspecific binding ranging from 9.8% at the protein bulk concentration $200 \mu\text{g/mL}$ to 14% at $20 \mu\text{g/mL}$ of the total amount of antibodies binding to the respective surfaces. A possible BSA contamination of the fibronectin solution might lead to an overestimation of the unspecific antibody binding values. However, this does not change the interpretation of the antibody results, since the above unspecific values are in general very low and not taken into further consideration in the paper.

In Figure 2A,B the QCM-D frequency shifts Δf_n at the frequency overtones, $n = 3, 5,$ and 7 are shown for the Fn adsorption on Au and Ha from protein solutions with the protein concentrations $20 \mu\text{g/mL}$, $200 \mu\text{g/mL}$, and $500 \mu\text{g/mL}$. It is clearly seen after scaling that the different overtones superimpose for

(41) Lubarsky, G. V.; Browne, M. M.; Mitchell, S. A.; Davidson, M. R.; Bradley, R. H. *Colloid Surf. B* **2005**, *44*, 56–63.

(42) Lubarsky, G. V.; Davidson, M. R.; Bradley, R. H. *Biosens. Bioelectron.* **2007**, *22*, 1275–1281.

(43) Pancera, S. M.; Gliemann, H.; Schimmel, Th.; Petri, D. F. S. *J. Colloid Interface Sci.* **2006**, *302*, 417–423.

(39) Dolatshahi-Pirouz, A.; Hovgaard, M. B.; Rechendorff, K.; Chevallier, J.; Foss, M.; Besenbacher, F. *Phys. Rev. B* **2008**, *77*, 115427–115431.

(40) de Feijter, J. A.; Benjamins, J.; Veer, F. A. *Biopolymers* **1978**, *17*, 1759–1772.

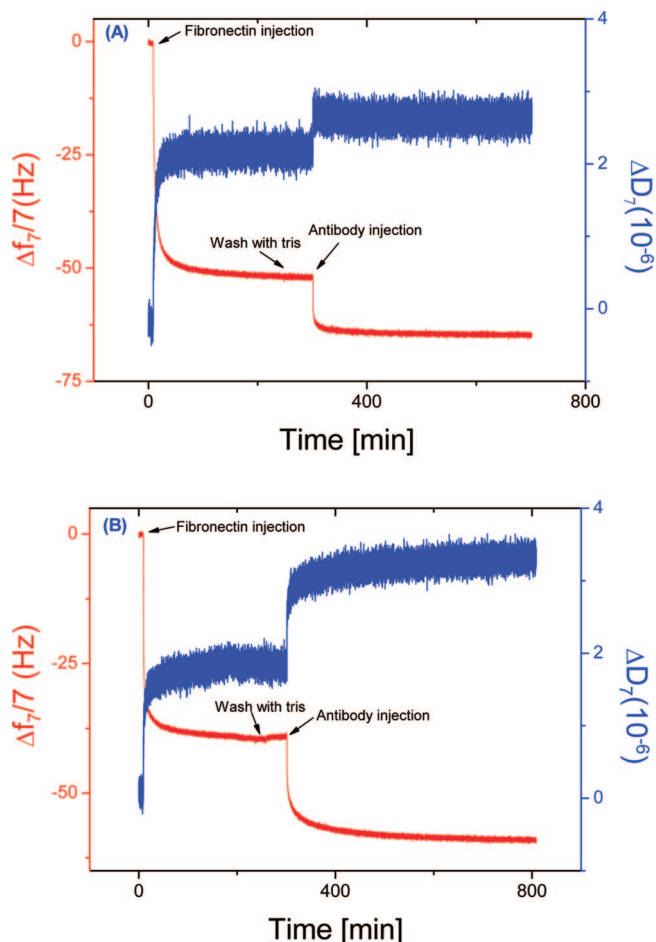


Figure 1. The change in dissipation, ΔD_7 , and frequency shift, Δf_7 , during the adsorption of $20 \mu\text{g/mL}$ Fn and after a subsequent anti-Fn injection on (A) a Au-coated surface and (B) Ha-coated crystals.

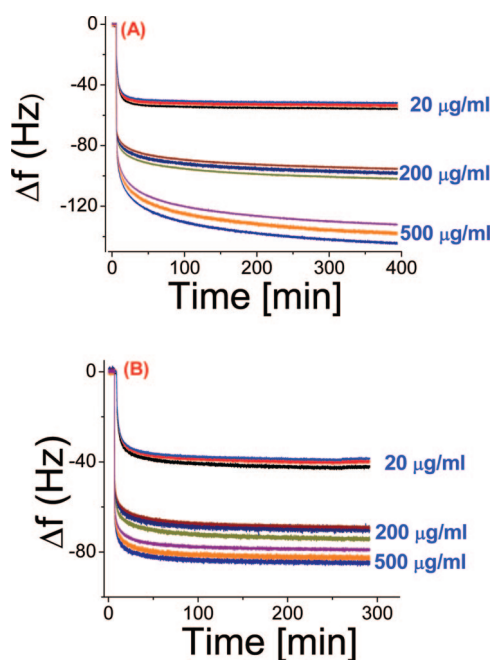


Figure 2. The scaling of the frequency shift, Δf , for the overtones $n = 3, 5, 7$ at different bulk concentrations, for (A) Au and (B) Ha.

almost all combinations of surface chemistry and protein bulk concentration, and that the frequency shift increases as the protein concentration increases for both the Au and Ha surface. The

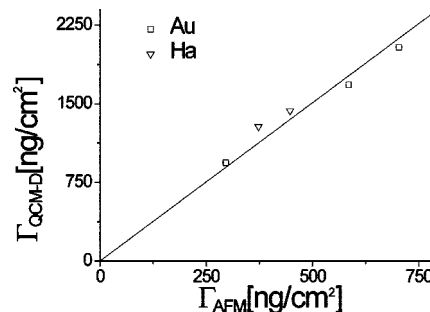


Figure 3. The relationship between the surface mass densities at the Fn bulk concentrations $20 \mu\text{g/mL}$, $200 \mu\text{g/mL}$, and $500 \mu\text{g/mL}$ for Au and $200 \mu\text{g/mL}$ and $500 \mu\text{g/mL}$ for Ha, as obtained with AFM and QCM-D. Data are fitted with a linear function $y = ax$ with the slope $a = 3.02 \pm 0.10$. The value was subsequently interpreted as the water factor in the different protein films.

scaling of the overtones as seen from Figure 2A,B strongly suggests that the simple Sauerbrey equation can be applied in the present study without any further notice except for the QCM-D results obtained for the Fn adsorption on Au at the concentration $500 \mu\text{g/mL}$, where a large spread in the different overtones is observed after the overtone scaling. Therefore, for this special case a Voight analysis³⁶ was conducted, and a deviation of approximately only 17% was found as compared to the surface mass density calculated from the Sauerbrey equation. Because of the similar results obtained with the two models and to simplify things, we chose to rely on the simple Sauerbrey equation throughout the paper.

The Protein Layer Height As Determined by the AFM Tip Scratch Method. As mentioned in the previous sections, both the dry mass of the protein film and the water coupled to the protein film^{37,38} contributes to the frequency shift response measured by the QCM-D technique. Here the thickness and accordingly the dry mass of the protein films are determined with the AFM tip scratch method.^{41–43} Besides its potential applications for the determination of protein film thicknesses, the AFM imaging itself also provides detailed information about the overall morphology of a protein film.^{41–43}

In order to convert the protein film thicknesses determined with the AFM tip scratch method for the different protein films to a surface mass density value, Γ_{AFM} , we used the generally accepted value 1.35 g/cm^3 ⁴⁴ as the density of the individual Fn molecules. These surface mass density values (Γ_{AFM}) were then depicted as a function of the QCM-D measured surface mass densities Γ_{QCM} in Figure 3. The results follow a straight line with a slope of 3.02, showing that the ratio of the observed surface mass densities ($\Gamma_{\text{QCM-D}}/\Gamma_{\text{AFM}}$), which expresses the relative amount of coupled water in a given protein layer (water factor), is approximately the same on the examined surface chemistries (Ha or Au) and the range of protein concentrations used. Using the constant water factor of 3.02 obtained from Figure 3, we were able to give an estimate of the protein dry masses present on the respective QCM-D sensor surfaces by dividing the QCM-D results with 3.02. These results are plotted against the protein bulk concentration and presented in Figure 4.

Moreover we also employed ellipsometry at the concentration $20 \mu\text{g/mL}$ on both Ha and Au (See Table 1). By ellipsometry a fibrinectin surface mass density value of $264 \pm 26 \text{ ng/cm}^2$ on Ha was found, which is not significantly different ($p > 0.05$) from the QCM-D dry mass results at $228 \pm 8 \text{ ng/cm}^2$ (see Table

(44) Fisher, H.; Polikarpov, I.; Craivich, A. F. *Protein Sci.* **2004**, *13*, 2825–2828.

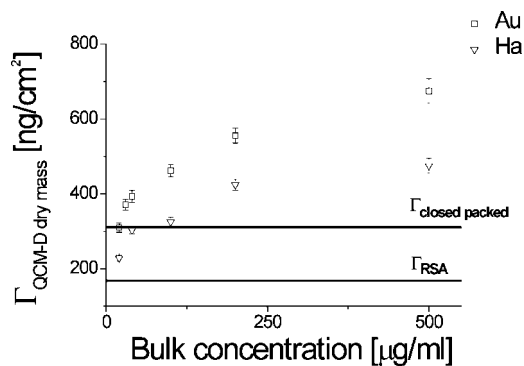


Figure 4. The protein dry mass determined from the QCM-D results using a water factor at 3.02, as a function of bulk concentration. Lines corresponding to the surface mass densities of the extended rod configuration are drawn ($\Gamma_{\text{closed packed}}$ and Γ_{RSA}).

1). On the other hand, on Au a significant difference ($p < 0.005$) between the ellipsometry result, $380 \pm 6 \text{ ng/cm}^2$, and the QCM-D dry mass result at $310 \pm 13 \text{ ng/cm}^2$ (see Table 1) was seen. However, the ellipsometry result on Au is still quite comparable with the corresponding QCM-D dry mass result, since the difference between these two results is around 20%. It is not unusual that small variations exist when the surface mass uptake obtained with different techniques are compared because of different experimental conditions,^{37,38} which in our case might arise from the different initial flow rates during protein solution injection and the different volumes available in the QCM-D and ellipsometry liquid chambers.

Since the ellipsometry results gave a water factor around 2.50 on both surfaces (Ha and Au), the assumption that the amount of water coupled to the protein layers on Au and Ha is similar is further strengthened by the ellipsometry measurements.

From Figure 4 we also observe that for both the Ha and the Au surfaces the saturated surface mass densities depend on the Fn concentration as expected, with an increase in the Fn surface mass density as the protein bulk concentration increases. In the case of Ha, a significant increase from $228 \pm 8 \text{ ng/cm}^2$ at low concentration to $475 \pm 20 \text{ ng/cm}^2$ at high concentration ($p < 0.0001$) occurred, corresponding to a total increase in surface mass density of 108%. For the Au surface a significant difference from $310 \pm 13 \text{ ng/cm}^2$ at low concentration to $675 \pm 33 \text{ ng/cm}^2$ at high concentration ($p < 0.0001$) corresponding to a total increase of 118% was seen.

Besides finding the thickness of the dehydrated protein film on the respective surfaces with the AFM tip scratch method, the overall morphology of the Fn-coated Ha and Au substrates was analyzed by AFM imaging as well (data not shown).

The AFM images revealed that the adsorbed Fn layer covered both the Ha and the Au surfaces in a homogeneous way both at low and high protein concentrations, which indicates that the lower surface mass densities observed at low concentrations was not due to an interface consisting of individual and separated Fn islands and that no Fn multilayer formation took place. Accordingly, the change in surface mass density with concentration is most likely caused by protein–protein repulsive interactions and postadsorption changes in the protein conformation on the surface,^{45,46} resulting in a subsequent change in the contact area between the surface and the individual Fn molecules.

To investigate how the surface conformation of the Fn molecules depend on the different protein solution concentrations

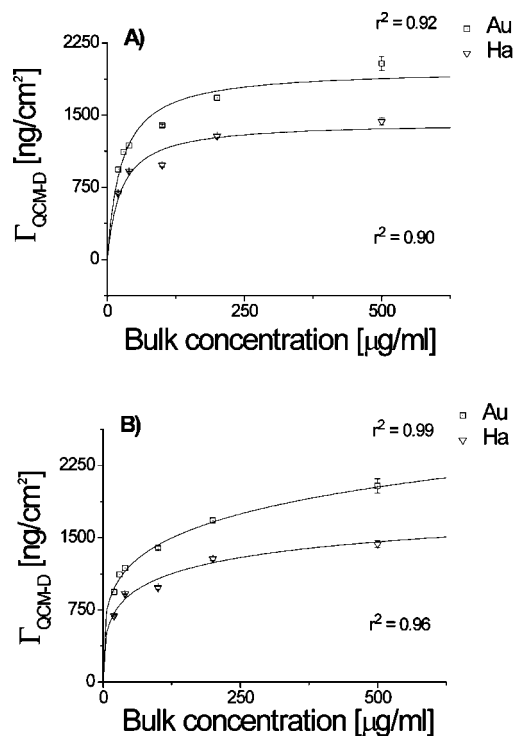


Figure 5. The QCM-D results are plotted together with the bulk concentration to investigate the Fn adsorption isotherms. The surface mass density increases with higher bulk concentration, gradually leveling off as the concentration is increased. Results are fitted with both (A) the Langmuir and the (B) Hill equation, and the goodness of each fit (r^2) is indicated as well.

more thoroughly, two simple models are considered: (i) An oblate ellipsoidal adsorption configuration identical to the native configuration of Fn in solution, with either a side-down or end-on orientation, and (ii) a configuration where Fn is in its surface-activated state, a highly unfolded adsorption state (extended state) with the rectangular dimensions $120 \text{ nm} \times 2 \text{ nm}$ in its side-down configuration.^{12–14,47} In Table 2, the contact area between the Fn molecules and the interface (footprint) together with the monolayer Fn surface coverage of the above configurations are presented under the assumption of two different adsorption scenarios: (i) A surface consisting of a closed packed Fn monolayer at saturation and (ii) within the context of the random sequential adsorption (RSA) model.⁴⁸

The measured saturated surface mass densities were generally much higher than a protein layer consisting of Fn molecules in the oblate side-down configuration both in the context of the RSA model and when considering a closed packed monolayer (Table 2). Accordingly, only a few select Fn molecules are expected to adsorb in states similar to this on the substrates. The observed saturation mass densities at low concentrations, however, are very close to a monolayer surface coverage of Fn molecules in the highly unfolded and extended configuration. In Figure 4 lines corresponding to surface mass densities of this extended configuration (adsorption scenarios i and ii are shown). From Figure 4 it is seen that the surface mass densities for the Ha surfaces at concentrations below $100 \mu\text{g/mL}$ lie in this interval, while the surface mass densities for Au in general are above the upper limit of the interval.

As the Fn concentration increases, the Fn surface mass density on both substrates increases as well until a point, where each

(45) Hemmersam, A. G.; Foss, M.; Chevallier, J.; Besenbacher, F. *Colloid Surf. B* **2005**, *43*, 208–215.

(46) Wertz, C. F.; Santore, M. M. *Langmuir* **2002**, *18*, 706–715.

(47) Engel, J.; Odermatt, E.; Engel, A. *J. Mol. Biol.* **1981**, *150*, 97–120.

(48) Talbot, J.; Tarjus, G.; Van Tassel, P. R.; Viot, P. *Colloid Surf. A* **2000**, *165*, 287–324.

Table 1. The Results Obtained with QCM-D and AFM Are Compared with Ellipsometry at the Protein Bulk Concentration 20 $\mu\text{g/mL}$

surface	$\Gamma_{\text{ellipsometry}}$ [ng/cm^2]	$\Gamma_{\text{QCM-D dry mass}}$ [ng/cm^2]	antibodies per protein (ellipsometry)	antibodies per protein (QCM-D)
Ha	264 ± 26	228 ± 8	1.25 ± 0.25	1.51 ± 0.03
Au	380 ± 6	310 ± 13	0.70 ± 0.10	0.708 ± 0.014

Table 2. The Theoretical Full Monolayer Surface Mass Density for Different Configuration of Fn on a Surface Is Presented Together with the Surface Mass Densities in the Context of the RSA Model with a Jamming Limit at 54%

configuration	area [nm^2]	$\Gamma_{\text{full monolayer}}$ [ng/cm^2]	Γ_{RSA} [ng/cm^2]
oblate side-down	598	125	68
oblate end-on	7	10686	5770
extended state	240	311	168

protein occupies a smaller surface area as compared to the footprint of the extended state (this is the case for concentrations above 100 $\mu\text{g/mL}$ for Ha and 20 $\mu\text{g/mL}$ for Au).

Accordingly, it is likely that the Fn molecules tend to unfold more rapidly after surface binding on Ha as compared to Au.

Fn Adsorption Isotherms. Adsorption isotherm curves are typically analyzed within the context of the well-known classical Langmuir adsorption theory.⁷ The Langmuir formalism is applicable provided that (a) only one type of adsorption binding is possible on the interface, (b) the adsorption process is fully reversible, and (c) interactions between the adsorbents are not allowed.⁷

In most cases, protein adsorption is almost irreversible and protein–protein interactions are non-negligible.⁴⁹ Despite these constraints, the Langmuir model is still frequently employed to describe protein adsorption isotherms:^{15–17,50–53}

$$\Gamma = \frac{\Gamma_{\text{max}} K_{\text{eq}} c}{1 + K_{\text{eq}} c} \quad (4)$$

where K_{eq} is the equilibrium binding constant, which is a measuring unit for the affinity of the adsorbent toward the sorbent, c the bulk concentration, and Γ_{max} is the surface mass density of the protein at its full monolayer coverage.

When more than one type of adsorption sites exists on the surface and interactions among the proteins on the surface are allowed, it is more appropriate to use the Hill equation:^{7,50}

$$\Gamma = \frac{\Gamma_{\text{max}} K_{\text{h}} c^n}{1 + K_{\text{h}} c^n} \quad (5)$$

where K_{h} and n are the Hill equilibrium binding constant and the Hill coefficient, respectively.

Besides information relating to the binding affinity between the sorbent and the adsorbent, a Hill plot also provides detailed insight into a more complex interaction scheme known as cooperative adsorption.⁵⁴ Cooperative adsorption typically occurs when proteins interact through different interaction schemes with an interface. Moreover, the Hill coefficient, n , describes the degree of cooperativity present during the adsorption. Protein adsorption is cooperative when $n > 1.0$, where a value of $n > 1.0$ also indicates that protein–protein interactions are attractive. Con-

Table 3. Fit Parameters Obtained by Fitting the Data in Figure 4 with Either the Langmuir or the Hill Equation

surface	K_{Hill}	Hill coefficient (n)	K_{Langmuir}
Ha	0.13 ± 0.05	0.40 ± 0.32	0.040 ± 0.012
Au	0.053 ± 0.107	0.270 ± 0.112	0.039 ± 0.009

versely, $n < 1.0$ means that the protein adsorption is noncooperative and a repulsive force exists between the proteins.^{50,54} When $n = 1.0$ only one class of adsorption sites is allowed, and in this case the Hill equation is identical to the Langmuir equation.^{7,50}

Both the Langmuir and Hill equations have been employed in several reports to gain additional information about the adsorption behavior of proteins on different substrates.^{7,50,53–57} Inspired by these previous studies, we analyze our QCM-D wet mass results in the same manner within the framework of eqs 4 and 5 (See Figure 5). We are allowed to do this since it was shown in the previous section that the water factor is independent of the substrate type (Ha or Au) and protein concentration.

Figure 5A clearly shows that the Langmuir equation does not fit the QCM-D results very well. The Hill equation, on the other hand, provided a very good fit on both surface chemistries (Ha and Au) with Hill coefficient values below 0.5 (see Table 3), indicating that the proteins interacted through different interaction schemes with the Au and Ha surface, either caused by the heterogeneous surface properties of proteins in general or heterogeneous binding sites present on the surface. An obvious reason behind the different possible interaction schemes between the proteins and the Ha substrate is the presence of the positively charged P sites (rich in phosphate ions) and negatively charged C sites (rich in calcium ions) on a Ha substrate.^{58,59} The low Hill coefficients also indicate that repulsive protein–protein interactions were present during the adsorption process in accordance with the discussion in the previous section, where it was concluded that no Fn aggregates formed on the surfaces.

Moreover the binding constant value K_{Hill} attains the highest value on Ha while similar binding constant values K_{Langmuir} are obtained with the Langmuir model on the Ha and Au surfaces. Even though the K_{Hill} value is larger on Ha as compared to Au, there is an overlap in the uncertainties associated with the K_{Hill} values. Therefore, it is not possible to show any significant difference between the Hill binding constant for the two surfaces.

The Relation between QCM-D Dissipation and Frequency Shift. Additional information on the interaction of the Fn molecules with the Ha and the Au surfaces can be obtained from the recorded $\Delta D/\Delta f$ results, which may reveal important information about the structural properties of the detected protein layer.^{22,25,38,60–62} For instance, a stiffer, more rigid and compact protein film in general leads to lower $\Delta D/\Delta f$ values.^{25,38,62} Moreover, concerning the interpretation of the $\Delta D/\Delta f$ values it is important to clarify that the dissipation depends on the properties of the total hydrated protein layer.^{25,37} However, since we found

(49) Israelachvili, J. *Intermolecular and Surface Forces*, 2nd ed.; Elsevier: San Diego, 2006.

(50) Chang, I.-N.; Lin, J.-N.; Andrade, J. D.; Herron, J. N. *J. Colloid Interface Sci.* **1995**, *174*, 10–23.

(51) Roach, P.; Farrar, D.; Perry, C. C. *J. Am. Chem. Soc.* **2006**, *128*, 3939–3945.

(52) Kurosawa, S.; Kamo, N.; Aizawa, H.; Muratsugu, M. *Biosens. Bioelectron.* **2007**, *22*, 2598–2603.

(53) Jackson, D. R.; Omanovic, S.; Roscoe, S. G. *Langmuir* **2000**, *16*, 5449–5457.

(54) Luo, Q.; Andrade, J. D. *J. Colloid Interface Sci.* **1998**, *200*, 104–113.

(55) Janzen, R.; Unger, K. K. *J. Chromatogr.* **1990**, *522*, 77–93.

(56) Gill, D. S.; Roush, D. J.; Willson, R. C. *J. Colloid Interface Sci.* **1994**, *167*, 1–7.

(57) Jennissen, H. P. *Biochemistry* **1976**, *15*, 5683.

(58) Kawasaki, T. *J. Chromatogr.* **1978**, *151*, 95–112.

(59) Kawasaki, T. *J. Chromatogr.* **1978**, *157*, 7–42.

(60) Otzen, D. E.; Oliveberg, M.; Höök, F. *Colloids Surf. B* **2003**, *29*, 67–73.

(61) Höök, F.; Rodahl, M.; Brzezinski, P.; Kasemo, B. *Langmuir* **1998**, *14*, 729–734.

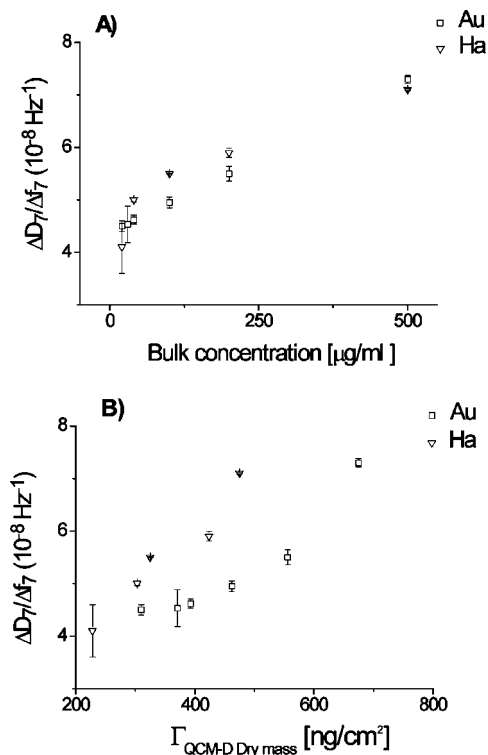


Figure 6. The dissipation shift per frequency shift $\Delta D/\Delta f$ obtained for Au and Ha at different (A) Fn bulk concentrations and (B) Fn surface mass densities.

that the water factor in this study did not depend on the substrate chemistries and protein concentrations chosen, we can directly compare the $\Delta D/\Delta f$ values obtained with QCM-D for the different experimental settings. Figure 6A displays the values of $\Delta D/\Delta f$ at different bulk concentrations for both the Ha and the Au surface. The decreasing $\Delta D/\Delta f$ value as the bulk concentration decreases corresponds well with an increasingly rigid coupling between the surface and the Fn molecules, as the incoming protein flux decreases and accordingly a stronger binding is established between the individual Fn molecules and the surface.

To further investigate the difference in the Fn adsorption on Ha and Au, the $\Delta D/\Delta f$ value was plotted against the surface mass density of the nonhydrated protein layer (Figure 6B). From Figure 6B we notice that Fn in general forms a stiffer layer on Au compared with Ha at comparable surface mass densities, which implies that the Fn proteins adsorb differently on the Ha as compared to the Au surface.

The lower $\Delta D/\Delta f$ values on Au further suggests that the protein film on Au is more compact.⁶² A similar low $\Delta D/\Delta f$ value has been reported previously⁶³ when Fn was bound in its native compact form on a negatively charged poly(propene-alt-maleic anhydride) (PPMA). The results presented in Figure 6B therefore supports the conclusions drawn from Figure 4, namely that Fn primarily adsorbs in an unfolded, and according to the literature^{11,14} perhaps even a more activated, configuration on Ha as opposed to a compact and nonactivated configuration on Au.

Antibody–Antigen Measurements. To further examine the properties of the resulting Fn protein layer on the Ha and Au surfaces, the interaction between monoclonal antibodies directed against the CB domain on Fn was monitored by QCM-D. QCM-D

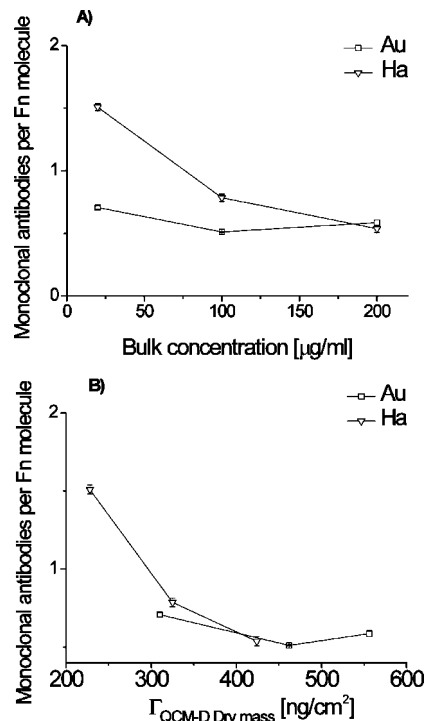


Figure 7. The number of monoclonal antibodies per Fn molecule on Ha and Au at (A) the concentrations $20 \mu\text{g/mL}$, $100 \mu\text{g/mL}$, and $200 \mu\text{g/mL}$ and (B) the corresponding Fn surface mass densities.

has proven to be a suitable setup for this task, and important information about the structural properties of proteins adsorbing on a surface has been achieved by probing them with antibodies.^{45,64–66} From the measured Δf values, an estimate of the number of antibodies that bind to each Fn molecule can be determined, under the assumption that the water content remains the same in the protein layer after antibodies bind to the protein film. The number of antibodies bound to every Fn molecule is then given as

$$\frac{N_{\text{antibody}}}{N_{\text{Fn}}} = \frac{\Delta f_{\text{antibody}}}{\Delta f_{\text{Fn}}} \frac{m_{\text{Fn}}}{m_{\text{antibody}}} \quad (6)$$

where $m_{\text{Fn}} = 450 \text{ kD}$, $m_{\text{antibody}} = 150 \text{ kD}$, and N_{antibody} and N_{Fn} is the number of antibodies and Fn molecules, respectively. The results on the interaction between antibodies and adsorbed Fn molecules from the protein bulk concentrations, $20 \mu\text{g/mL}$, $100 \mu\text{g/mL}$, and $200 \mu\text{g/mL}$, are shown in Figure 7A. From Figure 7A we observe that the number of antibodies per protein on Ha at the protein bulk concentration $200 \mu\text{g/mL}$ was 0.54 ± 0.03 which was not significantly different ($p > 0.05$) compared to the 0.59 ± 0.02 antibodies per protein obtained on Au at the same concentration. However, the number of antibodies per protein was in general larger on the Ha surfaces as compared to Au surfaces at bulk concentrations below $200 \mu\text{g/mL}$. For instance, at the protein bulk concentration $20 \mu\text{g/mL}$, 1.51 ± 0.03 antibodies bound per protein on Ha close to the maximum antibody binding capacity of a single Fn molecule (since the two subunits of Fn have a CB domain, a fully functional Fn molecule on the surface is able to bind two monoclonal antibodies), indicating that the Fn proteins are almost fully functional on the Ha substrates when

(64) Muratsugu, M.; Ohta, F.; Miya, Y.; Hosokawa, T.; Kurosawa, S.; Kamo, N.; Ikeda, H. *Anal. Chem.* **1993**, *65*, 2933–2937.

(65) Lord, M. S.; Cousins, B. G.; Doherty, P. J.; Whitelock, J. M.; Simmons, A.; Williams, R. L.; Milthorpe, B. K. *Biomaterials* **2006**, *27*, 4856–4862.

(66) Dolatshahi-Pirouz, A.; Rechendorff, K.; Hovgaard, M. B.; Foss, M.; Chevallier, J.; Besenbacher, F. *Colloids Surf., B* **2008**, *66*, 53–59.

(62) Höök, F.; Rodahl, M.; Brzezinski, P.; Kasemo, B. *J. Colloid Interface Sci.* **1998**, *208*, 63–67.

(63) Renner, L.; Pompe, T.; Salchert, K.; Werner, C. *Langmuir* **2005**, *21*, 4571–4577.

adsorbed from a low Fn bulk concentration. For comparison, the number of antibodies per Fn molecule on Au was 0.708 ± 0.014 at the protein bulk concentration $20 \mu\text{g/mL}$, far below the full binding capacity of a single Fn molecule and significantly smaller than the value obtained on Ha at the same concentration as estimated with a *t* test ($p < 0.005$).

That the cell-binding activity of Fn on Ha and Au is almost the same at concentrations above $200 \mu\text{g/mL}$ corresponds very well with the discussion in the previous sections and the conclusions drawn there, that is the Fn molecules are adsorbed in a highly unfolded Fn configuration and presumably in a more active state on Ha surfaces below the protein bulk concentration $100 \mu\text{g/mL}$,^{11,14} where on the other hand at concentrations higher than $100 \mu\text{g/mL}$, Fn adsorbed in a more compact and accordingly a less accessible configuration.

In Figure 7B the correlation between the Fn surface coverage and the number of antibodies binding per Fn molecule is depicted, and it is observed that the number of antibodies per protein depends on the Fn surface coverage prior to the injection of antibodies. On the Ha surfaces we observe a significant increase ($p < 0.005$) from 0.54 ± 0.03 to 1.51 ± 0.03 antibodies per protein from low to high Fn surface mass densities. For comparison, a smaller but still significant increase ($p < 0.05$) from 0.59 ± 0.02 to 0.708 ± 0.014 from low to high Fn surface mass densities is observed on Au. Looking more carefully at Figure 7B, we furthermore notice that almost the same number of antibodies bind per fibronectin molecule when the surface mass densities on Au and Ha are similar. Accordingly the same number of monoclonal antibodies per Fn molecule might also be found on Au if the same amount of Fn bound on Au as on Ha at low Fn bulk concentrations.

From the results in Figure 7A,B, we thus conclude that the CB domain is more accessible on Ha at a given protein bulk concentration since the saturated Fn surface mass densities in general are lower on Ha as compared to Au.

One important question that still remains to be addressed in relation to the results in Figure 7A,B is whether the assumption that the water content remains the same in the protein layer after antibodies bind to the protein film is correct. To investigate this, we carried out a series of antibody–antigen experiments with the ellipsometry technique on both Ha and Au at the protein bulk concentration $20 \mu\text{g/mL}$ (see Table. 1). By ellipsometry we obtained 1.25 ± 0.25 antibodies per protein on Ha which is not significantly different ($p > 0.05$) from the results obtained with QCM-D. On Au we found almost the same number of antibodies per protein at 0.70 ± 0.10 compared with the QCM-D results; moreover, as determined with a *t* test we did not observe any significant differences ($p > 0.05$) in the number of antibodies per protein on Au with the two techniques.

A coverage-dependent Fn activity similar to that observed in Figure 7A,B has also been reported previously. For instance, in previous work^{15,16} the number of adhering leukemia cells (L1210) onto a preadsorbed Fn layer on hydrophilic sulfonated and hydrophobic nonsulfonated substrates was quantified by applying a photographic method to count the number of cells. Here a higher surface activity of the individual Fn molecules was observed, when the Fn molecules were preadsorbed at lower

surface mass densities, a finding which was argued to be due to a more functional conformation of each individual Fn molecule on the hydrophilic substrate. In another study the adsorption of Fn onto positively and negatively charged polyelectrolyte layers and silica–titania was examined by quartz crystal microbalance (QCM) and optical waveguide light mode spectroscopy (OWLS),²⁰ and it was concluded that the silica–titania substrate adsorbed a lesser amount of Fn in comparison to the other substrates. A subsequent exposure of the substrates after coating them with Fn to human umbilical vein endothelial cells (HUVEC) showed a more intensified cell spreading on the Fn-coated silica–titania substrate. These reports suggest that even though the Fn surface mass uptake is lowest on hydrophilic surfaces corresponding to a more unfolded Fn configuration, Fn adsorb in a more active state on these hydrophilic surfaces. Since both the Ha and the Au surfaces used in this work were hydrophilic, another mechanism besides the hydrophilic nature of Ha must be responsible for the more activated Fn configuration on Ha for a given Fn concentration.

Taking into consideration that Ha is a heterogeneous charged surface with positive calcium sites and negative phosphate sites,^{58,59} one may argue that these oppositely charged sites interrupt the electrostatic interactions that stabilize the native and compact structure of Fn in solution. A similar scenario has previously been proposed^{14,63} to explain a surface-guided transition of Fn to a highly unfolded state on charged silica and PMMA-coated substrates.

Combining the results shown in Figure 7 with the discussions in the previous paragraphs and in other reports, we tentatively propose a scenario where the heterogeneous charge present on Ha interrupts the native configuration of Fn, and subsequently a surface-activated unfolding of Fn occurs where the hidden CB domain becomes more exposed to the surrounding environment as compared to the situation on the Au reference surface.

Conclusion

The adsorption of fibronectin (Fn) and its cell-binding activity has been investigated at different concentrations on Ha and Au-coated surfaces. The saturated surface coverage of Fn was found to closely resemble a full monolayer consisting of individual Fn molecules in a highly unfolded configuration on Ha at concentrations below $100 \mu\text{g/mL}$. On Au, however, the Fn surface mass uptake showed a smaller footprint per protein, indicating that it remains primarily in a compact configuration. This conclusion corresponds well with the dissipation vs frequency shift values obtained by the QCM-D technique, where it was found that in general a more compact Fn layer is formed on Au. From probing the cell-binding (CB) domain on Fn with monoclonal antibodies it was additionally observed that the CB domain was more accessible on Ha at a given protein bulk concentration.

Acknowledgment. We gratefully acknowledge the financial support from the Danish Research Councils to the Centre for NeuroEngineering (CNE) and from the Interdisciplinary Nanoscience Center (iNANO).

LA803142U

Interaction of human mesenchymal stem cells with osteopontin coated hydroxyapatite surfaces

Thomas H. L. Jensen^{1,2}, Alireza Dolatshahi-Pirouz¹, Morten Foss¹, Jørgen Baas², Jette Lovmand^{1,3}, Mogens Duch^{1,3}, Finn Skou Pedersen^{1,3}, Moustapha Kassem⁴, Cody Bünger², Kjeld Søballe², Flemming Besenbacher^{1,5}

¹Interdisciplinary Nanoscience Center (iNANO), Aarhus University, 8000 Aarhus C, Denmark

²Orthopaedic Research Laboratory, University Hospital of Aarhus, 8000 Aarhus C, Denmark

³Department of Molecular Biology, Aarhus University, 8000 Aarhus C, Denmark

⁴Department of Endocrinology and Metabolism, University Hospital of Odense, 5000 Odense C, Denmark

⁵Department of Physics and Astronomy, Aarhus University, 8000 Aarhus C, Denmark

Abstract

In vitro studies of the initial attachment, spreading and motility of human bone mesenchymal stem cells have been carried out on bovine osteopontin (OPN) coated hydroxyapatite (HA) and gold (Au) model surfaces. The adsorption of OPN extracted from bovine milk was monitored by the quartz crystal microbalance with dissipation (QCM-D) and the ellipsometry techniques, and the OPN coated surfaces were further investigated by antigen-antibody interaction. It is shown that the OPN surface mass density is significantly lower and that the number of antibodies binding to the resulting OPN layers is significantly higher on the HA as compared to the Au surfaces. The initial attachment, spreading and motility of human bone mesenchymal stem cells show a larger cell area, a faster arrangement of vinculin in the basal cell membrane and more motile cells on the OPN coated HA surfaces as compared to the OPN coated Au surfaces and to the uncoated Au and HA surfaces. These *in vitro* results indicate that there may be great potential for OPN coated biomaterials, for instance as functional protein coatings or drug delivery systems on orthopaedic implants or scaffolds for tissue-engineering.

1. Introduction

When designing new artificial biomaterials for application in the fields of bone tissue-engineering and orthopaedic implantology, it is mandatory to ensure a high degree of osteoconductivity and/or osteoinductivity. Hydroxyapatite (HA) $[\text{Ca}_{10}(\text{PO}_4)_6(\text{OH})_2]$, which is the most abundant inorganic mineral compound in skeletal tissue of vertebrates, is widely acknowledged in orthopaedic surgery, since the tissue response evoked by HA coated implants

and HA containing grafts displays a low degree of inflammation, low level of intervening fibrous tissue and good ingrowth of bone [1, 2]. Therefore HA coating of implants is generally considered “the golden standard” in orthopaedics.

The biological response of any biomaterial is related to how cells interact with the surface, which in turn is influenced by the adsorbed biomolecules at the surface [3]. A group of genetically linked bone proteins with similar structure and function, called small integrin binding ligand N-glycosylated proteins (SIBLINGs), are considered important in the generation and remodelling of skeletal tissue [4] and have in the past attracted considerable interest as biomolecular components in functional coatings that aim to improve the performance of orthopaedic materials for guided tissue engineering [5-8].

Osteopontin (OPN) is a SIBLING protein, which was recognized in bovine bone already in 1985 by Franzén *et al* [9] and later in human bone in 1988 [10]. The OPN protein consists of approximately 300 amino acids with small variations in the length of the amino-acid polypeptide chain depending on the species in question. The native structure of OPN closely resembles a random coil with a flexible peptide backbone [11] and contains the following domains, all of which are considered highly conserved among different species [11, 12]: i) A HA-binding polyaspartic acid sequence, ii) an integrin binding RGD sequence, iii) a cryptic integrin binding sequence (Human: SVVYGLR, Bovine: SVAYGLK), iv) a thrombin cleavage site, v) a CD44 binding domain, and vi) several glycosylation and phosphorylation sites that are present in a random fashion throughout the entire protein play an important part in the functional state of OPN [12, 13]. Bovine OPN consists of 266 amino acid residues and removal of the C-terminal fragment of thrombin-cleaved OPN has been reported to enhance the interaction between OPN and cells [14].

Numerous *in vitro* cell assays on different synthetic materials coated with OPN have been studied in the past with the purpose to explore whether OPN may influence the functionality of biomaterial surfaces [5, 6, 15-17]. For instance, it is found that OPN on hydrophilic polystyrene surfaces enhance the adhesion and spreading area of MG63 cells [15] and that the amine end-groups enhance the OPN mediated adhesion and spreading area of bovine endothelial cells as compared to carboxylic, hydroxylic and methylic functionalized surfaces [8]. It is reported that OPN attached to a 2-D interfacial collagen layer enhances the cell adhesion of the mouse pre-osteoblastic MC3T3-E1 cell line [16], whereas on HA no such influence was seen [5]. It was shown that OPN covalently immobilized on poly(hydroxyethyl methacrylic acid) (poly(HEMA)) increase the adhesion of bovine endothelial cells as compared to pure poly(HEMA) [17]. Previous studies [5, 6, 15-17] thus indicate that OPN may act as a functional coating on orthopaedic implants, e.g. for joint prostheses to improve remodelling of bone tissue around biomedical implants.

Naturally occurring OPN is present at the surfaces of the non-organic phase of mineralized tissues [18], and several *in vivo* studies have examined the influence of OPN in the formation and remodelling of mineralized tissue. Changes in hardness and relative mass of mineralized tissue have been reported as well as the speed of bone remodelling and vascularisation in OPN-knockout mice [19-22]. OPN coated coralline porous HA granulae was used in a rabbit cranial bone substitute model [6], where a positive effect of OPN on bony ingrowth from the periphery of the surgically produced defect in the rabbit crania was observed, whereas no effect in bony growth on the granulae was found. Besides a reported bone regenerative effect OPN is also found to have an inhibiting effect on the adversative foreign body reaction to implants [7, 23].

Despite the positive response of OPN on bone tissue remodelling, a crucial challenge for a more extended use of OPN in connection with functionalizations of implants or as drug delivery systems, is the costly purification process of OPN in most previous studies. Since bovine milk is an inexpensive and a readily available source of osteopontin, it is of interest to evaluate the potential usage of bovine OPN in connection with orthopaedic biomaterials.

The main goal of this project is therefore to study the influence of human bone mesenchymal stem cell adsorption on OPN coated HA surfaces. The adsorption of OPN extracted from bovine milk on HA surfaces was studied using the ellipsometry and quartz crystal microbalance with dissipation (QCM-D) techniques, and the results are complimented by antigen-antibody measurements. The surface mass density and the structural properties of the resulting protein layers were quantified and the effect of the resulting OPN coating was examined by investigating the initial motility, spreading area, morphology and vinculin distribution of human bone marrow mesenchymal stem cells interacting with HA and Au preadsorbed with OPN or standard cell medium.

2. Materials and Methods

2.1. Surfaces and characterization

Quartz crystal microbalance sensor surfaces coated with either a 10 nm thick HA layer (QSX-327) or with 10 nm thick Au thin film (QSX-301) were purchased from Q-Sense AB, Sweden. The sensor crystals (diameter 14 mm) were used as substrates in all experiments throughout the study. A Nanoscope IIIA Multimode SPM Atomic Force Microscope from Veeco

instruments, Santa Barbara, CA, was used to characterize the surface topography at the nanometer resolution at ambient conditions. The applied silicon cantilevers (NSG01, NT-MDT, Russia) had a resonance frequency around 150 kHz, a spring constant of 5.5 N/m and a tip curvature radius below 10 nm. The root mean square (RMS) roughness was determined to be 2.2 +/- 0.2 nm and 0.9 +/- 0.2 nm for the HA and Au surfaces, respectively, as quantified by SPIP software (Image Metrology, Copenhagen, Denmark) in accordance with the model employed in a previous study [24]. The HA coatings were furthermore examined with grazing incidence X-ray diffraction, and several peaks which belong to the crystalline phase of HA were observed alongside with the prominent Au peaks from the supporting Au layer below the HA coating. This showed that the HA coating was partly crystalline (data not shown). Water contact angle measurements were carried out with the sessile drop method using a DSA100 (Krüss, Hamburg, Germany) after the respective samples were ozone cleaned for 25-30 minutes (Bioforce Nanosciences UVO cleaner). Both the HA and Au surfaces were found to be hydrophilic with water contact angles less than 10°. To test the stability of the HA coating in liquid a dissolution test of the HA coated crystals was conducted by the QCM-D technique by injecting a 10 mM Tris buffer with 1 mM CaCl₂ and 100 mM NaCl adjusted with HCl and NaOH to pH = 7.4 at 37° in the QCM-D chambers and examining the QCM-D response over a time span of 30 hours. No QCM-D frequency shift was observed indicating that during this time span the HA substrates are stable/crystalline and suitable for protein adsorption and cell experiments. All surfaces were ozone cleaned for organic contaminants by means of the Bioforce Nanosciences UVO cleaner for 25-30 minutes immediately prior to use.

2.2. *OPN and Antibodies*

Osteopontin (OPN) was purified [25] by Arla Foods a/s, Denmark. The standard grade OPN used contains both full length OPN (35 kDa) and an N-terminal fragment cleaved immediately downstream of the cryptic integrin binding sequence (25 kDa). By weight the standard grade comprises 30% full length OPN and 70% cleaved OPN (unpublished results). No C-terminal fragments are present. Osteopontin extracted from bovine milk contains posttranslational modifications and is highly phosphorylated [26]. Polyclonal OPN antibodies from rabbits immunized with full length OPN purified from the standard grade OPN, were provided by Esben Skipper Sørensen, Department of Molecular Biology, Aarhus University, while goat albumin antibodies for unspecific binding were purchased at Sigma-Aldrich, Taastrup, Denmark. The proteins were dissolved in a 10 mM Tris buffer with 1 mM CaCl_2 and 100 mM NaCl adjusted with HCl and NaOH to $\text{pH} = 7.4$ at 37° . OPN was dissolved in the buffer at a concentration of 100 $\mu\text{g/ml}$ and the antibodies at 300 $\mu\text{g/ml}$. OPN solutions were kept in a freezer and thawed at room temperature prior to use. The dissolved antibodies were kept at 4°C at maximum time three months.

2.3. *The Ellipsometry studies*

Ellipsometry is a well established technique for quantification of surface mass densities of e.g. thin organic films at a solid-liquid interphase with a typical thickness resolution of 0.5 nm [27]. The method relies on the change in the polarization of elliptically polarized light reflected at the interface, and the observed change is caused by the change in ratio of electric field

amplitudes (Ψ) and the change in phase (Δ) between the p- and the s- component. The recorded signal refers to the complex reflectance ratio given by:

$$(1) \quad \rho = \frac{R_p}{R_s} = \tan(\Psi)e^{i\Delta}$$

where R_p and R_s are the reflection coefficients for the p- and s-components, respectively, as given by the Fresnel equations and ρ is the complex reflectance ratio [28]. By using a layer-by-layer combination of the Fresnel equations it is possible to derive the thickness of films[28]. The surface mass density of nonhydrated protein films, $\Gamma_{\text{Ellipsometry}}$, is subsequently calculated from the derived thickness by means of the de Feijters formula [29]:

$$(2) \quad \Gamma_{\text{Ellipsometry}} = d \frac{n_{\text{protein}} - n_{\text{buffer}}}{dn/dc}$$

where d is the thickness of the protein film, n_{protein} and n_{buffer} the refractive indices of protein layer and buffer, respectively, and dn/dc is the refractive index increment for a protein concentration change. The values used for the refractive indices are 1.465 and 1.335 for n_{protein} and n_{buffer} , respectively [30], while for dn/dc a value of 0.18 was chosen, in accordance with what is commonly reported in the literature [31, 32].

The surface mass densities were recorded with an ELX-02C (DRE GmbH, Ratzeburg, Germany) rotating analyzer ellipsometer setup with a single wavelength $\lambda=632.8$ nm He-Ne laser and a static liquid cell from DRE GmbH. A fixed angle-of-incidence of 70° was used to

detect the dynamic change in surface mass densities of OPN on the HA and Au surfaces during adsorption process at room temperature.

2.4. QCM-D

Quartz crystal microbalance with dissipation (QCM-D) is an acoustic technique suitable for direct quantification of surface mass densities and viscoelastic properties of thin films [31, 33-35]. The QCM-D technique relies on the use of a quartz crystal oscillating in shear mode. A change in mass on the crystal induce a measurable change in resonance frequency, and in case of a thin non-dissipative layer with no slip, the frequency shift, Δf , and mass change, Δm , are proportional as revealed by the simple Sauerbrey equation:

$$(3) \quad \Delta m = -\frac{C}{n} \Delta f_n$$

Here C is the mass sensitivity constant ($17.7 \text{ ng/cm}^2 \text{ Hz}^{-1}$ for a 5 MHz crystal), n (1, 3, 5...) is the overtone number, and Δf_n is the frequency shift of the n 'th overtone.

In addition to the frequency shifts, the change in energy dissipation of the n 'th overtone, ΔD_n , is also monitored, where the dissipation is defined as:

$$(4) \quad D = \frac{E_{\text{lost}}}{2\pi \cdot E_{\text{stored}}}$$

where E_{lost} is the energy dissipated during each oscillation cycle and E_{stored} is the total energy of the system. It is important to note that the QCM-D measured shifts in frequency and dissipation depend on both the dry protein mass in the protein layer, as well as water coupled to the protein layer at the solid liquid interface including hydration and trapped water in the pores of the protein film – often referred to as the “wet mass”. In the results section the water content is expressed as the water factor, which is the ratio of hydrated (QCM-D) to nonhydrated (ellipsometry) surface mass densities ($\Gamma_{\text{QCM-D}}/\Gamma_{\text{ellipsometry}}$).

All experiments were carried out under static (no flow) conditions at 22°C using a Q-Sense AB E4 system measuring at 3rd, 5th & 7th overtone. Since the seventh overtone (n=7) was found to be the most stable overtone throughout the study, it was used to calculate surface mass densities by means of eq. 3. The experiments included the adsorption of OPN on HA and Au surfaces followed by studies where OPN antibodies are bound to the adsorbed OPN-layer. Antibody binding to the OPN saturated surfaces results in a frequency shift and the additional mass is analyzed as an estimate of “epitope availability“ with equation 1 by the following equation:

$$(5) \quad \frac{N_{\text{antibody}}}{N_{\text{OPN}}} = \frac{\Delta f_{\text{antibody}}}{\Delta f_{\text{OPN}}} \frac{m_{\text{OPN}}}{m_{\text{antibody}}}$$

where N_{OPN} is the number of OPN molecules in the protein layer, N_{antibody} the number of antibodies bound to the protein layer, Δf_{OPN} and $\Delta f_{\text{antibody}}$ the respective frequency changes, and $m_{\text{OPN}} = 28$ kDa and $m_{\text{antibody}} = 150$ kDa the respective molecular weights.

2.5. Cell culture

For the cell experiments, adult human mesenchymal stem cells (hMSC) transduced with the telomerase reverse transcriptase gene (hTERT) (often named hMSC-TERT) was employed [36]. These cells exhibited 4.3 population doublings per week and the cells were used at a population doubling level (PDL) 266 at which level recent studies using the same cells have reported osteogenic potential [37, 38]. The cells were seeded at a density of 4,000 cells/cm² in 150 cm² flasks in modified essential medium (MEM) that contained 10% fetal bovine serum (FBS) (all products from Gibco, Taastrup, Denmark) and cultivated in a humidified atmosphere of 37°C and 5% CO₂. After 1 week, cells were washed in PBS (pH=7.4 at 37°C), trypsinized with 1.25% trypsin and 5 mM EDTA in PBS, seeded at 4,000 cells/cm² in 150 cm² flasks and cultivated for another week. Cells were trypsinized and used (PDL 274) for the experiments at a concentration of 40,000 cells/ml. The substrate seeding density in the cell studies was fixed at approximately 5,200 cells/cm². The effective cell density was most likely smaller since the cells were applied locally above the substrates, which were placed in a larger container (See 2.6 & 2.7).

2.6. Fixation/fluorescence staining

OPN was preadsorbed on the HA and Au surfaces by immersing the samples in TRIS with 100 µg/ml OPN and in control experiments, pure TRIS for 150 minutes at room temperature. Four different surfaces were prepared: OPN coated gold (Au+OPN), non-coated gold (Au-OPN), OPN coated hydroxyapatite (HA+OPN), and non-coated hydroxyapatite (HA-

OPN). After immersion in Tris buffer +/- OPN all the surfaces were immersed in 5 ml MEM/FBS at 37°C for 15 minutes, after which the surfaces were used immediately for the cell studies. 6-well culture plates precoated with agarosis gel (1% in MilliQ water, Sigma-Aldrich, Brøndby, DK) were filled with 5 ml MEM/FBS at 37 °C and afterwards one surface was transferred directly to each culture well. 200 µl cell suspension (8,000 cells) was seeded immediately beneath the air/liquid interphase by a pipette above the location of the surface. The culture plates were incubated in a humidified atmosphere of 37°C and 5% CO₂. At times 1h, 3h, 6h and 24h the surfaces were removed from culture plates, rinsed shortly in 37°C PBS and fixated with Lillies 10% neutral PBS buffered formalin (Gibco, Taastrup, Denmark).

An actin cytoskeleton and focal adhesion staining kit (Chemicon International, USA) was used to fluorescently stain the cells. Staining of actin was done with tetramethyl rhodamine isothiocyanate (TRITC) conjugated phalloidin to analyse cell morphology and cell nucleus with 4,6-diamidino-2-phenylindole (DAPI), while vinculin was stained with mouse monoclonal anti vinculin and fluorescein isothiocyanate (FITC) conjugated goat anti-mouse IgG to analyse the distribution of vinculin in the basal membrane. Details can be found in ref.....

Throughout the staining procedure phosphate buffered saline (PBS) was used as buffer. The surfaces were washed twice, permeabilized with 0.1% Triton X-100 and washed twice. 1% bovine serum albumin (lyophilized powder >98%, Sigma-Aldrich, Brøndby, DK) was used for blocking in 30 minutes at room temperature followed by washing twice. 1.25 µg/ml mouse monoclonal anti vinculin was added for 60 minutes at 37°C followed by washing three times. 10 µg/ml FITC conjugated goat anti mouse IgG and 37.5 ng/ml TRITC conjugated phalloidin in the same solution were added for 60 minutes at room temperature. Surfaces were washed three

times, 0.1 $\mu\text{g/ml}$ DAPI added for 5 minutes at room temperature and finally rinsed three times. Stained cells were kept in PBS at 4°C until the surfaces were investigated by optical microscopy.

Optical microscopy was performed with a Leica DM 6000B microscope, where 20 - 25 images at $\times 400$ magnification were acquired at random on each surface. Area and circularity of isolated cells were analyzed with the grain analysis tool provided with the ImageJ software [39]. Circularity is defined in the software as $4\pi(\text{area}/\text{perimeter}^2)$, so a circularity of 1.0 indicates a perfect circle and as the value approaches 0 indicates an increasingly elongated shape. Distribution of vinculin assemblies near the basal cell membrane was estimated and categorized by eye. The experiment was performed once with single surfaces and once with triplets. Data from all surfaces was included.

2.7. DIC cell surveillance

Differential interference contrast (DIC) microscopy is a suitable technique for time lapse observations of live and incubated cells. The technique was employed to analyse the cell motility during the first 8 hours after cell seeding.

Surfaces were OPN precoated in the same way as described earlier in Section 2.6. Four surfaces: HA+OPN, HA-OPN, Au+OPN and Au-OPN were placed in one single Petri dish precoated with agarosis gel (1% in double distilled sterile water). 200 μl cell suspensions (8,000 cells) were slowly seeded by a pipette immediately beneath the air/liquid interphase above each surface. The Petri dish was placed on an automated sample holder in an incubator at 37°C and 5% CO_2 mounted on a Leica DM 6000B microscope. The microscope was run in differential interference contrast (DIC) mode [40] at $\times 200$ magnification and programmed to obtain an

image every 4th minute at four predefined sites on each of the four surfaces. The seeded surfaces were analyzed in the period one to seven hours after seeding and cells lying isolated on the surfaces were selected for motility analysis. 28 minute intervals were used for calculation of motility. Cell position every 28th minute was determined as center of mass with the grain analysis tool provided with the basic ImageJ software [39] and the linear interval between positions was considered the distance migrated by the cell. Inaccuracies in the automated sample holder and surface movements were identified with a fixed surface spot and the position corrected accordingly before the migration distance was calculated. The motility experiment was performed once.

2.8. Data analysis

All data was analyzed parametrically and Students t-test was used to estimate significance of difference. A two-sided p-value less than 0.05 was considered significant. Unless otherwise stated data is presented as mean +/- standard error of mean (sem) along with sample size. Statistical analysis was performed with Stata v9.0 software, Statacorp, USA.

3. Results

3.1. Protein adsorption

In figure 1 the QCM-D results are shown for the n = 3, 5 & 7 overtones. After the injection of the OPN-containing buffer an immediate fast drop in frequency and increase in

dissipation is observed. Only very small frequency shifts and dissipation changes were observed 1-2 hours after the OPN injection and data was read after 2h. The second frequency decrease observed after 300 min is due to the injection of polyclonal antibodies, which interact with the OPN layer.

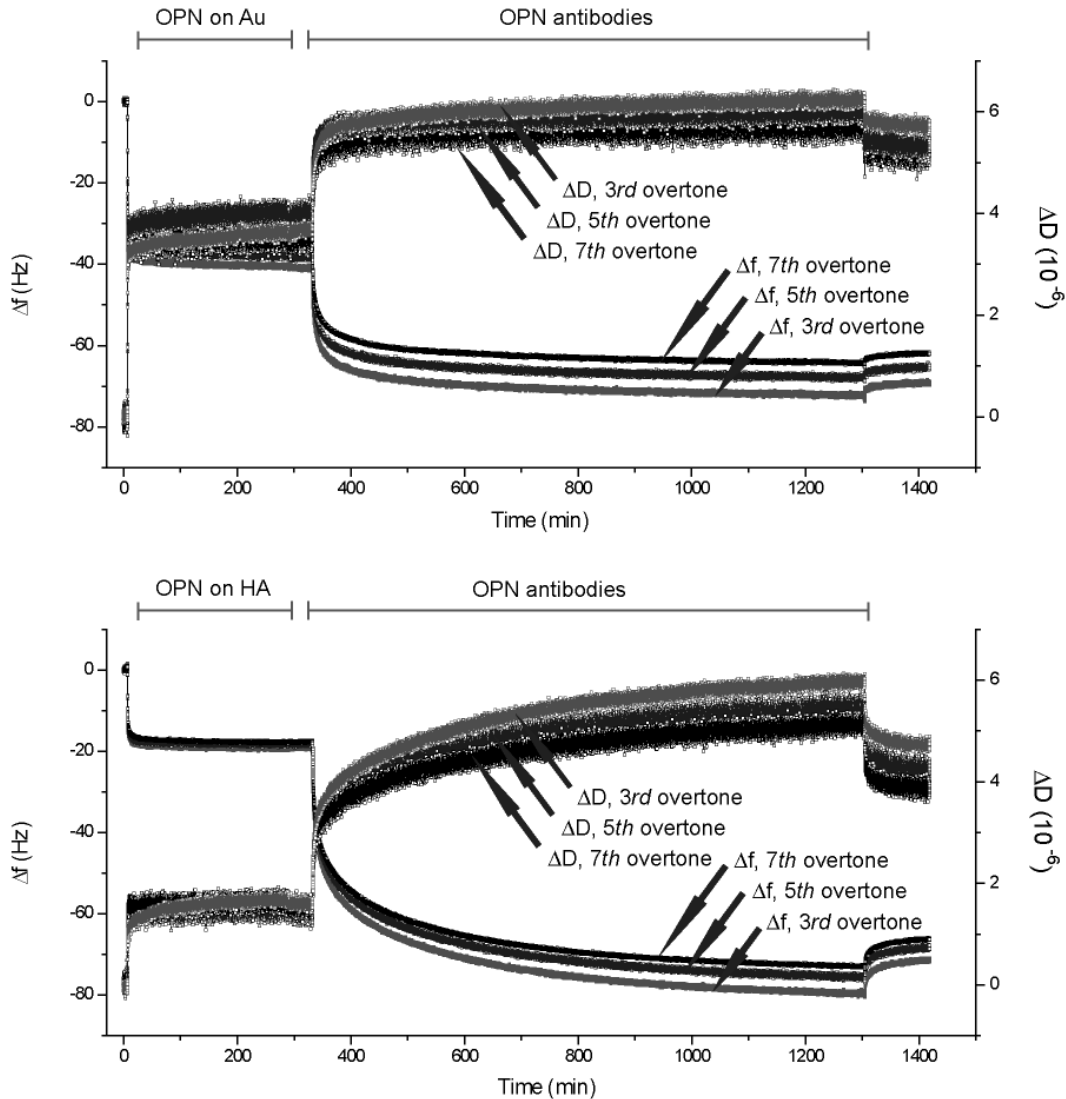


Figure 1. Typical adsorption curves on HA and Au of OPN and subsequent anti OPN binding obtained from QCM-D. On HA saturation is seen at approximately half the frequency change as compared to Au and binding of antibodies to OPN on HA results in a relatively larger frequency change.

From Fig.1 it is clearly seen that the OPN adsorption induced frequency shifts belonging to the different overtones nearly superimpose, when scaled by their respective overtone numbers: The relative difference in frequency shifts between third and seventh overtone on HA and Au was approximately 8% and 15%, respectively. Therefore the Sauerbrey equation is a valid approximation for estimating the OPN surface mass densities. In table 1, the hydrated surface mass densities of OPN layers measured by QCM-D and calculated with eq. 3, $\Gamma_{\text{QCM-D}}$, are listed, and it is shown that the hydrated OPN surface mass density for the HA surface is observed to be approximately 45% of that detected on Au.

Protein properties/ Materials	$\Gamma_{\text{QCM-D}}$ (ng/cm ²)	$\Gamma_{\text{Ellipsometry}}$ (ng/cm ²)	Water factor $\Gamma_{\text{qcm-D}}/\Gamma_{\text{Ellipsometry}}$	Endpoint $\Delta D_7/\Delta f_7$ (10 ⁻⁸ Hz ⁻¹)	Antibody per OPN
Hydroxyapatite	288 ± 11 (n=7)	95 ± 17 (n=4)	3.0 ± 0.5	-0.078 ± 0.003 (n=7)	0.57 ± 0.02 (n=3)
Gold	637 ± 7 (n=9)	240 ± 9 (n=3)	2.65 ± 0.10	-0.0975 ± 0.0010 (n=9)	0.141 ± 0.004 (n=3)

Table 1. Protein characteristics as observed with ellipsometry and Quartz crystal microbalance with dissipation. $\Gamma_{\text{Ellipsometry}}$ is the nonhydrated surface mass density as measured with ellipsometry. $\Gamma_{\text{QCM-D, 7th overtone}}$ the hydrated surface mass density as measured with QCM-D using the Sauerbrey equation with seventh overtone. The water factor is calculated from $\Gamma_{\text{Ellipsometry}}$ and $\Gamma_{\text{QCM-D, 7th overtone}}$. Endpoint $\Delta D_7/\Delta f_7$ is the average dissipation introduced by a single decrement in frequency change as measured with QCM-D. Antibody per OPN is the estimated amount of OPN antibodies on each OPN molecule as measured with QCM-D.

As seen in table 1 the same trend is observed with ellipsometry: A significantly higher surface mass density of a non-hydrated OPN film adsorbed to the Au as compared to the HA surface. The water contents of the protein films formed on HA and Au obtained from the ratio of hydrated to the nonhydrated surface mass densities ($\Gamma_{\text{QCM-D}}/\Gamma_{\text{ellipsometry}}$) are depicted in table 1. It is seen that the water factor is slightly higher on the HA (3.0 ± 0.5) coated substrates as compared to the Au (2.65 ± 0.10) surface.

3.2. Dissipation and antibody binding

The QCM-D technique also provides information on the dissipation in the resulting protein layer from the detected change in dissipation values per frequency shift ($\Delta D/\Delta f$) [31, 34]. A small but significant difference in the $\Delta D/\Delta f$ value was observed with -0.078 ± 0.003 and -0.0975 ± 0.0010 on the HA and Au surfaces, respectively (Table 1). This indicates that a stiffer protein layer is formed on the HA surface as compared to the Au surface.

The binding of polyclonal OPN antibodies to the OPN saturated surfaces results in an additional frequency change (see fig.1) and the additional detected mass was analyzed as an estimate of “epitope availability“ with equation 5. The results are listed in table 1 and on average 935 ng/cm^2 and 471 ng/cm^2 of antibodies are attached to OPN layers on HA and Au, respectively. This is approximately four times as many antibodies bound per OPN molecule on the HA as compared to the Au surface. Test for unspecific antibody binding to the surfaces showed an unspecific binding of less than 8 % of the specific antibody binding values observed on both the HA and the Au surfaces (data not shown).

3.3. Cell Area, Morphology and Vinculin Distribution

Over time a steady increase in area is evident on all surfaces apart from HA+OPN where a small decrease is observed between 6h and 24h (Fig. 2). At times 1, 3, and 6h the cell area on HA+OPN is approximately 100 % larger than the cell area on the remaining groups and at all times a p-value below 0.01 was observed between the area measured on the HA+OPN surfaces compared to the other reference surfaces (HA-OPN, Au+OPN & Au-OPN).

From the results depicted in table 2 it is seen that the cells initially exhibit a circular morphology when attached to the surfaces, after which the circularity decrease as a function of time on all surfaces. This indicates that the cells elongate after attachment to the respective surfaces. At 1, 3 and 24 h cells on the respective surfaces follow each other closely. After 6h HA+OPN clearly shows a lower circularity as compared to the remaining surfaces, which indicate a more rapid elongation of cells on this surface.

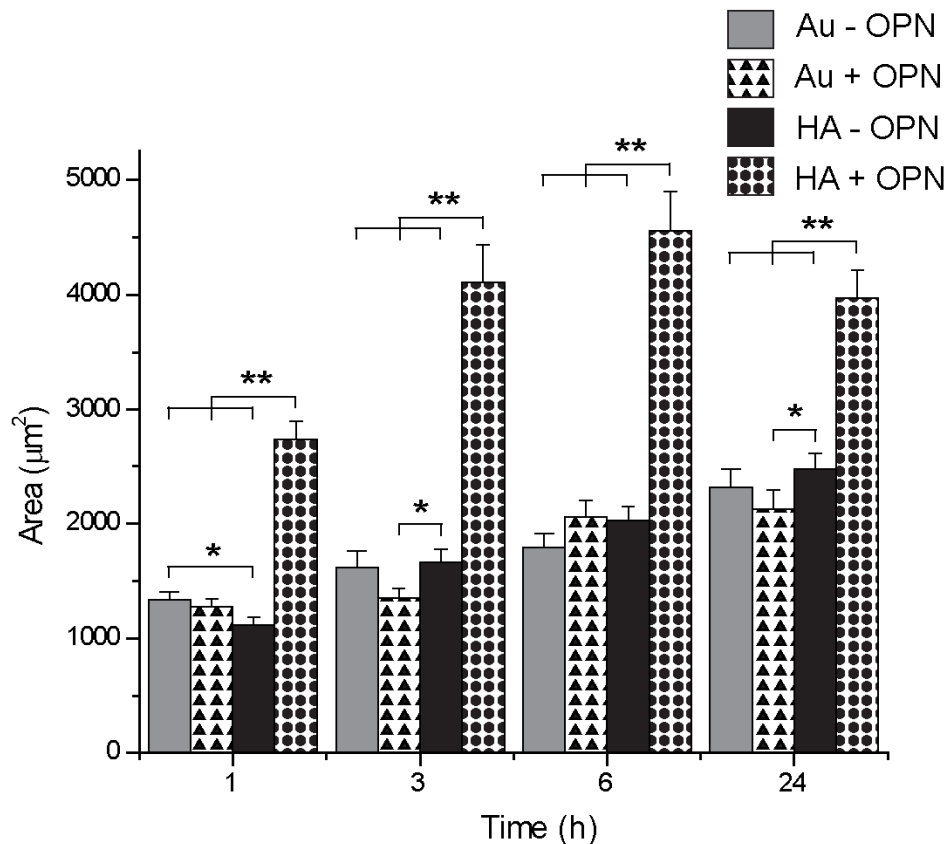


Figure 2. Area at times 1, 3, 6, and 24h. Sample size ranges from 141 to 211 cells. *Denotes $p < 0.05$ and **denotes $p < 0.01$ for indicated samples.

Vinculin assembly into detectable focal adhesion spots was observed on all surfaces at times from 3h and forward, and the vinculin assemblies were either distributed throughout the cell or mainly localized in a corona shaped band around the nucleus (Fig.3). The percentage of

cells on the respective surfaces dominated by corona distribution was estimated by eye observation of each cell and listed in table 2 with 20% interval designations. Corona distribution was most abundant at 3h, decreasing within 6h and completely absent on all surfaces 24h after seeding. At 3h Au-OPN and HA-OPN displayed the highest rate of cells with corona distribution, whereas Au+OPN displayed a lower rate (app. 50%), and HA+OPN the lowest rate. Intermediaries between corona and random distribution were observed. Furthermore, an overall tendency towards development from small round to larger fibrillar focal adhesion spots is observed during the observation time.

Cell characteristics	1h	3h	6h	24h
Au-OPN				
Circularity	0.670 ± 0.010	0.511 ± 0.014	0.414 ± 0.009	0.336 ± 0.011
Corona Distribution	N.A.	+++++	++	-
Au+OPN				
Circularity	0.672 ± 0.012	0.583 ± 0.012	0.445 ± 0.010	0.362 ± 0.011
Corona Distribution	N.A.	+++	+	-
HA-OPN				
Circularity	0.710 ± 0.007	0.583 ± 0.013	0.512 ± 0.012	0.269 ± 0.009
Corona Distribution	N.A.	++++	++	-
HA+OPN				
Circularity	0.679 ± 0.010	0.513 ± 0.014	0.293 ± 0.012	0.301 ± 0.009
Corona Distribution	N.A.	+	-	-

Table 2. Circularity of cells and presence of corona band distribution of vinculin. Corona band distribution is listed with approximate 20% interval designations. (+++++) = 80-100%, (+++++) = 60-80%, (++++) = 40-60%, (++) = 20-40%, (+) = 0-20% and (-) = none. Distinction between corona and non-corona was estimated by eye. Sample size ranges from 126 to 209.

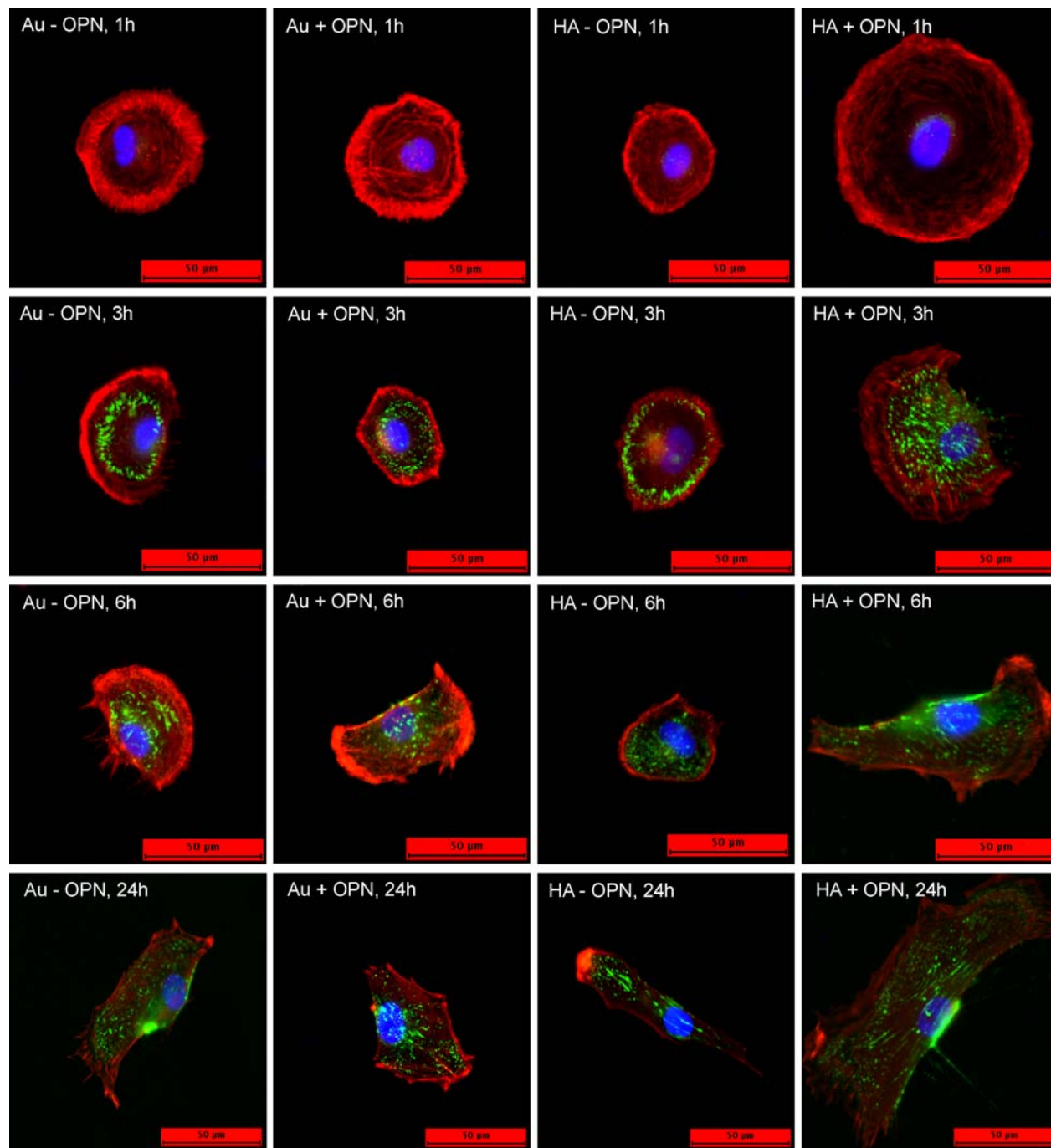


Figure 3. Representative fluorescence staining pictures. Actin (red), vinculin (green) and nucleus (blue) is stained. At each time point on the four surfaces a single cell was selected as representative regarding the vinculin distribution.

3.4. Cell Motility

Most cells moved in a single direction during the observation time and no change of direction in the remaining cells took place without at least an hour of standstill. Figure 4 displays the average migration velocity of cells in 28 minute intervals and figure 5 the cumulated movement of cells during the observation period. The migration velocity at every 28 minute time interval, as seen in figure 4, was significantly higher on the cells attached to HA+OPN surfaces resulting in a significant difference in cumulated movement, figure 5. The velocity on HA+OPN was initially 6 – 8 $\mu\text{m}/\text{h}$ and decreased to 4 – 5 $\mu\text{m}/\text{h}$ towards the end of observation. No significant differences were observed among the other surfaces.

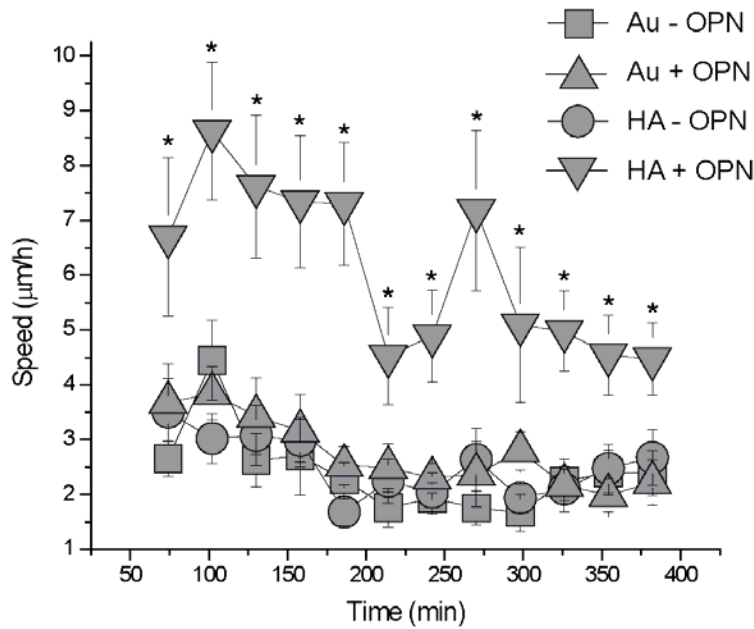


Figure 4. Average cell speeds in 28 minute intervals. Cells on HA+OPN moved at a significantly higher velocity at all intervals. Sample sizes ranging from 28 – 30 cells. *Denotes $p < 0.05$ for indicated samples.

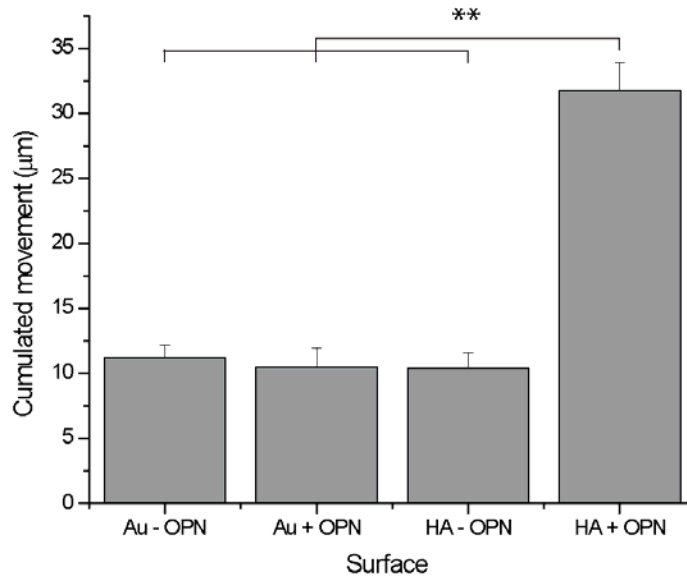


Figure 5. Cumulated cell migration in period 1 – 7 h following cell seeding. Sample sizes ranging from 28 – 30 cells. **Denotes $p < 0.01$ for indicated samples.

4. Discussion

4.1. Protein adsorption characteristics

OPN adsorption on HA and Au was characterized with the ellipsometry and QCM-D techniques and as seen from the results in Table 1, a significantly lower OPN surface mass density is observed on the HA surfaces as compared to Au surfaces. This difference in OPN surface mass uptake can be ascribed to a larger average protein contact area on HA as compared to Au.

Additional information about the dissipative properties of the resulting OPN-layer was obtained from the recorded QCM-D $\Delta D/\Delta f$ results. From table 1 it is seen that the $\Delta D/\Delta f$ value is slightly lower on the HA as compared to the Au surface, which indicates that the protein film

formed on the HA surface is stiffer and more rigid with proteins that establish a large contact area with the interface [31, 34].

The contact area of proteins typically increase as protein unfolding occur on a surface, which in turn might be reflected in a change of available epitopes on the protein due to both a different protein configuration/orientation on the surface and a changed degree of steric hindrance between the adsorbing antibodies and proteins attached to the surface. Several studies have shown that antibodies can be applied in combination with QCM-D studies as a binding probe to estimate the epitope availability [33, 35, 41]. By complimenting the QCM-D measurements with polyclonal antibody-antigen recognition, it was observed that the amount of antibodies binding to each OPN molecule on the Au surfaces was app. 25% as compared to the amount bound to the HA surfaces. Since the amount of unspecific binding was much smaller than the difference in the number of antibodies per protein found on Au and HA, the issue of a different amount of unspecific binding to the protein films on Au and HA was not taken into consideration. The observation of more antibodies binding to OPN on HA is in agreement with the OPN molecules binding in a configuration/orientation with higher epitope availability on HA as compared to Au. The protein studies suggest that OPN binds to the HA surface in a more active state with more available cell active domains as compared to the Au surface.

4.2. Initial cell interactions

The cell area, cell morphology (circularity), vinculin distribution and cell motility of human mesenchymal stem cells was studied dynamically on the HA and Au surfaces with and without the OPN precoating. On the HA surfaces it was observed that the presence of an OPN

adsorbed layer influenced both the cell area and changes in the cell morphology over time (drop in cell circularity), while the OPN coating on Au only had a minor impact on these cell surface interactions.

From the vinculin immunostaining images it was noticed that the vinculin distribution in the cells was affected by OPN which was in accordance with the cell area and morphology results. The distribution of vinculin observed on HA+OPN at 3, 6 and 24h after the cell seeding depicted in figure 3 is in agreement with expected characteristics of cells undergoing active change in morphology and migration: A low density of vinculin spots near the protruding edge, fibrillar assemblies in the center and larger diffuse assemblies at the rear end of the cells [42-45]. Moreover, a rather interesting corona distribution of vinculin assemblies dominates the remaining surfaces (HA-OPN, Au+OPN and Au-OPN) at 3h. The corona distribution is compatible with cells at an early stage of cell/surface interaction. Corona distribution of surface contact associated proteins in newly attached cells has been reported previously, but was present only shortly after attachment [46, 47]. Time-lapsed studies of the corona distribution presence in response to the substrate may have the potential to be a sensitive marker of early cell/substrate interactions. After 24 h a random distribution of mostly fibrillar like vinculin assemblies were observed on all surfaces, which is characteristic for more mature cell surface contacts [48].

Cell motility was analyzed as velocity in 28 minute intervals of single cells to provide a time-lapsed motility overview that is unbiased by change of direction. As expected from the results of the vinculin immunostaining, the cell motility was found to be promoted significantly by the presence of OPN on HA. Several bone related cells have been reported to be induced in migration by OPN: mesenchymal stem cells [49], osteoblasts [50] and osteoclasts [51].

The RGD-sequence is a well known integrin binding motif, which controls cell spreading [46, 52-54], motility [55] and focal adhesion spot assembly on the surface [52]. Several studies have shown that the RGD mediated cellular responses on interfaces mainly depend on the amount of available RGD sequences on the surface [46, 52-55]. For instance Maheshwari et al found cell motility of murine fibroblast cells to be controllable with different densities and clustering of RGD-peptides - higher RGD density generally promoted motility [55]. The OPN induced motility may not solely be connected with the RGD-sequence, since the CD44 ligand, which is also displayed by the OPN molecule, has also been shown to induce motility [49, 51, 56].

The impact on cell area, shape, vinculin distribution and motility further supports the assumption that a specific configuration/orientation of OPN bound to HA exists and it favours the availability of the OPN cell binding domains to the surrounding environment. This is in line with the protein results discussed previously, which showed that the individual OPN molecules are in general more exposed on the HA surface as compared to the Au surface.

5. Conclusion

We have studied the adsorption of osteopontin (OPN) on hydroxyapatite and gold and in particular the influence of the resulting OPN protein layer on the adsorption of human mesenchymal stem cells. It is found that the individual OPN molecules adsorb to hydroxyapatite coated surfaces with a larger contact area leading to a more rigid state with more cell-guiding domains exposed as compared to the reference Au surface. Furthermore, the OPN-layer attached to the hydroxyapatite surface catalyses a larger and faster cell spreading as well as higher cell

motility. From the present model studies it thus appear that osteopontin derived from bovine milk is indeed a new interesting bioactive molecule, for example for the functionalization of biomaterials, due to low cost and high availability. To further explore the full potential of OPN and the long term influence on cell activity in connection with new and novel biomaterials the present *in vitro* studies must be extended by *in vivo* animal studies to assay the *in vivo* response of OPN coated surfaces.

Acknowledgement

This study was financially supported by iNANO, the ProSurf research grant from Danish National Advanced Technology Foundation, the Toyota Foundation and The Danish Council for Independent Research (FTP 2052-01-0006). We would like to thank Kristian Albertsen, Arla Foods a.m.b.a for supplying the OPN, Prof Esben Skipper Sørensen for supplying the OPN polyclonal antibodies, Jacques Chevalier, Rune Hoff Lauridsen, Anette Baatrup and Anna Bay Nielsen for technical assistance, the Danish research agencies and the Carlsberg foundation for financial support.

Appendix

Figures with essential color discrimination. Figure 3 of this article is difficult to interpret in black and white. The full color images can be found in the on-line version at doi: x

References

- [1] Shepperd JA, Apthorp H, *J Bone Joint Surg Br* 87 (2005) 1046.
- [2] Søballe K, *Acta Orthop Scand Suppl* 255 (1993) 1.
- [3] Kasemo B, *Surface Science* 500 (2002) 656.
- [4] Qin C, Baba O, Butler WT, *Crit Rev Oral Biol Med* 15 (2004) 126.
- [5] Bernardis MT, Qin C, Jiang S, *Colloids Surf B Biointerfaces* 64 (2008) 236.
- [6] Gordjestani M, Dermaut L, De Ridder L, De Waele P, De Leersnijder W, Bosman F, *Int J Oral Maxillofac Surg* 35 (2006) 1127.
- [7] Liu L, Chen G, Chao T, Ratner BD, Sage EH, Jiang S, *J Biomater Sci Polym Ed* 19 (2008) 821.
- [8] Liu L, Chen S, Giachelli CM, Ratner BD, Jiang S, *J Biomed Mater Res A* 74 (2005) 23.
- [9] Franzén A, Heinegard D, *Biochem J* 232 (1985) 715.
- [10] Fisher LW, Hawkins GR, Tuross N, Termine JD, *J Biol Chem* 262 (1987) 9702.
- [11] Fisher LW, Torchia DA, Fohr B, Young MF, Fedarko NS, *Biochem Biophys Res Commun* 280 (2001) 460.
- [12] Gericke A, Qin C, Spevak L, Fujimoto Y, Butler WT, Sorensen ES, et al., *Calcif Tissue Int* 77 (2005) 45.
- [13] Kazanecki CC, Uzwiak DJ, Denhardt DT, *J Cell Biochem* 102 (2007) 912.
- [14] Smith LL, Cheung HK, Ling LE, Chen J, Sheppard D, Pytela R, et al., *J Biol Chem* 271 (1996) 28485.
- [15] Lee YJ, Park SJ, Lee WK, Ko JS, Kim HM, *Biomaterials* 24 (2003) 1059.
- [16] Liu L, Qin C, Butler WT, Ratner BD, Jiang S, *J Biomed Mater Res A* 80 (2007) 102.

- [17] Martin SM, Ganapathy R, Kim TK, Leach-Scampavia D, Giachelli CM, Ratner BD, J Biomed Mater Res A 67 (2003) 334.
- [18] McKee MD, Nanci A, Microsc Res Tech 33 (1996) 141.
- [19] Duvall CL, Taylor WR, Weiss D, Wojtowicz AM, Guldborg RE, J Bone Miner Res 22 (2007) 286.
- [20] Ishijima M, Rittling SR, Yamashita T, Tsuji K, Kurosawa H, Nifuji A, et al., J Exp Med 193 (2001) 399.
- [21] Kavukcuoglu NB, Denhardt DT, Guzelsu N, Mann AB, J Biomed Mater Res A 83 (2007) 136.
- [22] Yoshitake H, Rittling SR, Denhardt DT, Noda M, Proc Natl Acad Sci U S A 96 (1999) 8156.
- [23] Tsai AT, Rice J, Scatena M, Liaw L, Ratner BD, Giachelli CM, Biomaterials 26 (2005) 5835.
- [24] Rechendorff K, Hovgaard MB, Chevallier J, Foss M, Besenbacher F, Applied Physics Letters 87 (2005) 073105-1.
- [25] Sørensen ES, "Process for isolation of osteopontin from milk," US Patent 7,259,243 (21 Aug 2007)
- [26] Sørensen ES, Hojrup P, Petersen TE, Protein Sci 4 (1995) 2040.
- [27] Cuypers PA, Hermens WT, Hemker HC, Anal Biochem 84 (1978) 56.
- [28] Arwin H, Thin Solid Films 377-378 (2000) 48.
- [29] De Feijter JA, Benjamins J, Veer FA, Biopolymers 17 (1978) 1759.
- [30] Vörös J, Biophys J 87 (2004) 553.

- [31] Höök F, Vörös J, Rodahl M, Kurrat R, Böni P, Ramsden J, et al., *Colloids and surfaces B: Biointerfaces* 24 (2002) 155.
- [32] Rechendorff K, Hovgaard MB, Foss M, Zhdanov VP, Besenbacher F, *Langmuir* 22 (2006) 10885.
- [33] Hemmersam AG, Foss M, Chevallier J, Besenbacher F, *Colloids Surf B Biointerfaces* 43 (2005) 208.
- [34] Höök F, Kasemo B, Nylander T, Fant C, Sott K, Elwing H, *Anal Chem* 73 (2001) 5796.
- [35] Hovgaard MB, Rechendorff K, Chevallier J, Foss M, Besenbacher F, *J Phys Chem B* 112 (2008) 8241.
- [36] Simonsen JL, Rosada C, Serakinci N, Justesen J, Stenderup K, Rattan SI, et al., *Nat Biotechnol* 20 (2002) 592.
- [37] Bjerre L, Bünger CE, Kassem M, Mygind T, *Biomaterials* 29 (2008) 2616.
- [38] Mygind T, Stiehler M, Baatrup A, Li H, Zou X, Flyvbjerg A, et al., *Biomaterials* 28 (2007) 1036.
- [39] Abramoff MD, Magelhaes PJ, Ram SJ, *Biophotonics International* 11 (2004) 36.
- [40] Farnum CE, Turgai J, Wilsman NJ, *J Orthop Res* 8 (1990) 750.
- [41] Dolatshahi-Pirouz A, Rechendorff K, Hovgaard MB, Foss M, Chevallier J, Besenbacher F, *Colloids Surf B Biointerfaces* 66 (2008) 53.
- [42] Beningo KA, Dembo M, Kaverina I, Small JV, Wang YL, *J Cell Biol* 153 (2001) 881.
- [43] Broussard JA, Webb DJ, Kaverina I, *Curr Opin Cell Biol* 20 (2008) 85.
- [44] Webb DJ, Parsons JT, Horwitz AF, *Nat Cell Biol* 4 (2002) 97.
- [45] Zaidel-Bar R, Ballestrem C, Kam Z, Geiger B, *J Cell Sci* 116 (2003) 4605.

- [46] Cavalcanti-Adam EA, Volberg T, Micoulet A, Kessler H, Geiger B, Spatz JP, *Biophys J* 92 (2007) 2964.
- [47] Volberg T, Romer L, Zamir E, Geiger B, *J Cell Sci* 114 (2001) 2279.
- [48] Bershadsky AD, Tint IS, Neyfakh AA, Jr., Vasiliev JM, *Exp Cell Res* 158 (1985) 433.
- [49] Raheja LF, Genetos DC, Yellowley CE, *Biochem Biophys Res Commun* 366 (2008) 1061.
- [50] Shin H, Zygourakis K, Farach-Carson MC, Yaszemski MJ, Mikos AG, *Biomaterials* 25 (2004) 895.
- [51] Chellaiah MA, Hruska KA, *Calcif Tissue Int* 72 (2003) 197.
- [52] Arnold M, Cavalcanti-Adam EA, Glass R, Blummel J, Eck W, Kantlehner M, et al., *Chemphyschem* 5 (2004) 383.
- [53] Houseman BT, Mrksich M, *Biomaterials* 22 (2001) 943.
- [54] Schuler M, Owen GR, Hamilton DW, de Wild M, Textor M, Brunette DM, et al., *Biomaterials* 27 (2006) 4003.
- [55] Maheshwari G, Brown G, Lauffenburger DA, Wells A, Griffith LG, *J Cell Sci* 113 (Pt 10) (2000) 1677.
- [56] Weber GF, Ashkar S, Glimcher MJ, Cantor H, *Science* 271 (1996) 509.

Hydroxyapatite nanoparticles in PDLA coatings on porous titanium implants conducts bone formation

Thomas Jensen^{1,2}, Thomas Jacobsen¹, Jørgen Baas¹, Jens V. Nygaard², Alireza Dolatshahi-Pirouz², Mads B. Hovgaard², Morten Foss², Cody Bünger¹, Flemming Besenbacher^{2,3} & Kjeld Søballe¹.

¹Orthopaedic Research Laboratory, University Hospital of Aarhus, 8000 Aarhus C, Denmark

²Interdisciplinary Nanoscience Center (iNANO), Aarhus University, 8000 Aarhus C, Denmark

³Department of Physics and Astronomy, Aarhus University, 8000 Aarhus C, Denmark

Abstract

It is well established in the field of biomaterials that hydroxyapatite may provide interesting osteoconductive properties. In this study we in an *in vivo* animal model investigated the osseointegrational effect of a 50/50 vol% composite of hydroxyapatite (HA) nanoparticles and poly-D,L-lactic acid (PDLLA) coated on model titanium bone implants. The aim has been to evaluate how the addition of HA to PDLLA may improve bone formation and initial fixation of the implant. Two titanium implants coated with the PDLLA/HA composite and pure PDLLA, respectively, were implanted bilaterally in proximal part of humeri with a 2 mm periimplant gap in ten sheep. After 12 weeks remains of coatings were present on 20.3% and 19.8% of PDLLA/HA composite and PDLLA coated implants, respectively. It was observed that newly formed bone (39.3%) and fibrous tissue (58.3%) had replaced the PDLLA/HA composite, whereas pure PDLLA was replaced almost completely by fibrous tissue (96.2%). Consequently, the PDLLA/HA composite coated implants were better fixated as confirmed by pushout-tests. Using quantification of periimplant tissue and implant fixation as parameters, the present findings therefore clearly reveal that the addition of nanoparticulate HA to a PDLLA coating on titanium implants increases osseointegration.

1. Introduction

Long term survival of orthopaedic joint replacements is an issue of both social and economical importance. Because revision of loosened joint replacements constitutes a substantial and increasing fraction of total surgeries¹, further improvement of long term survival is highly motivated. Since early stable implant fixation is a prerequisite for a favourable long term prognosis^{2,3}, one strategy currently investigated is to design new osteoconductive implants that improve the early fixation by endorsing the formation of bone tissue of high tensile strength on the implant surface.

Recently, a new approach for providing osteoconductivity to implant surfaces has been introduced with the development of a drug releasing biodegradable polymer coating.⁴ The most widely used polymer coating is the biodegradable Poly-D,L-lactic acid (PDLLA). It is considered biocompatible since limited adverse reactions are evoked by its presence and the final degradation product is lactate, which is a non-toxic metabolite. A PDLLA coating with osteoconductive compounds added may act as a locally sustained drug delivery system for the tissue surrounding the implant. Different tested bone active drugs have advantageous effects when released from a PDLLA

coating: proteins^{5,6} antibiotics^{7,8} and bisphosphonates.^{9,10} A PDLLA coating loaded with proteinaceous growth factors has recently been reported to induce a 2½ fold increase in amount of bone in contact with the surface as compared to the situation for bare titanium.¹¹

Although promising as a local release system only little attention has been invested in improving the osteoconductivity of the PDLLA implant coating by adding HA particles. Impact on the tissue response from direct cell/surface interactions, as opposed to the effect of releasable drugs, could serve as an additional means of improving osteoconductivity. The use of a non-releasing osteoconductive coating is well known from hydroxyapatite (HA) coated implants as introduced in 1987.¹² In experimental settings imitating both primary and revision surgery of total joint prostheses, the HA coating improves the early implant fixation and amount of bone in direct contact with the implant surface.¹³⁻¹⁵ A coating that represents both the osteoconductivity of HA and the drug releasing ability of PDLLA could prove to be superior to both of the latter.

Studies in the field of tissue engineering have incorporated particulate HA in PDLLA scaffolds to provide osteoconductive properties.¹⁶⁻¹⁸ In a canine intramuscular implant model a composite scaffold of PDLLA and 40 – 480 µm HA particles (PDLLA/HA 30/70 weight%) was compared to a pure PDLLA scaffold. The composite was found to be osteoinductive, whereas no bone tissue was formed on pure PDLLA.¹⁶ In a rabbit bone implant study an identical composite scaffold was found to be equally osteoconductive compared to a pure HA scaffold - the composite, however, resorbed faster.¹⁷ In a rabbit cranial defect model study with PDLLA/HA composite scaffold with 50/50 weight% fractions, but including 100 nm particles it was found that the osteoconductivity was positively correlated to the exposure of HA in the material surface.¹⁸

Motivated by these results on composite scaffolds a sheep implant study was set up to evaluate the osteoconductive impact of adding nanoparticle sized HA to a PDLLA implant coating. The study offers insight into the effect of HA-particle sizes below 100 nm in a large animal of high clinical relevance. HA particles sized 20 – 70 nm dispersed in PDLLA were used in a 50/50 volume% (30% PDLLA and 70% HA by weight) composite coating and compared to a pure PDLLA coating. The combination of very small HA particles and PDLLA could serve as a base for further development of osteoconductive coatings to improve long term survival of implants. We hypothesized that HA addition to the PDLLA coating could increase the osseointegration of porous titanium implants.

2. Materials & methods

2.1. Study design

Twenty implants were inserted bilaterally in the proximal part of the humerus (Fig. 1) of ten domestic sheep. Sheep is due to its resemblance with humans regarding bone structure a commonly used large animal model in orthopaedic implant research.¹⁹ The animals were skeletally mature with a mean body weight of 41.5 kg (range: 34 kg - 50 kg). The study design was paired with PDLHA/HA coated implants inserted on one side and control PDLHA coated implants inserted on the contralateral side. The control side alternated with each animal. The observation time was 12 weeks. Approval for the study was obtained from the Danish Animal Research Inspectorate.

2.2. Implants

We used 20 porous-coated titanium alloy (Ti-6Al-4V) implants for the experiment, manufactured by Biomet Inc. (Warsaw, IN). The implants were cylindrical with a height of 10 mm and 6 mm in diameter. The porous titanium surface was plasma-sprayed, giving a mean pore diameter of 480 μm and a porosity of 44% (as specified by the manufacturer). Endcaps of 10 mm in diameter were attached to the implant ends. When inserted into a 10-mm drill hole, this centered the implant and provided a uniform two mm gap around it (Figure 1).

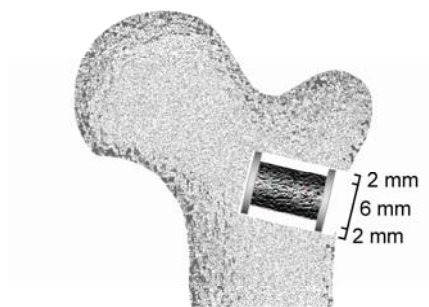


Figure 1. Implant Model. End-caps with same diameter as the drill hole (10 mm) are applied to the ends of the implant to maintain the implant (diameter 6mm) with a uniform gap (2mm).

In clinical settings erratic gaps between implant and surrounding bone bed are present²⁰, why experimental gap models are considered relevant in experimental implant research. In experimental studies 2 mm gaps are suggested as outer limit in implant/bone gaps, in that adequate implant fixation with gaps larger than 2 mm are considered beyond the natural ability of bone regeneration in periods less than a year.^{21,22}

2.3. Coating procedure and characterization with TEM, SEM and AFM

20 - 70 nm hydroxyapatite particles in ethanol (Berkeley advanced biomaterials, CA, USA) were used. A 10% dilution of the as-received particle/ethanol suspension was analyzed by transmission electron microscopy (TEM) (Philips CM20, Philips, Amsterdam, Netherlands) and atomic force microscopy (AFM) (Nanoscope IV (Veeco Instruments Inc., NY, USA) to confirm size and crystal character. A small droplet of the dilution was applied to a copper grid and on a mica surface and allowed to dry in ambient conditions before TEM and AFM studies, respectively. The HA-particles for the coating were dried under vacuum for 24 h in an exicator with silica gel. The vacuum dried particles were probe sonicated for 1 minute in milliQ water immersed in water with ice at 0.5 g/ml. The pH-value was adjusted to 7.4 with 1M phosphoric acid. The container was immediately after sonication immersed in liquid nitrogen to reduce the particle aggregation. The frozen particle dispersion was freeze dried for 5 days at -30°C and 100 mTor. The subsequent handling of components was carried out under sterile conditions. PDLA (Resomer 203, Boehringer-Ingelheim, Germany) was solved in ethylacetate at two concentrations, 50 mg PDLA in 1.5 ml and 100 mg PDLA in 1.5 ml. 125 mg freeze dried particles were added to the 50 mg solution. 2.5 mg HA particles for each mg PDLA give a 50/50 vol% composite assuming densities 3.15 and 1.25 g/cm³ for HA and PDLA, respectively. Both solutions were probe sonicated for 30 seconds prior to implant coating. The implants were dipped three times with 10 s intervals in the sonicated solution/dispersion, placed in a sterile exicator and vacuum dried for 48 h. Titanium coated silicon wafers were coated the same way with a single dip and subsequent drying. The size distribution of the coated surfaces were analyzed with AFM and the cantilevers used were NSG01 silicon cantilevers with tip radius below 10 nm (NT-MDT, Moscow, USA)). Afterwards the coated wafers were cooled in liquid nitrogen and sliced in order to obtain a cross section of the coatings for characterization with scanning electron microscopy (SEM) (Nova600 NanoSEM, FEI Company, USA).

2.4. Surgical procedure

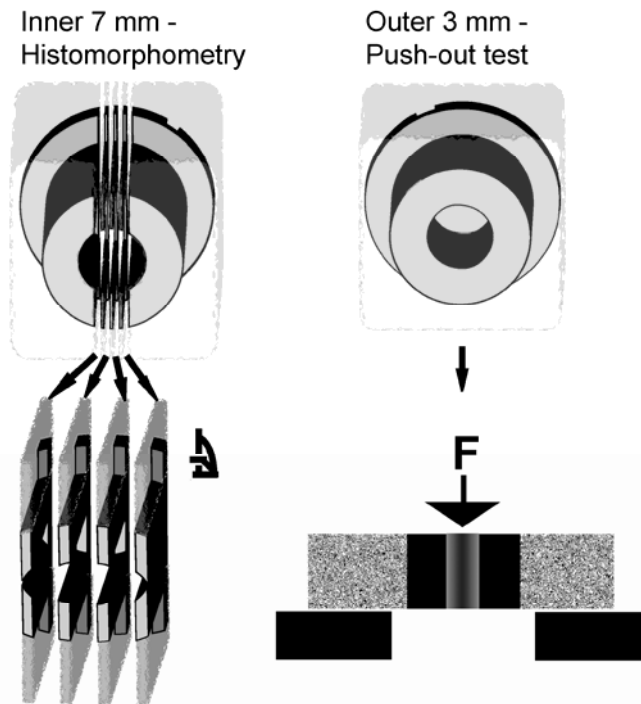
The proximal part of humerus was chosen because of the large amount of trabecular bone in this region, which is representative of the metaphyseal fixation of clinically used joint prostheses. The implants were inserted during general anesthesia under sterile conditions. The implantation site in the proximal part of the humerus was exposed through a lateral approach. The periosteum was removed immediately distal of the major tubercle peak where the implant was inserted. Initially, a guide wire was inserted, followed by a 10-mm cannulated drill. Drilling was performed at two rotations per second to prevent thermal trauma to the bone. A 10 mm diameter footplate was mounted on the 6 mm diameter implant to ensure centering in the 10 mm diameter drill hole with a uniform 2 mm defect between the implant surface and the surrounding bone (Figure 1). The overlying soft tissue was closed in layers. Pre- and postoperatively the sheep were given 1 g of dicloxacilin intravenously as antibiotic prophylaxis. A fentanyl transdermal patch (75 µg/h) lasting three days was given as postoperative analgesic treatment. All animals were allowed unlimited activity. After 12 weeks of observation time, the sheep were euthanized with an overdose of hypersaturated barbiturate.

2.5. Specimen preparation

The proximal humerii of the sheep were harvested and stored at -20 °C prior to preparation. Two transverse bone–implant specimens were cut on a water-cooled diamond band saw (Exakt Apparatebau, Norderstedt, Germany). The outermost specimen of 3 mm was used for mechanical testing, while the remaining 7 mm was fixed in 70% ethanol for histological evaluation (Fig. 2).

2.6. Mechanical test

Implants were tested to failure by a push-out test on an Instron universal test machine (Model 4302, Instron, UK). The specimens were placed on a metal support jig with a 7.4 mm circular opening. A preload of 2N was applied, to define contact position. Displacement rate was 5.0 mm/min. Ultimate shear strength (MPa), apparent shear stiffness (MPa/mm), and total energy absorption (J/m^2) were determined from the load–displacement curves.²³



Figur 2. Specimen preparation. From the central part of the inner 7 mm of implant four sections are cut for histomorphometry. The outer 3 mm of implant are exerted to pushout-test to evaluate the mechanical fixation.

2.7. Histomorphometry

The remaining 7 mm implant/bone specimens were dehydrated in graded ethanol (70–100%) containing 0.4% basic fuchsin and embedded in methylmethacrylate (Technovit 7200 VCL, Heraeus-Kulzer, Hanau, Germany). To obtain unbiased histomorphometric estimates the vertical section technique was applied and the embedded specimen were randomly rotated around the vertical axis and serially sectioned to 20 μm using a Leiden microtome (Leiden, Holland). Histomorphometry was performed blinded using an Olympus BX-50 light microscope and a stereological toolbox (C.A.S.T-Grid; Olympus, Denmark), which includes both software and a motorized stage. Area fractions in the sections of new woven bone, lamellar bone, fibrous tissue, and marrow space were quantified by the point-counting technique in 0–500 μm and 500–1500 μm zones adjacent to the implant and then used as estimates of volume fractions. On the implant surface, the surface area fractions of the same tissues were estimated by the line-interception technique. During counting 5 \times 5 pointgrids and sine weighted linegrids of 10 lines were used at a magnification of $\times 100$. These techniques provide highly reliable results with negligible bias.²³ Bone was surface-stained green and therefore, easy to distinguish from the other tissues. Newly formed bone was woven, appearing less organized with large, round osteocyte lacunae. Lamellar bone was

defined by its highly organized lamellas and lamella-oriented long, oval cell lacunae. The use of polarized light to enhance the lamellar structures was not considered. However, as expected, no lamellar bone was observed in the region of interest at this 12 week time postoperatively. The fibrous tissue was identified by the presence of clearly visible fibril fiber complexes and low cell density. The area of implant surface covered with nonresorbed PDLA or PDLA/HA coating was estimated with a line probe interception count. With an ocular line grid inset adjusted to perpendicular interception with the implant surface presence or no presence of coating was determined for each 200 μm .

2.8. Statistics

Statistical analysis was performed using STATA Intercooled 9.0 software (STATA, TX). Normal distribution could not be assumed on all data. Therefore, a nonparametric paired analysis was performed with Wilcoxon signed rank Tests (two-tailed). All data are, unless otherwise stated, presented as median and interquartile range. P-values less than 0.05 were considered statistically significant.

3. Results

3.1. Coating characterization

The TEM analysis show aggregates of elongated rod-like nanoparticles and from Fig. 3 it can be seen that the particles have a width of approximately 20 nm and a length between 50 and 100 nm. At higher magnification the detailed structure of the HA crystal lattice was revealed (Figure 3 - right): the nanoparticle in the lower left corner is oriented with the a- and b-axis of the hexagonal unit cell parallel to the TEM focal plane, while the remaining particles have the c-axis more or less parallel to the focal plane. The particle size of the HA particles and the surface features of the PDLA coating and PDLA/HA composite coating was also revealed by AFM images and the results are depicted in Fig. 4. The particles sizes as determined from the AFM images are slightly larger than what is observed with TEM, an effect which is due to the finite size of the AFM tip which leads to a convolution effect known to slightly overestimate particle sizes. The PDLA coating appears from the AFM images to be featureless, whereas the PDLA/HA preparation is presented as a composite, inhomogeneous surface. SEM images of the cross sections of the

resulting PDLLA (Figure 5 – left) and PDLLA/HA composite coatings (Figure 5 – right) display comparable thicknesses on flat substrates.

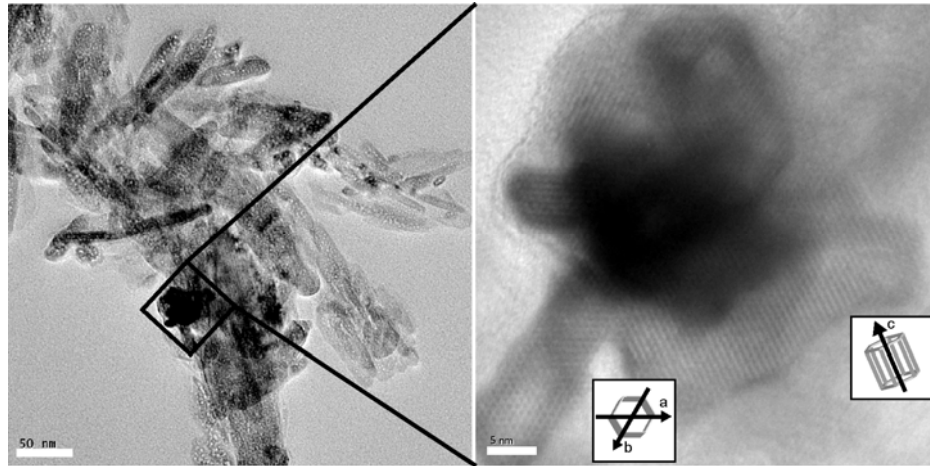


Figure 3. Transmission electron microscopy pictures of the as-received 20 – 70 nm HA particles. Left: Aggregate of rod-like particles with a width below 20 nm and length 50 – 100 nm. Right: Close-up picture of a small part of the aggregate. The characteristic hexagonal crystal lattice of HA is seen with both the ab plane and the c plane parallel to the focus plane as depicted by the small inserts.

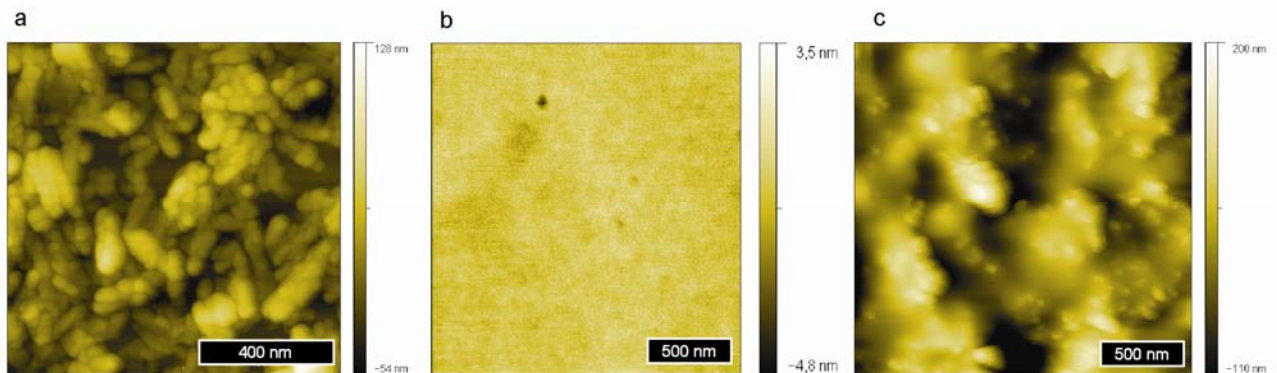


Figure 4. Atomic Force Microscopy of the as-received 20 – 70 nm HA particles (a). The particles appear larger than expected from the TEM pictures. This is most likely an effect of AFM tip convolution. The poly-D,L-Lactic Acid coating is shown in (b) and the PDLLA/HA 50/50 vol% composite coating in (c). The PDLLA coating appears featureless whereas particles and PDLLA are observed on the composite surface.

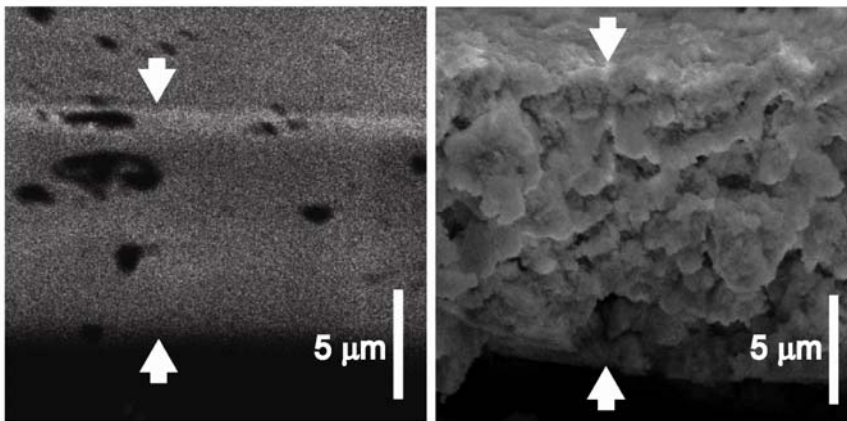


Figure 5. Scanning electron microscopy pictures of cross sections of the pure PDLLA coating (left) and the PDLLA/HA composite coating (right). Thicknesses are in the same range.

3.2. Observations on animals

All ten sheep were fully weight bearing within 3 days after surgery and completed the 12 weeks of observation period without signs of infection or other complications.

3.3. Mechanical tests

Implants with HA/PDLLA composite coating compared to PDLLA coated implants had better mechanical fixation at least ten-fold higher in all three mechanical parameters: Ultimate shear strength, apparent shear stiffness and total energy absorption (Tbl. 1). Three of the ten implants with pure PDLLA coating did not withstand the initial 2N preload required to define contact position and the force load detection of the instrument, explaining the zero as lower limit of interquartile range.

Table 1. Mechanical push-out test [median (interquartile range)]

Implant coating	Ultimate shear strength (MPa)	Apparent shear stiffness (MPa/mm)	Total energy absorption (J/m ²)
PDLLA	0.06 (0 – 0.10)	0.07 (0 – 0.20)	11 (0 – 20)
PDLLA/nHA	1.20 (0.12 – 2.33)*	7.20 (0.40 – 16.20)*	110 (23 – 369)*

(P-value below 0.05 with Wilcoxon signed ranks hypothesis test is denoted with a [*])

3.4. Histological observations

Overall no signs of infection or severe foreign body reaction were observed. In figure 6 representative sections of the implant/tissue interface are depicted at $\times 50$ and $\times 200$ magnification. Newly formed bone and fibrous tissue is seen on composite coated implant, whereas fibrous tissue alone is seen on pure PDLLA coated implants. Bone marrow-like tissue dominated by adipocytes

with sparse vascularisation and occasional streaks of fibrous tissue (fat marrow) is seen in the peripheral region. Only limited bony ingrowth from the drill hole periphery directed against the implant was observed. Apart from fat marrow in the gap only sealing and occasional bridging of intersected bone trabeculae forming a partial bony lining in the periphery was observed.

3.5. Histomorphometry results

Implants coated with the PDLLA/HA composite were covered 39.3% on average with a layer of newly formed bone and primarily fibrous tissue for the remainder (Tbl. 2).

Table 2 Histomorphometrical area tissue fractions on implant surface, histomorphometrical volumetric tissue fractions in gap zone 1 (0–500 µm around implant) and histomorphometrical volumetric fractions in gap zone 2 (500–1500 µm around implant) [median (interquartile range)].

	<i>Implant coating</i>	<i>New bone (%)</i>	<i>Fibrous tissue(%)</i>	<i>Marrow tissue (%)</i>
Area fractions on surface	PDLLA	0.2 (0.16 – 0.42)	96.2 (91.4 – 97.9)*	3.6 (1.7 – 7.6)
	PDLLA/HA	39.3 (37.9 – 42.8)*	58.3 (56.2 – 61.8)	1.2 (0.7 – 2.5)
Volume fractions zone 1	PDLLA	0 (0 – 0.6)	35.6 (26.1 – 54.8)	64 (45.2 – 73.9)
	PDLLA/HA	6.1 (4.3 – 10.8)*	30.2 (29.3 – 31.4)	61.7 (57.7 – 65.7)
Volume fractions zone 2	PDLLA	0.5 (0 – 1.2)	1.9 (0.7 – 6.1)	97.2 (87.3 – 99.1)
	PDLLA/HA	0.6 (0.59 – 1.0)	5 (2.7 – 7.7)	93.8 (88.5 – 96.7)

(P-value below 0.05 with Wilcoxon signed ranks hypothesis test is denoted with a [*])

Implants with pure PDLLA coating were almost exclusively covered with fibrous tissue and no bone was present (Tbl. 2). Correspondingly a larger amount of bone was seen in the inner 0 - 500 µm gap zone of implants coated with the composite (Tbl. 2). In the outer 500 – 1500 µm gap zone of both groups filled almost entirely with fatty marrow no and differences were observed (Tbl. 2). In the remaining outermost 500 µm of gap no differences were observed by microscopy inspection and this zone was not quantified by histomorphometry.

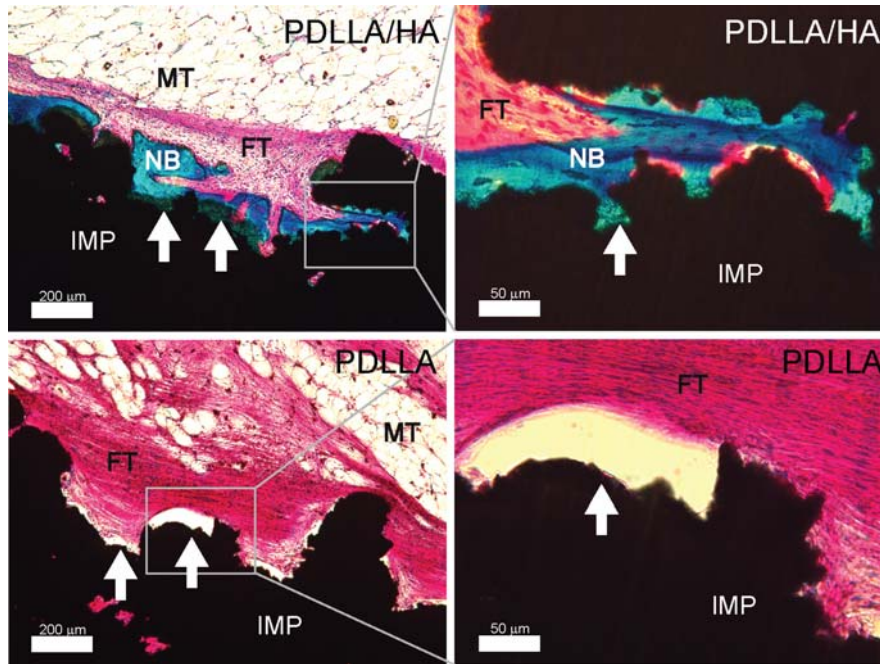


Figure 6. Representative pictures of the implant surfaces. HA/PDLLA coated implants in the upper row and PDLLA coated implants in the lower row. IMP: implant, NB: new bone, FT: Fibrous tissue, MT: marrow tissue. White arrows mark presence of nonresorbed coating. PDLLA/HA coating: On the composite coated implants extensive formation of new bone along with fibrous encapsulation is seen. The fat-marrow is seen in the gap. At high magnification (upper right) the newly formed bone is seen in direct contact with both titanium and composite. PDLLA coating: The pure polymer coated implants are covered exclusively with fibrous tissue. It appears more dense than on the composite. Fat marrow with streaks of fibrous tissue is seen in the gap. PDLLA presence appears as empty areas due to solvation in acetone during specimen preparation.

The coatings were partly resorbed during the 12 weeks of implantation. Remains of coatings were present on 20.3% +/- 4.3% and 19.8% +/- 5.2% (average +/- SD) of PDLLA/HA composite and PDLLA coated implant surface areas, respectively. Coating remains are depicted in figure 6.

4. Discussion

The aim of this study was to investigate the osseointegrative effect of PDLLA/HA composite versus pure PDLLA coatings on experimental titanium implants in a 2 mm in vivo gap model.

Biomechanical implant fixation and histomorphometrical analysis of tissue in contact with implant surface and periimplant tissue studies were performed. The composite PDLLA/HA coated implants showed significantly stronger fixation in all mechanical parameters and a larger amount of bone in direct contact with the implant surface was observed as compared to the implants with a pure PDLLA coating.

A paired study design using bilateral implant placement allowed a direct comparison of PDLLA/HA composite and pure PDLLA coatings within each animal. Thereby, the biological difference between individuals was reduced. Furthermore, it allowed a reduction in the number of

animals needed to be included in the study. The implant model is unloaded and thereby the effects associated with direct weight bearing conditions are not addressed in the study. The study design is also limited in that only one intervention implant group and one control implant group can be included. In the current study pure polymer and composite coatings are compared, but a bare titanium surface could be included as control with advantage. This would directly relate the tested coatings to a clinical standard. In previous studies using the same study design for testing implant coatings, the approach has been that of selecting bare titanium as control regardless of intervention, thereby ensuring a clinical offset, as opposed to insight into the function of the coating. For instance, Elmengaard et al²⁴ used bare titanium instead of titanium with cyclic RGE-peptide anchors as control for a titanium implant coated with cyclic RGD-peptide anchors. Lamberg et al¹¹ used bare titanium instead of titanium with a pure PDLLA coating as control for a PDLLA coating loaded with protein growth factors. Although the current study lags a clinically relevant control by not including titanium, it does, however, answer the conceptual question: Does hydroxyapatite nanoparticles in PDLLA conduct formation of bone?

The 50/50 vol% mixture of PDLLA and HA was chosen to allow for particle aggregation and the void between particles to be filled with polymer. The AFM images of the resulting coatings display a flat featureless PDLLA surface and on the PDLLA/HA composite a non-homogeneous presentation of both HA-particles and PDLLA. Given the coating technique a completely homogeneous composite surface cannot be anticipated due to formation of large HA-particle aggregates before evaporation of the organic solvent. This may result in voids within the bulk material of low HA presence and in HA-aggregate protrusions on the surface.

It is recognized that the volume of the resulting implant coatings should be the same to avoid potential biasing effects. Although coatings on the actual implants were not imaged, the similar coating thicknesses observed with SEM on flat titanium substrates (Fig. 5) argument that potential biases can not be overwhelming. Another aspect which could have been further enlightened by cross-sectional imaging of the coated implants is the extent, to which the coating alters the surface features of the implant. Porosities in particular may be obstructed by coating material and prevent ingrowth of tissue.

The mechanical fixation of the implants (Tbl. 1) can be ascribed to the tissue in contact with the implant surface and in the gap. No histological differences were observed in the outer gap zone and the fixation difference is thus a result of the bone formed on the PDLLA/HA composite coated implants. The fixation results emphasize the importance of applying an osteoconductive coating to

implants when attempting to improve initial fixation. *In vivo* sheep studies using HA coated implants in a non-gap model report stronger mechanical fixation^{25,26}, however, this is considered to be due to an effect of the bony bridging between existing bone and implant surface, which was not present in the present study due to the large gap. The three implants in the control group not withstanding the 2N preload during the mechanical testing are set to zero in the data analysis, although it is recognized that the fixation is between 0 and 2N. Whatever value between 0 and 2 was chosen for these implants it would not change the results. It should be noted that the part of the implant used in the mechanical test is separated from the remaining implant with a diamond band saw. In the sawing process where the implant is fixated the mechanical strength of the bone/implant interface may be weakened. It should also be noted that the bone tissue around the implant part was not examined histologically following the mechanical test. Although the implants are completely implanted in trabecular bone, the mechanical fixation may be weakened by resorption of the cortical bone surrounding the implant site. This potential bias cannot be accounted for - it is, however, not expected to impact the relative results.

The results presented in Table 2 are very comparable to the results of other studies using HA in biocompatible polymer composite system, where a consistently improved osteoconductivity have been reported an *in vitro* study.²⁷⁻³⁰ For instance, the attachment and differentiation of polycaprolactone/HA compositic scaffolds was recently reported to be larger when nanoscaled HA was used as compared to microscaled HA²⁷ – the effect was tentatively ascribed to a higher surface area to volume ratio of the smaller particles resulting in higher HA content on the composite surface. A high surface content of HA was observed in the 50/50 vol% composite used in this study (Fig. 4c), which may partly account for the improved osteoconductivity observed.

One of the landmarks of HA coated implants is the improved bone nucleation on the implant surface, which was also observed on the PDLLA/HA composite in the present study. This independent nucleation is a prerequisite for the favourable bi-directional growth (i.e. bone growing inward from the drill hole periphery and outward from the implant surface).³¹ The osteoconductivity of the PDLLA/HA composite in the current study is similar to that of a pure hydroxyapatite coating as reported from a sheep implant study³² and two comparable goat implant studies.^{22,33} The results are also in good agreement with a recent *in vivo* study on a 50/50 vol% PDLLA/HA scaffold containing micron-sized HA particles reported osteoconductive equal to a pure hydroxyapatite scaffold.¹⁷ The observed lag of supported bone growth on pure PDLLA corresponds well with

reports on PDLLA scaffolds¹⁶ and rods³⁴ and adds further consistency to the common interpretation that PDLLA is not osteoconductive.

The fibrous tissue encapsulation around both the implant coatings is a common observation in gap implant models - previously reported on both HA^{22,32,33} and titanium coatings.^{31,35} It is suggested to arise from the wound healing response of blood³⁶ and is not solely ascribed to adverse reaction arising from the implant surface.

The bone stimulating effect of the PDLLA/HA composite is evidently localized to the composite surface and/or the immediate vicinity (Figure 6). For both the coatings the gap lagged bony bridging and was primarily filled with fatty marrow as revealed in previous studies.^{22,32,33} Consequently, no histological differences are observed in the outer gap zone (Tbl. 2).

The osteoconductivity of HA is considered to be an effect of the direct interaction with cells, likely through selective adsorption and orientation of proteins. The primary feasibility of further research on HA containing composites is the extensive widening of possible advancements introduced by a two-component system. Optimizing the particle and polymer properties along with addition of bone active compounds could serve as means to extend the osteoconductivity beyond that of pure HA.

Conclusion

We have shown that addition of HA nanoparticles to a PDLLA implant coating improves the osseointegration in a sheep in vivo model. Nucleation of new bone and less fibrous tissue was observed on the PDLLA/HA composite coated implants and this resulted in an improved mechanical fixation as compared to that for the PDLLA coating. The results stimulate further research on HA nanoparticle containing composites in large animal models. The applicability of a two-component material with osteoconductive properties resembling that of pure HA reaches further than the area of implant coatings. Ease of device fabrication and wide possibilities for advancement in mechanical properties and functionalization might lead to replacement of HA with composites in orthopaedic application areas.

Acknowledgements

The authors wish to thank Anette Milton and Jane Pauli for technical assistance with histological sections and Marianne Vestermark, Henrik & Mikkel Saxø and David Kraft for surgical assistance. This study was financially supported by Augustinus Foundation, Korning Foundation and A.P. Møller Foundation.

References

1. Annual report 2007. Danish Hip Arthroplasty Registry. 2007.
2. Ryd L, Albrektsson BE, Carlsson L, Dansgård F, Herberts P, Lindstrand A, Regner L, Toksvig-Larsen S. Roentgen stereophotogrammetric analysis as a predictor of mechanical loosening of knee prostheses. *J Bone Joint Surg Br* 1995;77(3):377-83.
3. Kärrholm J, Herberts P, Hultmark P, Malchau H, Nivbrant B, Thanner J. Radiostereometry of hip prostheses. Review of methodology and clinical results. *Clin Orthop Relat Res* 1997(344):94-110.
4. Schmidmaier G, Wildemann B, Stemberger A, Haas NP, Raschke M. Biodegradable poly(D,L-lactide) coating of implants for continuous release of growth factors. *J Biomed Mater Res* 2001;58(4):449-55.
5. Schmidmaier G, Wildemann B, Ostapowicz D, Kandziora F, Stange R, Haas NP, Raschke M. Long-term effects of local growth factor (IGF-I and TGF-beta 1) treatment on fracture healing. A safety study for using growth factors. *J Orthop Res* 2004;22(3):514-9.
6. Wildemann B, Sander A, Schwabe P, Lucke M, Stockle U, Raschke M, Haas NP, Schmidmaier G. Short term in vivo biocompatibility testing of biodegradable poly(D,L-lactide)--growth factor coating for orthopaedic implants. *Biomaterials* 2005;26(18):4035-40.
7. Lucke M, Schmidmaier G, Sadoni S, Wildemann B, Schiller R, Haas NP, Raschke M. Gentamicin coating of metallic implants reduces implant-related osteomyelitis in rats. *Bone* 2003;32(5):521-31.
8. Price JS, Tencer AF, Arm DM, Bohach GA. Controlled release of antibiotics from coated orthopedic implants. *J Biomed Mater Res* 1996;30(3):281-6.
9. Greiner S, Kadow-Romacker A, Lubberstedt M, Schmidmaier G, Wildemann B. The effect of zoledronic acid incorporated in a poly(D,L-lactide) implant coating on osteoblasts in vitro. *J Biomed Mater Res A* 2007;80(4):769-75.
10. Greiner S, Kadow-Romacker A, Wildemann B, Schwabe P, Schmidmaier G. Bisphosphonates incorporated in a poly(D,L-lactide) implant coating inhibit osteoclast like cells in vitro. *J Biomed Mater Res A* 2007;83(4):1184-91.
11. Lamberg A, Schmidmaier G, Søballe K, Elmengaard B. Locally delivered TGF-beta1 and IGF-1 enhance the fixation of titanium implants: a study in dogs. *Acta Orthop* 2006;77(5):799-805.

12. Geesink RG, de Groot K, Klein CP. Chemical implant fixation using hydroxyl-apatite coatings. The development of a human total hip prosthesis for chemical fixation to bone using hydroxyl-apatite coatings on titanium substrates. *Clin Orthop Relat Res* 1987(225):147-70.
13. Baas J, Elmengaard B, Jensen TB, Jakobsen T, Andersen NT, Søballe K. The effect of pretreating morselized allograft bone with rhBMP-2 and/or pamidronate on the fixation of porous Ti and HA-coated implants. *Biomaterials* 2008;29(19):2915-22.
14. Søballe K. Hydroxyapatite ceramic coating for bone implant fixation. Mechanical and histological studies in dogs. *Acta Orthop Scand Suppl* 1993;255:1-58.
15. Søballe K, Mouzin OR, Kidder LA, Overgaard S, Bechtold JE. The effects of hydroxyapatite coating and bone allograft on fixation of loaded experimental primary and revision implants. *Acta Orthop Scand* 2003;74(3):239-47.
16. Hasegawa S, Neo M, Tamura J, Fujibayashi S, Takemoto M, Shikinami Y, Okazaki K, Nakamura T. In vivo evaluation of a porous hydroxyapatite/poly-DL-lactide composite for bone tissue engineering. *J Biomed Mater Res A* 2007;81(4):930-8.
17. Hasegawa S, Tamura J, Neo M, Goto K, Shikinami Y, Saito M, Kita M, Nakamura T. In vivo evaluation of a porous hydroxyapatite/poly-DL-lactide composite for use as a bone substitute. *J Biomed Mater Res A* 2005;75(3):567-79.
18. Kim SS, Sun Park M, Jeon O, Yong Choi C, Kim BS. Poly(lactide-co-glycolide)/hydroxyapatite composite scaffolds for bone tissue engineering. *Biomaterials* 2006;27(8):1399-409.
19. Aerssens J, Boonen S, Lowet G, Dequeker J. Interspecies differences in bone composition, density, and quality: potential implications for in vivo bone research. *Endocrinology* 1998;139(2):663-70.
20. Noble PC, Alexander JW, Lindahl LJ, Yew DT, Granberry WM, Tullos HS. The anatomic basis of femoral component design. *Clin Orthop Relat Res* 1988(235):148-65.
21. Dalton JE, Cook SD, Thomas KA, Kay JF. The effect of operative fit and hydroxyapatite coating on the mechanical and biological response to porous implants. *J Bone Joint Surg Am* 1995;77(1):97-110.
22. Clemens JA, Klein CP, Sakkers RJ, Dhert WJ, de Groot K, Rozing PM. Healing of gaps around calcium phosphate-coated implants in trabecular bone of the goat. *J Biomed Mater Res* 1997;36(1):55-64.
23. Baas J. Adjuvant therapies of bone graft around non-cemented experimental orthopedic implants stereological methods and experiments in dogs. *Acta Orthop Suppl* 2008;79(330):1-43.
24. Elmengaard B, Bechtold JE, Søballe K. In vivo study of the effect of RGD treatment on bone ongrowth on press-fit titanium alloy implants. *Biomaterials* 2005;26(17):3521-6.
25. Aebli N, Stich H, Schawalder P, Theis JC, Krebs J. Effects of bone morphogenetic protein-2 and hyaluronic acid on the osseointegration of hydroxyapatite-coated implants: an experimental study in sheep. *J Biomed Mater Res A* 2005;73(3):295-302.
26. Borsari V, Fini M, Giavaresi G, Rimondini L, Consolo U, Chiusoli L, Salito A, Volpert A, Chiesa R, Giardino R. Osteointegration of titanium and hydroxyapatite rough surfaces in healthy and compromised cortical and trabecular bone: in vivo comparative study on young, aged, and estrogen-deficient sheep. *J Orthop Res* 2007;25(9):1250-60.
27. Heo SJ, Kim SE, Wei J, Hyun YT, Yun HS, Kim DH, Shin JW. Fabrication and characterization of novel nano- and micro-HA/PCL composite scaffolds using a modified rapid prototyping process. *J Biomed Mater Res A* 2008.

28. Kim HW, Kim HE, Salih V. Stimulation of osteoblast responses to biomimetic nanocomposites of gelatin-hydroxyapatite for tissue engineering scaffolds. *Biomaterials* 2005;26(25):5221-30.
29. Teng SH, Lee EJ, Yoon BH, Shin DS, Kim HE, Oh JS. Chitosan/nanohydroxyapatite composite membranes via dynamic filtration for guided bone regeneration. *J Biomed Mater Res A* 2008.
30. Venugopal J, Low S, Choon AT, Kumar AB, Ramakrishna S. Electrospun-modified nanofibrous scaffolds for the mineralization of osteoblast cells. *J Biomed Mater Res A* 2008;85(2):408-17.
31. Hofmann AA, Bachus KN, Bloebaum RD. Comparative study of human cancellous bone remodeling to titanium and hydroxyapatite-coated implants. *J Arthroplasty* 1993;8(2):157-66.
32. Sachse A, Wagner A, Keller M, Wagner O, Wetzel WD, Layher F, Venbrocks RA, Hortschansky P, Pietraszczyk M, Wiederanders B and others. Osteointegration of hydroxyapatite-titanium implants coated with nonglycosylated recombinant human bone morphogenetic protein-2 (BMP-2) in aged sheep. *Bone* 2005;37(5):699-710.
33. Clemens JA, Klein CP, Vriesde RC, Rozing PM, de Groot K. Healing of large (2 mm) gaps around calcium phosphate-coated bone implants: a study in goats with a follow-up of 6 months. *J Biomed Mater Res* 1998;40(3):341-9.
34. Furukawa T, Matsusue Y, Yasunaga T, Nakagawa Y, Okada Y, Shikinami Y, Okuno M, Nakamura T. Histomorphometric study on high-strength hydroxyapatite/poly(L-lactide) composite rods for internal fixation of bone fractures. *J Biomed Mater Res* 2000;50(3):410-9.
35. Elmengaard B, Bechtold JE, Søballe K. In vivo effects of RGD-coated titanium implants inserted in two bone-gap models. *J Biomed Mater Res A* 2005;75(2):249-55.
36. Hofmann AA, Bloebaum RD, Rubman MH, Bachus KN, Plaster RL. Microscopic analysis of autograft bone applied at the interface of porous-coated devices in human cancellous bone. *Int Orthop* 1992;16(4):349-58.

Osteopontin functionalization of HA/PDLLA composite promotes bone formation

Jensen T^{1,2}, Baas J¹, Dolathshahi-Pirouz A², Jacobsen T¹, Singh G², Nygaard J², Foss M², Bechtold J¹, Bünger C¹, Besenbacher F^{1,3}, Søballe K¹.

¹Orthopaedic Research Laboratory, University Hospital of Aarhus, 8000 Aarhus C, Denmark

²Interdisciplinary Nanoscience Center (iNANO), Aarhus University, 8000 Aarhus C, Denmark

³Department of Physics and Astronomy, Aarhus University, 8000 Aarhus C, Denmark

Abstract

As reported previously a composite coating on porous titanium implants of Poly-D,L-Lactic-Acid (PDLLA) and nanoparticulate hydroxyapatite (nHA) was osteoconductive and promoted the osseointegration. In this study, to further enhance the osteoconductive tissue response of the composite coating, nHA was functionalized with osteopontin (OPN) prior to forming the composite. The OPN used is previously reported active towards cells when adsorbed on a HA surface. In a canine endosseous 0.75 mm gap implant model the osteointegrative impact of the osteopontin functionalized composite as an implant coating was tested with a non-functionalized composite as control. During 4 weeks of observation the OPN functionalized composite coating conducted significantly more new bone formation in the porosities of the implant, but no differences were observed in the gap. The study provides evidence that OPN may serve as an osteoconductive surface functionalization of particles in a polymer/particle composite.

1. Introduction

The duration of orthopaedic joint replacements is limited and revision surgery of loosened implants constitutes a substantial fraction of total surgeries [1].

Improvement of longevity would have a large socioeconomical impact. One strategy currently investigated is designing osteoconductive implants that improve the early fixation by endorsing formation of anchoring bone tissue on the implant surface. This research is encouraged by the fact that early stable fixation is a prerequisite for a favourable long term prognosis [2,3].

Osteopontin (OPN) is an extracellular bone protein discovered in 1985 [4]. It is part of the SIBLING family of proteins (Small integrin-binding ligand, N-linked glycoprotein) residing abundantly as surface proteins in the mineral/tissue interface of bone [5]. It contains a hydroxyapatite (HA) binding sequence and a cell binding domain with an RGD-sequence. OPN plays a key role in the bone remodelling process including the activity of bone resorbing osteoclasts and bone forming osteoblasts [6-9]. The protein has furthermore, been shown to promote angiogenesis

[6,10] and reduce the foreign body reaction to implants [11,12]. Applying the functionality of OPN to the surface of orthopaedic joint replacements might serve as a method for improving osteoconductivity.

The *in vitro* cell interaction of OPN depends on the chemistry of the surface to which the protein is adsorbed [13-16] and thrombin cleaving removes a C-terminal fragment allowing for better access to the cell binding domain [17]. In a recent study, it was shown that OPN from bovine milk consisting primarily of cleaved OPN, enhanced spreading and acted chemotactic on human mesenchymal stem cells when adsorbed on hydroxyapatite (HA) (Paper II).

Bovine milk offers large amounts of OPN at low cost thereby opening new opportunities for biomaterial design. Previous *in vivo* studies have focused on 2D surface functionalization of single component biomaterials requiring only small amounts of OPN, eg. by surface adsorption on HA [18] or by oriented covalent immobilization on polyHEMA[11].

OPN functionalization of one part of a two-component biomaterial could incorporate a larger effective functionalization area and a 3D distribution of the protein throughout the material.

Biodegradable two-component composites of poly-D,L-lactic-acid (PDLLA) and HA particles have consistently shown excellent osteoconductivity [19-21], and it appears to be correlated to the surface representation of Ha [21,22]. The osteoconductivity of HA is partly ascribed to selective adsorption and orientation of proteins effective at attracting bone forming cells [23]. Preadsorbing the HA particles of a PDLLA/HA composite with surface proteins could serve as a means to predetermine the functionality of the composite and preserve it through the degradation process. This is a new approach for integrating a protein signal in an osteoconductive material. OPN preadsorption could in theory make the composite susceptible to a bone directed remodelling process by attracting and activating bone resorbing osteoclasts and bone forming osteoblasts.

In this study, a novel implant coating of HA nanoparticles (20-70 nm) preadsorbed with OPN and mixed with PDLLA at 50/50 vol% is tested. In a canine 0.75 mm gap model evaluating implant osseointegration the OPN-functionalized implant coating is compared to a similar coating excluding OPN. Osseointegration is evaluated as mechanical implant fixation and relative amounts of bone, fibrous tissue and marrow tissue formed in the periimplant region. It is hypothesized that OPN

preadsorption on the HA-particles improves the mechanical fixation by increasing bone formation and reducing fibrous tissue formation.

2. Materials & Methods

2.1. Experimental Design (Fig. 1)

9 dogs were included and each animal received two implants in the proximal tibiae. The implants were surrounded by a 0.75 mm coaxial defect. The implants were coated either with a pure PDLLA/HA composite (COMP) coating as control or an OPN functionalized composite (OPN-COMP) as intervention. The two-armed study was conducted in a paired design where each dog received both treatments. The implantation site was alternated systematically with random start. The observation time was 4 weeks.

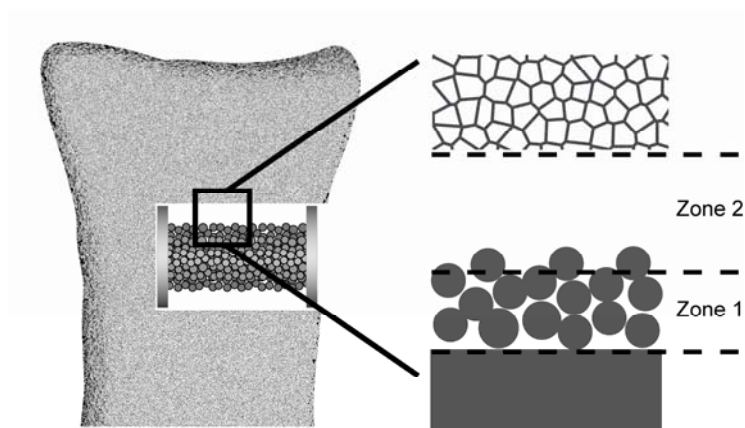


Figure 1. Implant model. End-caps with same diameter as the drill hole (7.5 mm) are applied to maintain the implant (diameter 6 mm) with a uniform gap (0.75 mm)

2.2. Implants

Custom made cylindrical titanium alloy core implants (Ti-6Al-4V) with commercially available pure titanium porous coating (Porocoat) manufactured by Depuy Inc., Warsaw, IN, USA were used. Dimensions including porous coating are length 10 mm and diameter 6 mm. The porosity is provided by multiple layers of titanium beads sintered on to the core implant giving an average porosity of 40% by volume and average pore size of 250 μm with lowest porosity and pore size (20%,

100 μm) at the core implant and highest at the outer boundary (90%, 500 μm) [24]. Endcaps of 7.5 mm in diameter were attached to implant ends. When inserted into a 7.5 mm drill hole, this centered the implant and provided a uniform 0.75 mm gap around it.

2.3. Coating procedure

The coating procedure is a slight modification of a previous reported method including characterization (Paper III). 20 - 70 nm HA particles in ethanol (Berkeley advanced biomaterials, Ca, USA) with a surface area of 110 m^2/g as specified by the manufacturer were used. The HA-particles were dried 24 h in a vacuumed exicator with silica gel. Two 1 g portions of dried particles were probe sonicated for 1 minute in cooled milliQ water at 50 mg/ml (20 ml) in 50 ml test tubes. The pH-value was adjusted to 7.4 with 1M phosphoric acid (Sigma-Aldrich, Brøndby, Denmark). 52 mg OPN was added to one particle dispersion as two ml 26 mg/ml solution in milliQ water and two ml pure milliQ was added to the second dispersion. Both solutions were hand stirred. After 1 minute both dispersions were probe sonicated for 10 - 15 s and immersed in liquid nitrogen to limit aggregation. The frozen dispersions were freeze dried for 5 days at -30°C and 100 mTor.

A small sample from each portion was taken for surface elemental analysis with X-ray photoelectron spectroscopy (XPS) (Kratos Axis Ultra, Manchester, England). A survey spectroscopy was performed at ultra high vacuum with a 5 kV beam at angle 0° giving a probing depth less than 10 nm. The electron binding energy spectrum was analyzed with CasaXPS version 2.3.14 software.

Henceforward all handling of components was done under sterile conditions. Two 50 mg in 1.5 ml solutions of PDLLA (Resomer 203, Boehringer-Ingelheim, Germany) in ethylacetate (Sigma-Aldrich, Brøndby, Denmark) were made in eppendorf-tubes and stirred regularly through one hour. 125 mg freeze dried HA particles with or without OPN were added to the PDLLA solutions. Both solutions were probe sonicated for 30 seconds prior to implant coating. Implants were dipped twice in the sonicated solution/dispersion with a 10 s interval, placed in a sterile exicator and vacuum dried for 48 h.

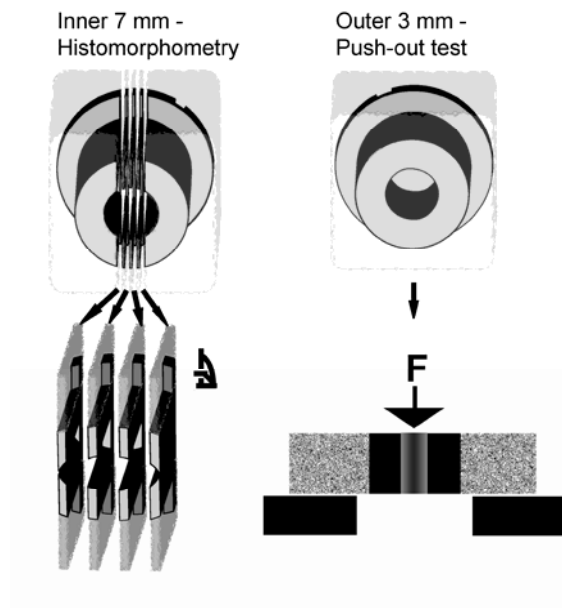
2.4. Animals and surgical procedure

Nine skeletally mature mongrel dogs with a mean weight of 25.1 kg were included in the study. The dogs were bred for scientific purposes, and the experiment was approved by the Danish Research Inspectorate and conformed to Danish law.

With the dogs under general anaesthesia and under sterile conditions, a skin incision was made with cautery on the medial proximal tibia leaving the medial collateral ligament intact. Periosteum was removed only at the implantation site. A guide wire was inserted anteromedially approximately 3.4 cm distal to the joint line oriented perpendicular to the surface. Over the guide wire, a cannulated drill (Ø 7.5 mm) was used to drill cylindrical cavities at a speed of maximum two rotations per second. The edge of the hole was trimmed with a scalpel to remove excessive periosteum, and the cavities were irrigated with 10 ml saline for removal of loose bone chips. In each drill hole, the implants with end-washers were inserted in a uniform central placement and the soft tissues closed in layers. The procedure was repeated for the opposite side. All 18 implants were operated on by the same surgeon. Pre- and postoperatively, the dogs were given 1 g of dicloxacillin intravenously as antibiotic prophylaxis. A fentanyl transdermal patch (75 mg/h) lasting three days was given as postoperative analgesic treatment. All animals were allowed unlimited activity. After four weeks observation time, the dogs were sedated and euthanized with an overdose of hypersaturated barbiturate.

2.5. Specimen preparation (figure 2)

The proximal tibiae were harvested and stored at -20 °C prior to preparation. Two transverse bone-implant specimens were cut on a Accutom-50 precision cut-off machine (Struers, Ballerup, DK). The outermost specimen of 3 mm was stored at -20 °C prior to mechanical testing. The innermost section was prepared for histomorphometry. These specimens were dehydrated in graded ethanol (70–100%) containing basic fuchsin, and embedded in methylmethacrylate (Technovit 7200 VCL, Heraeus-Kulzer, Hanau, Germany). Using vertical sectioning technique, each specimen was cut into four 30 µm thick histological sections with a microtome (KDG-95, MeProTech, Heerhugowaard, Holland). Finally, these were surface counterstained with 2% light green for 2 min, rinsed and mounted on glass. This preparation provided red staining for non-calcified tissue and green staining for calcified tissue.



Figur 2. Specimen preparation. From the central part of the inner 7 mm of implant four sections are cut for histomorphometry. The outer 3 mm of implant are exerted to pushout-test to evaluate the mechanical fixation.

2.6. Mechanical testing

Thawed specimens were tested to failure by axial push-out test on an Instron universal test machine (Model 4302, Instron, UK). Testing was performed blinded and in one session. The specimens were placed with the cortical side facing up on a metal support jig with the implant centred over a 7.4 mm opening and under a cylindrical test probe of 5 mm diameter. A preload of 2 N defined the contact position for the start of the test. The implants were then pushed out of the surrounding tissue in the direction of the implant axis at a velocity of 5 mm/min. Load vs implant displacement data were continuously recorded. From these data, the mechanical implant fixation parameters as described earlier were calculated: ultimate shear strength, apparent shear stiffness, and total energy absorption [25].

2.7. Histological testing

Histomorphometry was performed blinded using an Olympus BX-50 light microscope and a stereological toolbox (C.A.S.T-Grid; Olympus, Denmark), which includes both software and a motorized stage. With the aid of the software, two regions of interest were defined: zone 1 from the innermost part of the core implant surface and 400 μm of the porocoat porosity, and zone 2 from the outer limit of zone 1 to the outer limit of the drilled bone defect except for the outermost ten percent (see figure 1). In zone 1 the area fractions of new bone, fibrous tissue, and marrow space

on the implant surfaces were quantified by line-interception technique. In this zone point counting technique for sectional tissue area fractions to estimate volume fractions was not suitable. Given the narrow crevices of the porocoat the area fractions estimated with line interception technique are assumed representative estimates of the tissue volume presentations in the porous space. In zone 2 area fractions and volume fractions of the same tissues were estimated by line-interception technique and point-counting technique respectively. During counting 5×5 pointgrids and sine weighted linegrids of 10 lines were used at a magnification of ×100.

Bone was surface-stained green, and therefore, easy to distinguish from the other tissues. Fibrous tissue was identified by its presence of clearly visible fibril fiber complexes and low cell density. The fibrous tissue largely appeared oriented, dense and well-organized, but also as a loosely, not clearly oriented, interconnected fibrous network. Marrow space consisted of fat vacuoles and surrounding blood cells.

2.8. Statistics

Statistical analysis was performed using STATA Intercooled 9.0 software (STATAcorp, College Station, TX, USA). Normal distribution was assumed on all the data. Therefore, a parametric paired analysis was performed with Student's paired t-test (two-tailed). P-values less than 0.05 were considered statistically significant.

3. Results

3.1 XPS of HA particles ± OPN

The elemental composition of the particle surfaces as detected with XPS is listed in table 1. On both particles with and without OPN, calcium (Ca), phosphor (P), oxygen (O) and carbon (C) were present, whereas nitrogen (N) was found exclusively on particles with OPN. The Ca/P ratio is 1.68 and 1.71 for particles with and without OPN respectively. The theoretical Ca/P value for stoichiometric Ha is 1.67 (Ca/P). Although carbon is not present in pure Ha it was detected in relatively large amounts on both samples. On HA with OPN the carbon presence was slightly larger.

Table 1. X-ray photoelectron spectroscopy elemental analysis.

	Ca%	P%	N%	O%	C%
HA - OPN	14.7 ± 1.0	8.7 ± 0.5	0	52.0 ± 1.0	24.6 ± 0.8
HA + OPN	13.3 ± 0.4	7.8 ± 0.3	1.3 ± 0.4	49.3 ± 0.5	28.2 ± 0.5

3.2 Observations on animals

All nine dogs were fully weight bearing within three days after surgery and completed the four week observation period without signs of infection or other complications.

3.3 Mechanical test

Implants with OPN-COMP performed better in all parameters, although not significantly. The results are listed in Table 2. The total energy absorption of the bone/implant binding was on average 37.5% higher with OPN-COMP coating. The ultimate shear strength and apparent shear stiffness of the same implants were moderately larger (13.5% and 2.5% respectively) than the COMP coating.

Table 2. Mechanical push-out test. No significant differences observed.

Implant\Parameter	Total energy absorption (J/m ²)	Ultimate shear strength (MPa)	Apparent shear stiffness (MPa/mm)
- OPN	462 ± 306	2.5 ± 1.5	16.1 ± 8.7
+ OPN	635 ± 450	2.8 ± 2.4	16.5 ± 13.5

3.4 Histological observations

Overall no signs of infection or severe foreign body reaction were observed. In figure 3 representative sections of the implant/tissue interfaces for both coatings are depicted at low and high magnification. With both coatings newly formed bone trabeculae are observed in the gap and plaques of surface associated bone on the inner surfaces of the porosities in the porocoat. No apparent differences in the gaps are observed, whereas the porosities with OPN-COMP coating are clearly stuffed to a higher degree with newly formed bone. The remains of the porosities are dominated by fibrous tissue, whereas the gaps are dominated by marrow tissue.

3.5 Histomorphometry

Results from histomorphometry are listed in table 3. The pore zone 1 of implants coated with OPN-COMP were covered 29.8% on average with newly

formed bone and equal amounts of fibrous and marrow tissue for the remainder. Zone 1 of implants with COMP coating were covered with significantly lower 14.7% newly formed bone and primarily fibrous tissue (50.7%) for the remainder.

The outermost surfaces of the titanium porocoat corresponding to the innermost boundary of zone 2 were covered in both groups primarily with marrow tissue. On OPN-COMP coated implants a tendency towards higher ongrowth of bone and lower ongrowth of fibrous tissue was seen.

No striking differences in volume fractions are observed in the marrow tissue dominated gaps.

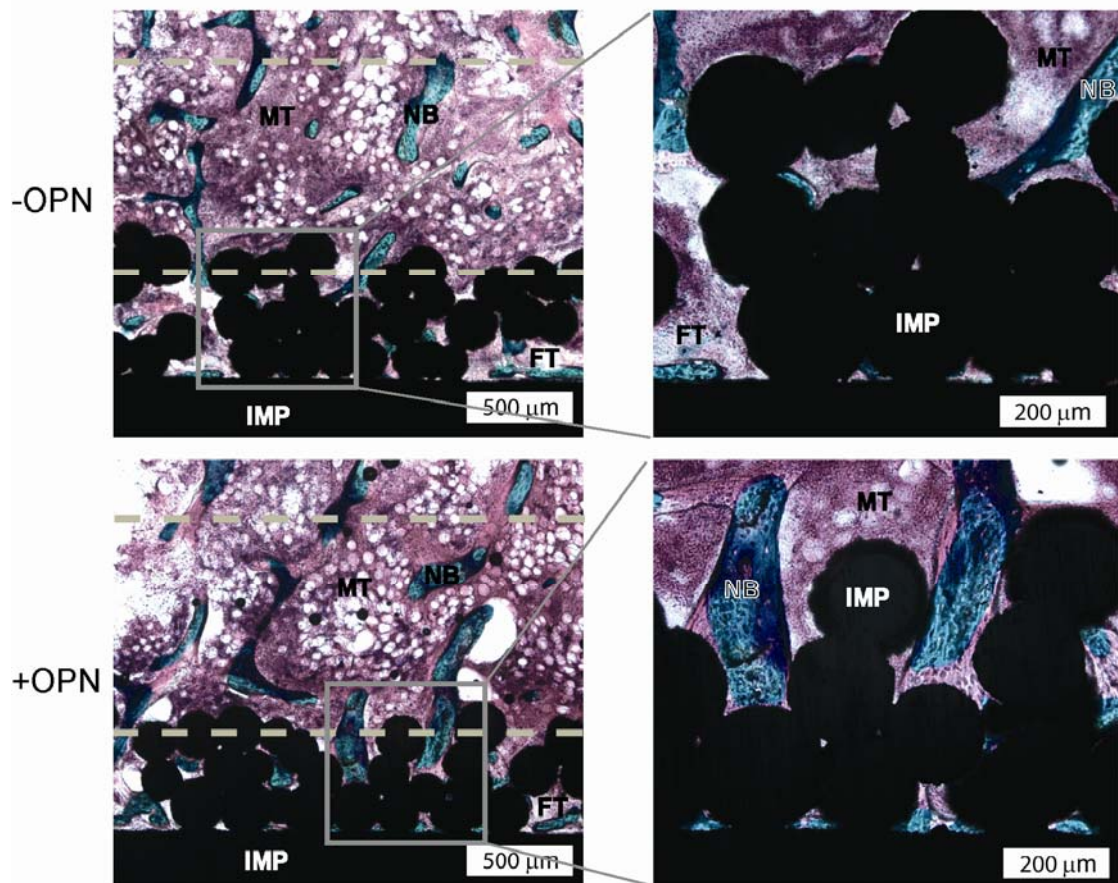


Figure 3. Representative pictures of the implant surfaces. COMP coated implants in the upper row (-OPN) and OPN-COMP coated implants in the lower row (+OPN). IMP: implant, NB: new bone, FT: Fibrous tissue, MT: marrow tissue. The porosities of the OPN-COMP coated implant are stuffed to a higher degree with new bone. No differences are observed in the marrow-dominated gaps.

Table 3. Histomorphometrical quantification of tissue area fractions on implant surface in zone 1, tissue area fractions on implant surface in zone 2 and volume fractions in gap zone 2. All data is presented as mean \pm sd.

Implant Parameter	New bone %	Fibrous tissue %	Marrow tissue %
Ongrowth zone 1			
- OPN	14.7 \pm 8.0	50.7 \pm 27.4	34.9 \pm 20.7
+ OPN	29.8 \pm 7.2*	35.2 \pm 16.2	34.9 \pm 11.3
Ongrowth zone 2			
- OPN	15.4 \pm 6.7	22.5 \pm 17.7	62.1 \pm 19.5
+ OPN	18.3 \pm 7	17.2 \pm 15.6	64.5 \pm 15.2
Volume Zone 2			
- OPN	19.0 \pm 11.6	9.7 \pm 7.9	71.3 \pm 17.0
+ OPN	21.3 \pm 11.5	7.7 \pm 6.6	71.0 \pm 15.3

(P-value below 0.05 with Student's paired T-test is denoted with a *)

4. Discussion

The purpose of the study was to test the osseointegrative effect of OPN functionalization of a PDLLA/Ha composite coating on experimental titanium implants. Biomechanical implant fixation and histomorphometrical analysis of tissue in contact with implant surface and periimplant tissue were used as parameters. OPN functionalization showed a significantly larger amount of bone formed in the implant porosities and stronger fixation, but not significantly, in all mechanical parameters.

Canine species are due to resemblance with humans regarding bone structure a commonly used large animal model in orthopaedic implant research. The proximal part of tibia was chosen because of the large amount of trabecular bone, which is representative of the bony fixation regions of clinically used joint prostheses. In clinical settings erratic gaps between implant and surrounding bone bed are present, why experimental gap models are considered relevant in experimental implant research. Gaps of 0.75 mm can be expected even with well-fitted uncemented implants [26,27].

Contralateral implants allow a paired study design, allowing OPN functionalized and non-functionalized composite coatings to be compared within each animal. Thereby, the biological difference between individuals, which can be significant, is reduced. It, furthermore, allows a reduction in the number of individuals needed to be included in the study. The implant model is unloaded and thereby limited as the effects of direct weightbearing conditions are not addressed.

The choice of using large amounts of OPN from a different species is debatable in a material intended for human clinical application. Potential transfer of disease and acute/chronic immunological reactions to the protein must be carefully considered and evaluated. In the very limited and conceptual frame of this study, no such occurrence was observed, further research, however, should emphasize this potential problem. The use of milk OPN also raises a mismatch question. It is well known that posttranslational modifications of OPN may vary in different tissues. Phosphorylations are considered particularly important in OPN function. Milk derived OPN is known to be highly phosphorylated, which is not the case for OPN in bone, where phosphorylation level fluctuates with functional status of the tissue [28]. High phosphorylation level OPN in general and bovine milk derived OPN in particular have been shown to promote osteoclastic resorption activity [29].

The choice of OPN amount for functionalization of HA particles corresponds to a particle surface coverage of 50% assuming full availability of the particle surface area [Paper II]. This amount was chosen to avoid free nonadsorbed OPN. It is recognized that preadsorbing the particles in the control coating with an inactive control protein, e.g. albumin, would be a more suitable control. This study, however, is an extension of a previous study in our group [PaperII]. Here OPN is characterized and tested in an *in vitro* cell study, where OPN is adsorbed on HA and compared to HA adsorbed with proteins from serum containing media. To maintain deductive continuity the HA particles in the control group of this study were not preadsorbed with proteins and instead allowed for random adsorption of serum proteins.

XPS survey spectroscopy was used to quantify the relative surface elemental composition of Ha-particles with and without protein. The C/P ratio for both samples indicates a slightly higher amount of P compared to stoichiometric Ha (1.67). This could be an effect of the pH adjustment done with phosphoric acid and, in case of functionalized particles, phosphate groups present on the adsorbed OPN. The carbon present on Ha-particles without OPN is most likely contamination, which is difficult

to avoid with XPS of non-carbonaceous particles [30]. With addition of OPN the analysis identifies an increase in carbon and appearance of nitrogen. The relative amount of nitrogen detected is in agreement with a previous study of full coverage protein adsorption on Ha microparticles [30].

The 50/50 vol% mixture of PDLLA and HA was chosen to allow for particle aggregation and the void between particles to be filled with polymer. The coating technique is identical to that used in reference [Paper III], which includes detailed description of the resulting coating including surface characterization with atomic force microscopy and thickness estimation with scanning electron microscopy. Given the coating technique a completely homogeneous composite surface cannot be anticipated due to formation of large HA-particle aggregates before evaporation of the organic solvent. This may result in voids within the bulk material of low HA presence and in HA-aggregate protrusions on the surface. Cross-sectional imaging with transmission electron microscopy of the resulting coatings could enlighten this further. Another aspect which could be further enlightened by cross-sectional imaging of the coated implants with conventional light microscope is the extent, to which the coating alters the surface features of the implant. Porosities in particular may be obstructed by coating material and prevent ingrowth of tissue.

The OPN-COMP coating displayed an overall better mechanical fixation but no significant differences are observed. It is recognized that four weeks observation time evaluates fixation before the mechanical properties of newly formed tissue are fully matured [31]. Further maturation might expand the observed difference. The short observation time, however, has previously proven very sensitive to the impact of bone active surface coatings in a gap model [32]. The results for both implant coatings are similar to that of pure Ha coating as tested with the same *in vivo* model and observation time [33]. It should be noted that the bone tissue around the implant part was not examined histologically following the mechanical test. Although the implants are completely implanted in trabecular bone, the mechanical fixation may be weakened by resorption of the cortical bone surrounding the implant site. This potential bias cannot be accounted for - it is, however, not expected to impact the relative results.

In the inner zone 1 of the implant porocoat a significantly larger amount of newly formed bone was covering the surface of implants coated with OPN-COMP. Furthermore a nonsignificant tendency towards lower fibrous tissue formation is

observed with OPN-COMP. While both coating types are resorbed during the observation time it appears that OPN functionalization improves the ability to guide formation of bone during degradation of the coating. Although the study does not address the tissue response on a cellular level the improved osteoconductivity is presumably a result of induced activity of bone forming cells. Studies evaluating prefunctionalization of 2D surfaces have proven the opportunity of using OPN for controlling the response to a surface *in vitro* [13-16] and *in vivo* [11], whereas releasable proteins in PDLA coatings have proven the opportunity for providing sustained protein activity *in vivo* [34-36]. In present study both modes of protein action must be considered. The improved activation of bone forming cells can be speculated to be either an effect of OPN acting as a surface protein facilitating the cell/material interaction, which was the intention with immobilization on the Ha-particles, or as an effect of OPN being released and acting paracrine. The positive impact of OPN on new bone formation was observed directly on the inner surface of the porosities where the coatings were present preoperatively. This argues that the impact was directly in the cell/material interaction or, in case of a protein release effect, a very localized paracrine effect.

On the outer limit of the implant porocoat corresponding to the inner part of zone 2, a non-significant tendency towards higher ongrowth of bone and lower ongrowth of fibrous tissue is observed on the intervention coated implants. Compared to zone 1, the OPN-COMP coated implants had a lower bone ongrowth and the control had approximately the same ongrowth in zone 2. Apparently the intervention coating had a lower impact in zone 2. Evidently, a larger amount of effective coating material is found in zone 1 caused by the larger area relative to space in the porosity. It could furthermore, be an effect of coating accumulation in the concavities of the implant during the dip-coating procedure which leaves a relatively thinner and less effective coating on the outer beads of the porocoat.

No significant differences are observed in the volumetric tissue fractions of zone 2. In a previous study in our lab of a coating identical with the composite coating without OPN in this study it was correspondingly seen that the osteoconductive effect was limited to the surface of the coating (Paper III).

OPN addition appears to have only local effect, which indicates that the protein activity is in the direct cell/material interaction. It is, nonetheless, not possible with the preparation technique to further elucidate the osteoconductive mechanism as

only tissue type can be distinguished and quantified. It may be that OPN enhances the activity of osteoclasts and osteoblasts directly in the material/tissue interface during material degradation. This was the intended mode of material/tissue interaction, but other scenarios are possible. It may be that the relatively large presence of protein on the particles surfaces changes the degradation profile of the composite thereby changing the presentation of Ha to the implant exterior. The study encourages further research in this new approach for functionalizing composites and particularly in the potential role of OPN from bovine milk in osteoconductive materials.

5. Conclusion

We have shown that preadsorption of osteopontin from bovine milk on the HA particles of a degradable PDLLA/HA composite can enhance the composite osteoconductive properties. The protein and the application approach stimulates further research in composite materials and their versatility as biocompatible materials with controllable properties at the molecular scale. The use of proteins derived from another species, however, should be carefully considered in further research. Within the conceptual frame, including 3D functionalization of a composite material, it may be necessary to develop alternatives to bovine milk OPN. Ease of device fabrication and wide possibilities for advancement in mechanical properties and functionalization of the material might lead to replacement of HA with composites in orthopaedic application areas.

Acknowledgements

The authors wish to thank Tony Meglich and Barbara Stickney for taking care of the animals and Mikkel & Henrik Saxø, Marianne Toft Vestermark and Kazra Zainali for assistance with surgery.

References

1. Annual report 2007. Danish Hip Arthroplasty Registry. 2007.

2. Kärholm J, Herberts P, Hultmark P, Malchau H, Nivbrant B, Thanner J. Radiostereometry of hip prostheses. Review of methodology and clinical results. *Clin Orthop Relat Res* 1997(344):94-110.
3. Ryd L, Albrektsson BE, Carlsson L, Dansgård F, Herberts P, Lindstrand A, Regner L, Toksvig-Larsen S. Roentgen stereophotogrammetric analysis as a predictor of mechanical loosening of knee prostheses. *J Bone Joint Surg Br* 1995;77(3):377-83.
4. Franzén A, Heinegård D. Isolation and characterization of two sialoproteins present only in bone calcified matrix. *Biochem J* 1985;232(3):715-24.
5. McKee MD, Nanci A. Osteopontin at mineralized tissue interfaces in bone, teeth, and osseointegrated implants: ultrastructural distribution and implications for mineralized tissue formation, turnover, and repair. *Microsc Res Tech* 1996;33(2):141-64.
6. Duvall CL, Taylor WR, Weiss D, Wojtowicz AM, Guldborg RE. Impaired angiogenesis, early callus formation, and late stage remodeling in fracture healing of osteopontin-deficient mice. *J Bone Miner Res* 2007;22(2):286-97.
7. Franzén A, Hulthenby K, Reinholt FP, Onnerfjord P, Heinegård D. Altered osteoclast development and function in osteopontin deficient mice. *J Orthop Res* 2008;26(5):721-8.
8. Ishijima M, Rittling SR, Yamashita T, Tsuji K, Kurosawa H, Nifuji A, Denhardt DT, Noda M. Enhancement of osteoclastic bone resorption and suppression of osteoblastic bone formation in response to reduced mechanical stress do not occur in the absence of osteopontin. *J Exp Med* 2001;193(3):399-404.
9. Yoshitake H, Rittling SR, Denhardt DT, Noda M. Osteopontin-deficient mice are resistant to ovariectomy-induced bone resorption. *Proc Natl Acad Sci U S A* 1999;96(14):8156-60.
10. Asou Y, Rittling SR, Yoshitake H, Tsuji K, Shinomiya K, Nifuji A, Denhardt DT, Noda M. Osteopontin facilitates angiogenesis, accumulation of osteoclasts, and resorption in ectopic bone. *Endocrinology* 2001;142(3):1325-32.
11. Liu L, Chen G, Chao T, Ratner BD, Sage EH, Jiang S. Reduced foreign body reaction to implanted biomaterials by surface treatment with oriented osteopontin. *J Biomater Sci Polym Ed* 2008;19(6):821-35.
12. Tsai AT, Rice J, Scatena M, Liaw L, Ratner BD, Giachelli CM. The role of osteopontin in foreign body giant cell formation. *Biomaterials* 2005;26(29):5835-43.
13. Bernards MT, Qin C, Jiang S. MC3T3-E1 cell adhesion to hydroxyapatite with adsorbed bone sialoprotein, bone osteopontin, and bovine serum albumin. *Colloids Surf B Biointerfaces* 2008;64(2):236-247.
14. Lee YJ, Park SJ, Lee WK, Ko JS, Kim HM. MG63 osteoblastic cell adhesion to the hydrophobic surface precoated with recombinant osteopontin fragments. *Biomaterials* 2003;24(6):1059-66.
15. Liu L, Chen S, Giachelli CM, Ratner BD, Jiang S. Controlling osteopontin orientation on surfaces to modulate endothelial cell adhesion. *J Biomed Mater Res A* 2005;74(1):23-31.
16. Liu L, Qin C, Butler WT, Ratner BD, Jiang S. Controlling the orientation of bone osteopontin via its specific binding with collagen I to modulate osteoblast adhesion. *J Biomed Mater Res A* 2007;80(1):102-10.

17. Smith LL, Cheung HK, Ling LE, Chen J, Sheppard D, Pytela R, Giachelli CM. Osteopontin N-terminal domain contains a cryptic adhesive sequence recognized by $\alpha 9 \beta 1$ integrin. *J Biol Chem* 1996;271(45):28485-91.
18. Gordjestani M, Dermaut L, De Ridder L, De Waele P, De Leersnijder W, Bosman F. Osteopontin and bone metabolism in healing cranial defects in rabbits. *Int J Oral Maxillofac Surg* 2006;35(12):1127-32.
19. Hasegawa S, Neo M, Tamura J, Fujibayashi S, Takemoto M, Shikinami Y, Okazaki K, Nakamura T. In vivo evaluation of a porous hydroxyapatite/poly-DL-lactide composite for bone tissue engineering. *J Biomed Mater Res A* 2007;81(4):930-8.
20. Hasegawa S, Tamura J, Neo M, Goto K, Shikinami Y, Saito M, Kita M, Nakamura T. In vivo evaluation of a porous hydroxyapatite/poly-DL-lactide composite for use as a bone substitute. *J Biomed Mater Res A* 2005;75(3):567-79.
21. Kim SS, Sun Park M, Jeon O, Yong Choi C, Kim BS. Poly(lactide-co-glycolide)/hydroxyapatite composite scaffolds for bone tissue engineering. *Biomaterials* 2006;27(8):1399-409.
22. Heo SJ, Kim SE, Wei J, Hyun YT, Yun HS, Kim DH, Shin JW. Fabrication and characterization of novel nano- and micro-HA/PCL composite scaffolds using a modified rapid prototyping process. *J Biomed Mater Res A* 2008.
23. Ducheyne P, Qiu Q. Bioactive ceramics: the effect of surface reactivity on bone formation and bone cell function. *Biomaterials* 1999;20(23-24):2287-303.
24. Smith TS. Characterization of Porous Coatings. In: *Advances in Biomaterials*, edited by Lee SM, CRC Press, 1987.
25. Baas J. Adjuvant therapies of bone graft around non-cemented experimental orthopedic implants stereological methods and experiments in dogs. *Acta Orthop Suppl* 2008;79(330):1-43.
26. Noble PC, Alexander JW, Lindahl LJ, Yew DT, Granberry WM, Tullos HS. The anatomic basis of femoral component design. *Clin Orthop Relat Res* 1988(235):148-65.
27. Schimmel JW, Huiskes R. Primary fit of the Lord cementless total hip. A geometric study in cadavers. *Acta Orthop Scand* 1988;59(6):638-42.
28. Kazanekki CC, Uzwiak DJ, Denhardt DT. Control of osteopontin signaling and function by post-translational phosphorylation and protein folding. *J Cell Biochem* 2007;102(4):912-24.
29. Razzouk S, Brunn JC, Qin C, Tye CE, Goldberg HA, Butler WT. Osteopontin posttranslational modifications, possibly phosphorylation, are required for in vitro bone resorption but not osteoclast adhesion. *Bone* 2002;30(1):40-7.
30. Capriotti LA, Beebe TP, Jr., Schneider JP. Hydroxyapatite surface-induced peptide folding. *J Am Chem Soc* 2007;129(16):5281-7.
31. Brånemark R, Öhrnell LO, Nilsson P, Thomsen P. Biomechanical characterization of osseointegration during healing: an experimental in vivo study in the rat. *Biomaterials* 1997;18(14):969-78.
32. Søballe K, Hansen ES, Brockstedt-Rasmussen H, Pedersen CM, Bunger C. Hydroxyapatite coating enhances fixation of porous coated implants. A comparison in dogs between press fit and noninterference fit. *Acta Orthop Scand* 1990;61(4):299-306.

33. Mouzin O, Søballe K, Bechtold JE. Loading improves anchorage of hydroxyapatite implants more than titanium implants. *J Biomed Mater Res* 2001;58(1):61-8.
34. Lamberg A, Schmidmaier G, Søballe K, Elmengaard B. Locally delivered TGF-beta1 and IGF-1 enhance the fixation of titanium implants: a study in dogs. *Acta Orthop* 2006;77(5):799-805.
35. Schmidmaier G, Wildemann B, Ostapowicz D, Kandziora F, Stange R, Haas NP, Raschke M. Long-term effects of local growth factor (IGF-I and TGF-beta 1) treatment on fracture healing. A safety study for using growth factors. *J Orthop Res* 2004;22(3):514-9.
36. Wildemann B, Sander A, Schwabe P, Lucke M, Stockle U, Raschke M, Haas NP, Schmidmaier G. Short term in vivo biocompatibility testing of biodegradable poly(D,L-lactide)--growth factor coating for orthopaedic implants. *Biomaterials* 2005;26(18):4035-40.

List of not appended papers

- I. The influence of fibronectin coated nano-meter scale topography on Human pulp derived stem cells**
Dolatshahi-Pirouz A, Jensen T, Kraft D, Foss M, Hansen JL, Larsen AM, Chevallier J, Besenbacher F.
Biomaterials (submitted)
- II. The effect of nanorough platinum surfaces on fibrin polymerization, monocyte cell adhesion and cell morphology**
Dolatshahi-Pirouz A, Jensen T, Vorup-Jensen T, Foss M, Chevallier J, Besenbacher F.
(In preparation)
- III. Influence of Nanoroughness and detailed surface morphology on structural properties water-coupling capabilities of surface-bound fibrinogen films.**
Dolatshahi-Pirouz A, Skeldal S, Hovgaard M, Jensen T, Foss M, Chevallier J, Besenbacher F.
J. Phys. Chem. C **2009**, *113*, 4406-4412
- IV. Synthesis of functional coatings via colloidal mask templating and glancing angle deposition (GLAD)**
Dolatshahi-Pirouz A, Jensen T, Vorup-Jensen T, Bech R, Chevallier J, Besenbacher F, Foss M, Sutherland D.
(In preparation)
- V. Thermodynamics of osteopontin adsorption on hydroxyapatite and gold**
Dolatshahi-Pirouz A, Kolman N, Arpanaei A, Jensen T, Foss M, Chevallier J, Kingshott P, Baas J, Søballe K, Besenbacher F.
(In preparation)

THESES FROM THE ORTHOPAEDIC RESEARCH GROUP

*PhD and Doctoral Theses from the Orthopaedic Research Group, www.orthoresearch.dk,
University Hospital of Aarhus, Denmark*

PhD Theses

1. Polyethylene Wear Analysis. Experimental and Clinical Studies in Total Hip Arthroplasty.
Maiken Stilling, June 2009
www.statsbiblioteket.dk
2. Surgical Advances in Periacetabular Osteotomy for Treatment of Hip Dysplasia in Adults
Anders Troelsen, March 2009
Acta Orthopaedica (Suppl 332) 2009;80
3. The Influence of Local Bisphosphonate Treatment on Implant Fixation
Thomas Vestergaard Jakobsen, December 2008
www.statsbiblioteket.dk
4. Adjuvant therapies of bone graft around non-cemented experimental orthopaedic implants. Stereological methods and experiments in dogs
Jørgen Baas, July 2008
Acta Orthopaedica (Suppl 330) 2008;79
5. CoCrMo alloy, *in vitro* and *in vivo* studies
Stig Storgaard Jakobsen, June 2008
www.statsbiblioteket.dk
6. Rehabilitation outcome after total hip replacement; prospective randomized studies evaluating two different postoperative regimes and two different types of implants
Mette Krintel Petersen, June 2008
www.statsbiblioteket.dk
7. Efficacy, effectiveness, and efficiency of accelerated perioperative care and rehabilitation intervention after hip and knee arthroplasty
Kristian Larsen, May 2008
www.statsbiblioteket.dk
8. Rehabilitation of patients aged over 65 years after total hip replacement - based on patients' health status
Britta Hørdam, February 2008
www.statsbiblioteket.dk
9. Evaluation of Bernese periacetabular osteotomy; Prospective studies examining projected load-bearing area, bone density, cartilage thickness and migration
Inger Mechlenburg, August 2007
Acta Orthopaedica (Suppl 329) 2008;79
10. Combination of TGF- β 1 and IGF-1 in a biodegradable coating. The effect on implant fixation and osseointegration and designing a new *in vivo* model for testing the osteogenic effect of micro-structures *in vivo*
Anders Lamberg, June 2007
www.statsbiblioteket.dk
11. On the longevity of cemented hip prosthesis and the influence on implant design
Mette Ørskov Sjøland, April 2007
www.statsbiblioteket.dk

12. Reaming procedure and migration of the uncemented acetabular component in total hip replacement
Thomas Baad-Hansen, February 2007
www.statsbiblioteket.dk
13. Studies based on the Danish Hip Arthroplasty Registry
Alma B. Pedersen, 2006
www.statsbiblioteket.dk
14. DEXA-scanning in description of bone remodeling and osteolysis around cementless acetabular cups
Mogens Berg Laursen, November 2005
www.statsbiblioteket.dk
15. Biological response to wear debris after total hip arthroplasty using different bearing materials
Marianne Nygaard, June 2005
www.bibliotek.dk
16. The influence of RGD peptide surface modification on the fixation of orthopaedic implants
Brian Elmengaard, December 2004
www.statsbiblioteket.dk
17. Stimulation and substitution of bone allograft around non-cemented implants
Thomas Bo Jensen, October 2003
www.statsbiblioteket.dk
18. Surgical technique's influence on femoral fracture risk and implant fixation. Compaction versus conventional bone removing techniques
Søren Kold, January 2003
www.statsbiblioteket.dk
19. The influence of hydroxyapatite coating on the peri-implant migration of polyethylene particles
Ole Rahbek, October 2002
www.statsbiblioteket.dk
20. Gene delivery to articular cartilage
Michael Ulrich-Vinther, September 2002
www.statsbiblioteket.dk
21. In vivo and vitro stimulation of bone formation with local growth factors
Martin Lind, January 1996
www.statsbiblioteket.dk

Doctoral Theses

1. Gene therapy methods in bone and joint disorders. Evaluation of the adeno-associated virus vector in experimental models of articular cartilage disorders, periprosthetic osteolysis and bone healing
Michael Ulrich-Vinther, March 2007
Acta Orthopaedica (Suppl 325) 2007;78
2. Adult hip dysplasia and osteoarthritis. Studies in radiology and clinical epidemiology
Steffen Jacobsen, December 2006
Acta Orthopaedica (Suppl 324) 2006;77
3. Calcium phosphate coatings for fixation of bone implants. Evaluated mechanically and histologically by stereological methods
Søren Overgaard, 2000
Acta Orthop Scand (Suppl 297) 2000;71

4. Growth factor stimulation of bone healing. Effects on osteoblasts, osteomies, and implants fixation
Martin Lind, October 1998
Acta Orthop Scand (Suppl 283) 1998;69
5. Hydroxyapatite ceramic coating for bone implant fixation. Mechanical and histological studies in dogs
Kjeld Søballe, 1993
Acta Orthop Scand (Suppl 255) 1993;54